7-4-2022 2:00 PM

# Applications of Gradient Representations in Resting-State fMRI

Geoffrey Ngo, *The University of Western Ontario*

Supervisor: Menon, Ravi S., *The University of Western Ontario*

A thesis submitted in partial fulfillment of the requirements for the Doctor of Philosophy degree in Medical Biophysics

# Abstract

Classical models of brain organization have often considered the brain to be made up of a mosaic of patches that are demarcated by discrete boundaries, often defined histologically. In contrast, emerging views have pointed towards an alternative paradigm – referred to as gradients – by conceptualizing brain organization as sets of organizational axes that characterizes spatial variation of differing connectivity principles over the extent of a region. Such organizational axes provide a well-suited framework for elucidating underpinnings of brain connectivity and has garnered widespread attention across various domains of neuroimaging. This work seeks to explore various applications of gradient estimation techniques, in combination with resting-state functional connectivity data, across the fields of basic, comparative, and clinical neuroscience.

First, gradient estimation was performed on resting-state functional connectivity (RSFC) patterns of the primary somatosensory cortex to unveil a secondary organizational axis that spans the region's anterior-posterior axis, akin to circuitry fundamental to sensory cortical information processing. Second, gradient techniques were used in a cross-species comparison study to unify connectivity principles of humans and marmosets by mapping them simultaneously onto a set of organizational axes. In doing so, this provided a systematic framework to compare the functional architecture of both species, facilitating novel insight of a well-integrated default-mode network in humans, compared to marmosets. Third, connectivity gradients, along with a myriad of other resting-state fMRI features were used to explore the implications of focal lesion pathophysiology on functional organization of the thalamus in individuals with Multiple Sclerosis. A lack of focal changes to resting-state related features was observed suggesting the limited role of focal thalamic lesions to functional organization in MS.

Together, these different avenues of research highlight the capacity for a gradient-centric view in neuroimaging to provide profound insights into brain organization, and its utility across the applications of basic, comparative, and clinical neuroscience.

## Summary for Lay Audience

Brain structure maps have typically been described by a set of areas separated by borders, much like countries on the globe. In this manner, brain mapping may overlook more subtle details of the brain – analogous to detailing a country's cities and neighbourhoods – that are equally important for understanding how brain functions arise. Towards this latter goal, the notion of *gradients* has been proposed as a way to reveal more nuanced details of the brain. Gradients in brain organization have emerged as a powerful approach for studying different fields of imaging neuroscience. In this thesis, gradients are broadly applied to study finer-grained connectional principles of the brain in domains of basic, comparative, and clinical neuroscience.

The first chapter applies gradients to the primary somatosensory cortex (S1) of the brain, revealing detailed connections that reflect the classical notion of information processing within this brain region. Additionally, this connectivity gradient demonstrated excellent correspondence to S1's structural properties, which previously have gone underappreciated. Collectively, this insight provides a way to link local brain structure and connectivity properties within S1 to one another, providing a principled approach for studying their interplay in clinical populations.

The second chapter uses gradients to systematically compare the human and marmoset brain. In doing so, differences in default-mode network brain organization were revealed. Given the importance of marmosets as a preclinical animal model, this difference may provide fundamental insights towards the limitations of the marmoset as an animal model for studying cognitive function, for which the default-mode network is thought to play a critical role in.

The third chapter uses gradients (in addition to other approaches) to provide a simplified view of neuronal and connectivity principles in the human thalamus following neural degeneration – specifically from Multiple Sclerosis lesions. No obvious qualitative disruptions of thalamic organization were observed when using a myriad of approaches. This may suggest that lesions in the thalamus do not play a substantial role in mediating thalamic reorganization in Multiple Sclerosis.

Overall, this thesis demonstrates the wide use of gradients to study brain organization across various applications of imaging neuroscience. This demonstrates the collective versatility and receptiveness of gradients as a general investigative tool for studying brain mapping.

## Keywords

Gradient estimation, brain organization, resting-state fMRI, resting-state functional connectivity, somatosensory cortex, marmosets, default-mode network, Multiple Sclerosis

# Co-Authorship Statement

The following thesis is presented in Integrated Article format and contains one published and two unpublished manuscripts.

**Chapter 2**: Ngo, G. N., Haak, K. V., Beckmann, C. F., & Menon, R. S. (2021). Mesoscale hierarchical organization of primary somatosensory cortex captured by resting-state-fMRI in humans. NeuroImage, 235, 118031. https://doi.org/10.1016/j.neuroimage.2021.118031

- Geoffrey N. Ngo: Project conceptualization, data processing, formal analysis, and writing of original draft of the manuscript.
- Dr. Koen V. Haak: Project conceptualization, provision of software, and revision of manuscript.
- Dr. Christian F. Beckmann: Project conceptualization, provision of software, and revision of manuscript.
- Dr. Ravi S. Menon: Project conceptualization, supervision and guidance, and revision of manuscript.

**Chapter 3**: Ngo, G. N., Hori, Y., Everling, S., & Menon, R. S. Joint-embeddings reveal functional differences in default-mode network architecture between marmosets and humans. (In preparation)

- Geoffrey N. Ngo: Project conceptualization, data processing, formal analysis, and writing of original draft of the manuscript.
- Dr. Yuki Hori: Project conceptualization, data processing, and revision of manuscript.
- Dr. Stefan Everling: Project conceptualization, and revision of manuscript.
- Dr. Ravi S. Menon: Project conceptualization, supervision and guidance, and revision of manuscript.

**Chapter 4**: Ngo, G. N., Morrow S. A., & Menon, R. S. Charting the effects of thalamic lesions on resting-state fMRI features in secondary-progressive Multiple Sclerosis. (In preparation)

- Geoffrey N. Ngo: Project conceptualization, data processing, formal analysis, and writing of original draft of the manuscript.
- Dr. Sarah A. Morrow: Project conceptualization, patient recruitment and evaluation, and revision of manuscript.
- Dr. Ravi S. Menon: Project conceptualization, supervision and guidance, and revision of manuscript.

# Acknowledgments

First and foremost, I would like to thank Ravi Menon for providing the opportunity to pursue a PhD in his interdisciplinary lab under his supervision. I am very grateful for his unwavering support throughout the past five years, providing me the flexibility to learn and engage in a broad range of research endeavours, and for constantly reminding me to reconsider the *big picture* when pursuing these various lines of research. I would like to thank my advisory committee members: Drs. Sarah Morrow, and Ali Khan, for their support and advice throughout my degree.

I would like to thank the CFMM (Center of Functional and Metabolic Mapping) for all their help to make a large portion of this research possible. This includes providing the immense administrative assistance in coordinating the longitudinal Multiple Sclerosis study, developing, and maintaining their advanced MR imaging capabilities, and ultimately acquiring all of the MR images from our research participants. I would like to extend this gratitude to the clinical team, led by Dr. Sarah Morrow who actively recruited participants for this study, and Heather Rosehart who was instrumental in the collective coordination of this research project. Additionally, I would like to give special thanks to all our participants for their generous commitment of time to research, without whom, would have made this research impossible. To all my other colleagues and friends in the lab, former and present, thank you for all your support throughout my PhD.

I would like to extend my thanks to Christian Beckmann for hosting me in his lab at the Donders Institute for a collaborative fellowship in the Spring of 2019. Many thanks also to Koen Haak for providing me the support and mentorship during this time and ultimately providing inspiration for my first paper.

Krystal, I could not have asked for a better person to share this journey with. Your never-ending support has enriched my past five years, motivating me to be my best self, and whose unparalleled encouragement has given me the innate desire to finish my PhD. Thank you for taking care of our dogs when I was at my busiest. Finally, I would like to thank my family; my parents, who have been supportive at every step throughout my academic endeavours, and my brother, who provided unconditional support throughout my PhD, and who at times, showed

more interest in my own research than myself. Lastly, I need to thank my two dogs, Pebbles and Remi, who have given me unconditional love through the ups and downs of my PhD journey.

# Table of Contents

# List of Tables

# List of Figures

# List of Abbreviations and Symbols

| | |
|---|---|
| A1 | Primary auditory cortex |
| ACF | Autocorrelation function |
| AD | Axial diffusivity |
| AN | Anterior nucleus |
| BOLD | Blood oxygen level-dependent signal |
| CBF | Cerebral blood flow |
| CON | Cingulo-opercular network |
| dlPFC | Dorsolateral prefrontal cortex |
| DMN | Default-mode network |
| DSC | Dice similarity coefficient |
| DTI | Diffusion tensor imaging |
| FA | Fractional anisotropy |
| FD | Framewise displacement |
| FEF | Frontal eye fields |
| fMRI | Functional magnetic resonance imaging |
| FPN | Frontoparietal network |
| FWHM | Full-width half max |
| HCP | Human Connectome Project |
| ICA | Independent component analysis |
| IL | Internal lamina |
| LGN | Lateral geniculate nucleus |
| LH | Left hemisphere |
| LL | Lower limb |
| LP | Lateral posterior |
| M1 | Primary motor cortex |
| MD | Medial dorsal |
| MGN | Medial geniculate nucleus |
| MNI | Montreal Neurological Institute |
| mPFC | Medial prefrontal cortex |
| MR | Magnetic resonance |
| MRI | Magnetic resonance imaging |
| MS | Multiple Sclerosis |

| | |
|---|---|
| MT | Middle temporal visual area |
| NHP | Non-human primate |
| NIH | National Institutes of Health |
| PCC | Posterior cingulate cortex |
| PD | Parkinson's Disease |
| PET | Positron emission tomography |
| PO | Posterior nucleus |
| PPC | Posterior parietal cortex |
| PuA | Anterior pulvinar |
| PuI | Inferior pulvinar |
| PuL | Lateral pulvinar |
| PuM | Medial pulvinar |
| RD | Radial diffusivity |
| RH | Right hemisphere |
| ROI | Region of interest |
| RSFC | Resting-state functional connectivity |
| rsfMRI | Resting-state functional magnetic resonance imaging |
| RSN | Resting-state network |
| S1 | Primary somatosensory cortex |
| S2 | Secondary somatosensory cortex |
| SD | Standard deviation |
| SEM | Standard error of the mean |
| SNR | Signal-to-noise ratio |
| SPMS | Secondary-progressive Multiple Sclerosis |
| T | Trunk |
| tSNR | Temporal signal-to-noise ratio |
| UL | Upper limb |
| UWO | Western University |
| V1 | Primary visual cortex |
| V2 | Secondary visual cortex |
| VA | Ventral anterior |
| VM | Ventral medial |
| VP | Ventral posterior |

# List of Appendices

# Chapter 1

# 1 General Introduction

## 1.1 Brain Organization

The human brain is an extraordinarily complex, interwoven, and scaffolded structure, serving as a substrate for the human mind while coordinating most of the body's critical functions. Central to understanding brain function is the concept of brain organization, broadly referring to the blueprint, or spatial arrangements of cortical areas, and their connections that underlie these functional processes. The brain works concurrently at different organizational levels, from microscale – cellular scale of neurons that form the basic building blocks of brain architecture – to macroscale – the aggregation of these building blocks that form larger cortical areas. Brain organization through varying connectional properties enables integration of information that likely gives rise to unique brain functions and human behaviours (Jbabdi et al. 2013). Indeed, individualized connectivity mapping has predictive value for localizing functional brain regions in both healthy (Tavor et al. 2015) and clinical populations (Wang et al. 2015), on a single subject basis. Furthermore, these connectivity maps can be used to characterize inter-individual connectivity differences (Finn et al. 2015) and their associations to human behaviour (Kong et al. 2019). Although immense progress has been made in the field of brain mapping thus far, the need to elucidate finer-grained details of brain organization continues to be a major goal within clinical and cognitive neuroscience.

### 1.1.1 Microscale architecture

In the early 20$^{th}$ century, the first characterization of human cerebral cortex microstructure was performed by describing the spatial distribution of neuronal cell bodies – referred to as cytoarchitecture – and myelinated nerve fibers – referred to as myeloarchitecture – in the works by Korbinian Brodmann and the Vogts, respectively (Brodmann, 1909; Vogt and Vogt, 1919). These features of microstructure revealed sharp demarcations between areas of the brain, describing compartmentalization of the cerebral cortex into many seemingly homogeneous cortical areas. At the time, the prevalent notion was that each

cortical area ascribed to a unique role, thus reinforcing the importance of each region for brain function. Although the Vogts described 185 cortical areas and Brodmann described only 43, the Vogts believed that Brodmann may have underestimated the number of cortical areas as they were convinced, upon further inspection of cyto- and myeloarchectonic maps, that boundaries coincided across imaging techniques (or modalities). Other contemporaries at this time also developed their own accounts of cerebral cortex cytoarchitecture, providing their own brain maps consisting of 150 areas (more than what Brodmann had estimated). These later contributions noted that some boundaries between cortical areas were more subtle, which ultimately led to inconsistencies in the reported number of brain areas (Von Economo and Koskinas, 1925). Continued research efforts have aimed to refine cytoarchitectonic brain maps by mitigating problems of inter-observer bias and inter-subject variability, and have led to subsequent iterations of cytoarchitectonic cortical area maps (Amunts et al. 2005; Caspers et al. 2006; Scheperjans et al. 2008; Caspers et al. 2013). It is important to note that evidence for some boundaries may be predicated on more complicated and subtle transitional patterns determined by quantitative methods, rather than sudden changes in cytoarchitecture that are qualitatively visible in these maps. For example, this is observed in the proposed boundary between secondary visual cortex (V2, or BA 18) and dorsally adjacent area hOc3d (Kujovic et al. 2013).

This ambiguity of boundary issues was acknowledged by Percival Bailey and Gerhardt von Bonin who proposed that parcellations did not fundamentally acknowledge the apparent heterogeneity of cytoarchitectonic data, suggesting that brain organization is optimally represented by gradual transitions, as opposed to homogeneous cortical areas (Bailey and von Bonin, 1951). They emphasized that although boundaries between Brodmann areas 17 and 18 are very clear, and boundaries between areas 18 and 19 are relatively vague, all three areas are nonetheless considered unique, providing a misleading representation of the data. That is, dividing the brain into distinct cortical areas does not reflect the extent to which these areas differ from one another, thus warranting further consideration on how best to represent brain organization.

Convergence of multimodal evidence towards the goal of defining cortical areas is another important factor in understanding brain organization. The integration of more modern techniques, such as quantitative in vitro receptor autoradiography (Zilles et al. 2002; Zilles et al. 2004; Amunts et al. 2010; Zilles and Amunts, 2009), gene expression assays (Hawrylycz et al. 2012), and positron emission tomography (PET) (Hansen et al. 2022), have provided different interpretations of brain architecture based on neurotransmitter receptor density, cortical gene expression, and mapping of neurotransmitter systems, respectively. Although some of these findings are consistent with cyto- and myeloarchitecture descriptions of brain parcellations, others suggest evidence towards the further division of these parcels into finer-grained areas.

Another fundamental property of brain organization is neural connectivity. Each cytoarchitectonic area corresponds to a different connectivity pattern with other cortical and deep brain areas, implying that connections observed on either side of a boundary will correspond to different pathways. Although this was primarily demonstrated ex-vivo within motor and somatosensory cortices of non-human primates [Burton et al.1995; Krubitzer et al. 1995], this concept is generally well-accepted in the field. More recently, congruent findings linking similarity of cytoarchitecture to anatomical connections have been demonstrated as a general governing principle across mammalian species, further emphasizing the importance of connectivity to cortical areas (Goulas et al. 2019).

### 1.1.2 Macroscale architecture

In the modern era of non-invasive, in-vivo neuroimaging, magnetic resonance imaging (MRI) has produced many metrics for indexing the brain's macroscale architecture – that is, on the scale of whole brain areas. Such metrics include, but are not limited to, cortical morphology (a surrogate of cyto- and myeloarchitecture), and large scale communication pathways. Such macroscale measurements have afforded a similar breadth of information that has been shown to reflect brain architecture outlined on the microscale level. For example, proposed MRI myelin surrogates have enabled clear demarcation of heavily myelinated regions of sensory areas that have been described in microscale architecture (Glasser et al. 2011). Furthermore, MRI-myelin surrogates have also demonstrated utility beyond the resolution of brain areas, specifically examining columnar and inter- and intra-

brain area profiles (Dinse et al. 2015; Geyer et al. 2011; Aggarwal et al. 2015; Glasser et al. 2011; Augustinack et al. 2014). However, some early in-vivo brain mappings of gyri and sulci (Lancaster et al. 2000; Tzourio-Mazoyer et al. 2002) do not correspond well with microscale architecture, despite providing consistent inter-subject landmarks that are useful in other applications (Robinson et al. 2014). For example, cortical morphology does not delineate boundaries between Brodmann area 4 and premotor cortex, whereas evidence of this is observed with microscale architecture (Geyer 2005).

## 1.2 Macroscale Connectivity

In-vivo structural and functional connectivity measures – referring to the estimation of large-scale connections between brain areas – are perhaps some of the most popular MRI methods used to study macroscale brain architecture. These include both diffusion weighted imaging and resting-state functional magnetic resonance imaging (fMRI).

Diffusion weighted imaging is an MRI technique that is sensitive to the diffusion of water molecules within various compartments of the brain (Le Bihan and Breton, 1985). Exploitation of restricted water diffusion processes have afforded the opportunity to delineate the orientation of axon fiber bundles – that is, the direction of anatomical connections, and subsequently using computational approaches, have permitted for estimations of connections between brain regions. This process, commonly referred to as tractography, has allowed for estimations of prominent fiber bundles (Jbabdi et al. 2015), and in-vivo annotation of the thalamus into coarse nuclei (Behrens et al. 2003). However, one criticism of tractography is the occasional estimation of false-positive tracts (Maier-Hein et al. 2017).

An alternative technique to infer macroscale brain connectivity is using resting-state functional connectivity (RSFC), which measures the statistical correlation of blood oxygen-level dependent signal (BOLD) between brain regions while the participant is at ‘rest’ (Biswal et al. 1995). Here, ‘rest’ refers to a task-free state in which the participant is asked to either stare at a fixed location, or keep their eyes closed without focusing their thoughts on anything in particular. BOLD relies on a neurovascular coupling effect that links neuronal activity to changes in cerebral blood flow and oxygenation. The BOLD

signal provides an indirect measure of neural activity that can be obtained using MRI. As resting-state fMRI (rsfMRI) is only concerned with association of inter-region BOLD activity, it follows that inference of connections cannot determine the nature of the anatomical connection. For example, rsfMRI would not be able to deduce whether observed connectivity arises due to polysynaptic connections, or monosynaptic connection. Herein, connectivity inferred by rsfMRI will be referred to as resting-state functional connectivity, or simply, functional connectivity. In this thesis, all three experiments (Chapters 3 through 5) will focus on the technique of rsfMRI as a method to provide inference on macroscale connectivity.

### 1.2.1 Blood oxygenation level-dependent signal (BOLD)

Neural brain activity has a high energy demand, which consequently requires a constant and large supply of oxygen to the site of activity. This supply is provided by hemoglobin, an iron-rich protein found in red blood cells that supplies oxygen when metabolic demand increases. Oxygen-saturated hemoglobin is referred to as oxyhemoglobin, whereas non-saturated hemoglobin is referred to as deoxyhemoglobin after it has released at least one of its four bounded oxygen molecules. To achieve a sufficient supply of oxygen, a cascade of metabolic events occurs and includes, initial vasodilation leading to increases in cerebral blood volume, a subsequent increase in blood flow and oxyhemoglobin (significantly more than is required by the active neurons), and finally a decrease in deoxyhemoglobin. This leads to a local increase in the ratio of oxyhemoglobin to deoxyhemoglobin (or blood oxygenation levels) in the veins and capillaries near the neural activity site. These fluctuations in blood oxygenation are represented in fMRI BOLD signals (Ogawa et al. 1990).

In fMRI, T2*-weighted images are the conventional contrast used to track changes in blood oxygenation. In the context of BOLD, the primary driver of the T2*-weighted contrast is hemoglobin. More specifically, oxyhemoglobin is diamagnetic, and deoxyhemoglobin is paramagnetic (Pauling and Coryell, 1936). With neural activity, increases in blood oxygenation leads to (1) a local shift in magnetic susceptibility, and (2) an increase in T2 of the blood, such that T2*-weighted signal increases (Thulborn et al. 1982). Taken together, changes in blood oxygenation modulates the T2*-weighted signal, thus allowing

for the inference of connectivity by assessing the synchrony of two brain area's BOLD-modulated time series. Figure 1.1 provides a schematic of the BOLD response as measured by fMRI.

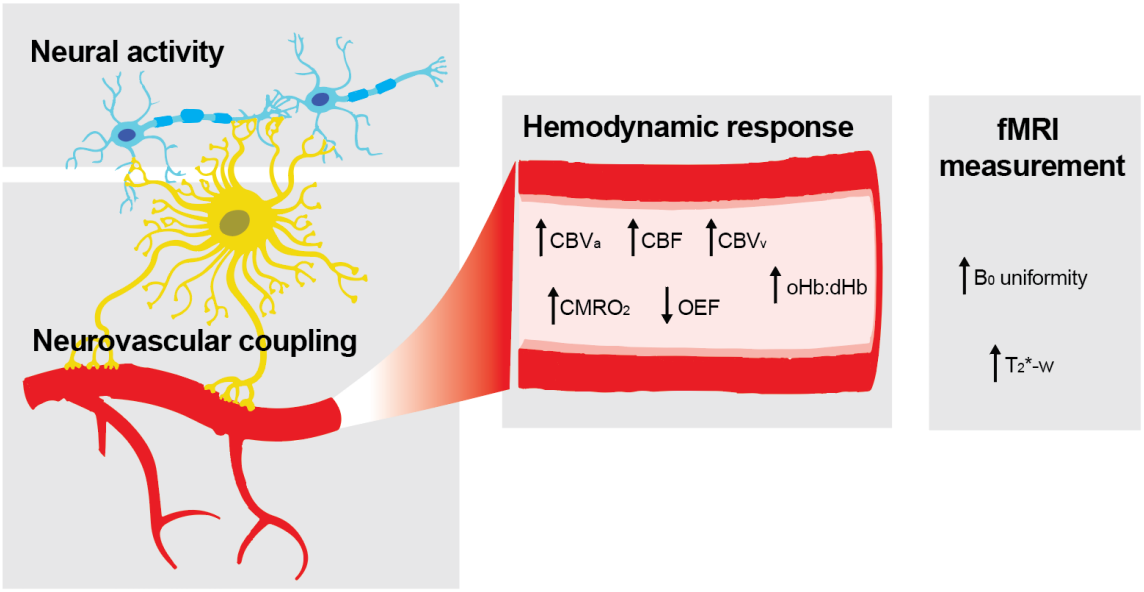


**Figure 1.1 A simple depiction of the BOLD response as measured in fMRI**

*The BOLD response begins with increased neural activity that initiates a complex neurovascular coupling cascade. This causes the hemodynamic response resulting in changes to numerous mediators, ultimately leading to changes in blood oxygenation levels (oHb:dHb). Dynamic changes in local deoxyhemoglobin concentrations modulates $T_2$*-weighted BOLD contrast which is measured by fMRI. Known mediators of the hemodynamic response includes arterial cerebral blood volume ($CBV_a$), cerebral blood flow (CBF), venous cerebral blood volume ($CBV_v$), cerebral vascular reactivity ($CMRO_2$), and oxygen extraction fraction (OEF).*

### 1.2.2 Functional magnetic resonance imaging paradigms

The two most common paradigms considered when collecting fMRI data are (1) task-based and (2) resting-state. In the former, fMRI data is collected while participants are performing a cognitive task in the MRI scanner. Here, the goal is to identify brain regions that are neuronally activated during the experimental paradigm to subsequently infer a brain area's

functional role. Many tasks have been developed and investigated to probe the vast range of cognitive processes and includes, but is not limited to, somatomotor, motor, visual, auditory, working memory, and emotional processes (Barch et al. 2013). The second paradigm, commonly referred to as resting-state fMRI (task-free), requires the participant to be scanned in a state of rest whereby they are told to either keep their eyes-closed, or open and fixated on a crosshair while letting their thoughts wander freely. As will be discussed in more detail in subsequent sections, rsfMRI provides a convenient way to probe brain organization without requiring external stimuli. Participants typically undergo multiple 10–15-minute scans in order to improve statistical power of analyses, especially in research settings.

In 1995, Biswal and colleagues measured resting-state fMRI in humans and found that low frequency (<0.1 Hz) BOLD time series of separate motor areas were strongly correlated with one another (Biswal et al. 1995), demonstrating the first use of rsfMRI to investigate functional connectivity. Subsequent studies have since used rsfMRI to map large-scale resting-state brain networks composed of distributed brain areas (Beckmann et al. 2005; Greicius et al. 2003; De Luca et al. 2005; Fox and Raichle, 2007; Fox et al. 2005), while demonstrating their replicability in subjects (Damoiseaux et al. 2006) and correspondence with brain activations from task-based paradigms (Smith et al. 2009). Although it is not a direct measure of anatomical connectivity, RSFC appears to provide insight into macroscale connectivity architecture (Vincent et al. 2007; Honey et al. 2009; Adachi et al. 2012) and presents itself as a viable in vivo tool for probing brain organization. Resting-state fMRI provides a unifying approach to probe whole brain organization in a single imaging session, which would otherwise not be possible with task-based fMRI paradigms.

### 1.2.3 The connectome

Resting-state functional connectivity investigations have often opted to use the "connectome" framework for studying brain organization (Sporns and Honey, 2006). In this framework, brain areas are referred to as nodes, and connections between brain areas as edges. Within the realm of rsfMRI, nodes are defined by sets of brain areas, or, "regions of interest (ROIs)", and mean time series values can be extracted from each ROI to represent the neural activity of the brain area. Subsequently, edges between pairs of ROIs

can be computed using the Pearson correlation coefficient – a statistical measure of linear dependency between two time series – as a way to assess the strength of their functional connectivity. Other edge metrics have also been proposed with the goal of achieving a more direct measure of connectivity, such as partial correlation (Marrelec et al. 2006), or to determine polarity of connections with causal inference (Friston et al. 2003). Generally, the field has leaned towards an edge-centric view of the human connectome, oftentimes investigating edge properties of brain connectivity, and applying this knowledge to better understand clinical populations.

Although historically edges have been the main focus when investigating resting-state fMRI data, there has been some open interest to assign values to nodes of the connectome. Here, the aim is to leverage edge features to provide values to every node in the connectome. In practice, this has been widely applied in connectivity literature to discover canonical "rich-club" organization of the human connectome (van den Heuvel and Sporns, 2011), or other measures of graph centrality (Sporns et al. 2007). In general, these measures elucidate nodes that express a higher degree of connectivity in the connectome, which has been postulated to underlie important integration regions of the brain. An alternative approach relies on spectral graph methods to assign values to each node, such that network proximity of the node is preserved. In other words, nodes that are closer together in the network are assigned relatively similar values. This allows the possibility to characterize the heterogeneity of connectivity patterns across the cerebral cortex, the subcortex, and associated subareas (Margulies et al. 2016; Tian et al. 2020; Haak et al. 2018; Vos de Wael et al. 2018). This is achieved by generating very fine-grained connectomes – that is, nodes are represented by individual voxels (the highest resolution provided by MRI), as opposed to a cortical area – followed by application of these spectral graph methods to assign values to each voxel (or node). Intuitively, this provides an understanding of how connectivity patterns spatially change over a region and provides additional insight into parcel heterogeneity of a brain region. Herein, voxels or nodes that have been characterized in this way are collectively referred to as "connectivity gradients" due to their ability to intuitively map changes in connectivity patterns over a ROI. More details on the mathematical formulation and intuition of these spectral graph methods will be discussed

in subsequent sections: 1.3.3-1.3.6. In this thesis, I work with resting-state fMRI to estimate connectivity gradients and explore their applications across different areas of neuroscience.

## 1.3 Connectivity Representations

Brain representations are typically classified under one of two paradigms: (1) condensing brain organization into a mosaic of binary areas, and (2) characterizing brain organization as smoothly varying properties over an area. The former is referred to as brain parcellation and assumes that the brain is composed of a mosaic of structurally and functionally distinct patches where the boundaries between these patches are marked by rapid transition zones. This viewpoint is akin to observations by Brodmann and the Vogts who were strong advocates of brain parcellations. The latter representation is commonly referred to as gradients, and contrary to parcellations, proposes that features of structure and connectivity may vary gradually over the spatial extent of a region, as was advocated by Percival Bailey and Gerhardt von Bonin (Bailey and von Bonin, 1951). The application of one representation over the other offers different granular levels of insight into brain organization. Historically, a majority of studies have opted to use the brain parcellation representation due to its offer of a more coarse and simplistic view of brain connectivity that increases computational, statistical, and interpretational efficiencies (Eickhoff et al. 2018). For example, the number of statistical comparisons performed in a connectivity analysis can be controlled within the research design by selecting the number of generated areas in a brain parcellation. However, while the general assumption is that a brain parcel is functionally specialized and by extension should express a homogeneous connectivity pattern, this is almost never the case (van den Heuvel and Hulshoff Pol, 2010; Van Essen and Glasser, 2018). Furthermore, if one is interested in voxel-level effects of pathology, then such coarse brain representations may lead to the blurring of a signal of interest over the entire parcel. Although studies often investigate RSFC through the lens of either parcellations or gradient representations, it is important to note that the two are not mutually exclusive, and together may provide unique perspectives for studying brain organization.

### 1.3.1 Parcellation

The goal of brain parcellation is to subdivide the brain into spatially discrete regions by applying data-driven methods to connectivity "fingerprints". Each brain region has its own connectivity fingerprint that can be calculated by computing the functional connectivity of itself to all other brain areas. In doing so, these fingerprints can be generally used to summarize a region's connectivity properties, whose unique characteristics have been postulated to underlie specific brain functions (Passingham et al. 2002). For example, consideration of connectivity fingerprints along the primary motor cortex reveals a clear dorsal-to-ventral separation. Specifically, different points along the motor strip express differential RSFC fingerprints, presumably underlying the different anatomical regions associated with somatotopy (Penfield and Rasmussen, 1950). It follows that parcellation of the primary motor cortex may reveal relevant somatotopic divisions and can be used as a more sensitive measure of motor-related behaviors. In this way, improvement of brain parcellations to better capture biologically-plausible brain functions motivates finer-grained descriptions of brain areas.

Methodologically, brain parcellation has been primarily achieved in one of two ways: (1) by clustering connectivity fingerprints or time series of voxels into brain areas (Power et al. 2011; Yeo et al. 2011; Craddock et al. 2013), or (2) by using boundary-mapping approaches to deduce brain areas based on abrupt changes in connectivity (Cohen et al. 2008; Nelson et al. 2010; Hirose et al. 2012; Wig et al. 2014; Laumann et al. 2015; Gordon et al. 2016). Other parcellation techniques, such as independent component analysis, or Bayesian modeling, have also been proposed as ways to achieve "soft" parcellations of the brain, whereby brain areas or networks are weighted and can therefore overlap with one another (Beckmann et al. 2005; Harrison et al. 2015). Together, these techniques have been widely applied to connectivity data to achieve whole brain, and cortical parcellations, in addition to parcellations of smaller brain areas, such as the thalamus (Zhang et al. 2008) and orbitofrontal cortex (Kahnt et al. 2012). Although there are many brain parcellation methodologies, each method comes with its own assumptions, strengths, and weaknesses, resulting in different parcellation schemes when applied to the same dataset (Arslan et al. 2018). Figure 1.2 shows four common whole brain parcellations that were generated using

different methods highlighting differences in granularity (i.e., numbers of cortical areas) and differences between parcellation schemes.

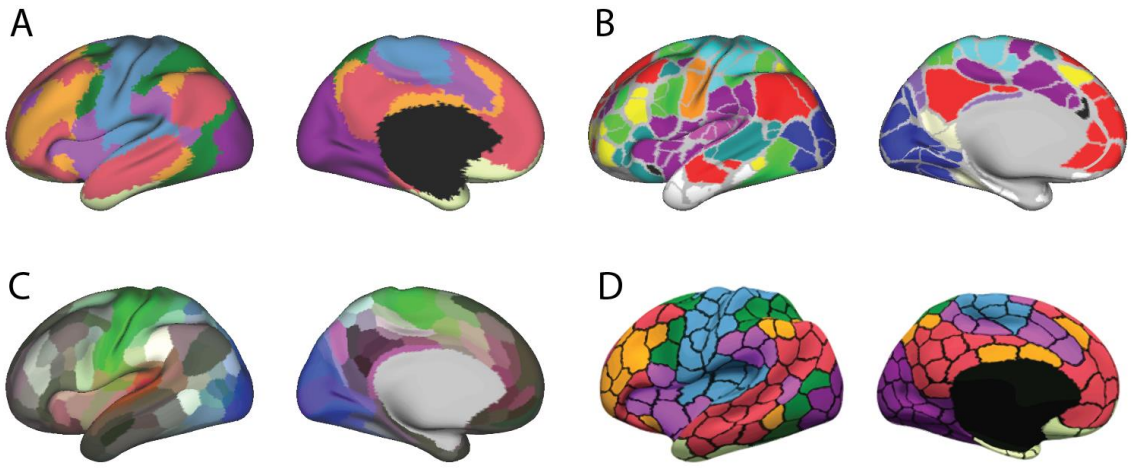


**Figure 1.2 Examples of resting-state functional connectivity derived brain parcellations**

*Examples of brain parcellations. (A) resting-state networks (Yeo et al. 2011), (B) resting-state functional connectivity derived parcellation using boundary mapping (Gordon et al. 2016), (C) multi-modal (Glasser et al. 2016), and (D) resting-state functional connectivity derived parcellation using a gradient-weighted Markov random field approach (Schaefer et al. 2018)*

Optimization of brain parcellations have often focussed on maximizing within-parcel homogeneity (Eickhoff et al. 2015). In principle, this parcellation solution would provide a set of brain regions that maximally expresses all connections inherent to the brain. In other words, voxels constituting a parcel should ideally possess very similar connectivity fingerprints. Additionally, maximizing parcel homogeneity also agrees with the theory that functionally specialized brain regions must be constrained by a unique set of anatomical connections. This means that a brain region that expresses differential connectivity patterns may have multiple brain functions, and further segregation should be considered. In a recent rsfMRI benchmarking paper, Dadi and colleagues showed that *functionally*-driven parcellations derived from resting-state fMRI data led to better prediction accuracies of psychological and clinical traits of individuals, compared to predictions using *structurally*-

derived parcellations (Dadi et al. 2019). Additionally, Schaeffer and colleagues developed a novel rsfMRI parcellation that demonstrated best performance, compared to all other previous atlases, based on parcel homogeneity, and importantly, demonstrated consistency with histological boundaries achieved by Glasser and colleagues' multimodal parcellation (Schaeffer et al. 2018; Glasser et al. 2016). Together, this shows that optimisation of parcel homogeneity indirectly improves other validations measures, such as clinical and human behaviour prediction accuracy and converges with multimodal evidence.

#### 1.3.1.1 Challenges

Numerous brain parcellations have been proposed, with dimensionalities varying from the seven canonical large-scale networks (Yeo et al. 2011), to hundreds of brain areas (Glasser et al. 2016). However, there appears to be no consensus on which parcellation is optimal, largely due to the absence of a ground truth (recall that even when considering microstructure architecture, there were differing opinions related to brain parcellation, in part, due to inter-observer bias). In the absence of a gold standard metric for validation of brain representations, the field has often sought to use various indirect metrics to attempt to validate brain parcellations, such as clinical and/or human behaviour prediction accuracy, within-parcel homogeneity, test-retest reliability, and convergence of inter-modal evidence. Moreover, although brain parcellations with maximized within-parcel homogeneity have offered biologically plausible representations of known cytoarchitecture, there is evidence that brain regions do have some degree of inherent heterogeneity (van den Heuvel and Hulshoff Pol, 2012; Van Essen and Glasser, 2018). Even with the application of finer-grained parcels, RSFC is not perfectly homogenous, suggesting that brain regions can serve multiple functions. This looming problem of brain heterogeneity warrants exploring alternative brain representations that can naturally characterize such diverse connections. Describing these diverse connections at finer-grained resolutions is pertinent to provide a detailed account of inter-subject variability in brain organization that is known to arise over the course of development, through rehabilitation, and owing to other genetic/biological determinants.

### 1.3.2 Connectivity gradients

The goal of gradient representations is to characterize overlapping, spatial variations of connectivity patterns over a region of interest. This overcomes issues of parcel homogeneity by considering connectivity measures on the voxel-level resolution of the fMRI image. It also presents a way to consider multiplicity of connectivity principles over a region of interest, broadly referring to the multiple overlapping sets of brain connectivity principles that underlie many brain regions, such as, somatosensory, visual, and entorhinal cortex, striatum, and the hippocampus (Jbabdi et al. 2013). In this section, I focus on methodologies underlying connectivity gradients and its applications, specifically to functional connectivity, as these two aspects are the focus of this thesis.

#### 1.3.2.1 Intuition of gradient methods

The motivation underlying gradient representations can be reframed as a data dimensionality reduction problem applied to voxel-resolved connectivity matrices. Here, voxel resolution of connectivity fingerprints are considered, and ensuing gradient representations therefore provide the highest possible details of brain organization that can be afforded by MRI. However, a common problem with using voxel-resolved connectivity matrices is that they typically span very large sizes that complicate computational and statistical analyses (i.e., performing a manifold learning algorithm on the neocortex, accounting for >64,000 vertices, may require 32-64 GB of RAM). Consider the following simplified example: a toy brain model consisting of a meager 1,000 voxels, in which case a connectivity fingerprint for a single voxel would correspond to a dimensionality of 1,000. To gain full appreciation for the spatial heterogeneity of the connectivity fingerprints of all the voxels together, one can naïvely visualize connectivity patterns for each of the 1,000 voxels separately. Of course, this process is both tedious and impractical, and in the end, only provides a qualitative understanding of the underlying data. Now consider that this problem is further exacerbated when using real brain data that may span tens of thousands of voxels; a typical mesh brain model of the cortex that assumes 2 mm spacing across left and right cerebral cortex hemispheres consists of >64,000 vertices (or brain coordinates), resulting in a connectivity matrix of size 64,000 by 64,000 (Glasser et al. 2013). Taken together, this raises the necessity to leverage methodological tools that can condense such

high dimensional data into a subset of features that can preserve the subtle nuances of voxel-resolved connectivity patterns. Fortunately, high-dimensional data – that is, connectivity patterns – are known to lie on a low-dimensional manifold that can be estimated and used to characterize such complex and heterogeneous connectivity patterns.


**Figure 1.3 A geodesic manifold**

*The left image shows points sampled (black dots) from a 2D S-manifold (grey). The red line indicates the Euclidean distance between two points, whereas the dark blue line indicates the geodesic distance. The middle image shows a nearest-neighbour graph that connects sampled points that are closest to one another, and by following the edges provides an approach to estimate the manifold shown in grey, on the left. The right image shows sampled points assigned with arbitrary values based on their projections onto the estimated manifold, revealing a new coordinate system that is illustrated by the colour-coded scheme, and can be used to infer the geodesic distance between pairs of points.*

In many cases, one can utilize a graph (a set of nodes connected by edges) to approximate the low-dimensional manifold and its underlying structure. For example, the graph in Figure 1.3 shows observed data points in 2D that exist along a 1D manifold, and by following graph edges of "nearest-neighbour" points, it allows for estimation of the 1D manifold of geodesic distances. In this example, the 1D manifold serves as an intrinsic coordinate system with geodesic distance between points (i.e., distance along the manifold surface) characterizing the degree of similarity between different observed points. Although this is a simple example of data dimensionality of 2D data projected onto a 1D

space, this intuition can be generalized to compress connectivity fingerprints of high dimensionality into smaller subspaces. Such subspaces – herein, referred to as *gradients* – provide an intrinsic coordinate system to understand the heterogeneity and multiplicity of connectivity patterns that arise within a brain area.

#### 1.3.2.2 Gradient estimation

To estimate connectivity gradients, a graph must be constructed from resting-state fMRI data. Formally, a graph is defined by $G = (V, E)$ where $V$ is a set of voxels from a brain area, and $E$ is a set of edges. [Note, in the context of this thesis, $V$ will refer to a set of voxels in the current section and in Chapter 4, but will refer to a set of vertices on a cortical surface in Chapters 2 and 3. The two terms (voxels and vertices) are interchangeable in this work]. An edge, $E_{ij}$, is a similarity measure between connectivity fingerprints of any two voxels $i$ and $j$. Here, connectivity fingerprints are used to calculate sets of edges between all voxels, as the focus of this work is on interpreting connectivity principles underlying a region. Neuroimaging literature has proposed many plausible similarity measures that can be used to compare connectivity fingerprints, including: cosine similarity measures (used in Chapters 3 and 4; Margulies et al. 2016), eta$^2$ coefficient (used in Chapter 2; Cohen et al. 2008; Haak et al. 2018), and normalized cosine similarity (Vos de Wael et al. 2020).

Graph, $G$ can be represented by the graph Laplacian (a matrix representation) as follows:

$$L = D - A$$

where $A$ denotes the weighted adjacency matrix of all edges in the graph ($A_{ij} = E_{ij}$, this is a similarity matrix generated from all voxel-wise connectivity fingerprints) and $D$ denotes the degree matrix, the sum of all columns in $A$.

$$D_{ij} = \sum_{j} A_{ij}$$

Using the graph Laplacian, $L$, the next aim is to estimate a low dimensional subspace for connectivity fingerprints that each voxel (or vertice) can be projected onto. Again, the goal is to map voxels onto a subspace such that local information is preserved (in other words,

pairs of voxels with very similar connectivity fingerprints are situated close to one another, and conversely, dissimilar voxels are far away on the manifold). This intuition is optimized as follows:

$$\hat{y} = \{U(y)\}, U(y) = \sum_{(i,j)\in E} A_{ij}(y_i - y_j)^2$$

where $\hat{y}$ is the vector that minimizes the cost function, $U(y)$. Note, that $A_{ij}$ measures the similarity between any two voxels, as such this objective function weights voxels with higher similarity as being relatively higher compared to dissimilar voxels, forcing similar voxels closer together in the vector $\hat{y}$.

After further optimization, this optimization problem can be written as:

$$\hat{y} = \{U(y)\} = \min_{y}\{y^T L y + \lambda(1 - y^T y)\}$$

and the solution to this minimization problem is:

$$Ly = \lambda y$$

The above equation is defined as the standard eigenvalue problem for the graph Laplacian matrix $L$. However, this eigenvalue problem is often biased by voxels with high degrees, $D_{ij}$, forcing these voxels to group together in $y$. This is often an uninteresting feature and is mitigated by solving for other variations of the graph Laplacian (random walk normalized Laplacian):

$$L_{rw} = D^{-1}L$$

In this graph Laplacian, $D^{-1}$ normalizes the high degree voxels, leading to the following standard eigenvalue problem:

$$Ly = \lambda D y$$

The solution to this eigenvalue problem provides a new subspace of $k$ eigenvectors (or gradients). This is also the same procedure used in the Laplacian eigenmap algorithm (used

for gradient estimation in Chapters 2 to 4) (Belkin and Niyogi, 2003). The subspace spanned by its eigenvectors forms a $V \times k$ matrix labeled as $Y$:

$$Y = [y_0|y_1|\dots|y_{k-1}]$$

The eigenvectors are sorted from smallest to highest based on their eigenvalues. In this way, the lowest eigenvalue is always 0 corresponding with the first eigenvector, $y_0$ which is always constant given that the graph is connected (every pair of voxels are connected to one another). As such, $y_0$ is uninformative and therefore only eigenvectors $y_1$ and higher are considered.

#### 1.3.2.3 Manifold coordinate system

Effectively, gradient estimation methods project each voxel's connectivity fingerprint onto a new coordinate system characterized by the manifold underlying all voxels' connectivity fingerprints (i.e., voxels with similar connectivity patterns will remain nearby in the reduced space). For example, eigenvector $y_1$ corresponds to the primary axis of variation along the estimated manifold, and distance between voxel pairs are interpreted as their geodesic distance. It follows that remapping of $y_1$ onto its brain area provides a qualitative way to visualize spatial changes in connectivity patterns over that area. Note that similar to boundary-mapping techniques, estimated gradients can characterize sharp discontinuities, while also being able to characterize areas of true parcellations (i.e., if two voxels have identical connectivity patterns, then they will be assigned the exact same coordinates on this manifold). In addition to $y_1$, subsequent eigenvectors (i.e., $y_2, \dots, y_{k-1}$) provide other dimensions along the connectivity fingerprints' manifold corresponding to axes with lower variation, and may describe other overlapping connectivity principles that exist within that area. Finally, unlike parcellations, gradient estimates provide a quantitative framework to assess the relationship of voxel-resolved connectivity organization to other modalities, which would otherwise not be possible when considering the high dimensionality nature of such connectivity fingerprints. In Chapter 2, I investigate the heterogeneity and multiplicity of the human somatosensory cortex using gradient estimation.

Recent work has extended this framework to merge connectivity fingerprints across individuals – referred to as joint embeddings. Briefly, this is done by expanding the graph to also include connectome information of other individuals, but importantly, also considers edges between inter-subject voxels (Nenning et al. 2020). In doing so, gradient estimation procedures provide a coordinate system that considers connectomes of multiple individuals simultaneously, and subsequently allows ways to conceptualize connectivity architecture over the human lifespan (Bethlehem et al. 2020), and in disease (Hong et al. 2019; joint embeddings can be used here to facilitate interindividual comparisons instead of using Procrustes shape analysis to align inter-subject gradients). This framework has also been generalized to study connectivity architectures across species by considering voxel-wise connectivity fingerprints defined using a set of homologous cortical areas (Mars et al. 2018), and considers edges between inter-species voxels during the graph construction process. Subsequent gradient estimation provides a coordinate system that aligns both species' connectivity patterns, as demonstrated in macaques and humans (Xu et al. 2020), and as I will show in Chapter 3, with marmosets and humans to specifically study the cross-species default-mode network.

Macroscale gradients have been studied in numerous neuropsychiatric illnesses and disorders, such as schizophrenia and autism disorder (Hong et al. 2019; Dong et al. 2020; Tian et al. 2019). However, no investigations have used gradient estimations to investigate connectivity amidst focal pathology, for example by demyelinating Multiple Sclerosis (MS) lesions. Again, gradient estimation of subcortical structures provides a qualitative framework to assess voxel-wise effects of pathology on connectivity architecture in single subjects. In Chapter 4, I investigate the impacts of focal MS thalamic lesions on thalamic connectivity architecture.

#### 1.3.2.4 Biological interpretation

First application of gradients on the whole cerebral cortex with RSFC revealed the primary organizational axis spanning unimodal to transmodal association cortices, whereas the secondary axis spanned visual/auditory to somatosensory/motor cortices (Margulies et al. 2016). It was postulated that these two axes provided a coordinate system that agreed with the theory of information processing that was proposed by Mesulam (Mesulam 1998).

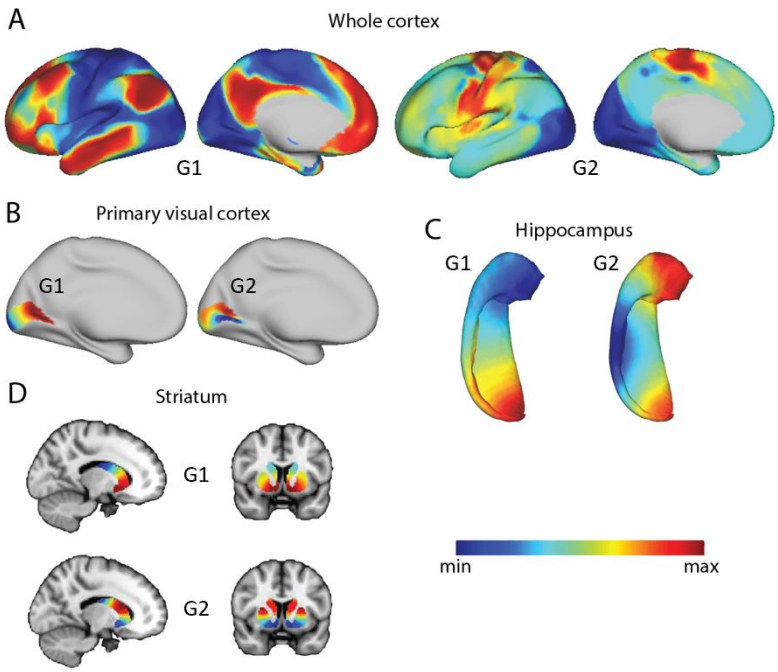


**Figure 1.4 Interpretation of resting-state functional connectivity gradients across various brain regions**

*Visualizations of gradient 1 (G1) and gradient 2 (G2) for various brain regions. The scale denotes a relative scaling of voxels/vertices with similar connection patterns and is represented as arbitrary units. (A) Whole cortex (Margulies et al. 2016). The first gradient corresponds to an organizational axis spanning unimodal-to-association cortices, and the second gradient corresponds to an organizational axis spanning somatomotor-and-auditory-to-visual cortices. Collectively, the two gradients were postulated to recapitulate the theory of cortical hierarchy as proposed by Mesulam (1998). (B) Primary visual cortex (Haak et al. 2018). The first gradient corresponds to retinotopic eccentricity, and the second gradient corresponds to polar angle. (C) Hippocampus (Vos de Wael et al. 2018). The first gradient corresponds to the hippocampal functional long-axis and the second gradient corresponds to its microstructure and infoldings. Hippocampal gradients were calculated using hippunfold surfaces (DeKraker et al. 2022). (D) Striatum (Marquand et al. 2017; Oldehinkel et al. 2022). The first gradient corresponds to goal-directed behaviour cortical-striatal circuitry and the second gradient corresponds to dopaminergic pathways.*

Subsequent work by Haak and colleagues focused on gradient mapping in cortical areas, emphasizing its ability to capture biologically plausible connectivity principles of the brain (Haak et al. 2018). For example, gradient estimation applied to the primary visual cortex revealed connectivity principles matching orthogonal representations of retinotopy. More specifically, the top two gradients were found to reflect eccentricity and polar angle, represented along and perpendicular to the calcarine sulcus, respectively. The ability to estimate such organization arises due to the presumed ability of resting-state fMRI to detect topographically organized retino-fugal, thalamo-cortical, and cortico-cortical connections to the primary visual cortex (Udin and Fawcett, 1988). Gradients have been estimated in other brain areas as well, such as the hippocampus (Vos de Wael et al. 2018; Przezdzik et al. 2019), where the first gradient was found to relate to its functionally differentiated long-axis (Strange et al. 2014), while the second gradient corresponded to its infoldings. Furthermore, cerebellar gradients corresponded to neuronal engagement of different cognitive tasks (Guell et al. 2018), and insular gradients were investigated to evaluate contentious debates of cortical organization within this region (Tian and Zalesky, 2018). Figure 1.4 shows various examples of connectivity gradients derived from different brain regions.

Without correspondence with ground truth knowledge of brain organization and related-surrogate measures, interpreting the biological relevance of ensuing gradients is problematic (Haak et al. 2018). This is especially true in association cortices where these regions' correspondence to microstructural measures become increasingly dissociated when moving from unimodal to transmodal cortical areas (Paquola et al. 2019). Developing a better understanding of the biological factors underlying such differences observed between connectivity gradients and other brain metrics remains to be seen.

## 1.4 Thesis Objectives

Over recent years gradient representations of macroscale connectivity data have emerged as an incredibly intuitive tool to unravel the multifaceted nature of brain connectomes. Due to the complexities of connectivity data, principled methodologies to interpret connectivity in relation to other multiscale neuroanatomical metrics, across human evolution, and in the presence of pathophysiology have been cumbersome. The overarching goal of this thesis

aims to provide a comprehensive understanding of gradient representations as a general framework for conceptualizing macroscale connectivity and its various use cases in neuroscience. Gradient representations offer a unifying framework to bridge the gap across these various applications, as will be explored in the domains of basic neuroscience (Chapter 2), comparative neuroscience (Chapter 3), and clinical neuroscience (Chapter 4).

### 1.4.1 Chapter 2: Mesoscale hierarchical organization of primary somatosensory cortex captured by resting-state-fMRI in humans

Chapter 2 examines multi-overlapping gradients in human somatosensory cortex (S1) to reconcile its long-understood organizational principles. Although organization of S1 along its dorsal-to-ventral somatotopic axis has been well-established with resting-state functional connectivity, organization along its anterior-to-posterior anatomical hierarchical axis remains elusive. To this end, we explored subsequent lower order connectivity gradients and assessed their correspondence with S1 microstructure and architectonic divisions (i.e., Brodmann areas 3a, 3b, 1 and 2). We further reconciled that anterior-posterior S1 subdivisions reflected thalamocortical connectivity that were consistent with non-human primate (NHP) literature.

### 1.4.2 Chapter 3: Joint-embeddings reveal functional differences in default-mode network architecture between marmosets and humans

Chapter 3 applies gradient estimations to holistically mapped marmoset and human connectomes onto a single coordinate system by considering connectivity fingerprints based on homologous regions. The ensuing coordinate system unveils candidate homologies across large-scale networks in both species in this novel framework. This new framework presents many advantages over previous cross-species connectivity fingerprinting studies that are hypothesis driven, and only consider comparisons of a small subset of brain areas between the two species. In comparison, ensuing cross-species gradients consider all permutations of voxel comparisons between species, thus providing insights into homologies that exist between species at finer-grained resolution. We use this framework to systematically compare cognitively relevant default-mode networks in

marmosets and humans to elicit possible insights into similarities and differences between species. We also offer qualitative insight into possible homology of the marmoset medial prefrontal cortex in humans using this gradient framework.

### 1.4.3 Chapter 4: Charting the effects of thalamic lesions on resting-state fMRI features in secondary-progressive Multiple Sclerosis

Chapter 4 applies gradient estimation to investigate connectivity changes in the presence of focal pathophysiology in Multiple Sclerosis (MS). MS pathophysiology (i.e., lesions), although traditionally considered to primarily occur in white matter, has also been widely documented in deep gray matter structures, including the thalamus. It is generally hypothesized that focal pathophysiology would disrupt connections associated with the afflicted site, which by extension, may be detectable using in-vivo connectivity measures. Here, we identified MS participants with focal thalamic lesions, and performed gradient estimation of the thalamus. The goal was to assess whether connectivity gradients – derived from whole-brain thalamocortical connectivity fingerprints – were able to detect the presence of focal lesions. In principle, if focal thalamic lesions do indeed affect connectivity metrics, then we might expect to see abrupt changes in connectivity at the site of the lesion, which should be detectable using connectivity gradients. Furthermore, to comprehensively chart the effects of focal thalamic lesions, we also considered its effects on more simple connectivity measures, in addition to a set of BOLD time series features.

### 1.4.4 Chapter 5: General Discussion and Conclusion

In the final chapter of this thesis, I will discuss and summarize the findings of Chapters 2 through 4, and review the limitations of each chapter in detail with consideration for future directions relating to each project. More generally, I conclude with my views on future directions of gradient estimation techniques in neuroimaging.

## 1.5 References

Adachi, Y., Osada, T., Sporns, O., Watanabe, T., Matsui, T., Miyamoto, K., & Miyashita, Y. (2012). Functional connectivity between anatomically unconnected areas is shaped by collective network-level effects in the macaque cortex. *Cerebral Cortex (New York, N.Y.: 1991)*, *22*(7), 1586–1592. https://doi.org/10.1093/cercor/bhr234

Aggarwal, M., Nauen, D. W., Troncoso, J. C., & Mori, S. (2015). Probing region-specific microstructure of human cortical areas using high angular and spatial resolution diffusion MRI. *NeuroImage*, *105*, 198–207. https://doi.org/10.1016/j.neuroimage.2014.10.053

Amunts, K., Kedo, O., Kindler, M., Pieperhoff, P., Mohlberg, H., Shah, N. J., … Zilles, K. (2005). Cytoarchitectonic mapping of the human amygdala, hippocampal region and entorhinal cortex: Intersubject variability and probability maps. *Anatomy and Embryology*, *210*(5–6), 343–352. https://doi.org/10.1007/s00429-005-0025-5

Amunts, Katrin, Lenzen, M., Friederici, A. D., Schleicher, A., Morosan, P., Palomero-Gallagher, N., & Zilles, K. (2010). Broca's region: Novel organizational principles and multiple receptor mapping. *PLoS Biology*, *8*(9), e1000489. https://doi.org/10.1371/journal.pbio.1000489

Arslan, S., Ktena, S. I., Makropoulos, A., Robinson, E. C., Rueckert, D., & Parisot, S. (2018). Human brain mapping: A systematic comparison of parcellation methods for the human cerebral cortex. *NeuroImage*, *170*, 5–30. https://doi.org/10.1016/j.neuroimage.2017.04.014

Augustinack, J. C., Magnain, C., Reuter, M., van der Kouwe, A. J. W., Boas, D., & Fischl, B. (2014). MRI parcellation of ex vivo medial temporal lobe. *NeuroImage*, *93 Pt 2*, 252–259. https://doi.org/10.1016/j.neuroimage.2013.05.053

Barch, D. M., Burgess, G. C., Harms, M. P., Petersen, S. E., Schlaggar, B. L., Corbetta, M., … WU-Minn HCP Consortium. (2013). Function in the human connectome: Task-fMRI and individual differences in behavior. *NeuroImage*, *80*, 169–189. https://doi.org/10.1016/j.neuroimage.2013.05.033

Beckmann, C. F., DeLuca, M., Devlin, J. T., & Smith, S. M. (2005). Investigations into resting-state connectivity using independent component analysis. *Philosophical Transactions of the Royal Society of London. Series B, Biological Sciences*, *360*(1457), 1001–1013. https://doi.org/10.1098/rstb.2005.1634

Behrens, T. E. J., Johansen-Berg, H., Woolrich, M. W., Smith, S. M., Wheeler-Kingshott, C. a. M., Boulby, P. A., … Matthews, P. M. (2003). Non-invasive mapping of connections between human thalamus and cortex using diffusion imaging. *Nature Neuroscience*, *6*(7), 750–757. https://doi.org/10.1038/nn1075

Bethlehem, R. A. I., Paquola, C., Seidlitz, J., Ronan, L., Bernhardt, B., Consortium, C.-C., & Tsvetanov, K. A. (2020). Dispersion of functional gradients across the adult lifespan. *NeuroImage*, *222*, 117299. https://doi.org/10.1016/j.neuroimage.2020.117299

Biswal, B., Yetkin, F. Z., Haughton, V. M., & Hyde, J. S. (1995). Functional connectivity in the motor cortex of resting human brain using echo-planar MRI. *Magnetic Resonance in Medicine*, *34*(4), 537–541. https://doi.org/10.1002/mrm.1910340409

Burton, H., Fabri, M., & Alloway, K. (1995). Cortical areas within the lateral sulcus connected to cutaneous representations in areas 3b and 1: A revised interpretation of the second somatosensory area in macaque monkeys. *The Journal of Comparative Neurology*, *355*(4), 539–562. https://doi.org/10.1002/cne.903550405

Caspers, J., Zilles, K., Eickhoff, S. B., Schleicher, A., Mohlberg, H., & Amunts, K. (2013). Cytoarchitectonical analysis and probabilistic mapping of two extrastriate areas of the human posterior fusiform gyrus. *Brain Structure & Function*, *218*(2), 511–526. https://doi.org/10.1007/s00429-012-0411-8

Caspers, S., Geyer, S., Schleicher, A., Mohlberg, H., Amunts, K., & Zilles, K. (2006). The human inferior parietal cortex: Cytoarchitectonic parcellation and interindividual variability. *NeuroImage*, *33*(2), 430–448. https://doi.org/10.1016/j.neuroimage.2006.06.054

Cohen, A. L., Fair, D. A., Dosenbach, N. U. F., Miezin, F. M., Dierker, D., Van Essen, D. C., … Petersen, S. E. (2008). Defining functional areas in individual human brains using resting functional connectivity MRI. *NeuroImage*, *41*(1), 45–57. https://doi.org/10.1016/j.neuroimage.2008.01.066

Craddock, R. C., Jbabdi, S., Yan, C.-G., Vogelstein, J. T., Castellanos, F. X., Di Martino, A., … Milham, M. P. (2013). Imaging human connectomes at the macroscale. *Nature Methods*, *10*(6), 524–539. https://doi.org/10.1038/nmeth.2482

Dadi, K., Rahim, M., Abraham, A., Chyzhyk, D., Milham, M., Thirion, B., … Alzheimer's Disease Neuroimaging Initiative. (2019). Benchmarking functional

connectome-based predictive models for resting-state fMRI. *NeuroImage*, *192*, 115–134. https://doi.org/10.1016/j.neuroimage.2019.02.062

Damoiseaux, J. S., Rombouts, S. a. R. B., Barkhof, F., Scheltens, P., Stam, C. J., Smith, S. M., & Beckmann, C. F. (2006). Consistent resting-state networks across healthy subjects. *Proceedings of the National Academy of Sciences of the United States of America*, *103*(37), 13848–13853. https://doi.org/10.1073/pnas.0601417103

De Luca, M., Beckmann, C. F., De Stefano, N., Matthews, P. M., & Smith, S. M. (2006). FMRI resting state networks define distinct modes of long-distance interactions in the human brain. *NeuroImage*, *29*(4), 1359–1367. https://doi.org/10.1016/j.neuroimage.2005.08.035

DeKraker, J., Haast, R. A., Yousif, M. D., Karat, B., Köhler, S., & Khan, A. R. (2021, December 5). *HippUnfold: Automated hippocampal unfolding, morphometry, and subfield segmentation* (p. 2021.12.03.471134). p. 2021.12.03.471134. bioRxiv. https://doi.org/10.1101/2021.12.03.471134

Dinse, J., Härtwich, N., Waehnert, M. D., Tardif, C. L., Schäfer, A., Geyer, S., … Bazin, P.-L. (2015). A cytoarchitecture-driven myelin model reveals area-specific signatures in human primary and secondary areas using ultra-high resolution in-vivo brain MRI. *NeuroImage*, *114*, 71–87. https://doi.org/10.1016/j.neuroimage.2015.04.023

Dong, D., Luo, C., Guell, X., Wang, Y., He, H., Duan, M., … Yao, D. (2020). Compression of Cerebellar Functional Gradients in Schizophrenia. *Schizophrenia Bulletin*, *46*(5), 1282–1295. https://doi.org/10.1093/schbul/sbaa016

Eickhoff, S. B., Thirion, B., Varoquaux, G., & Bzdok, D. (2015). Connectivity-based parcellation: Critique and implications. *Human Brain Mapping*, *36*(12), 4771–4792. https://doi.org/10.1002/hbm.22933

Eickhoff, S. B., Yeo, B. T. T., & Genon, S. (2018). Imaging-based parcellations of the human brain. *Nature Reviews. Neuroscience*, *19*(11), 672–686. https://doi.org/10.1038/s41583-018-0071-7

Finn, E. S., Shen, X., Scheinost, D., Rosenberg, M. D., Huang, J., Chun, M. M., … Constable, R. T. (2015). Functional connectome fingerprinting: Identifying individuals using patterns of brain connectivity. *Nature Neuroscience*, *18*(11), 1664–1671. https://doi.org/10.1038/nn.4135

Fox, M. D., & Raichle, M. E. (2007). Spontaneous fluctuations in brain activity observed with functional magnetic resonance imaging. *Nature Reviews. Neuroscience*, *8*(9), 700–711. https://doi.org/10.1038/nrn2201

Friston, K. J., Harrison, L., & Penny, W. (2003). Dynamic causal modelling. *NeuroImage*, *19*(4), 1273–1302. https://doi.org/10.1016/s1053-8119(03)00202-7

Geyer, S. (2004). The microstructural border between the motor and the cognitive domain in the human cerebral cortex. *Advances in Anatomy, Embryology, and Cell Biology*, *174*, I–VIII, 1–89. https://doi.org/10.1007/978-3-642-18910-4

Geyer, Stefan, Weiss, M., Reimann, K., Lohmann, G., & Turner, R. (2011). Microstructural Parcellation of the Human Cerebral Cortex—From Brodmann's Post-Mortem Map to in vivo Mapping with High-Field Magnetic Resonance Imaging. *Frontiers in Human Neuroscience*, *5*, 19. https://doi.org/10.3389/fnhum.2011.00019

Glasser, M. F., Coalson, T. S., Robinson, E. C., Hacker, C. D., Harwell, J., Yacoub, E., … Van Essen, D. C. (2016). A multi-modal parcellation of human cerebral cortex. *Nature*, *536*(7615), 171–178. https://doi.org/10.1038/nature18933

Glasser, M. F., & Essen, D. C. V. (2011). Mapping Human Cortical Areas In Vivo Based on Myelin Content as Revealed by T1- and T2-Weighted MRI. *Journal of Neuroscience*, *31*(32), 11597–11616. https://doi.org/10.1523/JNEUROSCI.2180-11.2011

Glasser, M. F., Sotiropoulos, S. N., Wilson, J. A., Coalson, T. S., Fischl, B., Andersson, J. L., … WU-Minn HCP Consortium. (2013). The minimal preprocessing pipelines for the Human Connectome Project. *NeuroImage*, *80*, 105–124. https://doi.org/10.1016/j.neuroimage.2013.04.127

Gordon, E. M., Laumann, T. O., Adeyemo, B., Huckins, J. F., Kelley, W. M., & Petersen, S. E. (2016). Generation and Evaluation of a Cortical Area Parcellation from Resting-State Correlations. *Cerebral Cortex (New York, N.Y.: 1991)*, *26*(1), 288–303. https://doi.org/10.1093/cercor/bhu239

Goulas, A., Majka, P., Rosa, M. G. P., & Hilgetag, C. C. (2019). A blueprint of mammalian cortical connectomes. *PLOS Biology*, *17*(3), e2005346. https://doi.org/10.1371/journal.pbio.2005346

Guell, X., Schmahmann, J. D., Gabrieli, J. D., & Ghosh, S. S. (2018). Functional gradients of the cerebellum. *ELife*, *7*, e36652. https://doi.org/10.7554/eLife.36652

Haak, K. V., Marquand, A. F., & Beckmann, C. F. (2018). Connectopic mapping with resting-state fMRI. *NeuroImage*, *170*, 83–94. https://doi.org/10.1016/j.neuroimage.2017.06.075

Hansen, J. Y., Shafiei, G., Markello, R. D., Smart, K., Cox, S. M. L., Nørgaard, M., … Misic, B. (2022, January 11). *Mapping neurotransmitter systems to the structural and functional organization of the human neocortex* (p. 2021.10.28.466336). p. 2021.10.28.466336. bioRxiv. https://doi.org/10.1101/2021.10.28.466336

Harrison, S. J., Woolrich, M. W., Robinson, E. C., Glasser, M. F., Beckmann, C. F., Jenkinson, M., & Smith, S. M. (2015). Large-scale probabilistic functional modes from resting state fMRI. *NeuroImage*, *109*, 217–231. https://doi.org/10.1016/j.neuroimage.2015.01.013

Hawrylycz, M. J., Lein, E. S., Guillozet-Bongaarts, A. L., Shen, E. H., Ng, L., Miller, J. A., … Jones, A. R. (2012). An anatomically comprehensive atlas of the adult human brain transcriptome. *Nature*, *489*(7416), 391–399. https://doi.org/10.1038/nature11405

Hirose, S., Watanabe, T., Jimura, K., Katsura, M., Kunimatsu, A., Abe, O., … Konishi, S. (2012). Local Signal Time-Series during Rest Used for Areal Boundary Mapping in Individual Human Brains. *PLOS ONE*, *7*(5), e36496. https://doi.org/10.1371/journal.pone.0036496

Honey, C. J., Sporns, O., Cammoun, L., Gigandet, X., Thiran, J. P., Meuli, R., & Hagmann, P. (2009). Predicting human resting-state functional connectivity from structural connectivity. *Proceedings of the National Academy of Sciences of the United States of America*, *106*(6), 2035–2040. https://doi.org/10.1073/pnas.0811168106

Hong, S.-J., Vos de Wael, R., Bethlehem, R. A. I., Lariviere, S., Paquola, C., Valk, S. L., … Bernhardt, B. C. (2019). Atypical functional connectome hierarchy in autism. *Nature Communications*, *10*(1), 1022. https://doi.org/10.1038/s41467-019-08944-1

Jbabdi, S., Sotiropoulos, S. N., & Behrens, T. E. (2013). The topographic connectome. *Current Opinion in Neurobiology*, *23*(2), 207–215. https://doi.org/10.1016/j.conb.2012.12.004

Jbabdi, S., Sotiropoulos, S. N., Haber, S. N., Van Essen, D. C., & Behrens, T. E. (2015). Measuring macroscopic brain connections in vivo. *Nature Neuroscience*, *18*(11), 1546–1555. https://doi.org/10.1038/nn.4134

Kahnt, T., Chang, L. J., Park, S. Q., Heinzle, J., & Haynes, J.-D. (2012). Connectivity-based parcellation of the human orbitofrontal cortex. *The Journal of Neuroscience: The Official Journal of the Society for Neuroscience*, *32*(18), 6240–6250. https://doi.org/10.1523/JNEUROSCI.0257-12.2012

Kong, R., Li, J., Orban, C., Sabuncu, M. R., Liu, H., Schaefer, A., … Yeo, B. T. T. (2019). Spatial Topography of Individual-Specific Cortical Networks Predicts Human Cognition, Personality, and Emotion. *Cerebral Cortex (New York, N.Y.: 1991)*, *29*(6), 2533–2551. https://doi.org/10.1093/cercor/bhy123

Krubitzer, L., Clarey, J., Tweedale, R., Elston, G., & Calford, M. (1995). A redefinition of somatosensory areas in the lateral sulcus of macaque monkeys. *The Journal of Neuroscience: The Official Journal of the Society for Neuroscience*, *15*(5 Pt 2), 3821–3839.

Kujovic, M., Zilles, K., Malikovic, A., Schleicher, A., Mohlberg, H., Rottschy, C., … Amunts, K. (2012). Cytoarchitectonic mapping of the human dorsal extrastriate cortex. *Brain Structure & Function*, *218*. https://doi.org/10.1007/s00429-012-0390-9

Lancaster, J. L., Woldorff, M. G., Parsons, L. M., Liotti, M., Freitas, C. S., Rainey, L., … Fox, P. T. (2000). Automated Talairach atlas labels for functional brain mapping. *Human Brain Mapping*, *10*(3), 120–131. https://doi.org/10.1002/1097-0193(200007)10:3<120::aid-hbm30>3.0.co;2-8

Laumann, T. O., Gordon, E. M., Adeyemo, B., Snyder, A. Z., Joo, S. J., Chen, M.-Y., … Petersen, S. E. (2015). Functional System and Areal Organization of a Highly Sampled Individual Human Brain. *Neuron*, *87*(3), 657–670. https://doi.org/10.1016/j.neuron.2015.06.037

Maier-Hein, K. H., Neher, P. F., Houde, J.-C., Côté, M.-A., Garyfallidis, E., Zhong, J., … Descoteaux, M. (2017). The challenge of mapping the human connectome based on diffusion tractography. *Nature Communications*, *8*(1), 1349. https://doi.org/10.1038/s41467-017-01285-x

Margulies, D. S., Ghosh, S. S., Goulas, A., Falkiewicz, M., Huntenburg, J. M., Langs, G., … Smallwood, J. (2016). Situating the default-mode network along a principal gradient of macroscale cortical organization. *Proceedings of the National Academy of Sciences of the United States of America*, *113*(44), 12574–12579. https://doi.org/10.1073/pnas.1608282113

Marquand, A. F., Haak, K. V., & Beckmann, C. F. (2017). Functional corticostriatal connection topographies predict goal-directed behaviour in humans. *Nature Human Behaviour*, *1*(8), 1–9. https://doi.org/10.1038/s41562-017-0146

Marrelec, G., Krainik, A., Duffau, H., Pélégrini-Issac, M., Lehéricy, S., Doyon, J., & Benali, H. (2006). Partial correlation for functional brain interactivity investigation in functional MRI. *NeuroImage*, *32*(1), 228–237. https://doi.org/10.1016/j.neuroimage.2005.12.057

Mars, R. B., Sotiropoulos, S. N., Passingham, R. E., Sallet, J., Verhagen, L., Khrapitchev, A. A., … Jbabdi, S. (n.d.). Whole brain comparative anatomy using connectivity blueprints. *ELife*, *7*, e35237. https://doi.org/10.7554/eLife.35237

Mesulam, M. M. (1998). From sensation to cognition. *Brain: A Journal of Neurology*, *121 ( Pt 6)*, 1013–1052. https://doi.org/10.1093/brain/121.6.1013

Nelson, S. M., Cohen, A. L., Power, J. D., Wig, G. S., Miezin, F. M., Wheeler, M. E., … Petersen, S. E. (2010). A parcellation scheme for human left lateral parietal cortex. *Neuron*, *67*(1), 156–170. https://doi.org/10.1016/j.neuron.2010.05.025

Nenning, K.-H., Xu, T., Schwartz, E., Arroyo, J., Woehrer, A., Franco, A. R., … Langs, G. (2020). Joint embedding: A scalable alignment to compare individuals in a connectivity space. *NeuroImage*, *222*, 117232. https://doi.org/10.1016/j.neuroimage.2020.117232

Ogawa, S., Lee, T. M., Kay, A. R., & Tank, D. W. (1990). Brain magnetic resonance imaging with contrast dependent on blood oxygenation. *Proceedings of the National Academy of Sciences of the United States of America*, *87*(24), 9868–9872. https://doi.org/10.1073/pnas.87.24.9868

Oldehinkel, M., Llera, A., Faber, M., Huertas, I., Buitelaar, J. K., Bloem, B. R., … Beckmann, C. F. (2022). Mapping dopaminergic projections in the human brain with resting-state fMRI. *ELife*, *11*, e71846. https://doi.org/10.7554/eLife.71846

Paquola, C., Vos De Wael, R., Wagstyl, K., Bethlehem, R. A. I., Hong, S.-J., Seidlitz, J., … Bernhardt, B. C. (2019). Microstructural and functional gradients are increasingly dissociated in transmodal cortices. *PLoS Biology*, *17*(5), e3000284. https://doi.org/10.1371/journal.pbio.3000284

Passingham, R. E., Stephan, K. E., & Kötter, R. (2002). The anatomical basis of functional localization in the cortex. *Nature Reviews. Neuroscience*, *3*(8), 606–616. https://doi.org/10.1038/nrn893

Pauling, L., & Coryell, C. D. (1936). The Magnetic Properties and Structure of Hemoglobin, Oxyhemoglobin and Carbonmonoxyhemoglobin. *Proceedings of the National Academy of Sciences of the United States of America*, *22*(4), 210–216. https://doi.org/10.1073/pnas.22.4.210

Power, J. D., Cohen, A. L., Nelson, S. M., Wig, G. S., Barnes, K. A., Church, J. A., … Petersen, S. E. (2011). Functional network organization of the human brain. *Neuron*, *72*(4), 665–678. https://doi.org/10.1016/j.neuron.2011.09.006

Przeździk, I., Faber, M., Fernández, G., Beckmann, C. F., & Haak, K. V. (2019). The functional organisation of the hippocampus along its long axis is gradual and predicts recollection. *Cortex; a Journal Devoted to the Study of the Nervous System and Behavior*, *119*, 324–335. https://doi.org/10.1016/j.cortex.2019.04.015

Robinson, E. C., Jbabdi, S., Glasser, M. F., Andersson, J., Burgess, G. C., Harms, M. P., … Jenkinson, M. (2014). MSM: A new flexible framework for Multimodal Surface Matching. *NeuroImage*, *100*, 414–426. https://doi.org/10.1016/j.neuroimage.2014.05.069

Schaefer, A., Kong, R., Gordon, E. M., Laumann, T. O., Zuo, X.-N., Holmes, A. J., … Yeo, B. T. T. (2018). Local-Global Parcellation of the Human Cerebral Cortex from Intrinsic Functional Connectivity MRI. *Cerebral Cortex (New York, N.Y.: 1991)*, *28*(9), 3095–3114. https://doi.org/10.1093/cercor/bhx179

Scheperjans, F., Hermann, K., Eickhoff, S. B., Amunts, K., Schleicher, A., & Zilles, K. (2008). Observer-independent cytoarchitectonic mapping of the human superior parietal cortex. *Cerebral Cortex (New York, N.Y.: 1991)*, *18*(4), 846–867. https://doi.org/10.1093/cercor/bhm116

Smith, S. M., Fox, P. T., Miller, K. L., Glahn, D. C., Fox, P. M., Mackay, C. E., … Beckmann, C. F. (2009). Correspondence of the brain's functional architecture during activation and rest. *Proceedings of the National Academy of Sciences of the United States of America*, *106*(31), 13040–13045. https://doi.org/10.1073/pnas.0905267106

Sporns, O., & Honey, C. J. (2006). Small worlds inside big brains. *Proceedings of the National Academy of Sciences of the United States of America*, *103*(51), 19219–19220. https://doi.org/10.1073/pnas.0609523103

Sporns, O., Honey, C. J., & Kötter, R. (2007). Identification and Classification of Hubs in Brain Networks. *PLOS ONE*, *2*(10), e1049. https://doi.org/10.1371/journal.pone.0001049

Strange, B. A., Witter, M. P., Lein, E. S., & Moser, E. I. (2014). Functional organization of the hippocampal longitudinal axis. *Nature Reviews. Neuroscience*, *15*(10), 655–669. https://doi.org/10.1038/nrn3785

Tavor, I., Parker Jones, O., Mars, R. B., Smith, S. M., Behrens, T. E., & Jbabdi, S. (2016). Task-free MRI predicts individual differences in brain activity during task performance. *Science (New York, N.Y.)*, *352*(6282), 216–220. https://doi.org/10.1126/science.aad8127

Thulborn, K. R., Waterton, J. C., Matthews, P. M., & Radda, G. K. (1982). Oxygenation dependence of the transverse relaxation time of water protons in whole blood at high field. *Biochimica Et Biophysica Acta*, *714*(2), 265–270. https://doi.org/10.1016/0304-4165(82)90333-6

Tian, Y., Margulies, D. S., Breakspear, M., & Zalesky, A. (2020). Topographic organization of the human subcortex unveiled with functional connectivity gradients. *Nature Neuroscience*, *23*(11), 1421–1432. https://doi.org/10.1038/s41593-020-00711-6

Tian, Y., & Zalesky, A. (2018). Characterizing the functional connectivity diversity of the insula cortex: Subregions, diversity curves and behavior. *NeuroImage*, *183*, 716–733. https://doi.org/10.1016/j.neuroimage.2018.08.055

Tian, Y., Zalesky, A., Bousman, C., Everall, I., & Pantelis, C. (2019). Insula Functional Connectivity in Schizophrenia: Subregions, Gradients, and Symptoms. *Biological Psychiatry. Cognitive Neuroscience and Neuroimaging*, *4*(4), 399–408. https://doi.org/10.1016/j.bpsc.2018.12.003

Tzourio-Mazoyer, N., Landeau, B., Papathanassiou, D., Crivello, F., Etard, O., Delcroix, N., … Joliot, M. (2002). Automated anatomical labeling of activations in SPM using a macroscopic anatomical parcellation of the MNI MRI single-subject brain. *NeuroImage*, *15*(1), 273–289. https://doi.org/10.1006/nimg.2001.0978

Udin, S. B., & Fawcett, J. W. (1988). Formation of topographic maps. *Annual Review of Neuroscience*, *11*, 289–327. https://doi.org/10.1146/annurev.ne.11.030188.001445

van den Heuvel, M. P., & Hulshoff Pol, H. E. (2010a). Exploring the brain network: A review on resting-state fMRI functional connectivity. *European Neuropsychopharmacology: The Journal of the European College of Neuropsychopharmacology*, *20*(8), 519–534. https://doi.org/10.1016/j.euroneuro.2010.03.008

van den Heuvel, M. P., & Hulshoff Pol, H. E. (2010b). Specific somatotopic organization of functional connections of the primary motor network during resting state. *Human Brain Mapping*, *31*(4), 631–644. https://doi.org/10.1002/hbm.20893

van den Heuvel, M. P., & Sporns, O. (2011). Rich-club organization of the human connectome. *The Journal of Neuroscience: The Official Journal of the Society for Neuroscience*, *31*(44), 15775–15786. https://doi.org/10.1523/JNEUROSCI.3539-11.2011

Van Essen, D. C., & Glasser, M. F. (2018). Parcellating Cerebral Cortex: How Invasive Animal Studies Inform Noninvasive Mapmaking in Humans. *Neuron*, *99*(4), 640–663. https://doi.org/10.1016/j.neuron.2018.07.002

Vincent, J. L., Patel, G. H., Fox, M. D., Snyder, A. Z., Baker, J. T., Van Essen, D. C., … Raichle, M. E. (2007). Intrinsic functional architecture in the anaesthetized monkey brain. *Nature*, *447*(7140), 83–86. https://doi.org/10.1038/nature05758

Vos de Wael, R., Benkarim, O., Paquola, C., Lariviere, S., Royer, J., Tavakol, S., … Bernhardt, B. C. (2020). BrainSpace: A toolbox for the analysis of macroscale gradients in neuroimaging and connectomics datasets. *Communications Biology*, *3*(1), 103. https://doi.org/10.1038/s42003-020-0794-7

Vos de Wael, R., Larivière, S., Caldairou, B., Hong, S.-J., Margulies, D. S., Jefferies, E., … Bernhardt, B. C. (2018). Anatomical and microstructural determinants of hippocampal subfield functional connectome embedding. *Proceedings of the National Academy of Sciences of the United States of America*, *115*(40), 10154–10159. https://doi.org/10.1073/pnas.1803667115

Wang, D., Buckner, R. L., Fox, M. D., Holt, D. J., Holmes, A. J., Stoecklein, S., … Liu, H. (2015). Parcellating cortical functional networks in individuals. *Nature Neuroscience*, *18*(12), 1853–1860. https://doi.org/10.1038/nn.4164

Wig, G. S., Laumann, T. O., Cohen, A. L., Power, J. D., Nelson, S. M., Glasser, M. F., … Petersen, S. E. (2014). Parcellating an individual subject's cortical and subcortical brain structures using snowball sampling of resting-state correlations. *Cerebral Cortex (New York, N.Y.: 1991)*, *24*(8), 2036–2054. https://doi.org/10.1093/cercor/bht056

Xu, T., Nenning, K.-H., Schwartz, E., Hong, S.-J., Vogelstein, J. T., Goulas, A., … Langs, G. (2020). Cross-species functional alignment reveals evolutionary hierarchy within the connectome. *NeuroImage*, *223*, 117346. https://doi.org/10.1016/j.neuroimage.2020.117346

Yeo, B. T. T., Krienen, F. M., Sepulcre, J., Sabuncu, M. R., Lashkari, D., Hollinshead, M., … Buckner, R. L. (2011). The organization of the human cerebral cortex estimated by intrinsic functional connectivity. *Journal of Neurophysiology*, *106*(3), 1125–1165. https://doi.org/10.1152/jn.00338.2011

Zhang, D., Snyder, A. Z., Fox, M. D., Sansbury, M. W., Shimony, J. S., & Raichle, M. E. (2008). Intrinsic functional relations between human cerebral cortex and thalamus. *Journal of Neurophysiology*, *100*(4), 1740–1748. https://doi.org/10.1152/jn.90463.2008

Zilles, K., Palomero-Gallagher, N., Grefkes, C., Scheperjans, F., Boy, C., Amunts, K., & Schleicher, A. (2002). Architectonics of the human cerebral cortex and transmitter receptor fingerprints: Reconciling functional neuroanatomy and neurochemistry. *European Neuropsychopharmacology: The Journal of the European College of Neuropsychopharmacology*, *12*(6), 587–599. https://doi.org/10.1016/s0924-977x(02)00108-6

Zilles, Karl, & Amunts, K. (2009). Receptor mapping: Architecture of the human cerebral cortex. *Current Opinion in Neurology*, *22*(4), 331–339. https://doi.org/10.1097/WCO.0b013e32832d95db

Zilles, Karl, Palomero-Gallagher, N., & Schleicher, A. (2004). Transmitter receptors and functional anatomy of the cerebral cortex. *Journal of Anatomy*, *205*(6), 417–432. https://doi.org/10.1111/j.0021-8782.2004.00357.x

# Chapter 2

# 2 Mesoscale hierarchical organization of primary somatosensory cortex captured by resting-state-fMRI in humans [1]

## 2.1 Introduction

The primary somatosensory cortex (S1) is integral to the somatosensory system and important for many functions, such as tactile recognition (Drevets et al., 1995; Bensmaia et al., 2008; Pei et al., 2010), bodily perception (Kim et al., 2015), and motor control (Disamond et al., 2008; Lee et al., 2008). Hierarchical organization of S1 along the anterior-to-posterior axis supports these functions through sequential processing of afferent somatosensory inputs Iwamura, 1998). A vast body of animal literature has supported the role of S1 integration for computations related to object localization (Kleinfeld and Deschênes, 2011) and texture decoding (Isett et al., 2018), and may have further implications in goal-directed somatosensory-related behaviours (Yamashita and Petersen, 2016). In humans, impairment to areas of S1 may lead to abnormal processing of somatosensory information and may contribute to sensorimotor related deficits commonly found in neurological disorders, such as stroke (Kim and Choi-Kwon, 1996), and Parkinson's Disease (Conte et al., 2013). Despite the relevance of S1 in cognitive and clinical neuroscience, a method to characterize hierarchical organization of S1 in-vivo within human cortex remains elusive.

To date, magnetic resonance imaging (MRI) using myelin mapping techniques have made it feasible to delineate S1 into anterior-to-posterior architectonic subdivisions – Brodmann areas 3a, 3b, 1 and 2 - corroborating findings from cytoarchitecture (Brodmann 1909; Glasser and Van Essen, 2011; Fischl et al., 2008). While structural MRI can sufficiently delineate architectonic boundaries with one or more MRI contrasts,

---

[1] A version of this chapter is published as:

**Ngo, G. N.**, Haak, K. V., Beckmann, C. F., & Menon, R. S. (2021). Mesoscale hierarchical organization of primary somatosensory cortex captured by resting-state-fMRI in humans. NeuroImage, 235, 118031. https://doi.org/10.1016/j.neuroimage.2021.118031

evidence from resting-state functional connectivity (RSFC) reveals further separation of S1 along its somatotopic boundaries following a ventral-to-dorsal axis (Yeo et al., 2011). In principle, measures of connectivity, in this case using macroscale RSFC patterns, should also align with architectonic S1 subdivisions along an anterior-to-posterior axis, as supported by non-human primate (NHP) anatomical studies (Krubitzer and Kaas, 1990; Pons and Kaas, 1986). However, a correspondence between mesoscale measures of structure and connectivity supporting notions of anatomical hierarchy on a millimetre scale have yet to be established in human S1. Here, mesoscale is defined as the spatial scale over which individual differences transition into species typicality.

Recent methodological developments have shown manifold learning as a viable tool to embed high dimensional RSFC data into a low dimensional space while preserving biologically meaningful structure, commonly referred to as RSFC gradients (Haak et al., 2018; Margulies et al., 2016). Macroscale gradients of the cerebral cortex have been shown to represent an embedding scheme that positions primary and transmodal cortices on opposite ends of a spectrum (Margulies et al., 2016). RSFC gradients estimated within specific cortical areas, referred to as ‘connectopic mapping’ (Haak et al., 2018), revealed biologically relevant interactions, such as linking hippocampus to microstructure (Vos de Wael et al., 2018), and striatum to goal-directed behaviours (Marquand et al., 2017). Additionally, this technique can be used to estimate multiple overlapping gradients, where each gradient may correspond to unique organizational principles of the cortical area. The aim of the current study was to extend the use of RSFC to investigate mesoscale hierarchical organization in human S1. We hypothesized that RSFC will enable characterization of S1 along an anterior-to-posterior axis in-vivo that spatially maps onto somatosensory Brodmann areas.

A central part of this investigation is to use accurate regions of interest (ROI) to characterize the anatomical hierarchy of S1 using RSFC. Here, we take advantage of the Human Connectome Project’s multimodal parcellation, which subdivides the cerebral cortex into 360 cortical areas, four of which represent S1’s architectonic subareas (i.e., Brodmann areas 1, 2, 3a, and 3b) (Glasser et al., 2016). Although not part of the parcellation, Glasser and colleagues also propose further subdivision of S1 into their

somatotopic subareas that relate directly to distinct body parts (Penfield and Rasmussen, 1950). With the goal to discover a mesoscale hierarchical gradient in S1 we explore other overlapping gradients, and the dominant gradients of S1 somatotopic subareas to see whether evidence of RSFC heterogeneity along the anterior-to-posterior axis exists.

Given these considerations, we chose to use measures of RSFC to investigate structural organization of S1. RSFC provides a measure of function that closely follows principles guided by anatomical connectivity (Wang et al., 2013; Jbabdi et al., 2015). Additionally, RSFC can predict interindividual differences of task-based fMRI activations across a wide variety of cognitive paradigms, supporting the notion that cognitively relevant functional interactions are preserved at rest (Tavor et al., 2016). Here, we used resting-state data from the WU-Minn Human Connectome Project (Van Essen et al., 2013; Smith et al., 2013) and S1 architectonically-defined regions as a proxy for anatomical hierarchy taken from Glasser and colleagues multi-modal parcellation of the cerebral cortex (Glasser et al., 2016). To characterize mesoscale structural organization of S1, we explore the principal gradient derived using RSFC of S1 somatotopic subareas and (1) demonstrate its use as a proxy for anatomical hierarchy, (2) its link to underlying tissue microstructure, and (3) its correspondence to Brodmann area boundaries – here, we specifically found evidence for a distinct functional division that exists between Brodmann areas 3b and 1, rather than four architectonic subareas. Finally, we demonstrate the application of this gradient scheme as a means to achieve a more comprehensive characterization of human thalamocortical connectivity profiles based on what is known in NHP literature. A characterization of S1 topography that follows governing principles of anatomical hierarchy and microstructure may provide insight into studying the interplay between mesoscale structure and function in humans. In doing so, this may further offer an interpretative framework for studying sensorimotor-related deficits across a wide range of neurological disorders. Together, this work provides new insight into the use of RSFC to characterize mesoscale structural organization of human S1.

## 2.2 Methods

### 2.2.1 Resting-state fMRI dataset and preprocessing

This 3T resting-state dataset was taken from N=100 unrelated participants from the Human Connectome Project (HCP) of the 1200-participant release (Van Essen et al., 2013). Each participant underwent four 14.4-minute rsfMRI scans (TR = 0.72 s) acquired across two days (two scans per day, acquired in opposite phase-encode direction [left-right/right-left]). Each scan was preprocessed through the HCP with details described in Smith et al., 2013, and includes spatial distortion, and head-motion correction, registration to a T1 weighted structural, resampling to a 2 mm Montreal Neurological Institute (MNI) space, global intensity normalisation, high-pass filtering (cut-off at 2000 s), and ICA-based artefact removal (FSL-FIX [Griffanti et al., 2014; Salimi-Khorshidi et al., 2014]). In addition to HCP minimal preprocessing, mean white matter and ventricular signal was regressed from the data, followed by smoothing with a 5 mm FWHM Gaussian kernel respecting the natural geometry of the brain. Specifically, surface-base smoothing was applied to the cortical ribbon, whereas volumetric-base smoothing was applied to the subcortex. All scans from a single subject were Z-score normalised to zero mean and unit standard deviation and concatenated into a single one-hour rsfMRI scan. The concatenated rsfMRI scan was used in subsequent connectopic mapping of contralateral S1 subregions.

### 2.2.2 Motion exclusion criteria

To mitigate biases from the effects of motion we only include participants who fell within our necessarily stringent motion exclusion criterion (Power et al., 2012). Specifically, participants who had a mean framewise displacement (FD) greater than 0.2 mm in any of their four scans were excluded from analyses. This resulted in N=65 (FD; mean = 0.138 mm, SD = 0.023 mm) subjects used across all analyses.

### 2.2.3 Region of interest definitions of S1 anatomical hierarchy

All regions of interest were obtained from a surface-based multi-modal parcellation of the cerebral cortex (Glasser et al., 2016). We used Brodmann areas 3a, 3b, 1, and 2, to define an anatomical hierarchy of S1. The Glasser atlas also proposes five somatotopic subregions

within S1: lower limb (LL), trunk (T), upper limb (UL), ocular and face. For this current study, we only consider somatotopic regions that traverse all S1-related Brodmann areas to best illustrate anatomical hierarchy. As such, only LL, T and UL are included going forward (i.e., the ocular region includes only Brodmann area 3, and the face region includes areas 3 and 1). The UL and LL region were guided by left/right hand, and feet task contrasts, respectively, whereas, the definition of the trunk region was interpreted and localized between the UL and LL representations due to the absence of trunk-related contrasts.

In summary, each somatotopic subregion under consideration (i.e., LL, T, and UL) can be further delineated by its hierarchical structure (i.e., Brodmann areas 3a, 3b, 1, and 2) permitting investigations of anatomical hierarchy in S1. Human S1 hierarchy was annotated using a hierarchical organization scheme as proposed in macaques (Felleman and Van Essen, 1991) with supporting evidence found in humans (Bodegård et al., 2001).

The thalamus was also considered for seed-based connectivity analyses to explore and validate anatomical hierarchy of S1. Here, the thalamus was defined using the Harvard-Oxford atlas, and further parcellated into thalamic nuclei using the Morel atlas. The lateral geniculate nucleus (LGN) and inferior pulvinar (PuI) were excluded from all thalamocortical connectivity analyses due to the lack of overlap between the thalamic ROI from the Harvard-Oxford atlas and the Morel atlas. We considered thalamocortical connectivity ipsilaterally, therefore seed-based analyses of left hemisphere S1 regions only aimed to probe connectivity to the left thalamic nuclei, and vice versa.

### 2.2.4 Connectopic mapping

Connectopic mapping is a data-driven technique which can be used to spatially quantify RSFC patterns within a region of interest. Full details of the procedure are described in Haak et al. 2018 (only the Laplacian eigenmap technique used to embed voxel-wise RSFC patterns were used in the present study). In brief, RSFC was calculated between each ROI voxel ($\boldsymbol{A_{t\times v}}$: $t$=time,$v$=number of voxels in the ROI) and the rest of the brain ($\boldsymbol{B_{t\times v'}}$: $v'$=number of voxels in the rest of the brain (i.e., cortical and subcortical voxels)). To maintain computational tractability, the cortex and subcortex timeseries matrix ($\boldsymbol{B_{t\times v'}}$) was

projected onto a subspace spanned by its principal components ($\widetilde{\boldsymbol{B}}_{\boldsymbol{t\times t-1}}$). A RSFC matrix ($\boldsymbol{C}_{\boldsymbol{v\times t-1}}$) was computed which describes an ROI's RSFC pattern. Next, similarity between inter-voxel RSFC patterns were computed resulting in a similarity matrix ($\boldsymbol{S}_{\boldsymbol{v\times v}}$).

The Laplacian eigenmap algorithm is applied on the graph Laplacian of the similarity matrix to obtain a low dimensional manifold representation of the data, or gradients. The graph Laplacian is denoted as follows:

$$\boldsymbol{L} = \boldsymbol{D} - \boldsymbol{W},$$

where $\boldsymbol{W}$ is a graph representation of $\boldsymbol{S}$ (sparsity is enforced such that the graph is connected), $\boldsymbol{D}$ is the degree matrix defined as $\boldsymbol{D}_{\boldsymbol{i,i}} = \sum_{\boldsymbol{i}} \boldsymbol{W}_{\boldsymbol{i}}$, and $\boldsymbol{L}$ is the graph Laplacian. Solving the generalized eigenvalue problem $\boldsymbol{Ly} = \lambda \boldsymbol{Dy}$ yields $m$ eigenvectors $\{y_1, \dots, y_m\}$ corresponding to the smallest $m$ non-zero eigenvalues $\{\lambda_1, \dots, \lambda_m\}$. Here, we focus on $y_1$, defined as the region's dominant gradient and reflects the greatest changes in RSFC connectivity over a ROI, whereas higher order gradients, denoted by $\boldsymbol{y}_{\boldsymbol{n}}$, $1 < n < m$, reflects more subtle changes in RSFC.

This procedure is performed to generate dominant gradients of each region (i.e., left and right LL, T, and UL) for each subject. The direction, or sign of all generated gradients are often-times ambiguous and may be dependent on the selected dataset, and ROI-choice. To ensure consistency, the direction of all generated gradients was matched to have the same orientation. Specifically, the anterior-to-posterior and ventral-to-dorsal gradients corresponded to increases in gradient value. Additionally, each subject's dominant gradients were normalized between 0 and 1 to ensure consistency in scale across the cohort. Dominant gradients for each ROI were used to investigate relationships to anatomical hierarchy and geodesic distance in subsequent analyses.

### 2.2.5 Structural MRI measures

We considered cortical thickness, and T1w/T2w (Glasser and Van Essen, 2011) as structural MRI surrogates of S1 anatomical hierarchy and compare them against our RSFC-derived gradients. Due to the effects of surface folding and curvature on cortical thickness, a curvature-corrected cortical thickness measure is used in subsequent analyses. Similarly,

to mitigate the effects of $B_1$ inhomogeneity, a bias-field-corrected T1w/T2w measure is used.

### 2.2.6 Geodesic distance

We considered geodesic distance to probe how the dominant gradient varies while traversing the anterior-to-posterior axis of S1 (i.e., a geodesic distance of zero indicates the most anterior portion of BA3a, and higher values indicate more posterior areas, moving towards BA2). In addition, geodesic distance may be able to capture inter-individual differences and may be relevant for interpreting subject-level behaviour. Here, geodesic distance was measured as the shortest vertex-to-vertex path across a cortical surface connecting the middle vertex of the Brodmann area boundaries (i.e., vertex-to-vertex path adjoining areas 3a & 3b, 3b & 1, and 1 & 2). The middle vertex of the anterior border of BA3a, and posterior border of BA2 was hand-selected due to ambiguity of where these regions begin and end, respectively. Vertex-to-vertex paths were generated for left and right, LL, T and UL ROIs separately and used to extract dominant gradient values (based on RSFC) along this trajectory for all subjects. We also repeated this procedure considering other vertex-to-vertex paths, specifically considering 1st quantile, and 3rd quantile vertices.

### 2.2.7 Evidence of a functional boundary

We define a functional boundary to exist if it separates two discrete parcels. In theory, this means a sharp transition in RSFC should be expected at the interface of a functional boundary. Each boundary between Brodmann areas 3a & 3b, 3b & 1, and 1 & 2 is considered separately: a ‘parcel line’ is drawn to represent parcellation of each pair of regions using the vertex-to-vertex path described in the previous section – i.e., vertices of the anterior Brodmann area is given a value of 1, and vertices of the posterior Brodmann area is given a value of 0 (the line is smoothed with a 5 mm FWHM Gaussian kernel to match rsfMRI preprocessing procedures). The RSFC values were extracted from the vertex-to-vertex paths for each pair of Brodmann areas (3a & 3b, 3b & 1, and 1 & 2) and normalized between 0 and 1 to match the scaling of the ‘parcel line’. Evidence for a functional boundary is defined by computing the L2 norm between the parcel line and

RSFC values extracted from the dominant gradient. A value of zero suggests a perfect overlap between the dominant gradient and parcel line to be used as evidence for a functional boundary.

### 2.2.8 Seed selection

K-means clustering was performed on the dominant gradient map to assess the degree of overlap between clusters and Brodmann areas. The number of clusters considered were $K = 2, 3, 4$. If the dominant gradient reliably clusters well into the architectonic Brodmann areas, then this may further substantiate structure and function relationship of cortical S1. We justify the use of a clustering scheme that optimizes overlap with Brodmann area regions. Furthermore, we used this clustering scheme to define seed ROIs in subsequent thalamocortical connectivity analyses.

Choice of cluster number (K) was optimized by calculating an average dice similarity coefficient (DSC) between each of the K-clusters and a configuration of the Brodmann areas such that the average DSC is maximized. The DSC measures the similarity between a set X and Y (i.e., a K-means cluster and its corresponding ground truth label), if the sets are identical (i.e., they contain the same vertices), the coefficient is equal to 1, while if X and Y have no vertices in common, then it is equal to 0, otherwise the DSC falls somewhere between 0 and 1 (Dice, 1945). A silhouette analysis was conducted to assess the choice of K clusters. Silhouette coefficients are calculated for each vertex in a clustered region, providing a similarity measure ranging between -1 to 1. A high coefficient value indicates that the vertex is well matched to its cluster, a value of 0 indicates the vertex is between two clusters, and a negative value indicates a possible incorrect cluster assignment.

### 2.2.9 Statistical methods

#### 2.2.9.1 Multiple comparisons corrections

All statistical comparisons were conducted using an $\alpha$-level of 5% fully Bonferroni corrected for the number of comparisons.

#### 2.2.9.2 Dependent correlation test

As a statistical test for the difference between similarities of the measures, we employed the dependent correlation test. This test provides a nonparametric test to compare the Spearman correlations of two variables against a common dependent variable using a bootstrapping approach (Wilcox, 2016). The dependent correlation test was used to compare Spearman rank correlation of different metrics to anatomical hierarchy.

#### 2.2.9.3 Polynomial regression

Trend lines in Fig. 2.2a-c were calculated using polynomial regression, a form of regression analysis in which the dependent variable is modelled as an $n^{th}$ degree polynomial (in this case we choose n = 2 to account for the U-shape observed in the data).

#### 2.2.9.4 Thalamocortical connectivity analyses

We considered each ipsilateral LL, T, and UL as its own functional unit, as such, thalamocortical connectivity analyses were performed for each of these ROIs independently. The average timeseries were extracted from architectonic subdivisions of S1 determined from the K-means clustering analysis. Partial correlations maps of the unilateral thalamus were calculated using the extracted timeseries. Thalamocortical connectivity between Brodmann areas 3a & 3b, and 1 & 2 of somatotopic S1 and the thalamus was quantified by calculating the average partial correlation in the thalamus. Next, dominant connectivity of architectonic subregions of S1 to the thalamus was assessed using a nonparametric one-sample t-test (Nichols and Holmes, 2002). Significant voxels are considered as areas demonstrating dominant connectivity ($P < 0.05$, correcting for multiple comparisons after threshold-free cluster enhancement). Using the t-statistic image obtained from the one-sample t-test permutation test, and the Morel atlas of the thalamus, we quantified which thalamic nuclei demonstrated peak thalamocortical connectivity in each ROI (Krauth et al., 2010). Lastly, differences in the magnitude of partial correlation scores (or thalamocortical connectivity) of Brodmann parcels to each thalamic nucleus were assessed ($P < 0.05$, nonparametric Wilcoxon signed-rank test).

### 2.2.10 Data and code availability statement

All relevant MRI data are publicly available at https://db.humanconnectome.org. The processed data including the S1, and somatotopic subarea gradients, in addition to K-means clustering analyses can be found in the following repository: https://github.com/gngo4/S1_RSFC_Gradients.

The code for connectopic mapping is available in the following repository: https://github.com/koenhaak/congrads. Note, connectopic mapping was performed to resting-state fMRI data in CIFTI format. To generate RSFC gradients, the CIFTI formatted resting-state fMRI data must first be converted to NIFTI format. For further requests please contact the corresponding author.

## 2.3 Results

### 2.3.1 The dominant gradient of resting-state functional connectivity captures S1 anatomical hierarchy and microstructure

To enable the study of anatomical hierarchy in S1 using RSFC, our first aim was to embed high-dimensional RSFC data of S1 into a lower dimensional space. Specifically, the Laplacian eigenmap algorithm was computed on voxel-wise RSFC patterns to obtain gradients of S1 where each gradient represents a one-dimensional embedding of a region of interest. Previous work looking at the dominant gradient, or the gradient corresponding to the lowest non-zero eigenvalue of precentral gyri (i.e. primary motor cortex as defined using FreeSurfer (M1)) revealed somatotopic organization (Haak et al., 2018). In line with this previous work, we replicated the observation of somatotopy in left and right S1 cortices derived from group data. The dominant gradient reflected somatotopy, as observed by a gradual change in RSFC moving from lower limb to upper limb areas, whereas a clear boundary distinguishing the face from the upper limb region was observed. Furthermore, higher order gradients 2 and 3 of S1 revealed subtler differences in connectivity between the S1 subfields (i.e., anterior-to-posterior), notably observed in LL, T, and UL (Fig. 2.1b). Together, these observations suggest variation in RSFC is sensitive to biologically plausible functional organization, in this case, of S1. Motivated by this, we applied this technique to investigate functional organization within each somatotopic region of S1 (i.e.,

left and right hemisphere, LL, T and UL regions) to tease apart subregion-specific RSFC differences, and we hypothesized that the dominant gradient will provide a non-invasive predictor for anatomical hierarchy in S1.

The dominant gradient obtained of left and right LL, T and UL regions, to some degree, revealed an anterior-to-posterior axis (Fig. 2.1c) which may be an indicator of S1 hierarchical organization. The dominant gradients across all somatotopic regions were stable across individual subjects: the mean pairwise Pearson correlation between subjects' dominant gradients were [0.89, 0.96, 0.99, 0.98, 0.79, 0.62] for left and right LL, T, and UL, respectively. In the case of right UL, we observed a clear change in RSFC traversing from anterior-to-posterior (i.e., Brodmann areas 3a to 2). However, it was also noted that the maximum and minimum values of the gradient occurred in a dorsal-to-ventral manner within the region. This may be due to an imprecise definition and over estimation of the right UL region in the most ventral portion of the ROI. Such a definition may include voxels of S1 that encodes somatosensory face information, reflected by voxels with differing RSFC patterns, which in turn, may skew the right UL embedding. Subsequent cropping of the right UL region by removing the ventral-most area (which appears to overlap with the somatosensory face information) revealed a gradient spanning the region's anterior-to-posterior axis (Supplementary Fig. 2.1). Specifically, the cropped right UL region was generated by removing 10% of the voxels with the lowest gradient values. As a result, this improvement was matched by a mean pairwise Pearson correlation between subjects' dominant gradient of 0.76 (compared to 0.62).

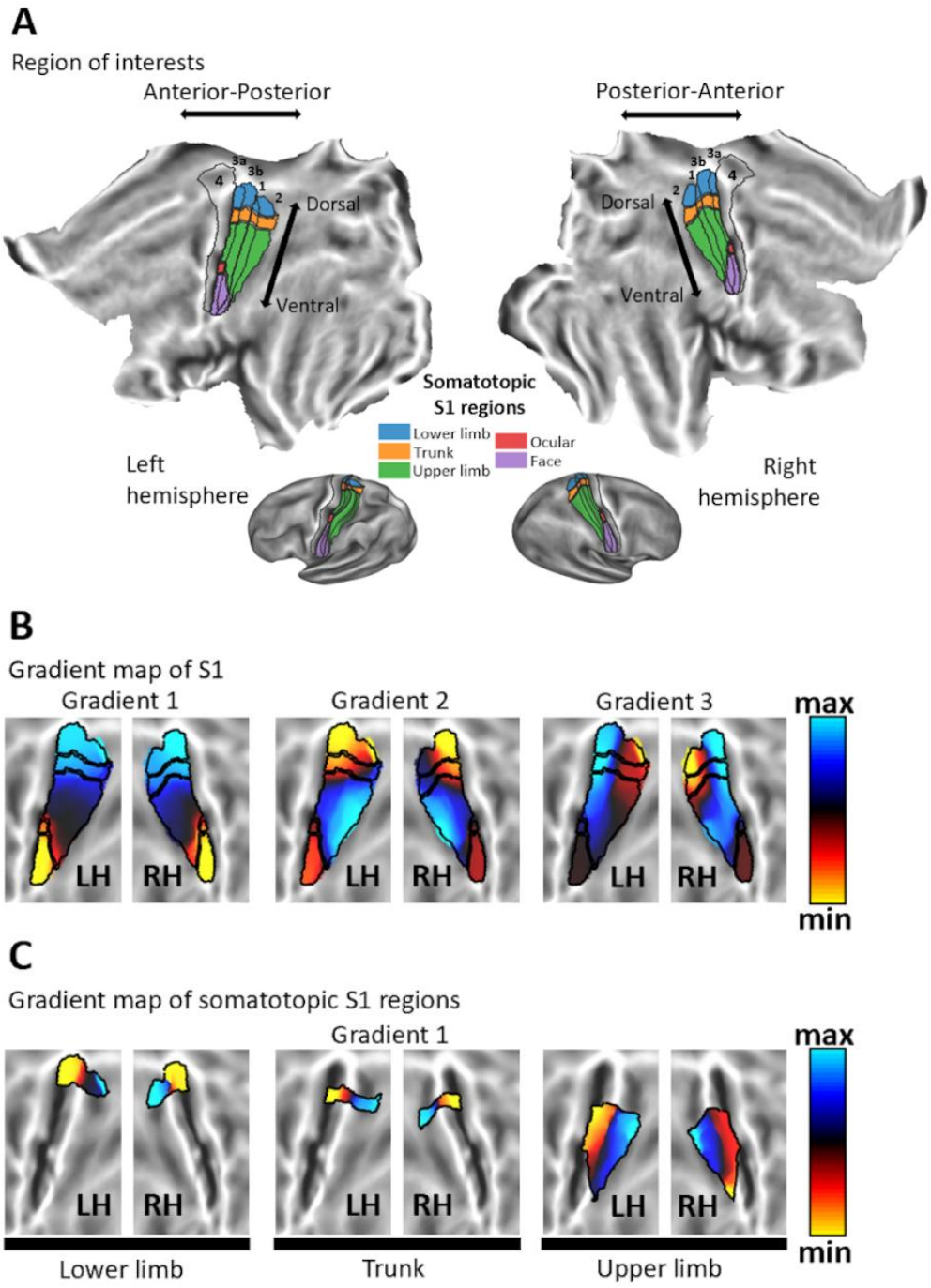


**Figure 2.1 Data-driven characterization of RSFC patterns in somatosensory cortex and somatotopic subregions**

*(A) ROI definitions mapped onto the cortical surface. (B) Group level gradients derived from S1 to whole brain and subcortex RSFC patterns (N = 65). The top three gradients are shown where each gradient represents a similarity embedding, as such, areas of similar*

*colours express similar connectivity patterns. The first gradient matches somatotopic organization, and the second and third gradient suggests separation of S1 along the anterior-to-posterior axis. (C) Group level gradients derived from somatotopic S1 subregions (i.e., LL, T, and UL) to whole brain and subcortex RSFC patterns (N = 65). All dominant gradients demonstrate a change in RSFC along the anterior-to-posterior axis. Gradient directionality is arbitrary; orientations have been matched to ensure consistency of interpretation.*

Next, we considered the ability of the dominant gradients to estimate anatomical hierarchical levels by comparing them to alternative surrogate measures derived from structural MRI. Based on previous work, measures of cortical thickness (Wagstyl et al., 2015) and T1w/T2w (i.e., considered as a proxy for microstructure/myelination) were considered: cortical thickness generally increases in areas higher up along the anatomical hierarchy, whereas the inverse is true for measures of myelination. Although all three measures were strongly associated with hierarchical levels of S1 ($***P < 10^{-4}$; Spearman correlation between all measures, and all somatotopic regions, see Fig. 2.2a-c), we found that the dominant gradients with the exception of right UL were more strongly correlated to hierarchical levels in S1 compared to cortical thickness ($***P < 10^{-4}$; dependent correlation test, see Fig 2.2d-e). Dominant gradients of left and right, LL and T performed better than T1w/T2w, whereas left UL performed the same, and right UL performed worse (presumably due to improper ROI definition) ($***P < 10^{-4}$; dependent correlation test, see Fig. 2.2d-e). Overall, we found that the dominant gradient was more strongly correlated to our annotated hierarchy scheme of S1 compared to structurally-derived surrogates. This finding provides evidence for the utility of RSFC-based gradients for characterizing anatomical hierarchy of S1.

Interestingly, the dominant gradient across all somatotopic regions strongly correlated to T1w/T2w intensity ($***P < 10^{-4}$; Pearson correlation, see Fig. 2.3) providing evidence of structure-function relationships in S1. With the exception of right UL, correlations

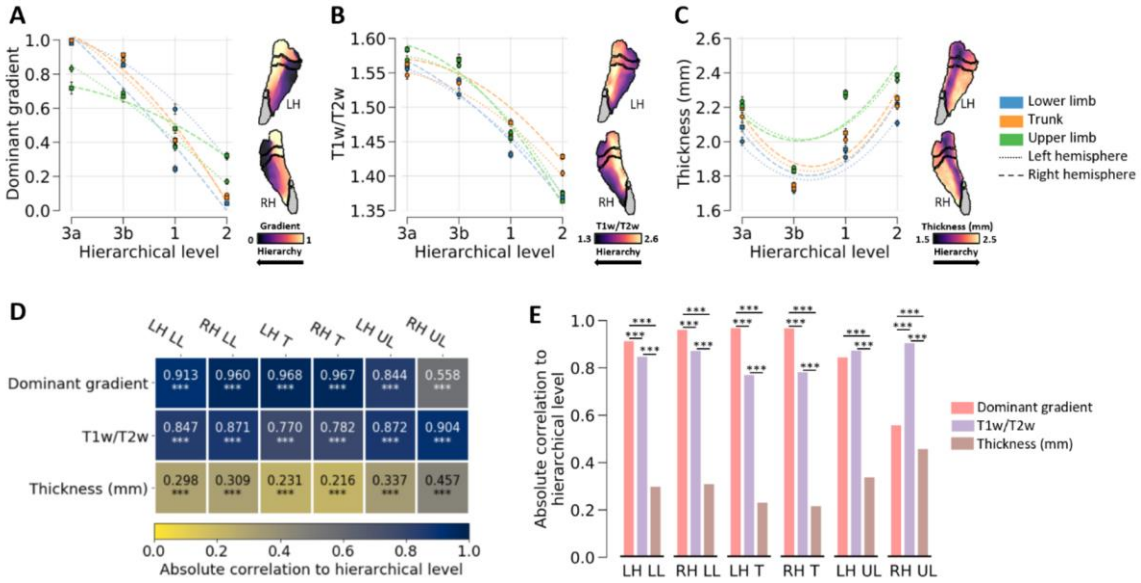


**Figure 2.2 Associations between anatomical hierarchies of S1 and metrics**

*(A) Correlation between anatomical hierarchy of somatotopic S1 subregions and their corresponding dominant gradients derived from RSFC data. (B) Correlation between anatomical hierarchy of somatotopic S1 subregions and T1w/T2w. (C) Correlation between anatomical hierarchy of somatotopic S1 subregions and cortical thickness. (D) Absolute spearman rank correlation between different metrics and anatomical hierarchy of S1 for each somatotopic subregion (***$P < 10^{-4}$ for all metrics and ROIs). (E) Comparison between metrics correlation to S1 anatomical hierarchy, across all somatotopic ROIs demonstrating RSFC gradient performs on par with T1w/T2w. Error bars in (A-C) indicate the SEM. Hierarchical levels (1, 2, 3, 4) correspond to (Brodmann areas 3a, 3b, 1, 2).*

were high across all regions (left LL: $r$=.84; left T: $r$=.90; left UL: $r$=.93; right LL: $r$=.91; right T: $r$=.87; right UL: $r$=.44). Although significance was observed between right UL's dominant gradient and T1w/T2w intensity, we attribute its low correlation values due to improper definition of this region as was previously suggested. In fact, an improved correlation value of $r$=.82 (compared to $r$=.44) was observed when using the truncated-right UL (Supplementary Fig. 2.2).

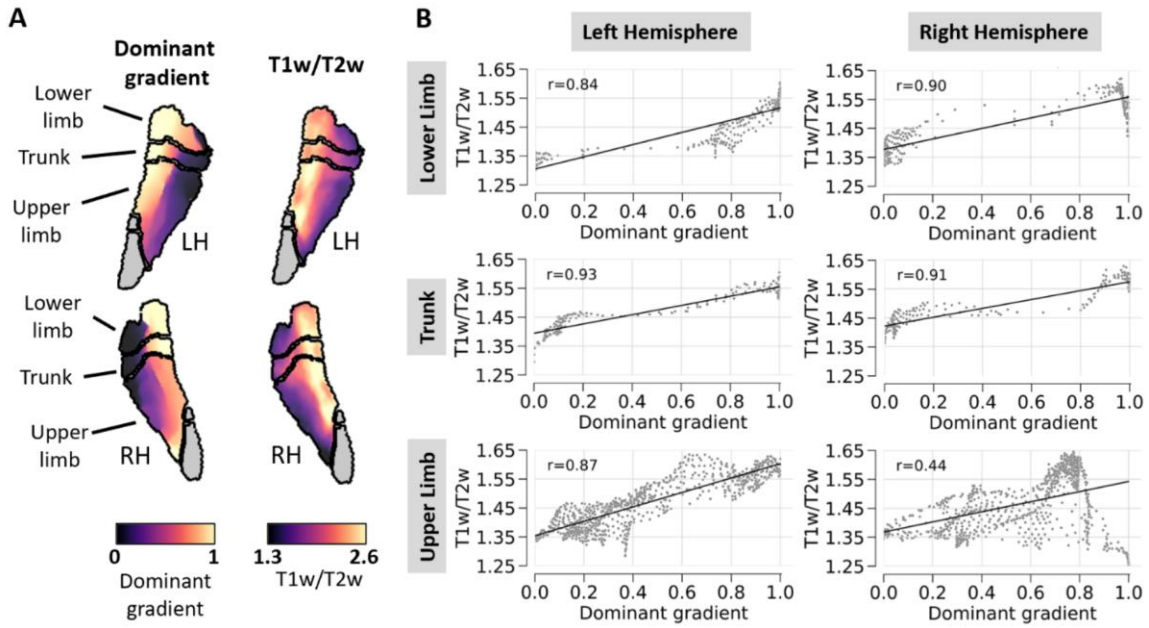


**Figure 2.3 Association between dominant gradient and T1w/T2w across left and right somatotopic S1 subregions**

*(A) Dominant gradient (left) and T1w/T2w intensities (right) for left and right, lower limb, trunk, and upper limb. (B) Correlation between the dominant gradient and T1w/T2w across all somatotopic S1 subregions (***$P < 10^{-4}$ for all ROIs).*

### 2.3.2 Characterising the anterior-to-posterior axis of S1 and correspondence to Brodmann areas

It is unclear how RSFC changes across the anterior-to-posterior axis in S1. Specifically, does RSFC within somatotopic S1 regions have discrete boundaries or does it gradually change over the space of the ROI? We considered the shortest vertex-to-vertex trajectory connecting the midpoint of adjacent Brodmann area boundaries to one another (i.e., a path joining Brodmann areas 3a, 3b, 1, and 2; see Fig. 2.4a) and used this path to investigate this question. We used geodesic distance away from the beginning of the trajectory to see how the RSFC embedding changes along this path, that is, a geodesic distance of zero corresponds to the most anterior portion of Brodmann area 3a. Figure 2.4b shows that RSFC gradually changes moving along this trajectory with gradual changes observed

within each Brodmann area as represented by the black points. Clear inter-individual variability in RSFC across the trajectory was also observed.

Next, we aimed to investigate whether discrete functional boundaries existed between Brodmann areas. To this end, boundaries between each adjacent Brodmann area were considered, such that a sharp transition exists at the interface between the two areas. These boundaries were additionally smoothed with a 5 mm FWHM Gaussian kernel to ensure consistency with the smoothing criterion that was used in the rsfMRI preprocessing steps. Three parcels boundaries were drawn as coloured lines adjoining areas 3a-to-3b, 3b-to-1, and 1-to-2 (i.e., blue, green, and purple, respectively; Fig. 2.4b), and the black points represent data from the dominant gradient. Any observed overlap between the coloured lines and points would suggest evidence for a discrete functional boundary. Comparisons of the average L2 norm between the definition of a parcel boundary, and dominant gradient suggests the most evidence (mean L2 norm closer to
zero) for a discrete boundary between Brodmann areas 3b and 1. Specifically, a significantly lower mean L2 norm was observed for the Brodmann area 3b-to-1 boundary, compared to boundaries between areas 3a-to-3b, and 1-to-2 in all somatotopic regions, with the exception of right UL and LL ($*P < 0.05$; nonparametric Wilcoxon signed-rank test, see bar plots in Fig. 2.4b). In the case of right UL, the evidence for a boundary was observed equally between areas 3b-to-1 and 1-to-2, and for right LL, evidence for a boundary was observed between areas 1-to-2. Similar observations were also observed when considering two other vertex-to-vertex paths (Supplementary Fig. 2.3 & 2.4). However, in both vertex-to-vertex paths, evidence for a boundary in the right UL (lowest L2 norm) were observed between Brodmann areas 3b-to-1. Overall, these results provide evidence for a discrete functional boundary between Brodmann areas 3b-to-1 as compared to the interfaces between Brodmann areas 3a-to-3b, and 1-to-2, which may be better characterized by a gradual change in RSFC.

Rather than investigating the gradients' trajectory, here we investigate the correspondence between each somatotopic ROIs' dominant gradients and Brodmann areas using K-means clustering. In the case of two clusters (K = 2), we found that the gradients clustered well into Brodmann areas 3a & 3b, and 1 & 2 (average dice

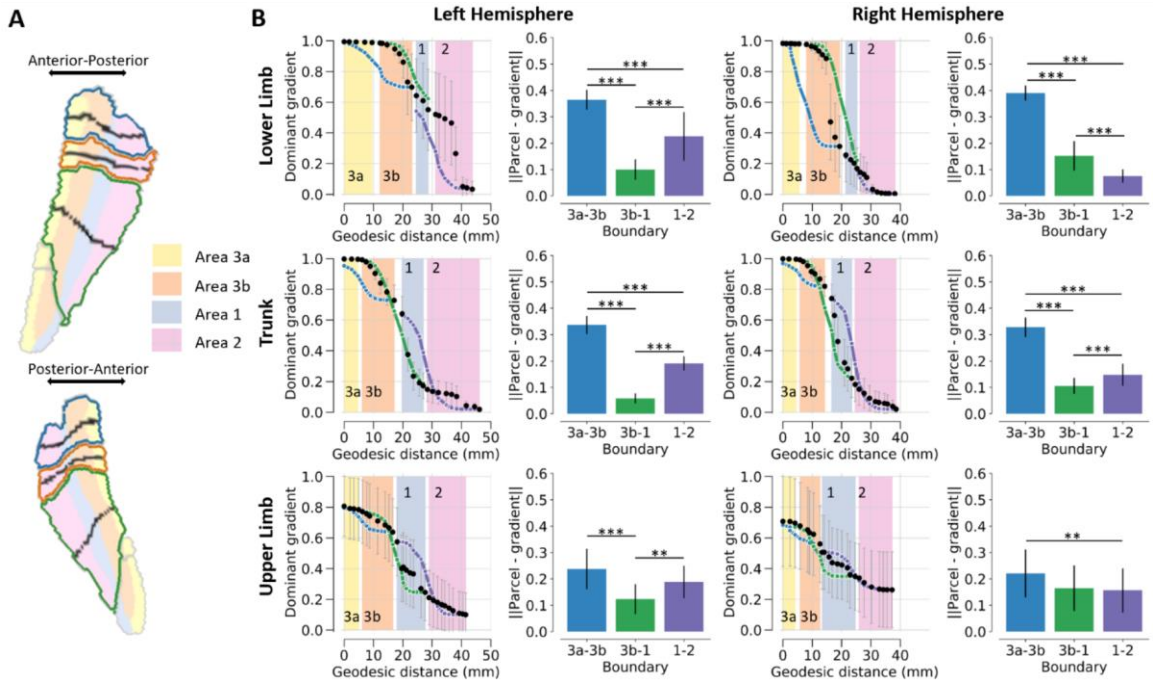


**Figure 2.4 Evidence of functional boundaries between Brodmann areas**

*(A) Left and right S1 separated by somatotopic regions and colour coded by architectonic Brodmann areas. Black lines in each somatotopic region indicates the vertex-to-vertex path (or trajectory) used to extract values from the RSFC-derived gradients. A geodesic distance of 0 indicates the most anterior vertex of the trajectory. (B) Left and right somatotopic regions' RSFC connectivity pattern plotted against geodesic distance as defined by a rostro-to-caudal vertex-to-vertex trajectory. Black points represent the average gradient value across all participants (N = 65). Overlaid are three 'parcel' definition lines drawn for each boundary between 3a & 3b, 3b & 1, and 1 & 2 (blue, green, and purple) smoothed with a 5 mm FWHM. Corresponding bar plots shows the L2 norm between parcel definition and RSFC connectivity pattern with a value closer to 0 suggesting more evidence for a functional boundary. Error bars in (B) indicate the standard deviation for all plots.* $*P < .05$, $***P < 10^{-4}$.

coefficient across all somatotopic regions: 0.856) as expected based on previous results. Using three and four clusters (K = 3, 4) led to a decrease in cluster performance, clustering of S1 into Brodmann areas 3a & 3b, 1, and 2, and Brodman areas 3a, 3b, 1, and 2, respectively (average dice coefficient across all somatotopic regions: 0.564 for K = 3;

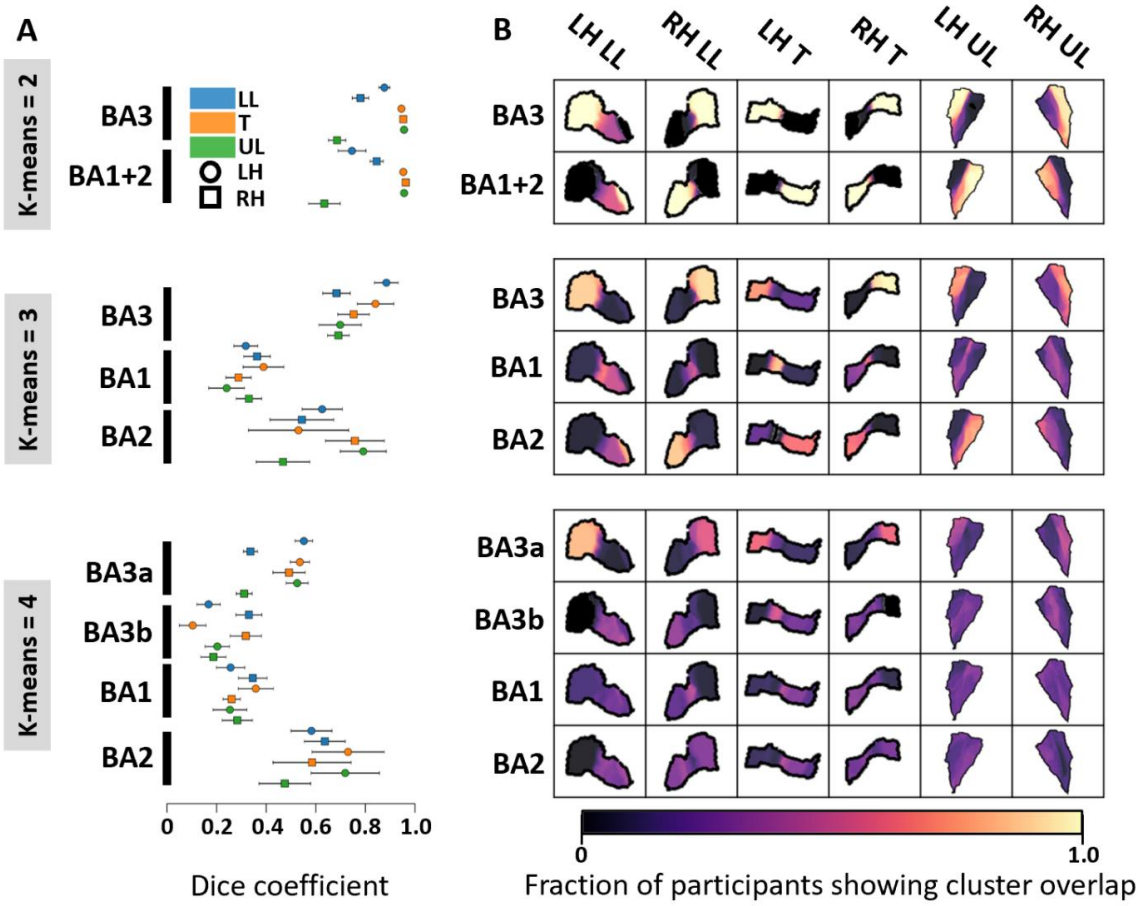


**Figure 2.5 Agreement between K-means clusters and Brodmann areas**

*(A) Average dice similarity coefficient scores (N = 65) for K clusters and their closest corresponding Brodmann areas. For K = 2, the DSC is calculated with Brodmann areas 3, and 1 & 2. For K = 3, the DSC is calculated with Brodmann areas 3, 1, and 2. For K = 4, the DSC is calculated with Brodmann areas 3a, 3b, 1, and 2. Bootstrap 95% confidence intervals are denoted by the error-bars. (B) Clustering performance using K = 2, 3, 4 clusters into their respective Brodmann areas. Maps show the fraction of participants (N = 65) showing overlap in the region.*

0.396 for K = 4). Fig. 2.5a provides further details regarding the performance of clustering for each somatotopic region. Furthermore, Fig. 2.5b shows the fraction of participants showing cluster overlap to each Brodmann area and demonstrating that high clustering stability was observed in Brodmann areas 3a & 3b, and areas 1 & 2 (i.e., K=2 clusters). The choice of K = 2 clusters was further validated by silhouette analyses, which

demonstrated highest average silhouette coefficient values at K = 2 clusters across all somatotopic regions, with incremental decreases observed with the choice of K = 3, and K = 4 clusters (Supplementary Fig. 2.5). Although variation in RSFC is not homogeneous in somatotopic S1 regions, here, we provided evidence for the separation of somatotopic S1 into two functional parcels that respect underlying architectonics, specifically, Brodmann areas 3a & 3b, and areas 1 & 2.

### 2.3.3 Thalamocortical connectivity reflects different Brodmann areas

Here, we applied the functional parcels defined by Brodmann areas 3a & 3b, and 1 & 2 to investigate thalamocortical connectivity for each somatotopic region. First, spatial maps showing areas of dominant thalamocortical connectivity between unilateral thalamus and Brodmann areas 3a & 3b, and 1 & 2 were examined to identify thalamic sites that are connected to S1. Fig. 2.6a shows each cortical component, and its significant areas of connectivity to the thalamus ($*P < 0.05$; nonparametric one-sample t-test). Qualitatively, these maps show Brodmann areas 3a & 3b have widespread connectivity to the whole thalamus across left and right, LL, T and UL. Contrary to this, thalamocortical connectivity of Brodmann areas 1 & 2, although widespread in the LL, was predominantly localized in the posterior of the thalamus. We investigated the dominant thalamocortical connectivity maps to further characterize which thalamic nuclei (i.e., using the Morel atlas [Krauth et al., 2010]) showed peak connectivity for each cortical ROI of S1. In general, we found peak thalamocortical connectivity to areas adjacent to VP nucleus (i.e., posterior nucleus [PO], medial geniculate nucleus [MGN], and anterior pulvinar [PuA]) (Fig. 2.6b), whereas only right Brodmann areas 1 & 2 showed peak connectivity to ventral posterior (VP) nucleus. Furthermore, left and right Brodmann areas 3a & 3b trunk showed peak connectivity to more anterior regions of the thalamus (i.e., medial dorsal [MD], and intralaminar [IL] nuclei), and the left T and UL of Brodmann areas 1 & 2 also showed peak connectivity to the lateral pulvinar (PuL). Next, we assessed whether the magnitude of RSFC differed between the functional parcels (Brodmann areas 3a & 3b, and areas 1 & 2) and each thalamic nucleus. In general, higher functional connectivity was observed between each thalamic nucleus and Brodmann

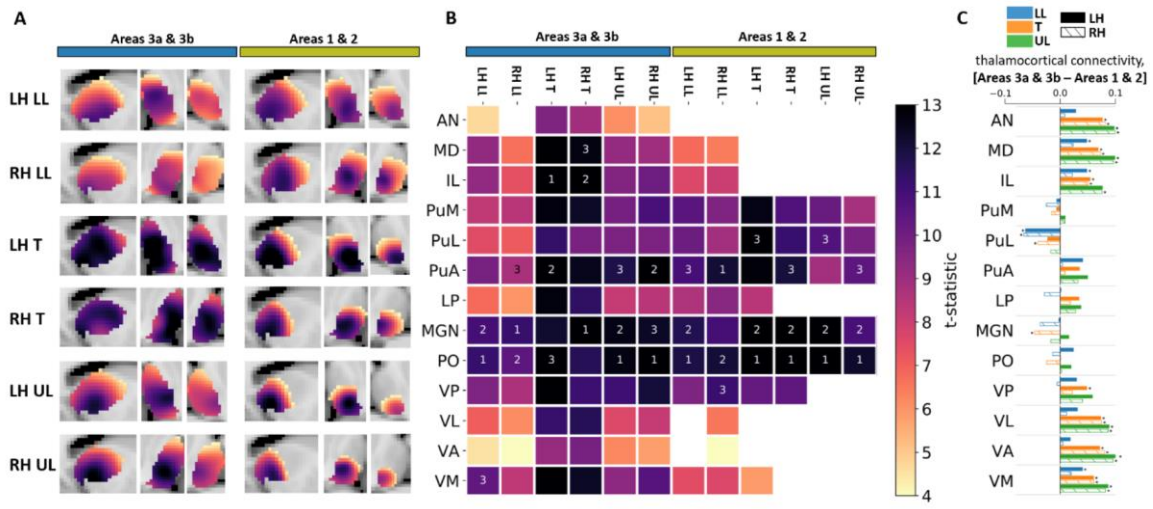


**Figure 2.6 Spatial analysis of dominant thalamocortical connectivity between ipsilateral thalamus and functional subdivisions of S1**

*(A) Areas of the thalamus significantly correlated with corresponding cortical region (*P < .05). To qualitatively assess areas of the thalamus that display higher connectivity, the t-statistic map is overlaid on these maps obtained from the one-sample t-test permutation test. (B) Mean t-statistic values for each thalamic nucleus based on the Morel atlas (Krauth et al., 2010). Only thalamic nuclei that were significantly correlated with the corresponding cortical region are shown. Numbers 1, 2, 3 corresponds to the top three thalamic nuclei with the highest t-statistic value in descending order. (C) Difference in thalamocortical connectivity (measured by partial correlation score) between Brodmann areas 3a & 3b, and 1 & 2 to each thalamic nucleus. Thalamocortical connections with significant differences are annotated by an asterisk (*P < .05). The 13 thalamic nuclei are as follows: anterior nucleus (AN), medial dorsal (MD), internal lamina (IL), pulvinar medial (PuM), pulvinar lateral (PuL), pulvinar anterior (PuA), lateral posterior (LP), medial geniculate nucleus (MGN), posterior nucleus (PO), ventral posterior (VP), ventral lateral (VL), ventral anterior (VA), and ventral medial (VM).*

areas 3a & 3b than with Brodmann areas 1 & 2. Specifically, thalamocortical connectivity was significantly higher between somatotopic Brodmann areas 3a & 3b and seven out of the 13 thalamic nuclei, compared to thalamocortical connections to areas 1 & 2: AN (left & right T, and left & right UL) , MD (left LL, left & right T, and left & right UL), IL (left

LL, left & right T, and right UL), VP (left T only), VL (left & right T, and left & right UL), VA (left & right T, and left & right UL), and VM (left LL ,left & right T, and left & right UL) ($*P < 0.05$; nonparametric Wilcoxon signed-rank test, specific details documenting all of the thalamic nuclei-to-S1 functional connections can be found in Fig. 2.6c with box plots shown in Supplementary Fig 2.6). Contrary to this, thalamocortical connectivity of the MGN (right T only), and PuL (right T, and right & left LL) were higher with Brodmann areas 1 & 2 compared to connections with areas 3a & 3b ($*P < 0.05$; nonparametric Wilcoxon signed-rank test). Overall, most thalamic nuclei demonstrated differences in thalamocortical connectivity between functional parcels with a trend towards having stronger connectivity to Brodmann areas 3a & 3b, than to areas 1 & 2. Together, these results demonstrate that VP and VP-adjacent nuclei are primarily connected to both S1 Brodmann parcels, as supported by NHP-related anatomical studies (Nelson and Kaas, 1981; Mayner and Kaas, 1986). We further showed that different Brodmann area parcels led to spatial differences in connectivity patterns to the thalamus, in addition to some differences in magnitude of connectivity to thalamic nuclei. Taken together, this suggests the application of the proposed gradient scheme in future RSFC-related connectivity studies.

## 2.4 Discussion

In the present study, we demonstrated the use of resting-state functional connectivity to characterize mesoscopic structural organization of primary somatosensory cortex. First, a novel technique, connectopic mapping, was applied to RSFC data and revealed a RSFC gradient in S1 which serves as a proxy for anatomical hierarchy of that region. Subsequent analysis of the RSFC gradient revealed evidence for two distinct functional parcels that delineate Brodmann areas 3a & 3b from areas 1 & 2. Thalamocortical connectivity using these parcels was then applied to reveal differing connectivity patterns that are supported by anatomical studies of NHPs, and further underscores the value of using this gradient scheme for future S1-related work in humans. Collectively, these results provide evidence for an anterior-to-posterior gradient in the resting primary somatosensory cortex and suggests close associations to anatomical hierarchy, microstructure, and Brodmann boundaries. Application of this novel technique provides new insight into bridging the gap

between mesoscale connectivity and microstructure along the architectonic axis of S1, and builds upon previous multimodal characterization of S1 along its somatotopic axis (Kuehn et al., 2017). Crucially, our work suggests a secondary direction of functional heterogeneity intrinsic to S1 and may be used in conjunction with structural MR measures to fully appreciate the interplay between functional connectivity and structure.

Manifold learning or 'connectopic mapping' was used to demonstrate that the dominant RSFC gradients of somatotopic S1 regions were able to accurately predict anatomical hierarchy, and in most cases, demonstrated stronger associations when compared to other structural MR metrics. As such, application of RSFC could be used as another surrogate for local mesoscopic hierarchy, and may be used in conjunction with structural MR metrics to investigate structure-function interplay. Evidence for using structural MR metrics as a surrogate for anatomical hierarchy is supported by close associations between patterns of feedforward/feedback innervations (Barbas and Rempel-Clower, 1997), laminar differentiation (Barbas, 1986), and cytoarchitecture (Dinse et al., 2015). In principle, structural organization revealed in this manner only accounts for intraregional characteristics and does not consider interregional connectivity. For example, it is possible that structural damage to S1-connected regions may have downstream effects on the dominant RSFC gradient which may not be evident using structural measures. This has far reaching implications for S1, as S1 has been shown to topographically map onto the cerebellum (Hahamy and Makin, 2019), primary motor cortex, supplementary motor cortex (Zeharia et al., 2012), operculum and insula (Brooks et al., 2005), and parietal cortex (Huang et al., 2012), among other regions. More critically, the notion of S1 interregional connectivity is fundamental for brain function as suggested in animals to facilitate whisker-detection tasks (Yamashita and Petersen, 2016; Kwon et al., 2016), and in humans for deep brain stimulation (Horn and Fox, 2020). Thus, the identification of a surrogate for anatomical hierarchy in humans that is grounded by the principles of RSFC may provide further insight into the relationships between structure-function, behaviour, and disease.

A more detailed analysis assessing the anterior-to-posterior gradients found in somatotopic regions of S1 revealed gradual changes in RSFC between boundaries of Brodmann areas 3a & 3b and 1 & 2, whereas a more pronounced change in RSFC can be identified between

areas 3b & 1, and suggests a possible functional boundary. Based on NHP anatomical studies it is well understood that different architectonic regions demonstrate distinct connectivity patterns (Krubitzer and Disbrow, 2008). Specifically, Brodmann area 3b connects primarily to adjacent S1 regions, such as areas 3a, 1, 2, secondary somatosensory cortex (S2), and primary motor cortex (M1) (Krubitzer and Kaas, 1990; Jones et al., 1979; Juliano et al., 1990; Darian-Smith et al., 1993). In comparison, Brodmann area 1 demonstrates more dispersed connections to areas 3b, 2, 7b, S2, in addition to sparse connections with areas 3a, M1 and frontal cortex (Pons and Kaas, 1986; Burton and Fabri, 1995; Burton et al., 1995). These separate connectivity patterns may explain the sharp divergence in RSFC patterns between Brodmann areas 3b & 1. Furthermore, Geyer and colleagues (Geyer et al., 1999) conducted a transmitter binding study which characterized the Brodmann areas with a 'neurochemical fingerprint', and the most differences in neurotransmitter binding sites were observed at the interface between areas 3b & 1, providing further evidence of a functional boundary between these two regions.

Gradual changes in functional topography observed between areas 3a & 3b, and 1 & 2 may be due to similar, but not identical connectivity patterns displayed by each pair of regions. Although area 3b is densely connected to area 3a, area 3a has additional connections to motor and posterior parietal areas of the cortex, as found in anatomical tracer studies in marmosets (Huffman and Krubitzer, 2001), and macaques (Jones et al., 1978; Darian-Smith et al., 1993). Similar findings have been observed in electrophysiological-guided tracer studies in macaques for Brodmann areas 1 and 2 (Pons and Kaas., 1985). Slightly differing connectivity patterns in these pair of regions may explain the gradual changes in RSFC observed in our data. Interestingly, we showed that RSFC also changes gradually within each Brodmann area (see Fig. 2.4b). These gradual changes reflect intrinsic RSFC heterogeneity in somatotopic areas along the anterior-to-posterior axis and may be related to possible connection topography of somatotopic ROIs onto other cortical areas. Such functional topography may be important for developing a better understanding of mesoscopic hierarchical function in humans.

Although thalamic connections to S1 predominantly originate in VP, it has been shown that thalamic inputs to areas 3a & 3b vary widely, whereas inputs to 1 & 2 localize more

to posterior nuclei. For example, NHP anatomical tracer literature has shown that in addition to inputs from VP, areas 3a & 3b receive collective input from pulvinar (Cusick and Gould, 1990) (Pu), ventral lateral (VL), ventral anterior (VA) and central medial thalamic nuclei (Lang et al., 1979) (CL; as part of the internal lamina (IL)), and areas 1 & 2 receive inputs from VL, and Pu (Pons and Kaas, 1985; Friedman and Jones, 1981). In the present study, connections were observed between all investigated thalamic nuclei and Brodmann areas 3a & 3b, while only some thalamic nuclei, majority of which were located in the posterior of the thalamus, showed connections to areas 1 & 2. Nuclei that were connected to both Brodmann parcels trended towards having stronger functional connectivity to Brodmann areas 3a & 3b, compared to areas 1 & 2. Perhaps the most important thalamic nucleus associated to S1 is VP, which is known to have more dense connections to Brodmann area 3 compared to area 1 (Mayner and Kaas, 1986). However, here we observed only a trend favouring stronger functional connectivity between areas 3a & 3b and VP. This inconsistency with existing NHP literature may be attributed to a reduced signal-to-noise ratio and sensitivity to blood-oxygenation-level-dependent signal in the subcortex (compared to the cortex) (Puckett et al., 2018). Despite the lack of significant differences in observed functional connectivity between VP (and VP-adjacent) nuclei and Brodmann parcels, here, we demonstrated the parcels' ability to accurately describe well-known NHP anatomical thalamocortical connections. Together, these findings suggest that consideration of S1 as two separate architectonic ROIs, rather than the common method of using whole S1 (Woodward et al., 2017; Chen et al., 2019), may provide complimentary information regarding thalamocortical RSFC. This approach could be used in clinical neuroscience to conduct more in-depth investigations into thalamocortical connectivity in future studies.

Interestingly, in Brodmann areas 3a & 3b, and 1 & 2, we saw ipsilateral thalamocortical connectivity to be higher in thalamic nuclei adjacent to VP (posterior nucleus (PO), medial geniculate nucleus (MGN), and anterior pulvinar (PuA)), compared to VP itself. It is possible that misregistration between the Morel cytoarchitectonic atlas (used to define the nuclei) may explain for these inconsistencies. For example, the Oxford thalamic connectivity probability atlas (Behrens et al., 2003) derived from diffusion tractography showed that PO, VP and PuA demonstrated similar likelihood of connectivity to the

somatosensory cortex (31, 26.8, and 23.6 %, respectively), suggesting that Morel's atlas definition of PO should be considered the primary relay nucleus of S1, which is traditionally acknowledged as VP. With these considerations in mind, our thalamocortical analyses of Brodmann areas suggests peak RSFC to VP or VP-adjacent nuclei, and further supports the VP-centric role of the thalamus for S1.

Our results are subject to several methodological limitations. In this study, the ensuing dominant gradients were generated from RSFC data which relies on inter-brain region timeseries correlation values during an at-rest paradigm. In principle, this technique cannot be used to draw inference on the functional role of a cortical region, whereas task-based multivariate fMRI analyses could be used to fill this gap (Yokoi and Diedrichsen, 2019). Nonetheless, RSFC enables an accessible way to index brain connectivity, and holds strong parallels to how anatomical hierarchy has been traditionally annotated based on anatomical connectivity information (Felleman and Van Essen, 1991). Furthermore, RSFC provides a more practical solution for acquiring data from clinical participants who may be unable to cooperate and perform task-related experimental designs.

Another limitation is that our results only investigate the primary gradient generated from each somatotopic S1 subregion while ignoring other higher order gradients. In the context of this work, constraining our investigations to only the primary gradient was sufficient for us to accurately characterize an anterior-to-posterior axis of the somatosensory cortex while demonstrating its correspondence with underlying cytoarchitectonic boundaries. It is acknowledged that multiple overlapping gradients may exist within any given ROI (for example, a retinotopic and visuotopic gradient in V1 [Haak and Beckmann, 2020]), thus future investigations could evaluate whether higher-order gradients provide further information towards the characterization of S1.

Finally, as this work uses previously defined ROIs, any limitations associated with ROI-based analyses are also shared with this study. To mitigate ROI-inaccuracies, we used Brodmann area ROIs taken from Glasser and colleagues' atlas which takes advantage of convergent multi-modal information to reduce errors associated with mis-defining of architectonic borders[23]. Furthermore, it is suggested that the medial-superior definition of

Brodmann area 2 may slightly overlap with area 5L (Scheperjans et al., 2008), which in turn, may skew embeddings of LH/RH upper limb. Nonetheless, although inaccuracies in ROI may attend this work, we believe our results demonstrate a clear anterior-to-posterior axis in somatotopic S1 that is strongly associated with microstructure and corresponds well with Brodmann areas. Moving towards finer-grained descriptions of functional topography using RSFC, we stress the importance of accurate ROI definition to reliably capture biologically meaningful gradients.

The present study uses RSFC data to demonstrate anatomical hierarchy of S1 in humans, in addition to its association with microstructure and correspondence to Brodmann areas. Such insight suggests close coupling between structure and function and offers a framework for studying structure-function interplay in humans. Beyond this, examination of S1 at the systems level could lead to improved understanding of sensorimotor behaviours, and deficits whose pathophysiology is not well understood.

## 2.5 References


Barbas, H. (1986). Pattern in the laminar origin of corticocortical connections. *The Journal of Comparative Neurology*, *252*(3), 415–422. https://doi.org/10.1002/cne.902520310

Barbas, H., & Rempel-Clower, N. (1997). Cortical structure predicts the pattern of corticocortical connections. *Cerebral Cortex*, *7*(7), 635–646. https://doi.org/10.1093/cercor/7.7.635

Behrens, T. E. J., Johansen-Berg, H., Woolrich, M. W., Smith, S. M., Wheeler-Kingshott, C. a. M., Boulby, P. A., … Matthews, P. M. (2003). Non-invasive mapping of connections between human thalamus and cortex using diffusion imaging. *Nature Neuroscience*, *6*(7), 750–757. https://doi.org/10.1038/nn1075

Bensmaia, S. J., Denchev, P. V., Dammann, J. F., Craig, J. C., & Hsiao, S. S. (2008). The Representation of Stimulus Orientation in the Early Stages of Somatosensory Processing. *Journal of Neuroscience*, *28*(3), 776–786. https://doi.org/10.1523/JNEUROSCI.4162-07.2008

Bodegård, A., Geyer, S., Grefkes, C., Zilles, K., & Roland, P. E. (2001). Hierarchical processing of tactile shape in the human brain. *Neuron*, *31*(2), 317–328. https://doi.org/10.1016/s0896-6273(01)00362-2

Brodmann, K. 1909. Vergleichende Lokalisationslehre der Großhirnrinde in ihren Prinzipien dargestellt auf Grund des Zellenbaues. Barth, Leipzig.

Brooks, J. C. W., Zambreanu, L., Godinez, A., Craig, A. D. B., & Tracey, I. (2005). Somatotopic organisation of the human insula to painful heat studied with high resolution functional imaging. *NeuroImage*, *27*(1), 201–209. https://doi.org/10.1016/j.neuroimage.2005.03.041

Burton, H., & Fabri, M. (1995). Ipsilateral intracortical connections of physiologically defined cutaneous representations in areas 3b and 1 of macaque monkeys: Projections in the vicinity of the central sulcus. *The Journal of Comparative Neurology*, *355*(4), 508–538. https://doi.org/10.1002/cne.903550404

Burton, H., Fabri, M., & Alloway, K. (1995). Cortical areas within the lateral sulcus connected to cutaneous representations in areas 3b and 1: A revised interpretation of the second somatosensory area in macaque monkeys. *The Journal of Comparative Neurology*, *355*(4), 539–562. https://doi.org/10.1002/cne.903550405

Chen, P., Ye, E., Jin, X., Zhu, Y., & Wang, L. (2019). Association between Thalamocortical Functional Connectivity Abnormalities and Cognitive Deficits in Schizophrenia. *Scientific Reports*, *9*, 2952. https://doi.org/10.1038/s41598-019-39367-z

Conte, A., Khan, N., Defazio, G., Rothwell, J. C., & Berardelli, A. (2013). Pathophysiology of somatosensory abnormalities in Parkinson disease. *Nature Reviews. Neurology*, *9*(12), 687–697. https://doi.org/10.1038/nrneurol.2013.224

Cusick, C. G., & Gould, H. J. (1990). Connections between area 3b of the somatosensory cortex and subdivisions of the ventroposterior nuclear complex and the anterior pulvinar nucleus in squirrel monkeys. *The Journal of Comparative Neurology*, *292*(1), 83–102. https://doi.org/10.1002/cne.902920106

Darian-Smith, C., Darian-Smith, I., Burman, K., & Ratcliffe, N. (1993). Ipsilateral cortical projections to areas 3a, 3b, and 4 in the macaque monkey. *The Journal of Comparative Neurology*, *335*(2), 200–213. https://doi.org/10.1002/cne.903350205

Diamond, M. E., von Heimendahl, M., Knutsen, P. M., Kleinfeld, D., & Ahissar, E. (2008). "Where" and "what" in the whisker sensorimotor system. *Nature Reviews Neuroscience*, *9*(8), 601–612. https://doi.org/10.1038/nrn2411

Dice, L. R. (1945). Measures of the Amount of Ecologic Association Between Species. *Ecology*, *26*(3), 297–302. https://doi.org/10.2307/1932409

Dinse, J., Härtwich, N., Waehnert, M. D., Tardif, C. L., Schäfer, A., Geyer, S., … Bazin, P.-L. (2015). A cytoarchitecture-driven myelin model reveals area-specific signatures in human primary and secondary areas using ultra-high resolution in-vivo brain MRI. *NeuroImage*, *114*, 71–87. https://doi.org/10.1016/j.neuroimage.2015.04.023

Drevets, W. C., Burton, H., Videen, T. O., Snyder, A. Z., Simpson, J. R., & Raichle, M. E. (1995). Blood flow changes in human somatosensory cortex during anticipated stimulation. *Nature*, *373*(6511), 249–252. https://doi.org/10.1038/373249a0

Felleman, D. J., & Van Essen, D. C. (1991). Distributed hierarchical processing in the primate cerebral cortex. *Cerebral Cortex (New York, N.Y.: 1991)*, *1*(1), 1–47. https://doi.org/10.1093/cercor/1.1.1

Fischl, B., Rajendran, N., Busa, E., Augustinack, J., Hinds, O., Yeo, B. T. T., … Zilles, K. (2008). Cortical folding patterns and predicting cytoarchitecture. *Cerebral Cortex (New York, N.Y.: 1991)*, *18*(8), 1973–1980. https://doi.org/10.1093/cercor/bhm225

Friedman, D. P., & Jones, E. G. (1981). Thalamic input to areas 3a and 2 in monkeys. *Journal of Neurophysiology*, *45*(1), 59–85. https://doi.org/10.1152/jn.1981.45.1.59

Geyer, S., Schormann, T., Mohlberg, H., & Zilles, K. (2000). Areas 3a, 3b, and 1 of human primary somatosensory cortex. Part 2. Spatial normalization to standard anatomical space. *NeuroImage*, *11*(6 Pt 1), 684–696. https://doi.org/10.1006/nimg.2000.0548

Glasser, M. F., Coalson, T. S., Robinson, E. C., Hacker, C. D., Harwell, J., Yacoub, E., … Van Essen, D. C. (2016). A multi-modal parcellation of human cerebral cortex. *Nature*, *536*(7615), 171–178. https://doi.org/10.1038/nature18933

Glasser, M. F., & Van Essen, D. C. (2011). Mapping human cortical areas in vivo based on myelin content as revealed by T1- and T2-weighted MRI. *The Journal of Neuroscience: The Official Journal of the Society for Neuroscience*, *31*(32), 11597–11616. https://doi.org/10.1523/JNEUROSCI.2180-11.2011

Griffanti, L., Salimi-Khorshidi, G., Beckmann, C. F., Auerbach, E. J., Douaud, G., Sexton, C. E., … Smith, S. M. (2014). ICA-based artefact removal and accelerated fMRI acquisition for improved resting state network imaging. *NeuroImage*, *95*, 232–247. https://doi.org/10.1016/j.neuroimage.2014.03.034

Haak, K. V., & Beckmann, C. F. (2020). Understanding brain organisation in the face of functional heterogeneity and functional multiplicity. *NeuroImage*, *220*, 117061. https://doi.org/10.1016/j.neuroimage.2020.117061

Haak, K. V., Marquand, A. F., & Beckmann, C. F. (2018). Connectopic mapping with resting-state fMRI. *NeuroImage*, *170*, 83–94. https://doi.org/10.1016/j.neuroimage.2017.06.075

Hahamy, A., & Makin, T. R. (2019). Remapping in Cerebral and Cerebellar Cortices Is Not Restricted by Somatotopy. *Journal of Neuroscience*, *39*(47), 9328–9342. https://doi.org/10.1523/JNEUROSCI.2599-18.2019

Horn, A., & Fox, M. D. (2020). Opportunities of connectomic neuromodulation. *NeuroImage*, *221*, 117180. https://doi.org/10.1016/j.neuroimage.2020.117180

Huang, R.-S., Chen, C., Tran, A. T., Holstein, K. L., & Sereno, M. I. (2012). Mapping multisensory parietal face and body areas in humans. *Proceedings of the National Academy of Sciences*, *109*(44), 18114–18119. https://doi.org/10.1073/pnas.1207946109

Huffman, K. J., & Krubitzer, L. (2001). Area 3a: Topographic organization and cortical connections in marmoset monkeys. *Cerebral Cortex (New York, N.Y.: 1991)*, *11*(9), 849–867. https://doi.org/10.1093/cercor/11.9.849

Isett, B. R., Feasel, S. H., Lane, M. A., & Feldman, D. E. (2018). Slip-Based Coding of Local Shape and Texture in Mouse S1. *Neuron*, *97*(2), 418-433.e5. https://doi.org/10.1016/j.neuron.2017.12.021

Iwamura, Y. (1998). Hierarchical somatosensory processing. *Current Opinion in Neurobiology*, *8*(4), 522–528. https://doi.org/10.1016/S0959-4388(98)80041-X

Jbabdi, S., Sotiropoulos, S. N., Haber, S. N., Van Essen, D. C., & Behrens, T. E. (2015). Measuring macroscopic brain connections in vivo. *Nature Neuroscience*, *18*(11), 1546–1555. https://doi.org/10.1038/nn.4134

Jones, E. G., Coulter, J. D., & Hendry, S. H. (1978). Intracortical connectivity of architectonic fields in the somatic sensory, motor and parietal cortex of monkeys. *The Journal of Comparative Neurology*, *181*(2), 291–347. https://doi.org/10.1002/cne.901810206

Juliano, S. L., Friedman, D. P., & Eslin, D. E. (1990). Corticocortical connections predict patches of stimulus-evoked metabolic activity in monkey somatosensory cortex. *The Journal of Comparative Neurology*, *298*(1), 23–39. https://doi.org/10.1002/cne.902980103

Kim, J. S., & Choi-Kwon, S. (1996). Discriminative sensory dysfunction after unilateral stroke. *Stroke*, *27*(4), 677–682. https://doi.org/10.1161/01.str.27.4.677

Kim, S. S., Gomez-Ramirez, M., Thakur, P. H., & Hsiao, S. S. (2015). Multimodal interactions between proprioceptive and cutaneous signals in primary somatosensory cortex. *Neuron*, *86*(2), 555–566. https://doi.org/10.1016/j.neuron.2015.03.020

Kleinfeld, D., & Deschênes, M. (2011). Neuronal Basis for Object Location in the Vibrissa Scanning Sensorimotor System. *Neuron*, *72*(3), 455–468. https://doi.org/10.1016/j.neuron.2011.10.009

Krauth, A., Blanc, R., Poveda, A., Jeanmonod, D., Morel, A., & Székely, G. (2010). A mean three-dimensional atlas of the human thalamus: Generation from multiple histological data. *NeuroImage*, *49*(3), 2053–2062. https://doi.org/10.1016/j.neuroimage.2009.10.042

Krubitzer, L. A., & Disbrow, E. (2008) The evolution of parietal areas involved in hand use in primates. In: The Senses: A Comprehensive Reference; Kaas JH and Gardner E (Eds.), Volume 6, Somatosensation, Chapter 10 (pp. 183-214). Elsevier, London.

Krubitzer, L. A., & Kaas, J. H. (1990a). The organization and connections of somatosensory cortex in marmosets. *The Journal of Neuroscience: The Official Journal of the Society for Neuroscience*, *10*(3), 952–974.

Krubitzer, L. A., & Kaas, J. H. (1990b). The organization and connections of somatosensory cortex in marmosets. *The Journal of Neuroscience: The Official Journal of the Society for Neuroscience*, *10*(3), 952–974.

Kuehn, E., Dinse, J., Jakobsen, E., Long, X., Schäfer, A., Bazin, P.-L., … Margulies, D. S. (2017). Body Topography Parcellates Human Sensory and Motor Cortex. *Cerebral Cortex (New York, N.Y.: 1991)*, *27*(7), 3790–3805. https://doi.org/10.1093/cercor/bhx026

Kwon, S. E., Yang, H., Minamisawa, G., & O'Connor, D. H. (2016). Sensory and decision-related activity propagate in a cortical feedback loop during touch perception. *Nature Neuroscience*, *19*(9), 1243–1249. https://doi.org/10.1038/nn.4356

Lang, W., Büttner-Ennever, J. A., & Büttner, U. (1979). Vestibular projections to the monkey thalamus: An autoradiographic study. *Brain Research*, *177*(1), 3–17. https://doi.org/10.1016/0006-8993(79)90914-4

Lee, S., Carvell, G. E., & Simons, D. J. (2008). Motor modulation of afferent somatosensory circuits. *Nature Neuroscience*, *11*(12), 1430–1438. https://doi.org/10.1038/nn.2227

Margulies, D. S., Ghosh, S. S., Goulas, A., Falkiewicz, M., Huntenburg, J. M., Langs, G., … Smallwood, J. (2016). Situating the default-mode network along a principal gradient of macroscale cortical organization. *Proceedings of the National Academy of Sciences*, *113*(44), 12574–12579. https://doi.org/10.1073/pnas.1608282113

Marquand, A. F., Haak, K. V., & Beckmann, C. F. (2017). Functional corticostriatal connection topographies predict goal directed behaviour in humans. *Nature Human Behaviour*, *1*(8), 0146. https://doi.org/10.1038/s41562-017-0146

Mayner, L., & Kaas, J. H. (1986). Thalamic projections from electrophysiologically defined sites of body surface representations in areas 3b and 1 of somatosensory cortex of Cebus monkeys. *Somatosensory Research*, *4*(1), 13–29. https://doi.org/10.3109/07367228609144595

Nelson, R. J., & Kaas, J. H. (1981). Connections of the ventroposterior nucleus of the thalamus with the body surface representations in cortical areas 3b and 1 of the cynomolgus macaque, (Macaca fascicularis). *The Journal of Comparative Neurology*, *199*(1), 29–64. https://doi.org/10.1002/cne.901990104

Nichols, T. E., & Holmes, A. P. (2002). Nonparametric permutation tests for functional neuroimaging: A primer with examples. *Human Brain Mapping*, *15*(1), 1–25. https://doi.org/10.1002/hbm.1058

Pei, Y.-C., Hsiao, S. S., Craig, J. C., & Bensmaia, S. J. (2010). Shape Invariant Coding of Motion Direction in Somatosensory Cortex. *PLOS Biology*, *8*(2), e1000305. https://doi.org/10.1371/journal.pbio.1000305

Penfield, W., Rasmussen, T., & National Institute on Drug Abuse,. (1950). *The cerebral cortex of man: A clinical study of localization of function.* New York: Macmillan.

Pons, T. P., & Kaas, J. H. (1985). Connections of area 2 of somatosensory cortex with the anterior pulvinar and subdivisions of the ventroposterior complex in macaque monkeys. *The Journal of Comparative Neurology*, *240*(1), 16–36. https://doi.org/10.1002/cne.902400103

Pons, T. P., & Kaas, J. H. (1986). Corticocortical connections of area 2 of somatosensory cortex in macaque monkeys: A correlative anatomical and electrophysiological study. *The Journal of Comparative Neurology*, *248*(3), 313–335. https://doi.org/10.1002/cne.902480303

Power, J. D., Barnes, K. A., Snyder, A. Z., Schlaggar, B. L., & Petersen, S. E. (2012). Spurious but systematic correlations in functional connectivity MRI networks arise from subject motion. *NeuroImage*, *59*(3), 2142–2154. https://doi.org/10.1016/j.neuroimage.2011.10.018

Puckett, A. M., Bollmann, S., Poser, B. A., Palmer, J., Barth, M., & Cunnington, R. (2018). Using multi-echo simultaneous multi-slice (SMS) EPI to improve functional MRI of the subcortical nuclei of the basal ganglia at ultra-high field (7T). *NeuroImage*, *172*, 886–895. https://doi.org/10.1016/j.neuroimage.2017.12.005

Salimi-Khorshidi, G., Douaud, G., Beckmann, C. F., Glasser, M. F., Griffanti, L., & Smith, S. M. (2014). Automatic denoising of functional MRI data: Combining independent component analysis and hierarchical fusion of classifiers. *NeuroImage*, *90*, 449–468. https://doi.org/10.1016/j.neuroimage.2013.11.046

Scheperjans, F., Eickhoff, S. B., Hömke, L., Mohlberg, H., Hermann, K., Amunts, K., & Zilles, K. (2008). Probabilistic maps, morphometry, and variability of cytoarchitectonic areas in the human superior parietal cortex. *Cerebral Cortex (New York, N.Y.: 1991)*, *18*(9), 2141–2157. https://doi.org/10.1093/cercor/bhm241

Smith, S. M., Andersson, J., Auerbach, E. J., Beckmann, C. F., Bijsterbosch, J., Douaud, G., … Glasser, M. F. (2013). Resting-state fMRI in the Human Connectome Project. *NeuroImage*, *80*, 144–168. https://doi.org/10.1016/j.neuroimage.2013.05.039

Tavor, I., Jones, O. P., Mars, R. B., Smith, S. M., Behrens, T. E., & Jbabdi, S. (2016). Task-free MRI predicts individual differences in brain activity during task performance. *Science*, *352*(6282), 216–220. https://doi.org/10.1126/science.aad8127

The Cerebral Cortex of Man: A Clinical Study of Localization of Function. (1950). *Journal of the American Medical Association*, *144*(16), 1412–1412. https://doi.org/10.1001/jama.1950.02920160086033

Van Essen, D. C., Smith, S. M., Barch, D. M., Behrens, T. E. J., Yacoub, E., Ugurbil, K., & WU-Minn HCP Consortium. (2013). The WU-Minn Human Connectome Project: An overview. *NeuroImage*, *80*, 62–79. https://doi.org/10.1016/j.neuroimage.2013.05.041

Wael, R. V. de, Larivière, S., Caldairou, B., Hong, S.-J., Margulies, D. S., Jefferies, E., … Bernhardt, B. C. (2018). Anatomical and microstructural determinants of hippocampal subfield functional connectome embedding. *Proceedings of the National Academy of Sciences*, *115*(40), 10154–10159. https://doi.org/10.1073/pnas.1803667115

Wagstyl, K., Ronan, L., Goodyer, I. M., & Fletcher, P. C. (2015). Cortical thickness gradients in structural hierarchies. *NeuroImage*, *111*, 241–250. https://doi.org/10.1016/j.neuroimage.2015.02.036

Wang, Z., Chen, L. M., Négyessy, L., Friedman, R. M., Mishra, A., Gore, J. C., & Roe, A. W. (2013). The relationship of anatomical and functional connectivity to resting state connectivity in primate somatosensory cortex. *Neuron*, *78*(6), 1116–1126. https://doi.org/10.1016/j.neuron.2013.04.023

Wilcox, R. R. (2016). Comparing dependent robust correlations. *The British Journal of Mathematical and Statistical Psychology*, *69*(3), 215–224. https://doi.org/10.1111/bmsp.12069

Woodward, N. D., Giraldo-Chica, M., Rogers, B., & Cascio, C. J. (2017). Thalamocortical dysconnectivity in autism spectrum disorder: An analysis of the Autism Brain Imaging Data Exchange. *Biological Psychiatry. Cognitive Neuroscience and Neuroimaging*, *2*(1), 76–84. https://doi.org/10.1016/j.bpsc.2016.09.002

Yamashita, T., & Petersen, C. C. (2016). Target-specific membrane potential dynamics of neocortical projection neurons during goal-directed behavior. *ELife*, *5*, e15798. https://doi.org/10.7554/eLife.15798

Yeo, B. T. T., Krienen, F. M., Sepulcre, J., Sabuncu, M. R., Lashkari, D., Hollinshead, M., … Buckner, R. L. (2011). The organization of the human cerebral cortex estimated by intrinsic functional connectivity. *Journal of Neurophysiology*, *106*(3), 1125–1165. https://doi.org/10.1152/jn.00338.2011

Yokoi, A., & Diedrichsen, J. (2019). Neural Organization of Hierarchical Motor Sequence Representations in the Human Neocortex. *Neuron*, *103*(6), 1178-1190.e7. https://doi.org/10.1016/j.neuron.2019.06.017

Zeharia, N., Hertz, U., Flash, T., & Amedi, A. (2012). Negative blood oxygenation level dependent homunculus and somatotopic information in primary motor cortex and supplementary motor area. *Proceedings of the National Academy of Sciences*, *109*(45), 18565–18570. https://doi.org/10.1073/pnas.1119125109

## 2.6 Supplementary Figures

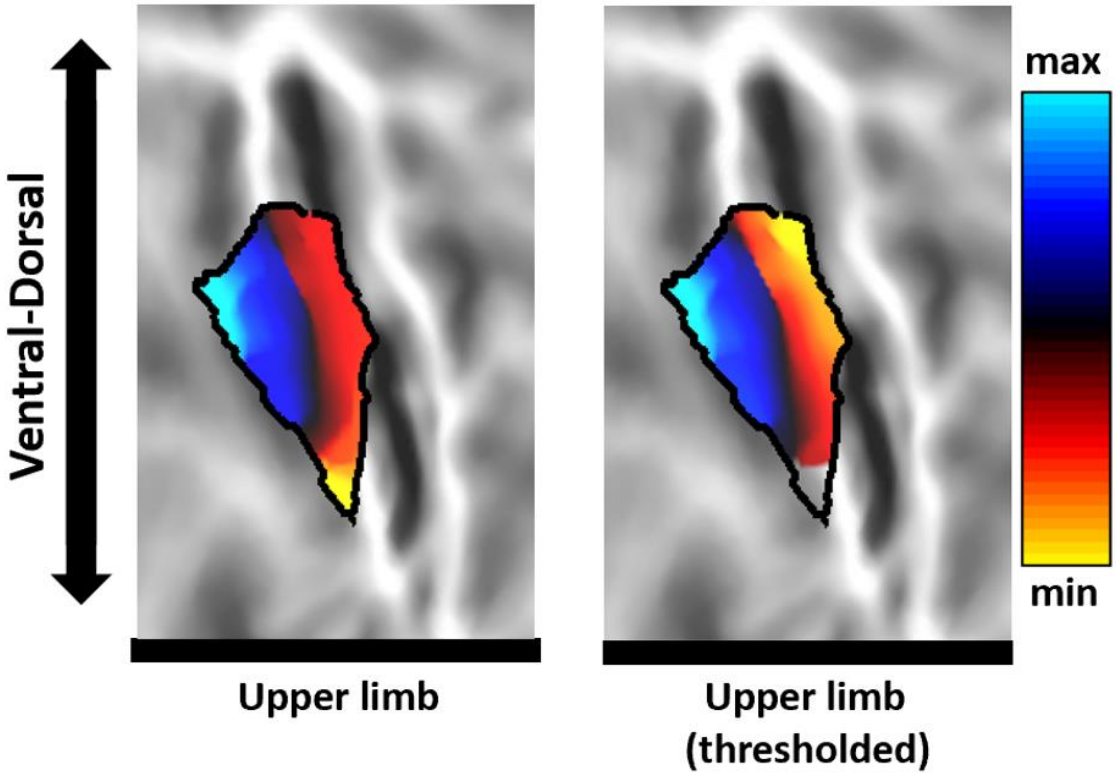


**Supplementary Figure 2.1 Dominant gradient of right hemisphere upper limb ROI**

*(Left) Group level gradients derived from right hemisphere upper limb ROI. The minimum and maximum of the gradient spans the ventral-dorsal axis. The ROI definition may include spatial information encoding somatosensory face information skewing the behaviour of the dominant gradient. (Right) Removal of the ventral portion of the right hemisphere upper limb ROI definition yields a dominant gradient where the minimum and maximum of the gradient spans the anterior-posterior axis indicative of S1 hierarchical organization.*

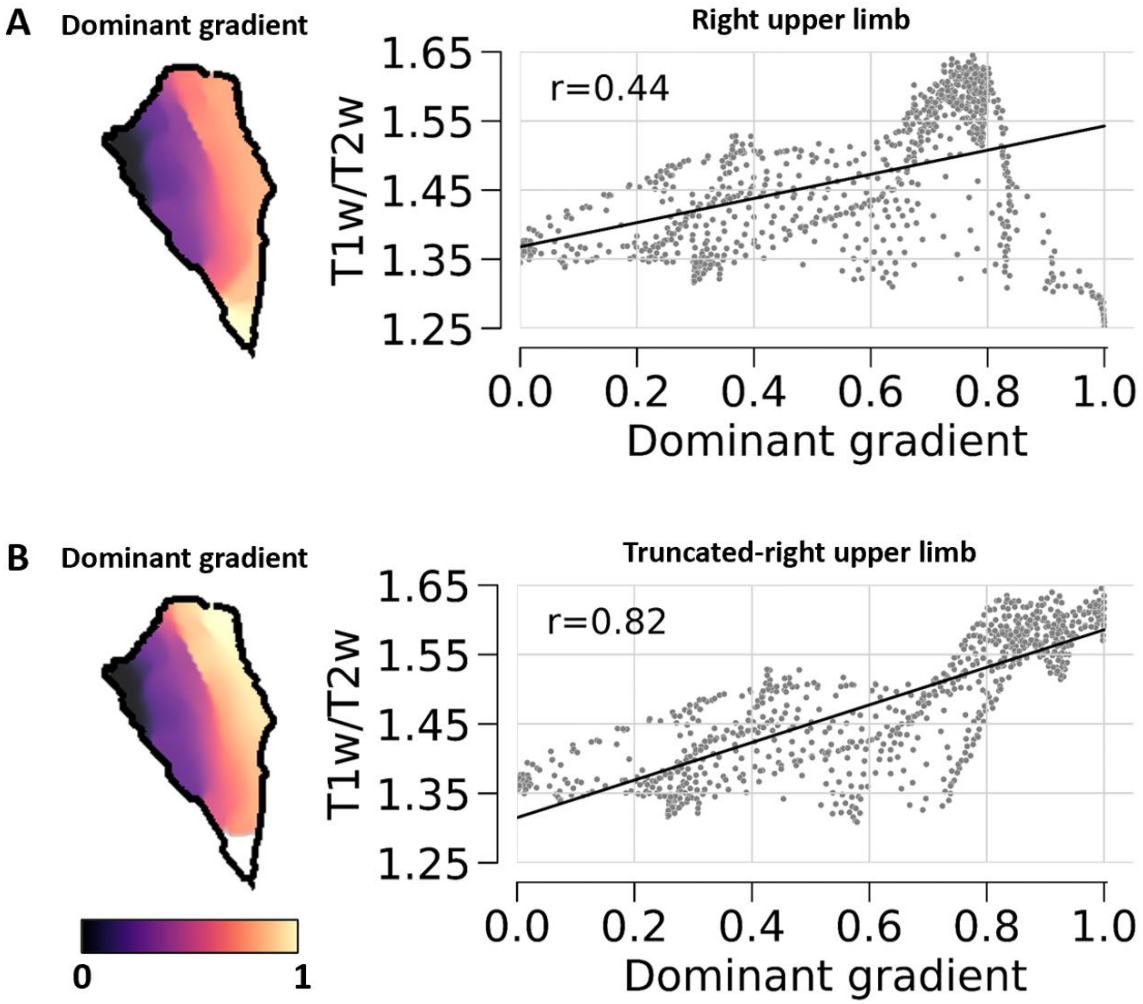


**Supplementary Figure 2.2 Association between dominant gradient and T1w/T2w of the right upper limb ROI**

*(A) Dominant gradient (left) and the correlation between the dominant gradient and T1w/T2w for the full right upper limb ROI. (right) (B) Dominant gradient (left) and the correlation between the dominant gradient and T1w/T2w for the truncated right upper limb ROI. (***$P < 10^{-4}$ for both ROIs).*

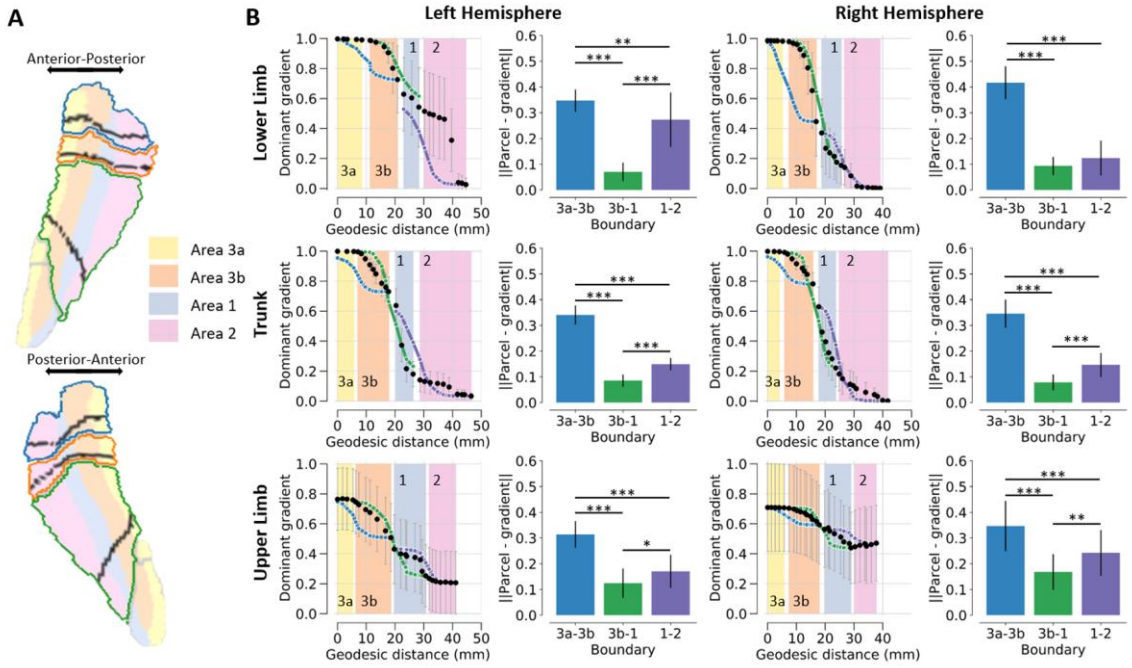


**Supplementary Figure 2.3 Evidence of functional boundaries between Brodmann areas (using 3rd quantile vertices)**

*(A) Left and right S1 separated by somatotopic regions and colour coded by architectonic Brodmann areas. Black lines in each somatotopic region indicates the vertex-to-vertex path (or trajectory) used to extract values from the RSFC-derived gradients. A geodesic distance of 0 indicates the most anterior vertex of the trajectory. (B) Left and right somatotopic regions' RSFC connectivity pattern plotted against geodesic distance as defined by a rostro-to-caudal vertex-to-vertex trajectory. Black points represent the average gradient value across all participants (N = 65). Overlaid are three 'parcel' definition lines drawn for each boundary between 3a & 3b, 3b & 1, and 1 & 2 (blue, green, and purple) smoothed with a 5 mm FWHM. Corresponding bar plots shows the L2 norm between parcel definition and RSFC connectivity pattern with a value closer to 0 suggesting more evidence for a functional boundary. Error bars in (B) indicate the standard deviation for all plots.* $*P < .05$, $**P < 10^{-3}$,$***P < 10^{-4}$.

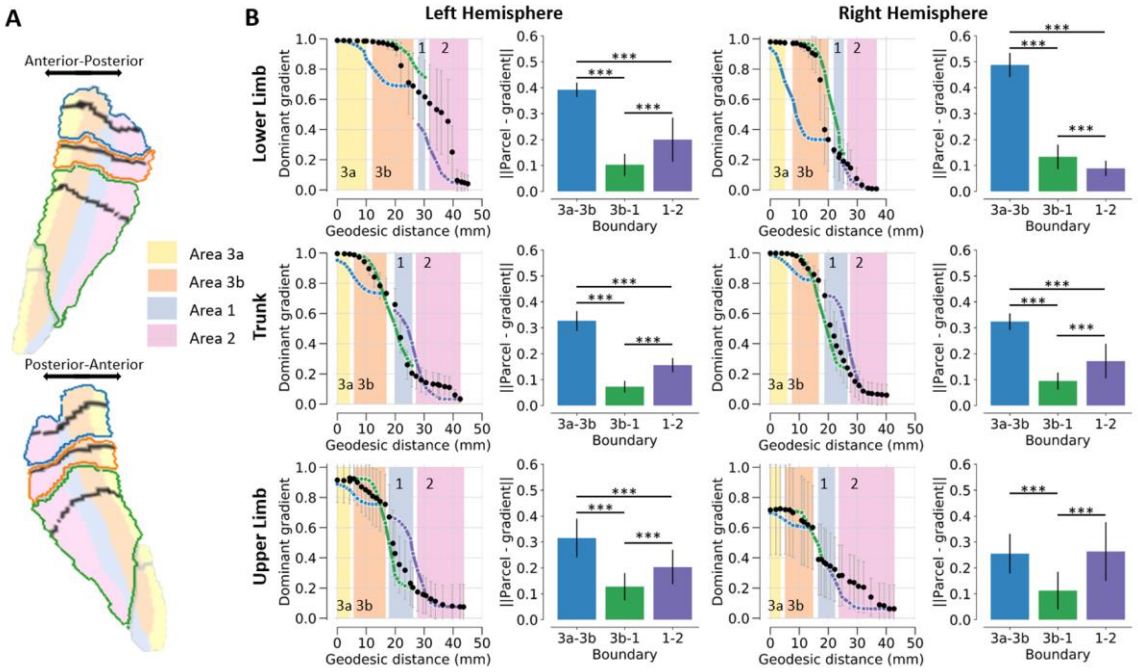


**Supplementary Figure 2.4 Evidence of functional boundaries between Brodmann areas (using 1st quantile vertices)**

*(A) Left and right S1 separated by somatotopic regions and colour coded by architectonic Brodmann areas. Black lines in each somatotopic region indicates the vertex-to-vertex path (or trajectory) used to extract values from the RSFC-derived gradients. A geodesic distance of 0 indicates the most anterior vertex of the trajectory. (B) Left and right somatotopic regions' RSFC connectivity pattern plotted against geodesic distance as defined by a rostro-to-caudal vertex-to-vertex trajectory. Black points represent the average gradient value across all participants (N = 65). Overlaid are three 'parcel' definition lines drawn for each boundary between 3a & 3b, 3b & 1, and 1 & 2 (blue, green, and purple) smoothed with a 5 mm FWHM. Corresponding bar plots shows the L2 norm between parcel definition and RSFC connectivity pattern with a value closer to 0 suggesting more evidence for a functional boundary. Error bars in (B) indicate the standard deviation for all plots.* $*P < .05$, $**P < 10^{-3}$,$***P < 10^{-4}$.

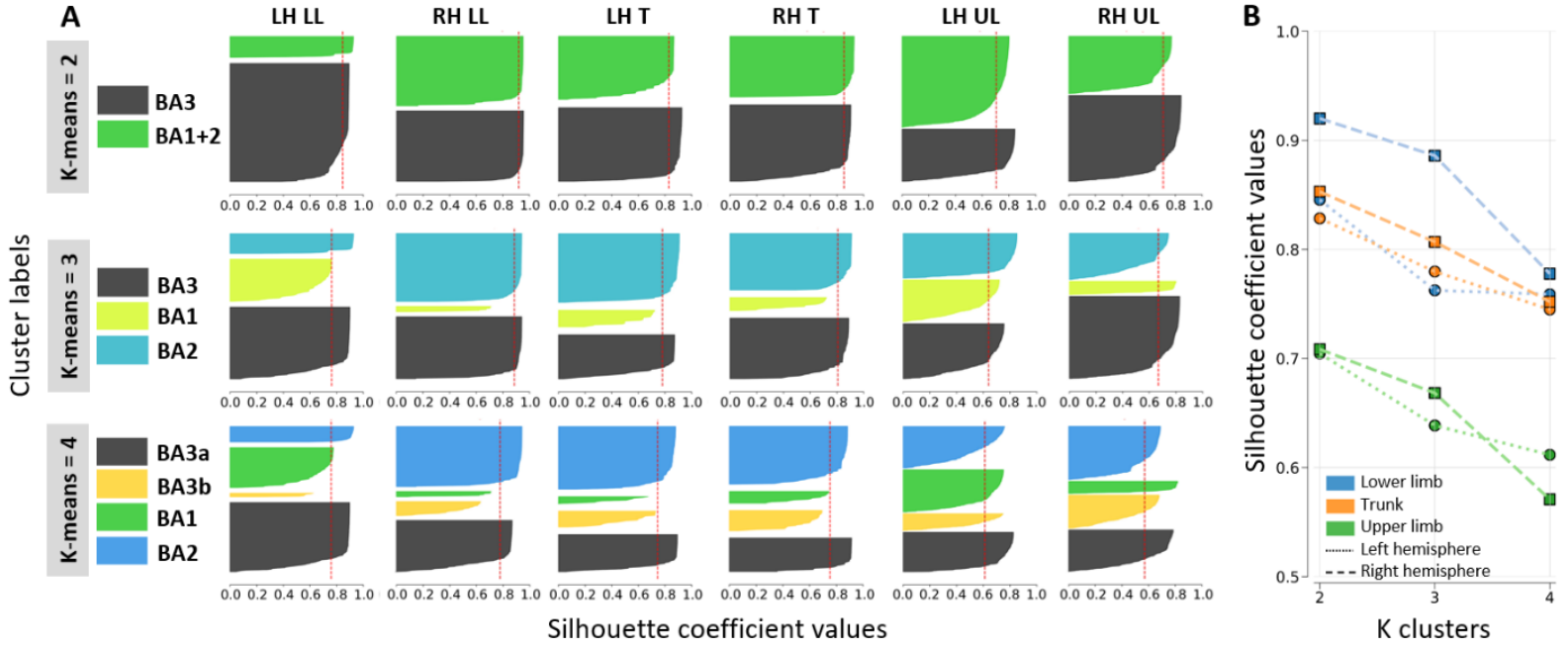


**Supplementary Figure 2.5 Silhouette analyses of each somatotopic ROI for determining the choice of K clusters**

*(A) Silhouette plots of group-level gradients for each K-means cluster choice (i.e., K=2, 3, 4) across each somatotopic ROI (i.e., left and right, LL, T and UL). Each plot displays the silhouette coefficient and assesses the closeness of each clustered vertices to all neighbouring clusters. The average silhouette coefficient value across all vertices in each K-cluster case is indicated by the vertical dotted red line. (B) Average silhouette coefficient values plotted against K-clusters for each somatotopic ROI. All somatotopic ROIs demonstrate highest average silhouette coefficient values at K = 2 clusters.*

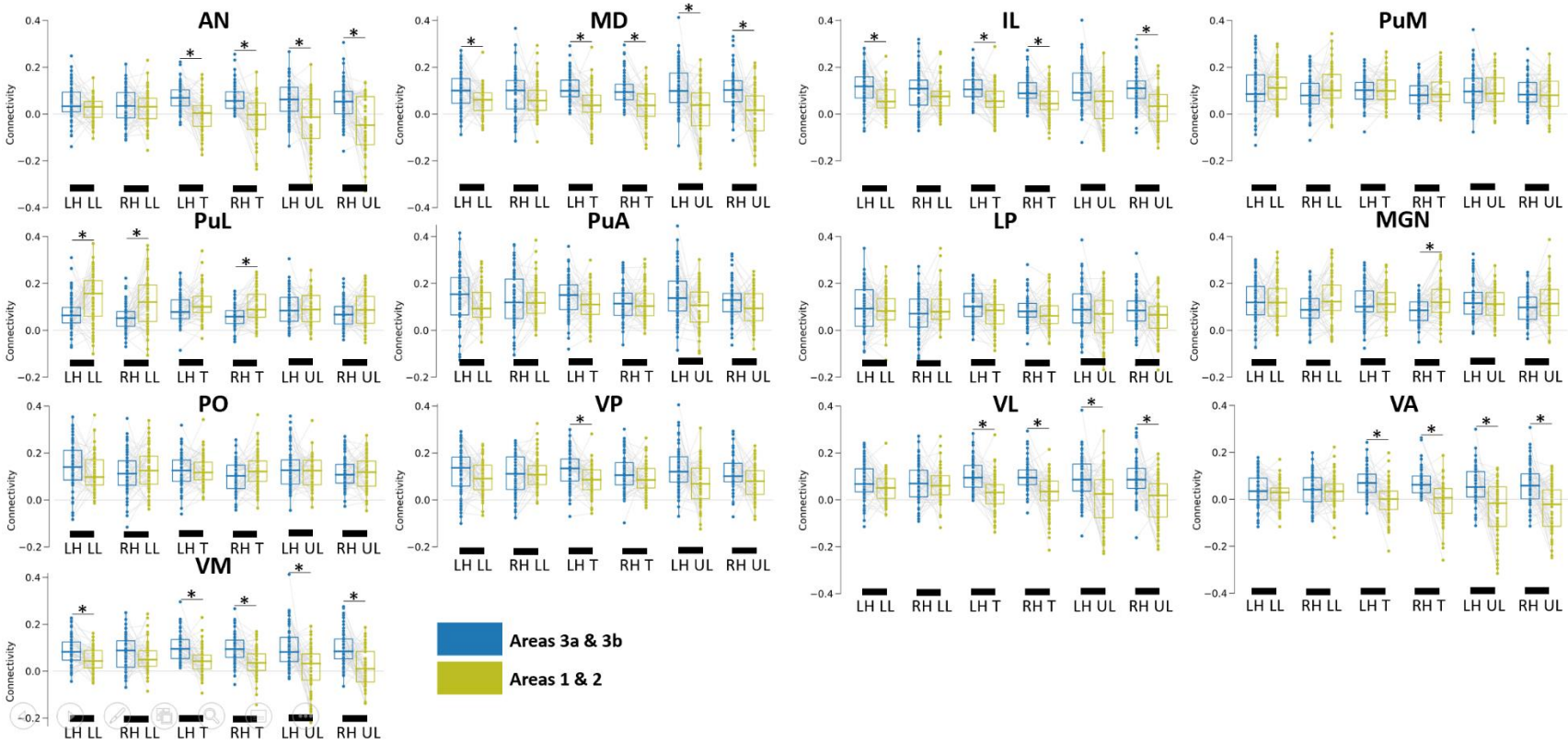


**Supplementary Figure 2.6 Connectivity between ipsilateral thalamic nuclei and functional subdivisions of S1**

*Connectivity strength (mean partial correlation coefficient across ipsilateral thalamic nuclei; each plot shows data from a different thalamic nuclei) calculated for left and right somatotopic region (i.e., LL, T, and UL). Points represent connectivity strength for each participant (N=65), and gray lines indicate pairwise changes. *P* $< .05$

# Chapter 3

# 3 Joint-embeddings reveal functional differences in default-mode network architecture between marmosets and humans

## 3.1 Introduction

Dynamic reconfiguration of functional brain organization is essential for supporting diverse cognitive tasks in humans (Sporns, 2010; Bassett and Bullmore, 2017). Cognitive tasks that are complex in nature rely on increases in functional integration between segregated systems, whereas simpler tasks may rely on only a single isolated system (Deco et al. 2015; Shine, 2019). Since diverse cognitive processes can exist in either of these two juxtaposed task-states, the resting-brain must dwell in an equilibrium condition that can support adaptive switching during various cognitive demands (Wang et al. 2021). In this regard, the default-mode network (DMN) – composed of a set of tightly interconnected cortical association areas (Raichle 2001; Buckner et al. 2008) – is postulated to subserve a role in broader cortical dynamics, as it is optimally positioned between sensory cortices, serving as convergence zones for neural activity (Margulies et al. 2016). DMN nodes have been shown to mediate interaction between other macroscopic functional networks (Braga et al. 2013; Kernbach et al. 2018), and have also been shown to adaptively reconfigure during tasks involving heavy cognitive load (Braun et al. 2015; Finc et al. 2020). Collectively, the DMN's ability to subserve higher-order cognitive functions may be anchored by its capacity to integrate diffuse cortical dynamics across the cerebral cortex. While evidence supporting this view is widely recognized in the DMN of *humans*, the generalizability of this DMN architecture to pre-clinical animal models that are used to investigate higher-order cognition must be validated. This is particularly important for translational research, since animal models are invariably used to develop and assess therapeutics at the pre-clinical stage for many brain disorders that have a major cognitive component.

The common marmoset is a favored non-human primate animal model for studying sophisticated cognitive and social behaviours, such as those encapsulated by the DMN (Miller et al. 2016; Jennings et al. 2017; Okano et al. 2016). Within-species research has shown that, similar to humans, macroscopic networks occupy cortical association areas of the marmoset brain (Buckner and Margulies, 2019), among which is believed to be the marmoset DMN consisting of three nodes: dorsolateral prefrontal cortex (dlPFC), posterior cingulate cortex (PCC), and posterior parietal cortex (PPC; Liu et al. 2019). Interestingly, the medial prefrontal cortex (mPFC), which is considered to be part of the human DMN, appears to be absent in the marmoset DMN (Liu et al. 2019). Although general conservation of the DMN between these two species is evident, relative to humans, primate DMN nodes corresponding to cortical association areas are expanded (Stephan et al. 1981; Chaplin et al. 2013) and display nuanced discrepancies in wiring principles (Goulas et al. 2019). Given that these differences between humans and marmosets emerge through increasing phylogenetic distances, an intriguing question arises: To what extent does the default-mode network architecture differ between these two species?

Our cross-species comparison study of marmosets and humans interrogated the extent of divergence in DMN architecture between these two primate species, providing critical insight into the utility of the marmoset as an animal model for higher cognition and clues as to the evolution of this fundamental brain network that appears to be conserved to varying degrees across all mammals studied to date. To this end, we used joint embeddings to map candidate homologous RSFC gradients in human and marmoset cortices (Xu et al. 2020). Next, we identified the canonical DMN-centric gradient used to empirically compare interspecies DMN architecture. We found an expanded DMN gradient in the marmoset compared to human, and this was attributed to the dlPFC, which (1) was weakly bounded, and (2) expressed spatially inconsistent connection topography compared to posterior DMN-nodes. Due to the importance of mPFC in the human DMN and its previously-suggested absence in the marmoset DMN (Liu et al. 2019), we also identified a subsequent joint gradient that included a mPFC area in both marmosets and humans. Interestingly, the human mPFC component of the joint gradient was located caudally relative to the known DMN mPFC area. Our exploration using joint gradients suggests marked differences in anterolateral-posterior DMN architecture (dlPFC-PCC-PPC) and

provides clarity towards identifying provisional homology between human and marmoset mPFC. Taken together, these findings suggest the default-mode network of the marmoset may lack the functional architecture to efficiently integrate neural information to subserve broader cortical dynamics and diverse cognitive demands, as compared to humans.

## 3.2 Methods

### 3.2.1 Resting-state fMRI dataset and preprocessing

#### 3.2.1.1 Human data

This 3T resting-state dataset was taken from $N = 100$ unrelated young adults from the Human Connectome Project (HCP) of the 1200-participant release (https://www.humanconnectome.org/study/hcp-young-adult). Each participant underwent four 14.4-minute rsfMRI scans (TR = 0.72 s) acquired across two days (two scans per day, acquired in opposite phase-encode direction [left-right/right-left]). Each scan was preprocessed through the HCP with details described by Smith and colleagues, and includes spatial distortion, and head-motion correction, registration to a T1 weighted structural, resampling to a 2 mm Montreal Neurological Institute (MNI) space, global intensity normalisation, high-pass filtering (cut-off at 2000 s), and ICA-based artefact removal (FSL-FIX) (Glasser et al. 2013; Griffanti et al. 2014; Salimi-Khorshidi et al. 2014; Smith et al. 2013). In addition to HCP minimal preprocessing, mean white matter and ventricular signal was regressed from the data, followed by cortical surface smoothing with a 5 mm FWHM Gaussian kernel, bandpass filtering (0.01-0.1 Hz) and downsampling to a 10k (10,242 vertices) mid-cortical surface. All scans from a single subject were Z-score normalised to zero mean and unit standard deviation.

To mitigate biases from the effects of motion we only include participants who fell within our necessarily stringent motion exclusion criterion (Power et al. 2012). Specifically, participants who had a mean framewise displacement (FD) greater than 0.2 mm in any of their four scans were excluded from analyses. This resulted in $N = 65$ (FD; mean = 0.138 mm, SD = 0.023 mm) subjects used across all analyses.

#### 3.2.1.2 Awake marmoset data

Marmoset resting-state datasets were taken from https://www.marmosetbrainconnectome.org (Schaeffer et al. 2022) and includes two datasets from Western University (UWO; $N = 5$) and the National Institutes of Health (NIH; $N = 26$). Each marmoset from the UWO dataset was acquired using a 9.4 T, 31 cm horizontal bore magnet (Varian/Agilent, Yarnton, UK) and underwent 4-6 15-minute rsfMRI scans (TR = 1.5 s) acquired in an anterior-posterior phase encode direction over multiple days. Each marmoset from the NIH dataset was acquired using a 7T 30 cm horizontal bore magnet (Bruker BioSpin Corp, Billerica, MA, USA) and underwent 4-8 17.1-minute rsfMRI scans (TR = 2.0 s) acquired in opposite phase encode direction [left-right/right-left] of a single session. Additionally, a T2-weighted structural was acquired during one of the multi-session scans for the UWO dataset (voxel size = 0.133 × 0.133 × 0.5 mm), and during the single-session scan for the NIH dataset (voxel size = 0.25 × 0.25 × 0.5 mm). Specific details regarding awake marmoset scanning methodology (i.e., acclimatization of marmosets to MRI environment), MRI acquisition parameters, and preprocessing details are described in Schaeffer et al. 2022. Apart from phase-encoding distortion correction that was applied to the NIH dataset, all pre-processing of rsfMRI scans were identical. Briefly, pre-processing includes removal of the first ten timeframes (for magnetization to reach a steady-state), time-series despiking, slice-timing correction, and motion correction. In addition, nuisance regression was performed to further mitigate motion parameters, and to achieve linear and non-linear detrending and bandpass filtering (0.01-0.1 Hz). Resampling of the rsfMRI data to the NIH marmoset brain atlas (Liu et al. 2021) was conducted by concatenating a linear registration between the mean functional and T2 weighted structural images with a non-linear registration between the structural and template images. Next, the preprocessed rsfMRI data was projected onto the NIH marmoset brain atlas surfaces where surface smoothing using a 1.5 mm FWHM Gaussian Kernel, and downsampling to a 10k (10,242 vertices) graymid surface was performed (i.e., a surface located at the midpoint between the white matter and pial surfaces). All scans from a single marmoset were Z-score normalized to zero mean and unit standard deviation.

### 3.2.2 Region of interest definitions for joint embedding

Homologous region of interests (ROIs) of humans and marmosets were obtained from a surface-based multi-modal parcellation of the human cortex (Glasser et al. 2016) and Paxinos' histological-based atlas of the marmoset cortex (Paxinos et al. 2012; Majka et al. 2021), respectively. A total of 13 candidate homologous ROIs were selected across humans and marmosets and includes areas V1, V2, A1, M1, 3a, 3b, 1+2, FEF, MT, dlPFC, PCC, PPC, and hippocampus (Solomon and Rosa, 2014; Kaas 2004; Liu et al. 2019). Oftentimes it is difficult to identify homologies in higher-order areas due to lack of convergent multimodal evidence (i.e., cytoarchitecture, function, anatomical connectivity), such as for areas FEF, dlPFC, PCC, and PPC. Nonetheless, association areas were carefully included as we wanted to include a wide range of cortical areas into the joint embedding algorithm. A summary of ROIs used in the joint embedding can be found in Supplementary table 3.1.

A likely candidate for marmoset FEF is marmoset area A8aV as supported by tract-tracing (Reser et al. 2013), microstimulation (Selvanayagam et al. 2019), RSFC, and task-based fMRI (Schaeffer et al. 2019)). A corresponding homologous human FEF was defined using the human multi-modal parcellation (Glasser et al. 2016).

Candidate marmoset DMN areas (i.e., dlPFC, PCC, and PPC) were selected based on Liu and colleagues' definitions (Liu et al. 2019). In concordance with their methodology, ICA was performed on all of the marmoset data (scans of all marmosets were temporally concatenated) using MELODIC in FSL (Jenkinson et al. 2012). Thirty ICA components were estimated, and the candidate DMN network was identified based on the inclusion of a dlPFC, PCC, and PPC component. Furthermore, the selected DMN network was visually assessed to ensure that each DMN node included marmoset areas corresponding to peaks areas of ICA activation as previously described (i.e., dlPFC, PCC, and PPC included marmoset areas A8aD, PGM, and LIP, respectively). Lastly, the DMN ICA component was thresholded at a level of 0.5 using a mixture model and alternative hypothesis testing approach and masked with a threshold of $Z>6.0$ to obtain ROIs of each DMN node. Spatially consistent DMN were identified independently in both cohorts (NIH and UWO) supporting the use temporally concatenated data, across all cohorts, for identification of the ROIs for the marmoset DMN (see Supplementary Fig. 3.1).

Human homologous DMN areas dlPFC, PCC and PPC were hand selected using HCP labels that were reannotated with canonical RSNs (Ji et al. 2019). Specifically, human dlPFC was assigned to area 8Ad, PCC was assigned to area 7m, and PPC was assigned to area PG (includes areas PGi & PGs). With the consideration that human PCC includes multiple human areas, RSFC analyses of other PCC areas demonstrated strong internode connectivity, and similar spatial topography of RSFC, as such, choice of human PCC ROI should not affect ensuing joint embedding results.

### 3.2.3 Joint embeddings

Joint embedding is a spectral embedding technique that can be used to spatially quantify and align RSFC patterns across individuals (Nenning et al. 2017). Recently, this technique has been extended to achieve spatial alignment using RSFC patterns between the human and macaque cortex (Xu et al. 2020). In this work, joint embeddings were achieved by generating a joint similarity matrix ($W_{joint}$) that integrates RSFC information from humans and marmosets, as follows:

$$\boldsymbol{W}_{\mathbf{joint}} = \begin{bmatrix} \boldsymbol{I^h} & \boldsymbol{W^{h-to-m}} \\ \boldsymbol{W^{m-to-h}} & \boldsymbol{I^m} \end{bmatrix}$$

where $\boldsymbol{I^h}$ and $\boldsymbol{I^m}$ represents the identity matrices whose size corresponds to the number of cortical vertices (superscripts $\boldsymbol{h}$ and $\boldsymbol{m}$ annotates humans and marmosets, respectively). Here, the identity matrix was chosen to represent intraspecies similarity to remove all interaction of intraspecies cortical vertices. This was done to ensure that ensuing joint gradients considers only vertex-wise interspecies similarity ($\boldsymbol{W^{m-to-h}}$ and $\boldsymbol{W^{h-to-m}}$) similar to typical connectivity fingerprint analyses (Mars et al. 2018).

Interspecies similarity matrices ($\boldsymbol{W^{m-to-h}}$ and $\boldsymbol{W^{h-to-m}}$) were generated by first, calculating vertex-to-vertex RSFC for each species ($\boldsymbol{C^y_{M\times M}}$: $\boldsymbol{M}$=number of cortical vertices, and $y$ corresponds to the species [i.e., human or marmoset]). Note that $\boldsymbol{C^y_{M\times M}}$ was calculated by computing the group average across all subjects in a cohort. This was followed by row-wise thresholding of each vertex' RSFC pattern, preserving only relatively strong resting-state functional connections. Next, the average RSFC patterns for

each homologous ROI were calculated resulting in $\boldsymbol{L}^{\boldsymbol{y}}_{\boldsymbol{N}\times\boldsymbol{M}}$ ($\boldsymbol{N}$=number of homologous ROIs, $\boldsymbol{M}$=number of cortical vertices, and $\boldsymbol{y}$ corresponds to the species [i.e., human or marmoset]). Next, cosine similarity between RSFC patterns of homologous ROIs ($\boldsymbol{L}^{\boldsymbol{y}}_{\boldsymbol{N}\times\boldsymbol{M}}$) and RSFC patterns of the whole brain ($\boldsymbol{C}^{\boldsymbol{y}}_{\boldsymbol{M}\times\boldsymbol{M}}$) was calculated resulting in $\boldsymbol{S}^{\boldsymbol{y}}_{\boldsymbol{N}\times\boldsymbol{M}}$, representing the similarity in RSFC patterns between homologous ROIs and the whole brain. Finally, cosine similarity between $\boldsymbol{S}^{\boldsymbol{h}}_{\boldsymbol{N}\times\boldsymbol{M}^{h}}$ and $\boldsymbol{S}^{\boldsymbol{m}}_{\boldsymbol{N}\times\boldsymbol{M}^{m}}$, across all vertices of humans and marmosets can be computed as they share the same number of homologous ROIs ($\boldsymbol{N}$), resulting in the cross-species similarity matrix, $\boldsymbol{W}^{\mathbf{h-to-m}}_{\boldsymbol{M}^{h}\times\boldsymbol{M}^{m}}$. Note that $\boldsymbol{W}^{\mathbf{m-to-h}}_{\boldsymbol{M}^{m}\times\boldsymbol{M}^{h}}$ corresponds to the transverse of $\boldsymbol{W}^{\mathbf{h-to-m}}_{\boldsymbol{M}^{h}\times\boldsymbol{M}^{m}}$. See figure 1b for schematic overview of the construction of the joint similarity matrix ($\boldsymbol{W}_{\boldsymbol{joint}}$).

To perform spectral embeddings, the Laplacian eigenmap algorithm was applied on the graph Laplacian of the joint similarity matrix to obtain a low dimensional manifold representation (Belkin and Niyogi, 2003), commonly referred to as gradients. The graph Laplacian is denoted as follows:

$$\boldsymbol{L} = \boldsymbol{D} - \boldsymbol{W},$$

where $\boldsymbol{W}$ is the adjacency matrix defined by $\boldsymbol{W}_{\mathbf{joint}}$, $\boldsymbol{D}$ is the degree matrix defined as $\boldsymbol{D}_{\boldsymbol{i},\boldsymbol{i}} = \sum_{\boldsymbol{i}} \boldsymbol{W}_{\boldsymbol{i}}$, and $\boldsymbol{L}$ is the graph Laplacian. Solving the generalized eigenvalue problem $\boldsymbol{L}\boldsymbol{y} = \lambda\boldsymbol{D}\boldsymbol{y}$ yields $m$ eigenvectors $\{y_1, \ldots, y_m\}$ corresponding to the smallest $m$ non-zero eigenvalues $\{\lambda_1, \ldots, \lambda_m\}$. Critically, each eigenvector, or gradient, can be mapped back onto the cortices of the human and marmoset, to describe axes of matched RSFC organization across species. Additionally, all gradients were normalized between 0 and 1 to ensure consistency in scale.

To determine the thresholding parameter of intraspecies RSFC (i.e., $\boldsymbol{C}^{\boldsymbol{y}}_{\boldsymbol{v}\times\boldsymbol{v}}$), a sparsity of 1%, 5% and 10% was used. Selection of 1% row-wise sparsity was chosen for subsequent analyses as this sparsity parameter led to the most similar gradient profiles between all homologous ROIs. Note that varying the sparsity parameter only minimally affect the joint gradients that are subsequently investigated in this work.

### 3.2.4 Joint embeddings validation

To ensure joint embeddings describe cross-species homology, average gradient values from the top 12 gradients were extracted from all pre-defined homologous ROIs in humans and marmosets. Selection of only the top 12 gradients were obtained because subsequent gradients (i.e., gradients 13 and higher) were noisy and did not explain cross-species homology. The correlation of gradient profiles between species were assessed for all homologous pairs of homologous ROIs.

### 3.2.5 DMN joint gradient analyses

Investigations looking at the joint gradient distributions corresponding to the human DMN was performed to examine differences in gradient values between DMN nodes, intraspecies, and interspecies. To do this, we identified the joint gradient with a human component that spatially corresponded with the canonical human sensorimotor-to-DMN gradient (Margulies et al. 2016), then we extracted and compared joint gradient values from the following DMN nodes: dlPFC, PCC, and PPC. Selection of marmoset areas dlPFC, PCC, and PPC was identified using an ICA approach as previously described (Liu et al. 2019). Due to a well annotated and established DMN in humans (Glasser et al. 2016; Ji et al. 2019), more expansive ROIs were chosen to capture a broader representation of the human DMN, as compared to those selected for the joint embedding approach. Here, human dlPFC corresponded to areas 8Ad and 8Av, PCC corresponded to areas 7m, 31pd, 31pv, 31a, v23ab, d23ab, 23d and POS1, and PPC corresponded to areas PGi and PGs. Note that mPFC was excluded as recent evidence has suggested its exclusion from the marmoset DMN and was outside the scope of this investigation (Liu et al. 2019).

### 3.2.6 DMN RSFC analyses

To provide interpretation for differences observed from the DMN joint gradient results, we conducted (1) internode DMN RSFC, and (2) seed based RSFC analyses using each DMN ROI. Average timeseries were extracted from left and right hemisphere of each DMN node for each scan session (each subject had multiple sessions for humans and marmosets). For each session computations of (1) internode DMN RSFC and (2) RSFC maps for each DMN

node were performed. Next, the average was calculated across each subjects' scan sessions and used in subsequent analyses.

Internode DMN RSFC analyses examined group-level differences between humans and marmosets. We postulated that homology between DMN nodes of humans and marmosets would imply consistent differences in RSFC strength between all pairs of DMN nodes. For example, if human DMN nodes are all strongly connected with one another, a similar observation would be expected between marmoset DMN nodes, however the difference in RSFC magnitude may be offset by a constant magnitude due to differences in rsfMRI scanning acquisition parameters. To conduct inference, a bootstrapping approach (n=1,000) was used to iteratively calculate group-level differences in RSFC strength of humans and marmosets for each pair of DMN nodes. Lastly, group-level differences in RSFC between pairs of DMN nodes were assessed ($P < 0.05$, nonparametric Mann-Whitney U test).

Seed based RSFC analyses were conducted to assess the similarity and differences between spatial topography of RSFC connections of each DMN node. Here, cortical connections of each DMN node were assessed using a nonparametric one-sample t-test (Nichols and Holmes, 2002). Significant vertices are considered as areas of connections ($P < 0.05$, correcting for multiple comparisons). Significant vertices were used to mask group-level connectivity maps for visualization purposes. Next, the significant vertices of each DMN node were treated as binary masks and the dice similarity coefficient (DSC) between pairs of binary masks were calculated to measure the degree of overlap between the spatial topography pairs of DMN nodes. The DSC measures the similarity between a set X and Y (i.e., a thresholded connectivity map of dlPFC and PCC), if the sets are identical (i.e., they contain the same vertices), the coefficient is equal to 1, while if X and Y have no vertices in common, then it is equal to 0, otherwise the DSC falls somewhere between 0 and 1 (Dice, 1945). Furthermore, these analyses were repeated by varying the stringency level of the nonparametric one-sample t-test, to probe for cortical connections with higher RSFC strength ($\boldsymbol{r_0}$) across each species' cohort.

### 3.2.7 Statistical methods

#### 3.2.7.1 Multiple comparisons

All statistical comparisons were conducted using an $\alpha$-level of 5% fully Bonferroni corrected for the number of comparisons.

#### 3.2.7.2 Spatial autocorrelation-preserving surrogate map test

We employed the spatial autocorrelation-preserving surrogate map test to identify correspondence between topographies of two brain maps (Burt et al. 2020). This allows for statistical inference to be conducted between brain maps while accounting for spatial autocorrelation. The spatial autocorrelation-preserving surrogate map test was used to determine statistical associations between pairs of brain maps (i.e., human intra-species and cross-species somatomotor-to-DMN gradient).

### 3.2.8 Data and code availability statement

Code is made available on Github (https://github.com/gnngo4/cross-species-embeddings_2022). Resting-state functional connectivity data of humans can be obtained from the Human Connectome Project (https://db.humanconnectome.org), and data of marmosets can be obtained from the Marmoset Functional Brain Connectivity Resource (www.marmosetbrainconnectome.org).

## 3.3 Results

### 3.3.1 Common brain architecture between humans and marmosets using joint embeddings

A common embedding space to enable marmoset and human comparison was generated by adapting a recently developed cross-species joint embedding approach (Xu et al. 2020). In brief, spectral embedding was applied to a joint similarity matrix – constructed by concatenating four submatrices: identity matrices were placed on the diagonals and

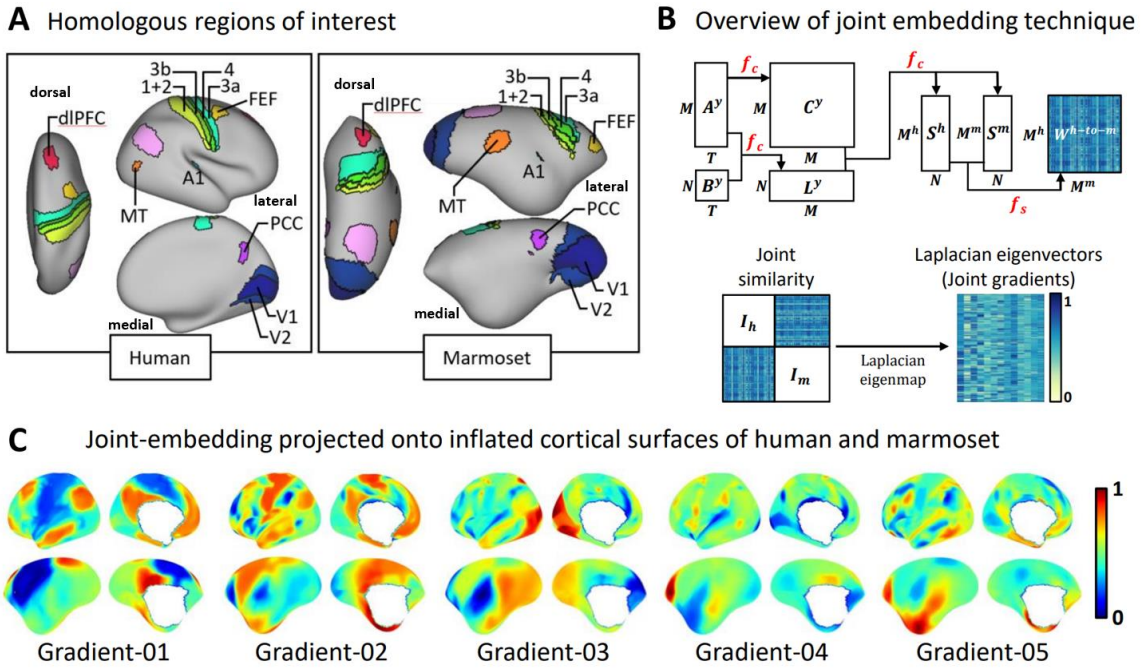


**Figure 3.1 Joint gradient characterization of functional connectivity fingerprinting in humans and marmosets**

*(A) Homologous ROIs mapped onto left hemisphere inflated cortical surfaces of humans and marmosets. (B) A schematic overview for generating joint gradients. Timeseries across the whole cortex and across all homologous regions are denoted by* ($\boldsymbol{A}$), ($\boldsymbol{B}$), *respectively. Group averaged cortex-to-cortex* ($\boldsymbol{C}$) *and homologous ROI-to-cortex* ($\boldsymbol{L}$) *connectivity matrices were generated for humans and marmosets. The similarity matrix* ($\boldsymbol{S}$) *in connectivity fingerprints between pairs of cortical vertices and homologous ROIs was computed using cosine similarity. Next, the similarity in similarity fingerprints between pairs of cortical vertices in humans and marmosets was computed using cosine similarity, yielding the cross-species similarity matrix* ($\boldsymbol{W^{h-to-m}}$). *Concatenation of the cross-species similarity matrix on off-diagonals and identity matrix on diagonals yielded the joint similarity matrix. Eigendecomposition were computed on the graph Laplacian of the joint similarity matrix resulting in ensuing eigenvectors (or joint gradients).* $\boldsymbol{M}$, *number of cortical vertices;* $\boldsymbol{N}$, *number of homologous ROIs;* $\boldsymbol{T}$, *number of time frames;* $\boldsymbol{f_c}$ , *Pearson correlation;* $\boldsymbol{f_s}$ , *cosine similarity. (C) Visualization of the top five joint gradients mapped onto right hemisphere inflated cortical surfaces for humans (top row) and marmosets*

*(bottom row). Lateral view (left) and medial view (right). Each gradient shows continuous variation in functional connectivity fingerprinting across the cortices of humans and marmosets. Details of homologous ROI selections are provided in Supplementary Table 3.1.*

interspecies similarity matrices were placed on the off diagonals (see Fig. 3.1b for more details) – resulting in multiple Laplacian eigenvectors (referred to as joint gradients). Each joint gradient can be mapped vertex-wise onto the human and marmoset cortices representing a common feature space describing brain regions with similar connectivity fingerprints across both species (Fig. 3.1c).

After mapping joint gradients onto the human and marmoset cortices, we qualitatively observed that similar colours within each joint gradient describes candidate homologs in both species. For example, joint gradient 1 of the human describes the previously established somatomotor-to-DMN gradient (Margulies et al. 2016) (***$P < 10^{-4}$; spatial autocorrelation-preserving surrogate map test; LH: $r$=.88; RH: $r$=.90, see Supplementary Fig. 3.2), as quantified by ascending gradient values starting from the somatomotor network, and increasing towards the DMN. Similarly, joint gradient 1 of the marmoset describes a similar organizational axis, with lower, and higher gradient values describing the somatomotor areas, and marmoset DMN homolog, respectively (Fig. 3.1c). Although joint gradient 1 revealed a matching organizational axis in both species, we also observed striking differences in intensity values of DMN nodes inter-species, and intra-species. For example, differences in intensities of DMN nodes between species, and between distal marmoset DMN nodes were observed (i.e., the marmoset dlPFC was annotated with higher gradient values). These deviations suggest differences in underlying functional connectivity patterns and will be revisited in subsequent sections.

In addition to joint gradient 1, evidence of homology was also observed with subsequent gradients, for example, red areas of gradient 2 appear to describe both somatomotor, and DMN regions. In gradient 3, visual regions (i.e., V1, V2 and MT) can be described by red and orange (or higher gradient values) in humans and marmosets, respectively, and auditory areas are described by blue (or lower gradient values). Interestingly, finer grain

features are also noted in joint gradient 11, specifically delineating ventral somatomotor regions in both species which is akin to separation along this region's somatotopic axis and consistent with previous intraspecies findings (Thomas Yeo et al. 2011; Hori et al. 2020) (See Supplementary Fig. 3.3).

Visualizations of the top 12 joint gradients are shown in Supplementary Fig. 3.3 and replicated twice using group averaged RSFC data of two marmoset cohorts (NIH and UWO) and a single human cohort (HCP). Here, only the top 12 joint gradients are visualized, as the subsequent mappings (i.e., gradients 13 and higher) described noisy features. Next, we validated the joint gradients' ability to describe marmoset and human homology by examining the similarity of the gradient profiles across all the pre-defined homologous ROIs. Strong associations between mean gradient values of humans and marmosets in most pre-defined homologous ROIs were observed, except for areas A1, FEF, and PPC ($*P < 0.05$; Pearson correlation using top 12 joint gradients ranging from $r$=0.803 [dlPFC] to $r$=0.950 [V1], see Supplementary Fig. 3.4). It is noteworthy that out of all homologous ROIs that yielded strong interspecies correlations, dlPFC and PCC had the lowest correlation coefficients. In addition to marmoset A1, this might suggest marmoset association cortices are not as evolutionarily conserved, relative to primary motor and sensory cortices.

### 3.3.2 A compact default-mode network in humans compared to marmosets

Having assessed the validity of the joint gradients to estimate cross-species homology, all remaining investigations aim to empirically compare the proposed marmoset DMN homolog to the human DMN. Here, we use joint gradient 1 for subsequent analyses as it recapitulates the well-established somatomotor-to-DMN gradient in both species. As such, distribution of joint gradient values of the DMN, and associated nodes can be compared between species. DMN nodes of humans were based on Ji and colleagues' relabeling of the HCP parcellation with canonical RSN labels (Glasser et al. 2016; Ji et al. 2019) and marmoset DMN nodes was determined using an ICA approach (Liu et al. 2019). This provided two sets of DMN nodes that include ROIs for dlPFC, PCC, and PPC in both species (Fig. 3.2a). The distribution of gradient values in the human DMN core was

markedly reduced, compared to that of the marmoset (mean$\pm$SD: 0.786$\pm$0.043 and 0.846$\pm$0.057, for humans and marmosets, respectively) (***$P < 10^{-4}$; Mann-Whitney U test, see Fig. 3.2b). This is attributed to the inclusion of marmoset dlPFC (0.947$\pm$0.040) which had significantly higher gradient values compared to all other pairs of DMN nodes in humans and marmosets (***$P < 10^{-4}$; Mann-Whitney U test; Cohen's d = [4.14, 4.58, 3.21, 2.56, 3.29] for human dlPFC, PCC, PPC and marmoset PCC, PPC, respectively, see Fig. 3.2c). The joint somatomotor-to-default-mode gradient provides evidence positioning the marmoset dlPFC further away from all other DMN nodes in both humans and marmosets.

We next used the marmoset DMN nodes to probe other marmoset and human areas that had similar gradient values ($P > .05$; Mann-Whitney U test). This analysis was performed in marmosets to identify areas with similar gradient values as each DMN node. This was also repeated to probe human cortical areas to validate that marmoset nodes did indeed match closest to human DMN areas, and not other higher order RSNs. Marmoset dlPFC matched to area A6DR; PCC matched to areas PGM, A30, V3A, LIP, A8b; and PPC matched to areas LIP, PGM, A30, A8b, A8aD. Worth noting, heterogeneity in gradient values of certain ROIs were observed making it difficult to interpret some of the matches. Nonetheless, marmoset DMN nodes tend to localize with other distant DMN and DMN-adjacent nodes. Similarly, we found human DMN, and in some cases DMN-adjacent frontoparietal areas to be situated closest to each marmoset DMN node along the somatomotor-to-DMN axis.

### 3.3.3 Comparing internode DMN connectivity between marmosets and humans

Group level RSFC analyses using DMN nodes of marmosets and humans were performed to disseminate the factors underlying differences in gradient values that were observed in the previous section. First, RSFC analysis of inter-node connectivity of the DMN in each species was conducted and revealed consistent RSFC strength between all areas of the human DMN core (i.e., between left & right dlPFC, PCC, and PPC). By contrast, varying degrees of RSFC strength were observed between DMN nodes in the marmoset (i.e., left & right dlPFC appeared to have relatively weaker RSFC to all other DMN nodes) (Fig.

3.3a). This was recapitulated when calculating the difference in DMN inter-node RSFC between species (i.e., group-level marmoset subtracted from human DMN RSFC), which

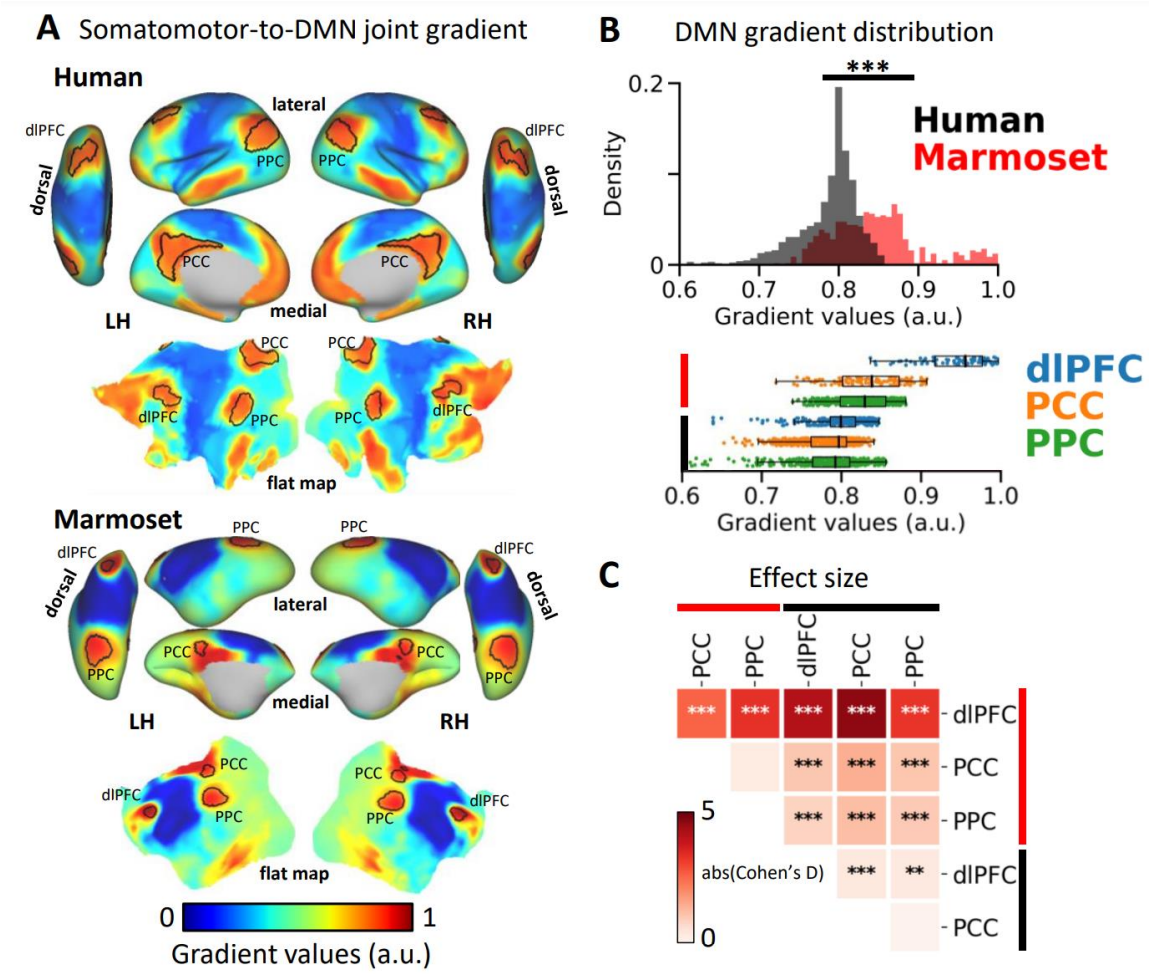


**Figure 3.2 Positioning the human and marmoset DMN along the somatomotor-to-DMN joint gradient**

*(A) Visualization of the somatomotor-to-DMN joint gradient is shown on medial/lateral/dorsal and flat map views of the surface to capture full display of the dlPFC-PCC-PPC DMN core in marmosets and humans (black). (B) Gradient value distributions of the human DMN (black) and marmoset DMN (red). Boxplots show more detailed gradient value distributions for each species' DMN node (dlPFC – blue; PCC – orange; PPC – green). (C) Absolute effect size of gradient value differences in all pairs of DMN nodes.* ** $P < 10^{-3}$ , *** $P < 10^{-4}$

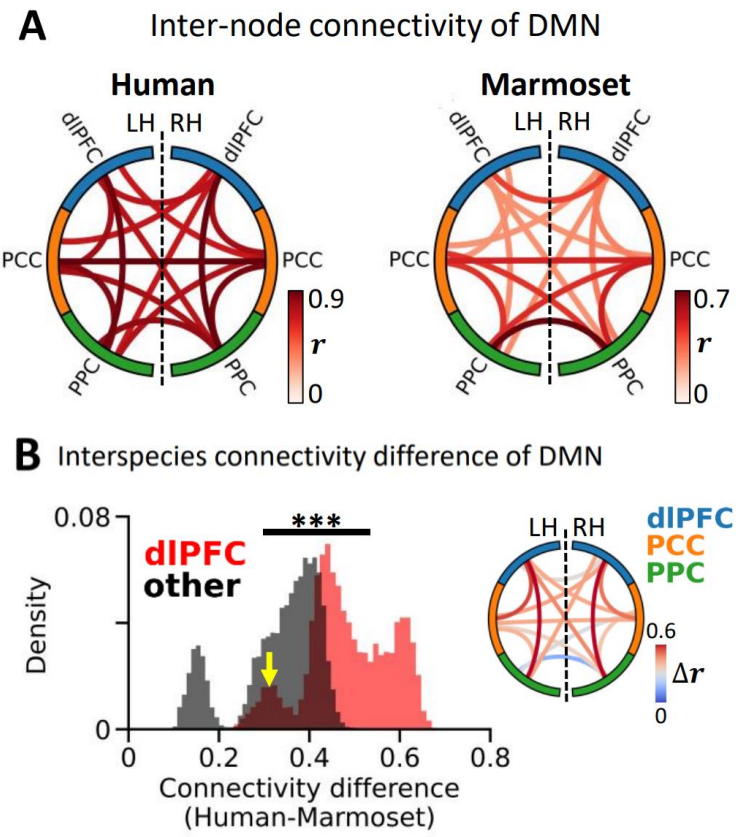


**Figure 3.3 Interspecies comparison of dlPFC-PCC-PPC internode functional connectivity**

*(A) Visualization of internode DMN functional connectivity in humans and marmosets. (B) Distribution of group-level internode DMN functional connectivity differences between humans and marmosets were generated using a bootstrapping approach (n=1,000). Asymmetry in connectivity differences (human – marmoset) is observed with highest magnitudes in dlPFC connections compared to all other connections (***$P < 10^{-4}$). Yellow arrow denotes interhemispheric dlPFC connections.*

revealed a disproportionately large change in RSFC of dlPFC connections compared to all other connections ($P < .05$; Mann-Whitney U test with bootstrapped RSFC differences, Fig. 3.3b shows distributions of bootstrapped RSFC differences [n=1000]). The largest differences were observed between connections of dlPFC & PPC, followed by dlPFC & PCC, whereas the difference in interhemispheric dlPFC connectivity remained relatively low and appears to be consistent with all other non-dlPFC connections (interhemispheric

dlPFC connections denoted by yellow arrow, see Fig 3.3b). As inconsistent internode RSFC was observed in marmosets, we conducted subsequent control experiments to test whether tSNR was a main contributing factor. Although a significant association was observed between absolute tSNR difference and RSFC across all DMN node pairs, we identified a subset of the marmoset cohort that demonstrated the opposite effect and supports the overall observation of weaker dlPFC connections in the marmoset DMN (Supplementary Fig. 3.5). This places the marmoset dlPFC as the weakest bounded node within the marmoset DMN, a finding that is inconsistent with that of the human DMN.

### 3.3.4 Dissimilar spatial topography of connectivity in the marmoset DMN core

To further understand the potential divergence of the marmoset dlPFC from the marmoset DMN core observed in the joint gradient results, seed-based analyses were conducted to probe the spatial topography of RSFC from each DMN node in both humans and marmosets. The goal was to evaluate the consistency of overlap between RSFC patterns generated from each DMN node to each other, and to further identify inter-species differences using RSFC. Figure 3.4a-b shows each DMN node and its corresponding spatial topography of RSFC to the rest of the cortex corresponding to a connectivity threshold of $r_0 = 0.1$ and $r_0 = 0.05$ for humans and marmosets respectively ($*P < 0.05$; nonparametric one-sample t-test). RSFC maps of humans revealed consistent topography of RSFC across all DMN nodes (i.e., dlPFC, PCC, and PPC). Contrary to this, the spatial RSFC maps of marmosets revealed the most consistent topography of RSFC patterns between PCC and PPC, whereas the dlPFC displayed relatively sparser corticocortical connections. Specifically, the marmoset PCC and PPC displayed widespread connections to adjacent areas, as well as connections to the dlPFC and adjacent areas. Interestingly, the marmoset dlPFC showed sparse and weaker connections to posterior DMN regions that encompassed the PCC and PPC, but stronger connections to its own adjacent areas. Connection topography at varying degrees of RSFC strength are shown in supplementary figure 3.6 and 3.7.

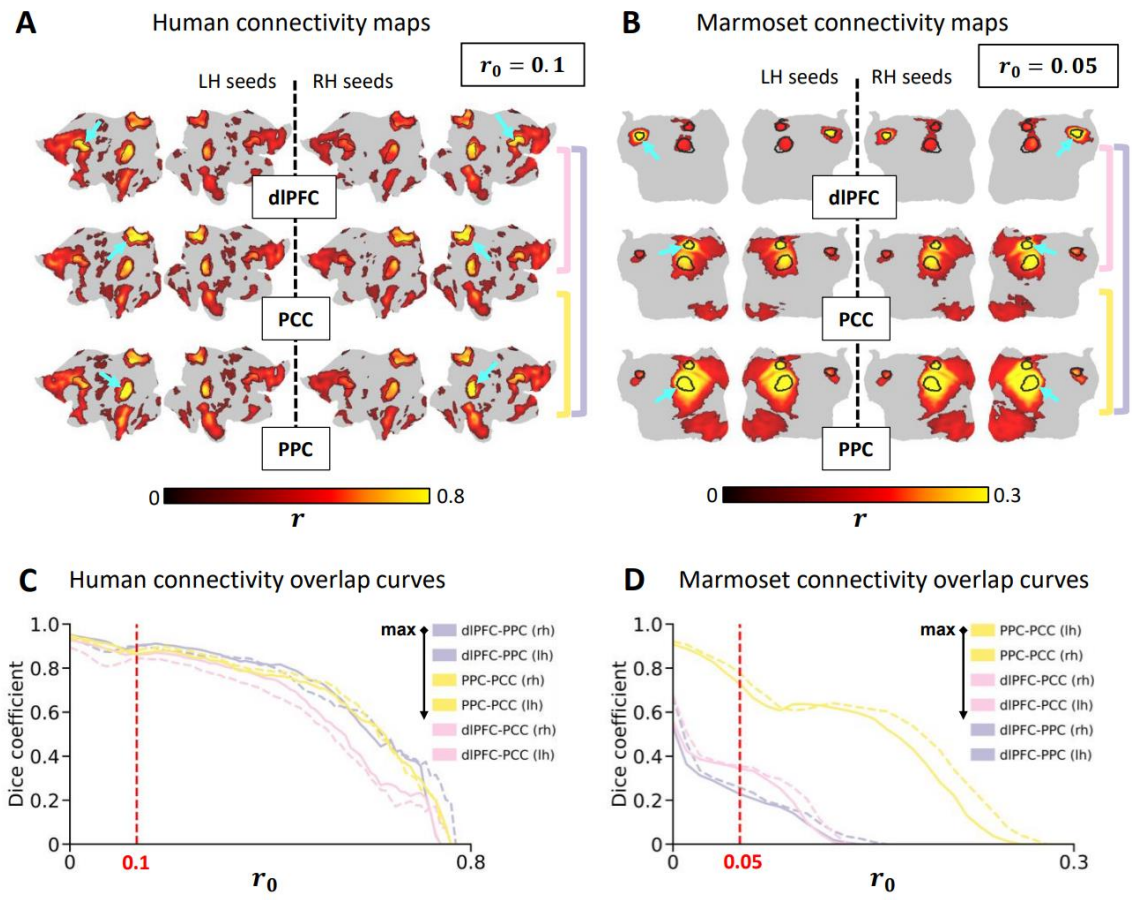


**Figure 3.4 Functional connection topography of human and marmoset DMN nodes**

*Areas of the cortex significantly correlated with the corresponding cortical DMN node (*$P < .05$) in each species. Significant areas are obtained from a one-sample t-test permutation test probing areas of the cortex with higher than 0.1 and 0.05 correlation score for humans and marmosets, respectively. To qualitatively assess areas of the cortex that display higher connectivity, the correlation maps are overlaid on the significant areas. Teal arrows denote the seeded DMN node. (A) Human DMN connection topographies. (B) Marmoset DMN connection topographies. Connectional topography dice coefficient overlap curves at varying degrees of connectivity strength ($\boldsymbol{r_0}$) determined by a one-sample t-test permutation test for (C) humans and (D) marmosets. Overlap of DMN node pairs were organized in descending order by calculating the area under the curve.*

The degree of overlap between the spatial topography of activation maps was assessed over a range of thresholds, where higher thresholds indicated areas associated with stronger

RSFC (*$P < 0.05$; nonparametric one-sample t-test, see Fig. 3.4c-d). In descending order, the overlap of human RSFC maps was highest between areas dlPFC & PPC, followed by PPC & PCC, and dlPFC & PCC (measured by area under the curve). In the low threshold regime, spatial overlap was high between all pairs of DMN nodes (i.e., Dice coefficient $>$ 0.8), and an increasing threshold led to spatial maps with decreasing overlap, but importantly, preservation of overlap in connectivity between distant DMN nodes was still conserved (Supplementary Fig. 3.6). Contrary to this finding, marmoset RSFC maps displayed the highest degree of overlap between areas PPC & PCC, followed by dlPFC & PCC, and dlPFC & PPC. Increasing the threshold led to spatial maps with only connections to adjacent areas, with overlap only observed between areas PCC & PPC, and leaving the RSFC map of the dlPFC completely segregated from posterior DMN areas (Supplementary Fig. 3.7). Taken together, humans and marmosets showed inconsistent RSFC patterns across DMN nodes, with inter-species differences largely attributed to RSFC topography of the marmoset dlPFC.

### 3.3.5 Details of a separate joint gradient that comprises marmoset mPFC

Given that the human DMN includes a large mPFC component which was absent in the marmoset's somatomotor-to-DMN joint gradient, we investigated subsequent marmoset joint gradients that included a mPFC component to better elucidate candidate marmoset-human homology. Visualization of joint gradient 3 of the marmoset (Fig. 3.5a) revealed a visual-to-auditory/mPFC axis, with lower and higher gradient values describing auditory/mPFC and visual areas, respectively. The spatial topography of lower gradient values (i.e., blue areas) included mPFC areas (i.e., A10, A32, A32V, A11 and A9) and temporal association areas (i.e., lower, and higher order auditory areas, and area TPO) which is generally consistent with marmoset anatomical connectivity findings, with the exception of TE3 (Buckner and Margulies, 2019). Buckner and colleagues (2019) also described sparse anatomical connections from mPFC and temporal association areas to other posterior DMN nodes (i.e., PCC and PPC), however this is not evidently seen in

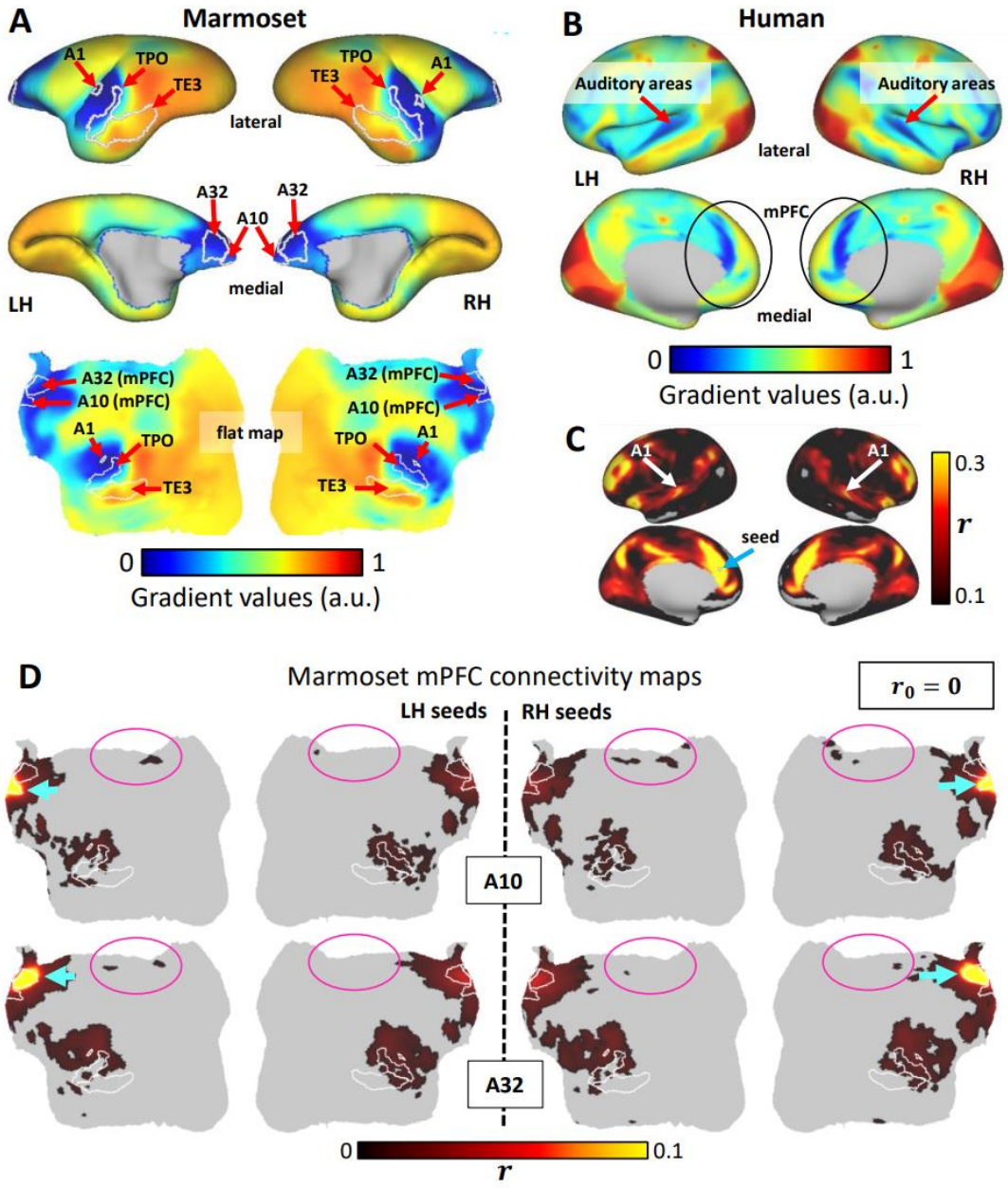


**Figure 3.5 Details of mPFC-centric joint gradient in marmosets**

*(A) Visualization of marmoset joint gradient 3 reveals a visual-to-mPFC/auditory axis. Red arrows & white label boundaries annotate candidate homologous marmoset mPFC (A10/A32) and anatomically-connected temporal association areas (TPO/TE3) (Buckner et al. 2019; Liu et al. 2019). (B) Visualization of human joint gradient 3 shows consistent spatial configuration to the marmoset. Red arrow (lateral view) annotates human auditory regions, and the black circle (medial view) annotates a candidate homologous mPFC*

*region in the human. (C) An exploratory cortical vertex seed was placed in the caudal mPFC of the left hemisphere yielding a functional connectivity map that includes the auditory region. White and blue arrow denotes A1 and the seed vertex, respectively. (D) Areas of the cortex significantly correlated with the corresponding cortical mPFC nodes (A10/A32) and demonstrates connectivity to auditory and auditory-adjacent temporal lobe areas (*$P < .05$). Significant areas are obtained from a one-sample t-test permutation test probing areas of the marmoset cortex with higher than 0 correlation score. Pink circles denote sparse connections to posterior cingulate cortex.*

joint gradient 3. Subsequent RSFC seed-based analyses using mPFC areas A10 and A32, demonstrate a consistent connection topography with the joint gradient results, in addition to weak and sparse connections observed in PCC areas ($*P < 0.05$; nonparametric one-sample t-test; see Fig. 3.5d).

The corresponding human joint gradient described an organizational axis akin to the marmoset, with lower gradient values describing auditory and a caudally situated mPFC area, in addition to other distributed regions (Fig. 3.5b). In this gradient, the proximal mPFC areas localized to the cingulo-opercular network (CON) and frontoparietal network (FPN), respectively, which are positioned caudally to the DMN's mPFC, and includes areas 8BM, a32pr, and p24 (Supplementary Fig. 3.8). By conducting an exploratory seed-based analysis using a vertex within the proximal mPFC ROI from joint gradient 3, we were able to demonstrate a connection topography that includes human auditory areas consistent with marmoset mPFC RSFC findings (Fig. 3.5c; shows a correlation analysis using a left hemisphere vertex). Similar observations can be reproduced using other proximally located vertices in both hemispheres. Together, this provides evidence for candidate homology between marmoset mPFC and the human proximal mPFC areas, specifically areas 8BM, a32pr, and p24, which notably does not include human DMN mPFC areas.

## 3.4 Discussion

Marmosets are a propitious animal model for studying higher-order cognitive and social functions (Miller et al. 2016; Jennings et al. 2016; Okano et al. 2016), such as the DMN, which in the human, has been prescribed as a candidate functional substrate (Buckner et

al. 2008; Smallwood et al. 2021). This has spurred recent interests to thoroughly characterize a marmoset DMN homologue composed of a collection of distributed regions that includes the dlPFC, PCC, and PPC (Liu et al. 2019). Here, we used joint embeddings' for studying homology between humans and marmosets and conducted subsequent supportive analyses and found that the marmoset dlPFC, although known to correspond to an anatomically connected anterior node of the DMN, displays inconsistent RSFC properties with the rest of the DMN core (i.e., PCC and PPC). This presents evidence for a less evolutionarily conserved area in the dlPFC compared to the rest of its connected DMN constituents.

Braga and Buckner (2017) previously indicated the presence of two juxtaposed DMN components - DMN-A and DMN-B - as demonstrated in single subject human RSFC data (Braga and Buckner, 2017). In the marmoset, it has been proposed that DMN-A includes the frontopolar A10 region, despite the lack of evidence showing A10-to-posterior parietal connections (Buckner and Margulies, 2019). Meanwhile, other evidence suggests the dlPFC-PCC-PPC as a homologous candidate for DMN-B (Liu et al. 2019). Revealed here, joint gradients identified correspondence between the human DMN, and marmoset DMN-B as described by Liu and colleagues, with no evidence of a mPFC component (or DMN-A-like component) in the marmoset. Worth noting, is that because group-level RSFC data was used to identify the human DMN, it likely blurs together DMN subtypes A & B, and yet, no evidence of an anterior mPFC was observed in the marmoset.

To further highlight this distinction, we found spatial consistency between RSFC patterns of marmoset mPFC areas and another joint gradient which included marmoset mPFC, auditory, and auditory-adjacent temporal lobe areas. Marmoset mPFC RSFC connection topographies were proximally consistent with monosynaptic anatomical connectivity findings which demonstrated connections between mPFC and auditory-adjacent temporal lobe areas, whereas connections to auditory cortex was minimal and contrary to the findings here (Buckner and Margulies, 2019). This difference may be attributed to spatial smoothing that is typical during RSFC preprocessing, or to polysynaptic connections that might be enabled by RSFC (i.e., RSFC between mPFC and auditory areas may be mediated by monosynaptic connections from area A10 to TPO, and TPO to auditory areas). In

concordance with the marmoset mPFC gradient, a similar spatial configuration was observed in the corresponding human joint gradient component which included three medial frontal regions (i.e., 8BM, a32pr, and p24) that primarily localized to the CON and FPN. In humans, these RSNs are known to support executive control functions, such as error processing (Dosenbach et al. 2007), executive control during goal-directed behaviours (Dosenbach et al. 2006), and likely includes other variety of executive control functions. Intriguingly, areas 24 and 32, found in joint gradient 3 of both species, are known to be involved in the "cingulate vocalization pathway" important for executive control of innate and affective vocalization (Jürgens and Pratt, 1979; Hammerschmidt and Fischer, 2008). Furthermore, connections between auditory and frontal areas may support integration of auditory information known to also assist operant control of vocal productions (Hage and Nieder, 2015). It is interesting to the postulate the functional role of marmoset mPFC and whether it supports similar executive control functions to the human CON and FPN, in addition to vocalization. Development of more complex behavioural assays (Oikonomidis et al. 2017; Pomberger et al. 2019) and further investigations to validate the functional role of the marmoset mPFC will be necessary. Taken together, joint gradient analyses revealed evidence for candidate homology between marmoset mPFC and human CON/FPN, as opposed to the DMN-A.

Perhaps more interesting, and is the primary focus of this work, are the notable differences observed in the marmoset dlPFC, which displayed distinguishably larger gradient values compared to all other DMN areas in marmosets (PCC & PPC) and humans (all DMN areas). Subsequent analyses implicate these differences are due to a weaker internode DMN connectivity, as well as overall differences in the spatial topography of node-to-cortex RSFC patterns of the marmoset dlPFC. This observation is consistent with conventional methods to identify the DMN using task suppression analyses (Raichle et al. 2001), which only showed deactivations in posterior DMN nodes during a simple visual task, whereas deactivation of the dlPFC was absent (Liu et al. 2019). This was rationalized by the simplicity of the task; however, it is possible that marmoset dlPFC subserves a different brain function from the posterior DMN as supported by its differential circuitry, and thus may not deactivate even during more complex tasks. Additionally, cross-species movie-driven fMRI experiments did not describe correspondence between anterior DMN areas of

marmosets and humans, whereas correspondence between cross-species posterior DMN areas (i.e., marmoset adjacent intraparietal areas to human areas PGi & PGs) were established, further recapitulating evidence of apparent functional differences between anterior and posterior DMN areas (Hori et al. 2021). Moreover, in the present study, the marmoset-human joint gradient demonstrated a wider distribution of gradient values across the marmoset DMN core relative to humans, likely attributed to the dlPFC. Similar findings of widely-distributed gradient values have been shown using joint gradients with macaques and humans (Xu et al. 2020), and may be attributed to a weakly connected anterior-posterior DMN (Mantini et al. 2011). Together, this alludes to an evolutionarily divergent anterior-posterior DMN axis between humans and primates.

Understanding the similarities and differences between spatial topography of RSFC patterns through different DMN nodes may provide a better understanding of the DMN's relevance to function. For example, many forms of complex processing, such as episodic memory (Moscovitch et al. 2016), semantic memory (Ritchey and Cooper, 2020) and emotion (Gendron and Barrett, 2018) are thought to rely on widely distributed sets of processes, and the DMN offers itself as a useful substrate to facilitate these functions (Smallwood et al. 2021). In line with this, we found that all distant human DMN nodes (i.e., dlPFC, PCC, PPC) are highly interconnected and demonstrated a high degree of overlap across all their RSFC profiles. This suggests the possibility for efficient processing of local sensory information across distributed DMN nodes. Inconsistent with humans, we found that spatial topography of RSFC from the marmoset dlPFC displayed sparse and weak connections to posterior DMN areas, while also displaying relatively less RSFC to adjacent areas compared to the adjacent RSFC that was observed in posterior DMN areas. It is possible that non-human primates lack (1) a disproportionate expansion of prefrontal areas (Smaers et al. 2017) and/or (2) an increase in underlying white matter volume (Donahue et al. 2018) that would facilitate the necessary anatomical connections to enable convergent and overlapping connection topographies between prefrontal and posterior DMN nodes, such as that seen in humans.

Our results are subject to several methodological limitations. One of the goals of this work was to draw inferences of homology of the DMN between marmosets and humans using

joint gradients (Xu et al. 2020) which heavily relied on a-priori definitions of interspecies homologous areas. Relative to macaques (Van Essen and Dierker, 2007; Neubert et al. 2014), marmosets have only more recently gained traction as an animal model, and as such, established human-marmoset homologous areas remain lacking. It is unclear whether a reduced alignment in gradient profiles of homologous association regions (i.e., FEF and PPC) and A1 is due to this fact, or due to evolutionarily divergence in these regions. Nonetheless, robust identification of homologous of large-scale networks was achieved in the work presented here.

This study also relied on group-level analyses to demonstrate joint gradients and can in future works be generalized to joint pairs of individual human and marmoset subjects. To do so, sufficient data collection and high quality data, in addition to personalization of homologous ROIs must be achieved to account for sufficient SNR and anatomical variability (Rajkowska and Goldman-Rakic, 1995). Individualized joint gradients may be able to enable more accurate matching of canonical DMN subtypes (i.e., A & B [Braga and Buckner, 2017]) in the humans and marmosets. Here, we also relied heavily on group-derived atlases (i.e., Paxinos histological atlas [Majka et al. 2021]) which oftentimes described ROIs with high variability of gradient values. Advances in marmoset atlas development derived using unimodal resting-state fMRI data would be beneficial, taking advantage of techniques such as gradientography (Tian et al. 2020) in combination with histological data, to allow for more comprehensive RSFC studies of the marmoset.

Finally, discussion of the functional implications of a divergent anterior-posterior DMN axis in the marmoset is largely conjecture. Here, we draw inferences based purely on interspecies differences that was observed between humans and marmosets. It will be prudent to conduct further interspecies investigations to see how different DMN areas, including the marmoset mPFC, engage during different task-states to fully appreciate their roles in the landscape of cognition and higher-order functions.

## 3.5 References

Bassett, D. S., & Bullmore, E. T. (2017). Small-World Brain Networks Revisited. *The Neuroscientist: A Review Journal Bringing Neurobiology, Neurology and Psychiatry*, *23*(5), 499–516. https://doi.org/10.1177/1073858416667720

Belkin, M., & Niyogi, P. (2003). Laplacian Eigenmaps for Dimensionality Reduction and Data Representation. *Neural Computation*, *15*(6), 1373–1396. https://doi.org/10.1162/089976603321780317

Braga, R. M., & Buckner, R. L. (2017). Parallel Interdigitated Distributed Networks within the Individual Estimated by Intrinsic Functional Connectivity. *Neuron*, *95*(2), 457-471.e5. https://doi.org/10.1016/j.neuron.2017.06.038

Braga, R. M., Sharp, D. J., Leeson, C., Wise, R. J. S., & Leech, R. (2013). Echoes of the Brain within Default Mode, Association, and Heteromodal Cortices. *Journal of Neuroscience*, *33*(35), 14031–14039. https://doi.org/10.1523/JNEUROSCI.0570-13.2013

Braun, U., Schäfer, A., Walter, H., Erk, S., Romanczuk-Seiferth, N., Haddad, L., … Bassett, D. S. (2015). Dynamic reconfiguration of frontal brain networks during executive cognition in humans. *Proceedings of the National Academy of Sciences*, *112*(37), 11678–11683. https://doi.org/10.1073/pnas.1422487112

Buckner, R. L., Andrews-Hanna, J. R., & Schacter, D. L. (2008). The brain's default network: Anatomy, function, and relevance to disease. *Annals of the New York Academy of Sciences*, *1124*, 1–38. https://doi.org/10.1196/annals.1440.011

Buckner, R. L., & Margulies, D. S. (2019). Macroscale cortical organization and a default-like apex transmodal network in the marmoset monkey. *Nature Communications*, *10*(1), 1976. https://doi.org/10.1038/s41467-019-09812-8

Burt, J. B., Helmer, M., Shinn, M., Anticevic, A., & Murray, J. D. (2020). Generative modeling of brain maps with spatial autocorrelation. *NeuroImage*, *220*, 117038. https://doi.org/10.1016/j.neuroimage.2020.117038

Chaplin, T. A., Yu, H.-H., Soares, J. G. M., Gattass, R., & Rosa, M. G. P. (2013). A conserved pattern of differential expansion of cortical areas in simian primates. *The Journal of Neuroscience: The Official Journal of the Society for Neuroscience*, *33*(38), 15120–15125. https://doi.org/10.1523/JNEUROSCI.2909-13.2013

Deco, G., Tononi, G., Boly, M., & Kringelbach, M. L. (2015). Rethinking segregation and integration: Contributions of whole-brain modelling. *Nature Reviews Neuroscience*, *16*(7), 430–439. https://doi.org/10.1038/nrn3963

Dice, L. R. (1945). Measures of the Amount of Ecologic Association Between Species. *Ecology*, *26*(3), 297–302. https://doi.org/10.2307/1932409

Donahue, C. J., Glasser, M. F., Preuss, T. M., Rilling, J. K., & Essen, D. C. V. (2018). Quantitative assessment of prefrontal cortex in humans relative to nonhuman primates. *Proceedings of the National Academy of Sciences*, *115*(22), E5183–E5192. https://doi.org/10.1073/pnas.1721653115

Dosenbach, N. U. F., Fair, D. A., Miezin, F. M., Cohen, A. L., Wenger, K. K., Dosenbach, R. A. T., … Petersen, S. E. (2007). Distinct brain networks for adaptive and stable task control in humans. *Proceedings of the National Academy of Sciences*, *104*(26), 11073–11078. https://doi.org/10.1073/pnas.0704320104

Dosenbach, N. U. F., Visscher, K. M., Palmer, E. D., Miezin, F. M., Wenger, K. K., Kang, H. C., … Petersen, S. E. (2006). A Core System for the Implementation of Task Sets. *Neuron*, *50*(5), 799–812. https://doi.org/10.1016/j.neuron.2006.04.031

Finc, K., Bonna, K., He, X., Lydon-Staley, D. M., Kühn, S., Duch, W., & Bassett, D. S. (2020). Dynamic reconfiguration of functional brain networks during working memory training. *Nature Communications*, *11*(1), 2435. https://doi.org/10.1038/s41467-020-15631-z

Gendron, M., & Barrett, L. F. (2018). Emotion Perception as Conceptual Synchrony. *Emotion Review*, *10*(2), 101–110. https://doi.org/10.1177/1754073917705717

Glasser, M. F., Coalson, T. S., Robinson, E. C., Hacker, C. D., Harwell, J., Yacoub, E., … Van Essen, D. C. (2016). A multi-modal parcellation of human cerebral cortex. *Nature*, *536*(7615), 171–178. https://doi.org/10.1038/nature18933

Glasser, M. F., Sotiropoulos, S. N., Wilson, J. A., Coalson, T. S., Fischl, B., Andersson, J. L., … Jenkinson, M. (2013). The minimal preprocessing pipelines for the Human Connectome Project. *NeuroImage*, *80*, 105–124. https://doi.org/10.1016/j.neuroimage.2013.04.127

Goulas, A., Majka, P., Rosa, M. G. P., & Hilgetag, C. C. (2019). A blueprint of mammalian cortical connectomes. *PLOS Biology*, *17*(3), e2005346. https://doi.org/10.1371/journal.pbio.2005346

Griffanti, L., Salimi-Khorshidi, G., Beckmann, C. F., Auerbach, E. J., Douaud, G., Sexton, C. E., … Smith, S. M. (2014). ICA-based artefact removal and accelerated fMRI acquisition for improved resting state network imaging. *NeuroImage*, *95*, 232–247. https://doi.org/10.1016/j.neuroimage.2014.03.034

Haak, K. V., Marquand, A. F., & Beckmann, C. F. (2018). Connectopic mapping with resting-state fMRI. *NeuroImage*, *170*, 83–94. https://doi.org/10.1016/j.neuroimage.2017.06.075

Hage, S. R., & Nieder, A. (2015). Audio-Vocal Interaction in Single Neurons of the Monkey Ventrolateral Prefrontal Cortex. *Journal of Neuroscience*, *35*(18), 7030–7040. https://doi.org/10.1523/JNEUROSCI.2371-14.2015

Hammerschmidt, K., & Fischer, J. (2008). Constraints in Primate Vocal Production. In *Evolution of Communicative Flexibility*. The MIT Press. https://doi.org/10.7551/mitpress/9780262151214.003.0005

Hori, Y., Cléry, J. C., Selvanayagam, J., Schaeffer, D. J., Johnston, K. D., Menon, R. S., & Everling, S. (2021). Interspecies activation correlations reveal functional correspondences between marmoset and human brain areas. *Proceedings of the National Academy of Sciences*, *118*(37). https://doi.org/10.1073/pnas.2110980118

Hori, Y., Schaeffer, D. J., Yoshida, A., Cléry, J. C., Hayrynen, L. K., Gati, J. S., … Everling, S. (2020). Cortico-Subcortical Functional Connectivity Profiles of Resting-State Networks in Marmosets and Humans. *Journal of Neuroscience*, *40*(48), 9236–9249. https://doi.org/10.1523/JNEUROSCI.1984-20.2020

Jenkinson, M., Beckmann, C. F., Behrens, T. E. J., Woolrich, M. W., & Smith, S. M. (2012). FSL. *NeuroImage*, *62*(2), 782–790. https://doi.org/10.1016/j.neuroimage.2011.09.015

Jennings, C. G., Landman, R., Zhou, Y., Sharma, J., Hyman, J., Movshon, J. A., … Feng, G. (2016). Opportunities and challenges in modeling human brain disorders in transgenic primates. *Nature Neuroscience*, *19*(9), 1123–1130. https://doi.org/10.1038/nn.4362

Ji, J. L., Spronk, M., Kulkarni, K., Repovš, G., Anticevic, A., & Cole, M. W. (2019). Mapping the human brain's cortical-subcortical functional network organization. *NeuroImage*, *185*, 35–57. https://doi.org/10.1016/j.neuroimage.2018.10.006

Jürgens, U., & Pratt, R. (1979). The cingular vocalization pathway in the squirrel monkey. *Experimental Brain Research*, *34*(3), 499–510. https://doi.org/10.1007/BF00239145

Kaas, J. H. (2004). Evolution of somatosensory and motor cortex in primates. *The Anatomical Record Part A: Discoveries in Molecular, Cellular, and Evolutionary Biology*, *281A*(1), 1148–1156. https://doi.org/10.1002/ar.a.20120

Kernbach, J. M., Yeo, B. T. T., Smallwood, J., Margulies, D. S., Thiebaut de Schotten, M., Walter, H., … Bzdok, D. (2018). Subspecialization within default mode nodes characterized in 10,000 UK Biobank participants. *Proceedings of the National Academy of Sciences*, *115*(48), 12295–12300. https://doi.org/10.1073/pnas.1804876115

Liu, C., Yen, C. C.-C., Szczupak, D., Tian, X., Glen, D., & Silva, A. C. (2021). Marmoset Brain Mapping V3: Population multi-modal standard volumetric and surface-based templates. *NeuroImage*, *226*, 117620. https://doi.org/10.1016/j.neuroimage.2020.117620

Liu, C., Yen, C. C.-C., Szczupak, D., Ye, F. Q., Leopold, D. A., & Silva, A. C. (2019). Anatomical and functional investigation of the marmoset default mode network. *Nature Communications*, *10*(1), 1975. https://doi.org/10.1038/s41467-019-09813-7

Majka, P., Bednarek, S., Chan, J. M., Jermakow, N., Liu, C., Saworska, G., … Rosa, M. G. P. (2021). Histology-Based Average Template of the Marmoset Cortex With Probabilistic Localization of Cytoarchitectural Areas. *NeuroImage*, *226*, 117625. https://doi.org/10.1016/j.neuroimage.2020.117625

Mantini, D., Gerits, A., Nelissen, K., Durand, J.-B., Joly, O., Simone, L., … Vanduffel, W. (2011). Default Mode of Brain Function in Monkeys. *Journal of Neuroscience*, *31*(36), 12954–12962. https://doi.org/10.1523/JNEUROSCI.2318-11.2011

Margulies, D. S., Ghosh, S. S., Goulas, A., Falkiewicz, M., Huntenburg, J. M., Langs, G., … Smallwood, J. (2016). Situating the default-mode network along a principal gradient of macroscale cortical organization. *Proceedings of the National Academy of Sciences of the United States of America*, *113*(44), 12574–12579. https://doi.org/10.1073/pnas.1608282113

Mars, R. B., Passingham, R. E., & Jbabdi, S. (2018). Connectivity Fingerprints: From Areal Descriptions to Abstract Spaces. *Trends in Cognitive Sciences*, *22*(11), 1026–1037. https://doi.org/10.1016/j.tics.2018.08.009

Miller, C. T., Freiwald, W. A., Leopold, D. A., Mitchell, J. F., Silva, A. C., & Wang, X. (2016). Marmosets: A Neuroscientific Model of Human Social Behavior. *Neuron*, *90*(2), 219–233. https://doi.org/10.1016/j.neuron.2016.03.018

Moscovitch, M., Cabeza, R., Winocur, G., & Nadel, L. (2016). Episodic Memory and Beyond: The Hippocampus and Neocortex in Transformation. *Annual Review of Psychology*, *67*(1), 105–134. https://doi.org/10.1146/annurev-psych-113011-143733

Nenning, K.-H., Liu, H., Ghosh, S. S., Sabuncu, M. R., Schwartz, E., & Langs, G. (2017). Diffeomorphic functional brain surface alignment: Functional demons. *NeuroImage*, *156*, 456–465. https://doi.org/10.1016/j.neuroimage.2017.04.028

Nichols, T. E., & Holmes, A. P. (2002). Nonparametric permutation tests for functional neuroimaging: A primer with examples. *Human Brain Mapping*, *15*(1), 1–25. https://doi.org/10.1002/hbm.1058

Oikonomidis, L., Santangelo, A. M., Shiba, Y., Clarke, F. H., Robbins, T. W., & Roberts, A. C. (2017). A dimensional approach to modeling symptoms of neuropsychiatric disorders in the marmoset monkey. *Developmental Neurobiology*, *77*(3), 328–353. https://doi.org/10.1002/dneu.22446

Okano, H., Sasaki, E., Yamamori, T., Iriki, A., Shimogori, T., Yamaguchi, Y., … Miyawaki, A. (2016). Brain/MINDS: A Japanese National Brain Project for Marmoset Neuroscience. *Neuron*, *92*(3), 582–590. https://doi.org/10.1016/j.neuron.2016.10.018

Paxinos, G., Watson, C. R. R., Petrides, M., Rosa, M. G., & Tokuno, H. (2012). *The Marmoset Brain in Stereotaxic Coordinates*. Elsevier. Retrieved from https://research.monash.edu/en/publications/the-marmoset-brain-in-stereotaxic-coordinates

Pomberger, T., Risueno-Segovia, C., Gultekin, Y. B., Dohmen, D., & Hage, S. R. (2019). Cognitive control of complex motor behavior in marmoset monkeys. *Nature Communications*, *10*(1), 3796. https://doi.org/10.1038/s41467-019-11714-8

Power, J. D., Barnes, K. A., Snyder, A. Z., Schlaggar, B. L., & Petersen, S. E. (2012). Spurious but systematic correlations in functional connectivity MRI networks arise from subject motion. *NeuroImage*, *59*(3), 2142–2154. https://doi.org/10.1016/j.neuroimage.2011.10.018

Raichle, M. E., MacLeod, A. M., Snyder, A. Z., Powers, W. J., Gusnard, D. A., & Shulman, G. L. (2001). A default mode of brain function. *Proceedings of the National Academy of Sciences*, *98*(2), 676–682. https://doi.org/10.1073/pnas.98.2.676

Rajkowska, G., & Goldman-Rakic, P. S. (1995). Cytoarchitectonic Definition of Prefrontal Areas in the Normal Human Cortex: II. Variability in Locations of Areas 9 and 46 and Relationship to the Talairach Coordinate System. *Cerebral Cortex*, *5*(4), 323–337. https://doi.org/10.1093/cercor/5.4.323

Reser, D. H., Burman, K. J., Yu, H.-H., Chaplin, T. A., Richardson, K. E., Worthy, K. H., & Rosa, M. G. P. (2013). Contrasting Patterns of Cortical Input to Architectural Subdivisions of the Area 8 Complex: A Retrograde Tracing Study in Marmoset Monkeys. *Cerebral Cortex*, *23*(8), 1901–1922. https://doi.org/10.1093/cercor/bhs177

Ritchey, M., & Cooper, R. A. (2020). Deconstructing the Posterior Medial Episodic Network. *Trends in Cognitive Sciences*, *24*(6), 451–465. https://doi.org/10.1016/j.tics.2020.03.006

Salimi-Khorshidi, G., Douaud, G., Beckmann, C. F., Glasser, M. F., Griffanti, L., & Smith, S. M. (2014). Automatic denoising of functional MRI data: Combining independent component analysis and hierarchical fusion of classifiers. *NeuroImage*, *90*, 449–468. https://doi.org/10.1016/j.neuroimage.2013.11.046

Schaeffer, D. J., Gilbert, K. M., Hori, Y., Hayrynen, L. K., Johnston, K. D., Gati, J. S., … Everling, S. (2019). Task-based fMRI of a free-viewing visuo-saccadic network in the marmoset monkey. *NeuroImage*, *202*, 116147. https://doi.org/10.1016/j.neuroimage.2019.116147

Schaeffer, D. J., Klassen, L. M., Hori, Y., Tian, X., Szczupak, D., Yen, C. C.-C., … Silva, A. C. (2022). An open access resource for functional brain connectivity from fully awake marmosets. *NeuroImage*, *252*, 119030. https://doi.org/10.1016/j.neuroimage.2022.119030

Selvanayagam, J., Johnston, K. D., Schaeffer, D. J., Hayrynen, L. K., & Everling, S. (2019). Functional Localization of the Frontal Eye Fields in the Common Marmoset Using Microstimulation. *Journal of Neuroscience*, *39*(46), 9197–9206. https://doi.org/10.1523/JNEUROSCI.1786-19.2019

Shine, J. M. (2019). Neuromodulatory Influences on Integration and Segregation in the Brain. *Trends in Cognitive Sciences*, *23*(7), 572–583. https://doi.org/10.1016/j.tics.2019.04.002

Smaers, J. B., Gómez-Robles, A., Parks, A. N., & Sherwood, C. C. (2017). Exceptional Evolutionary Expansion of Prefrontal Cortex in Great Apes and Humans. *Current Biology*, *27*(5), 714–720. https://doi.org/10.1016/j.cub.2017.01.020

Smallwood, J., Bernhardt, B. C., Leech, R., Bzdok, D., Jefferies, E., & Margulies, D. S. (2021). The default mode network in cognition: A topographical perspective. *Nature Reviews. Neuroscience*, *22*(8), 503–513. https://doi.org/10.1038/s41583-021-00474-4

Smith, S. M., Beckmann, C. F., Andersson, J., Auerbach, E. J., Bijsterbosch, J., Douaud, G., … Glasser, M. F. (2013). Resting-state fMRI in the Human Connectome Project. *NeuroImage*, *80*, 144–168. https://doi.org/10.1016/j.neuroimage.2013.05.039

Solomon, S. G., & Rosa, M. G. P. (2014). A simpler primate brain: The visual system of the marmoset monkey. *Frontiers in Neural Circuits*, *8*. Retrieved from https://www.frontiersin.org/article/10.3389/fncir.2014.00096

Sporns, O. (2010). *Networks of the Brain*. Cambridge, MA, USA: MIT Press.

Stephan, H., Frahm, H., & Baron, G. (1981). New and revised data on volumes of brain structures in insectivores and primates. *Folia Primatologica; International Journal of Primatology*, *35*(1), 1–29. https://doi.org/10.1159/000155963

Thomas, Yeo, B. T., Krienen, F. M., Sepulcre, J., Sabuncu, M. R., Lashkari, D., Hollinshead, M., … Buckner, R. L. (2011). The organization of the human cerebral cortex estimated by intrinsic functional connectivity. *Journal of Neurophysiology*, *106*(3), 1125–1165. https://doi.org/10.1152/jn.00338.2011

Tian, Y., Margulies, D. S., Breakspear, M., & Zalesky, A. (2020). Topographic organization of the human subcortex unveiled with functional connectivity gradients. *Nature Neuroscience*, *23*(11), 1421–1432. https://doi.org/10.1038/s41593-020-00711-6

Van Essen, D. C., & Dierker, D. L. (2007). Surface-based and probabilistic atlases of primate cerebral cortex. *Neuron*, *56*(2), 209–225. https://doi.org/10.1016/j.neuron.2007.10.015

Wang, R., Liu, M., Cheng, X., Wu, Y., Hildebrandt, A., & Zhou, C. (2021). Segregation, integration, and balance of large-scale resting brain networks configure different cognitive abilities. *Proceedings of the National Academy of Sciences*, *118*(23), e2022288118. https://doi.org/10.1073/pnas.2022288118

Xu, T., Nenning, K.-H., Schwartz, E., Hong, S.-J., Vogelstein, J. T., Goulas, A., … Langs, G. (2020). Cross-species functional alignment reveals evolutionary hierarchy within the connectome. *NeuroImage*, *223*, 117346. https://doi.org/10.1016/j.neuroimage.2020.117346

## 3.6 Supplementary Tables

**Supplementary Tables 3.1 Details of homologous regions of interest**

| | Homologous region label | Human label (Glasser et al. 2016) | Marmoset label (Paxinos et al. 2012) | References |
|---|---|---|---|---|
| 1 | V1 | V1 | V1 | Solomon and Rosa, 2014 |
| 2 | V2 | V2 | V2 | Solomon and Rosa, 2014 |
| 3 | A1 | A1 | AuA1 | |
| 4 | M1 | 4 | A4ab+A4c | Kaas 2004 |
| 5 | 3a | 3a | A3a | Kaas 2004 |
| 6 | 3b | 3b | A3b | Kaas 2004 |
| 7 | 1+2 | 1+2 | 1+2 | Kaas 2004 |
| 8 | FEF | FEF | A8Av | Solomon and Rosa, 2014 |
| 9 | MT | MT | V5 | Solomon and Rosa, 2014 |
| 10 | dlPFC | 8Ad | Localized w/ICA | Ji et al. 2019, Liu et al. 2019 |
| 11 | PCC | 7m | Localized w/ICA | Ji et al. 2019, Liu et al. 2019 |
| 12 | PPC | PGi+PGs | Localized w/ICA | Ji et al. 2019, Liu et al. 2019 |
| 13 | Hippocampus | Hippocampus | Hippocampus | |

## 3.7 Supplementary Figures

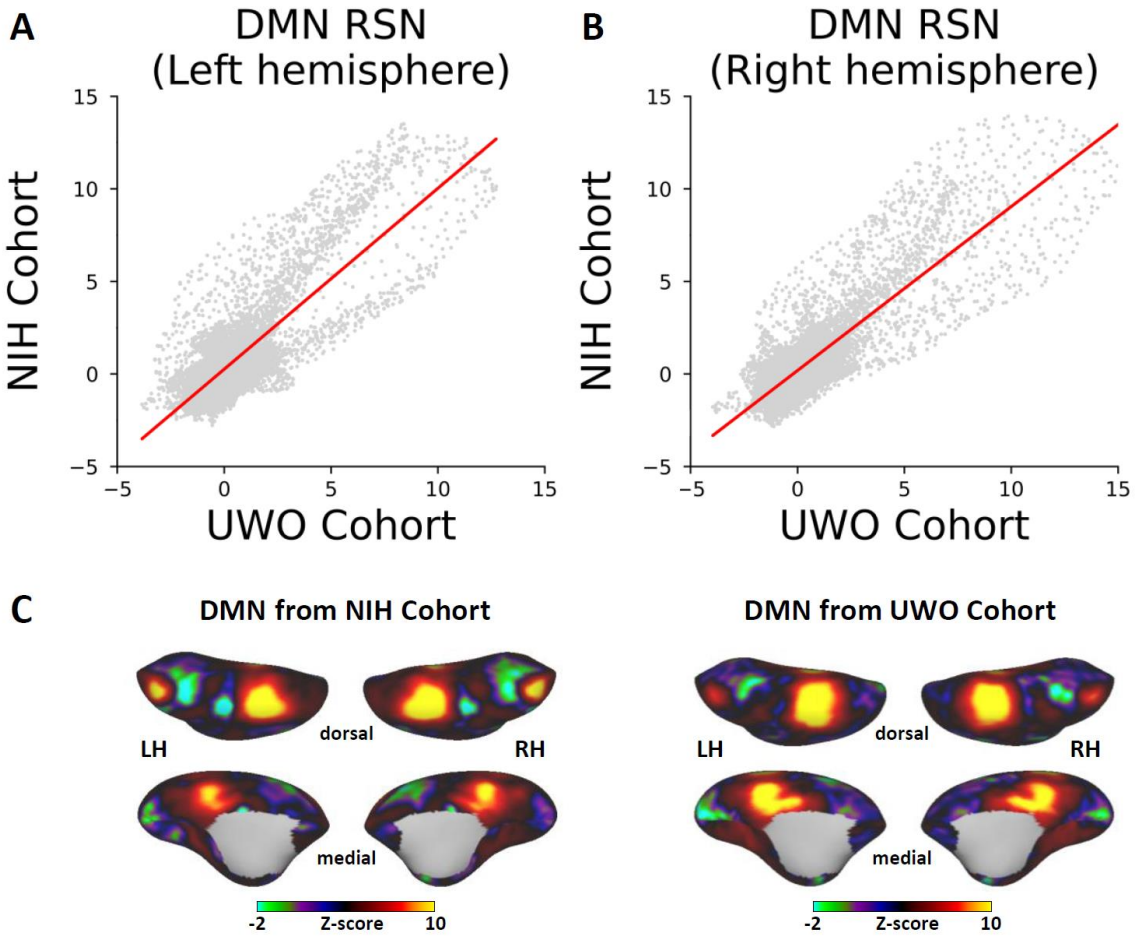


**Supplementary Figure 3.1 Association between DMN RSN of the NIH and UWO marmoset cohort**

*Correlation between group level DMN RSN of the NIH (n=26) and UWO (n=5) marmoset cohort. Group level DMN RSN of the marmoset cohorts were derived using ICA (dimensionality of 30) applied to each cohort's resting-state-fMRI data. The DMN RSN of each cohort was hand-selected for comparison. (A) Left hemisphere and (B) right hemisphere. (C) Visualization of the DMN in the NIH (left) and UWO (right) cohort. (***$P < 10^{-4}$ for both hemispheres)*

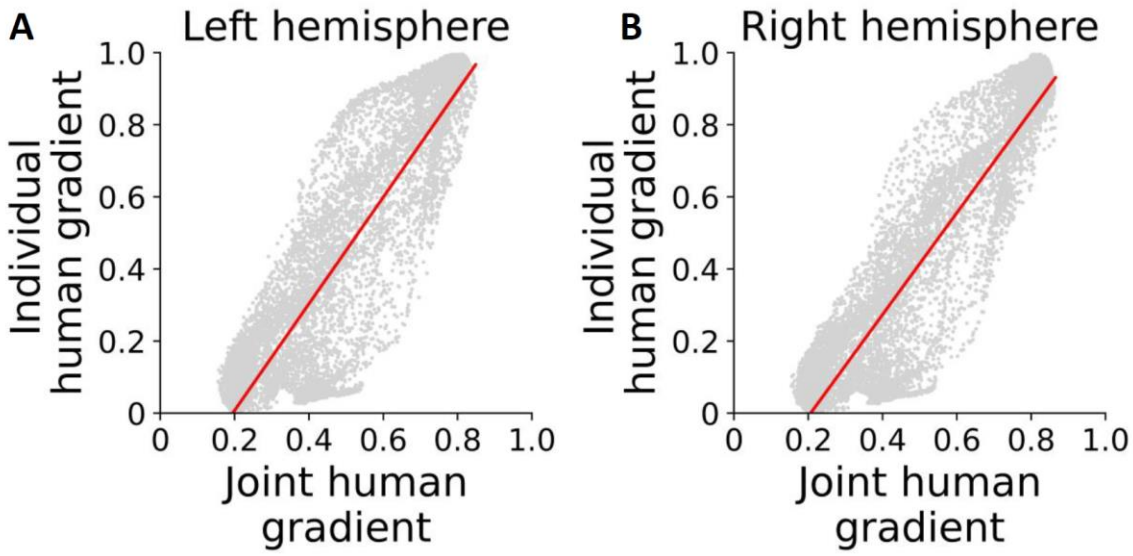


**Supplementary Figure 3.2 Association between human individual and joint somatomotor-to-DMN gradients**

*Correlation between group level human somatomotor-to-DMN gradient derived from human cortex-to-cortex functional connectivity patterns (N = 65), and human somatomotor-to-DMN joint gradients derived using the joint gradient approach that considers both human and marmoset group level functional connectivity patterns. (A) Left hemisphere and (B) right hemisphere. (***$P < 10^{-4}$ for both hemispheres)*

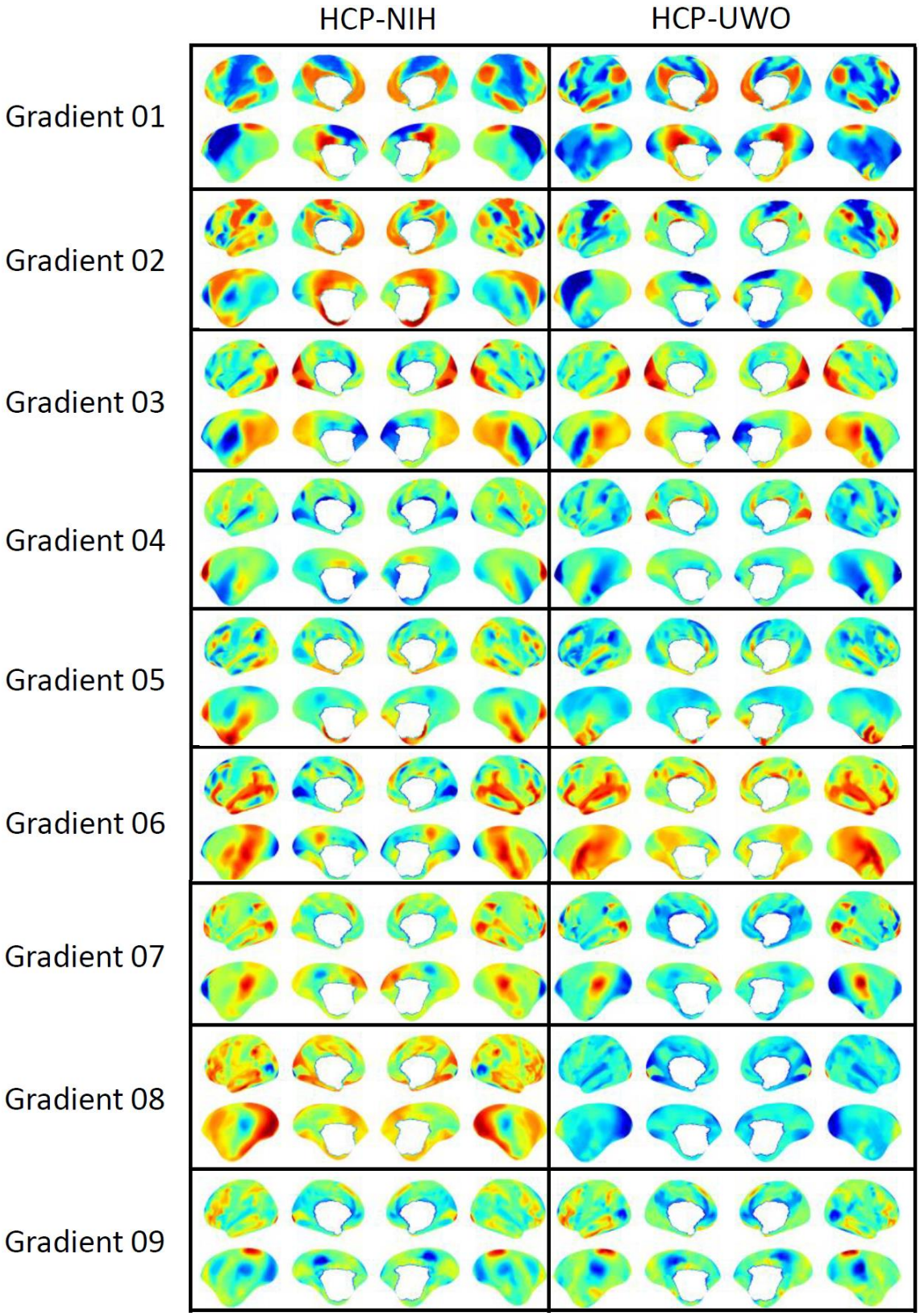
HCP-NIH
HCP-UWO
Gradient 01
Gradient 02
Gradient 03
Gradient 04
Gradient 05
Gradient 06
Gradient 07
Gradient 08
Gradient 09

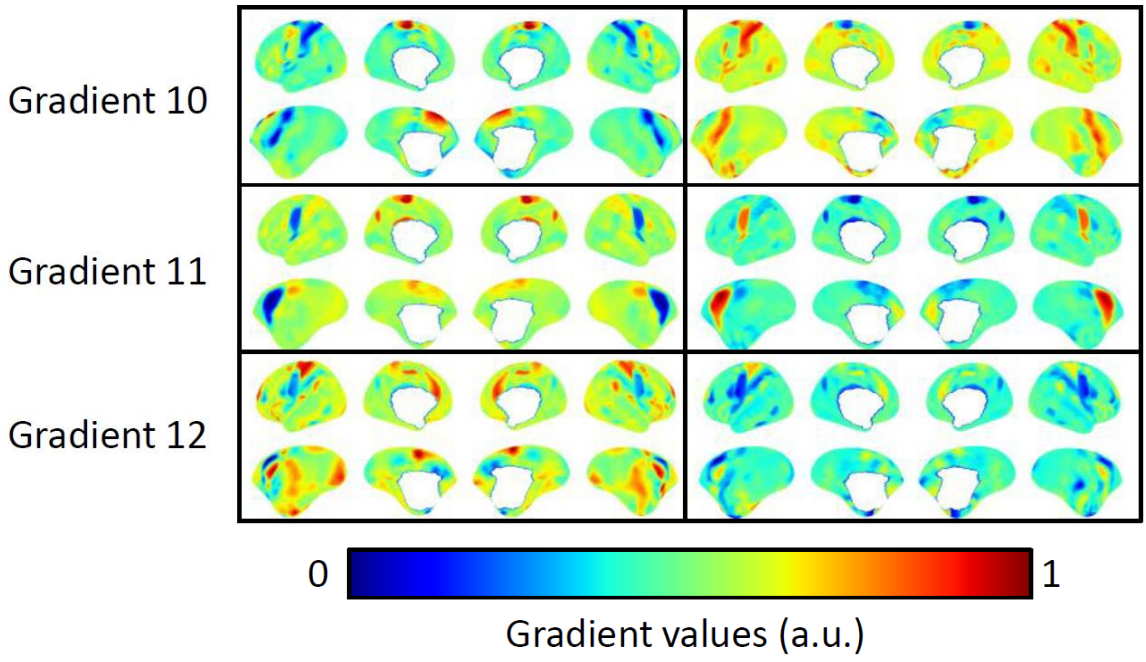


**Supplementary Figure 3.3 Top 12 joint gradients in humans and marmosets**

*Joint gradients computed using human and marmoset group-averaged RSFC data, and subsequently mapped onto the human and marmoset cortices. Results shown here include joint gradients computed twice using two marmoset cohorts (NIH and UWO) paired with a single human cohort (HCP100).*

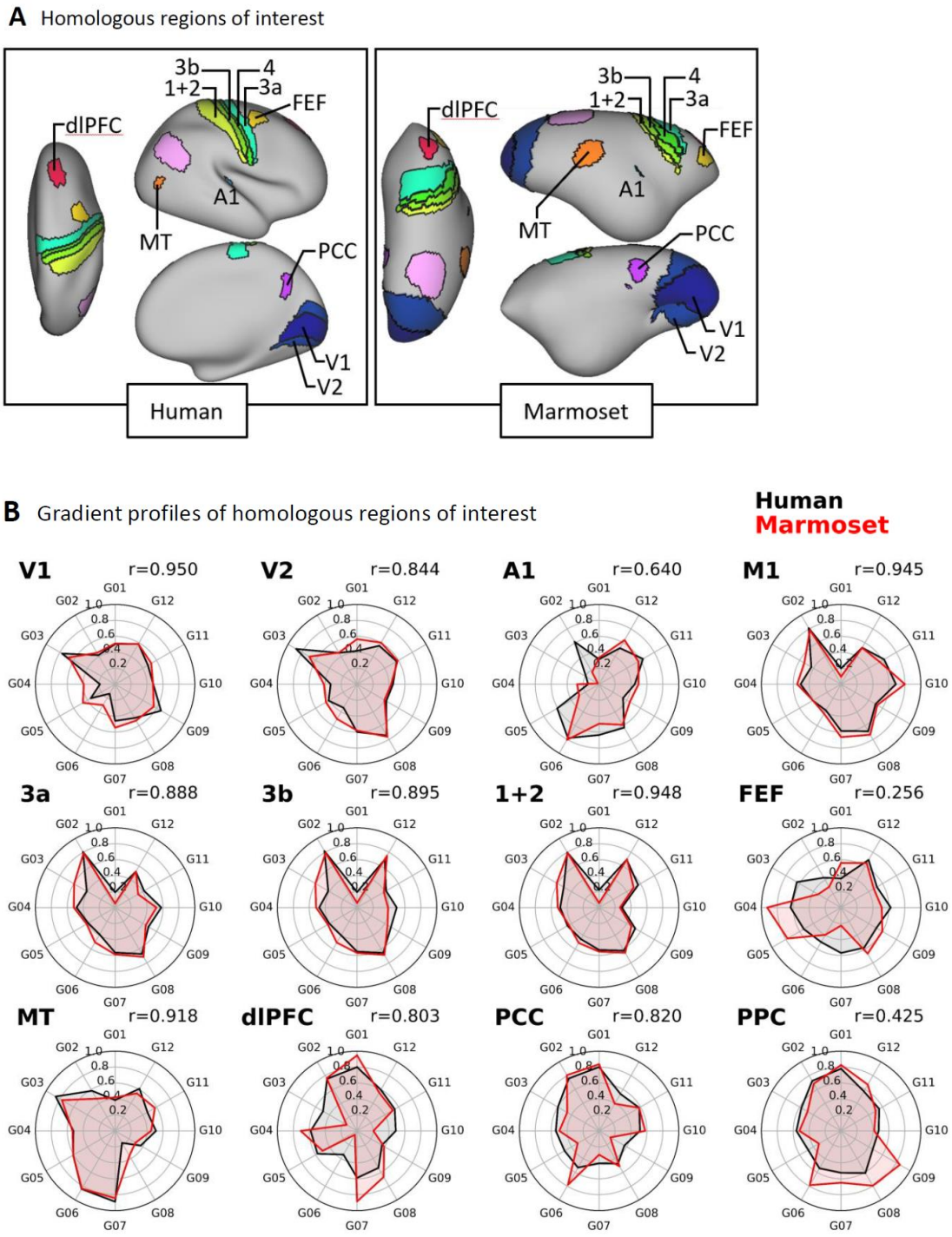


**Supplementary Figure 3.4 Gradient profiles of homologous regions of interests**

*(A) Homologous ROIs mapped onto the cortical surface of humans and marmosets. (B) Gradient profiles of mean gradient values extracted from the top 12 joint gradients in humans (black) and marmosets (red).*

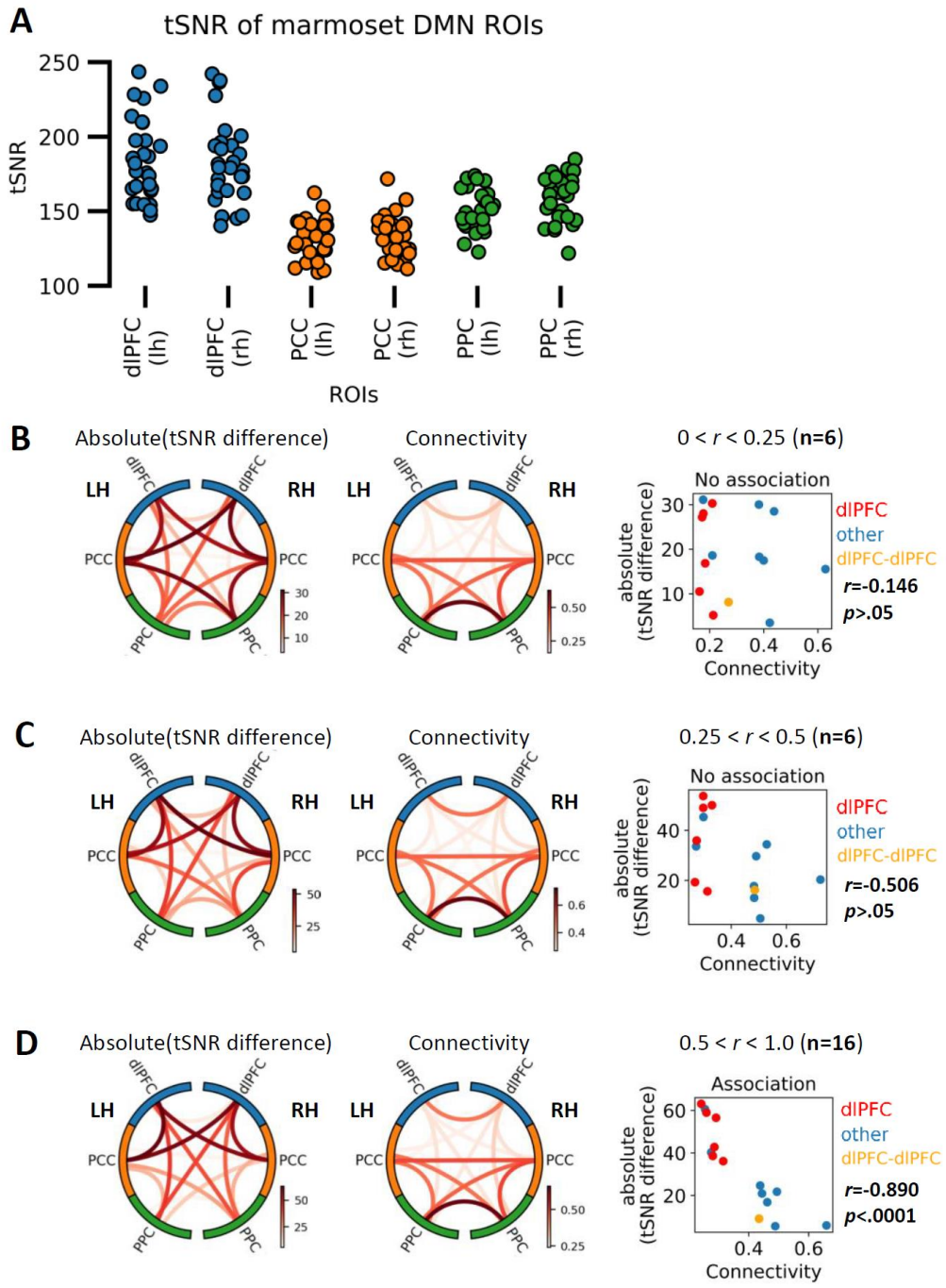


**Supplementary Figure 3.5 Association between tSNR and connectivity between DMN nodes of marmoset resting-state fMRI data**

*(A) Single-subject averaged tSNR across DMN nodes in marmosets (n = 31). Differences were observed across all pairs of DMN nodes (dlPFC–blue; PCC –orange; PPC –green). (B-D) Left and middle chord diagrams visualizes internode DMN tSNR differences and*

*functional connectivity in marmosets, respectively. Right scatter plot visualizes group level correlation between the absolute tSNR difference and the connectivity between all permuted pairs of DMN nodes (all dlPFC connections –red; dlPFC-dlPFC connection –orange; all other connections –blue), stratified into three groups based on single-subject magnitude of this correlation. Here, DMN internode functional connectivity are stable and reproducible (middle chord diagram across B-D), even in a subset of the population (B & C) where tSNR is not confounding the connectivity results (right scatter plot across B & C).*

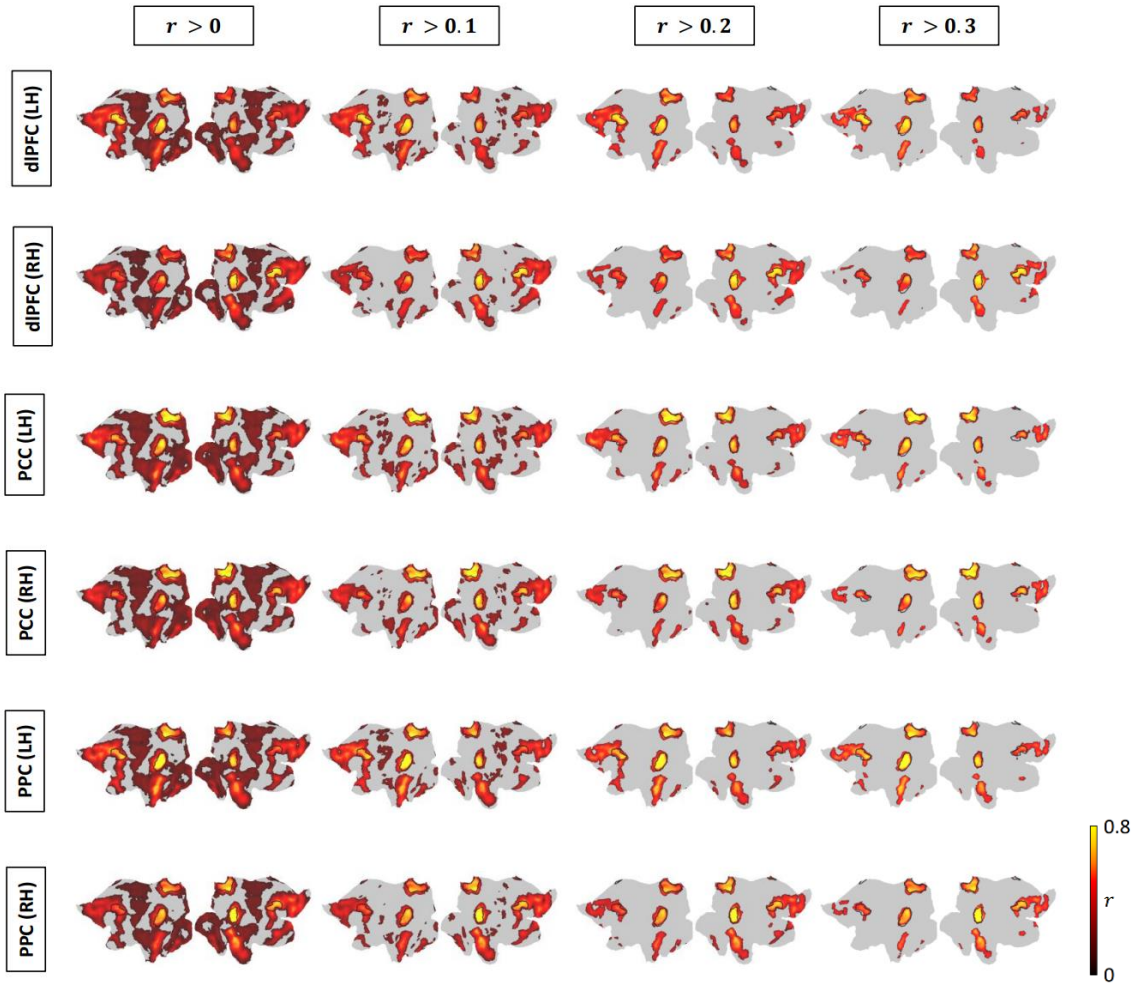


**Supplementary Figure 3.6 Connection topography of DMN nodes at varying connectivity strengths in humans**

*Areas of the human cortex significantly correlated with the corresponding cortical DMN node at varying degrees of connectivity strength (**r0** > 0, 0.1, 0.2, and 0.3 [*P* < .05; one-sample t-test permutation test]). Correlation maps were overlaid onto significant areas.*

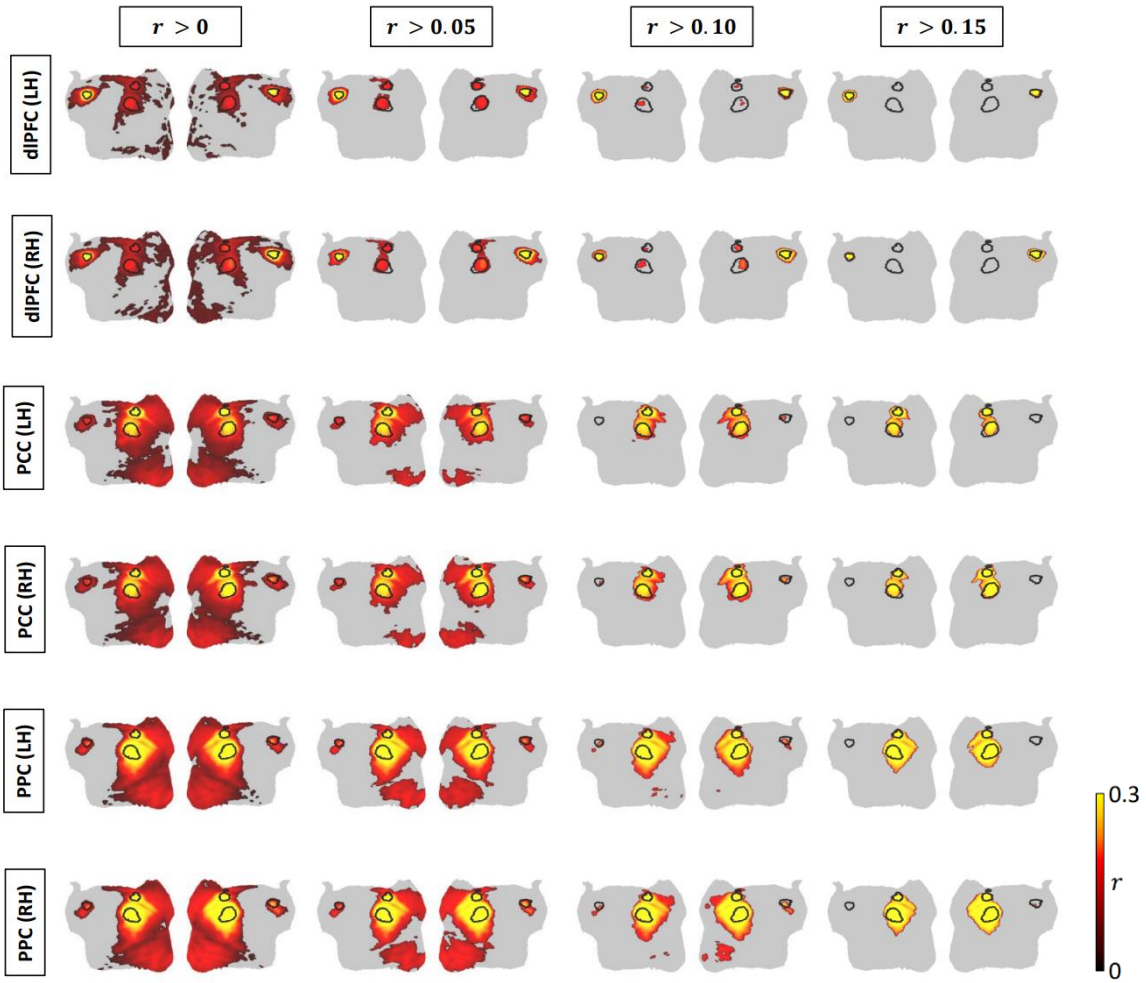


**Supplementary Figure 3.7 Connection topography of DMN nodes at varying connectivity strengths in marmosets**

*Areas of the marmoset cortex significantly correlated with the corresponding cortical DMN node at varying degrees of connectivity strength (**r 0** > 0, 0.05, 0.10, and 0.15 [*P <* .05; one-sample t -test permutation test]). Correlation maps were overlaid onto significant areas.*

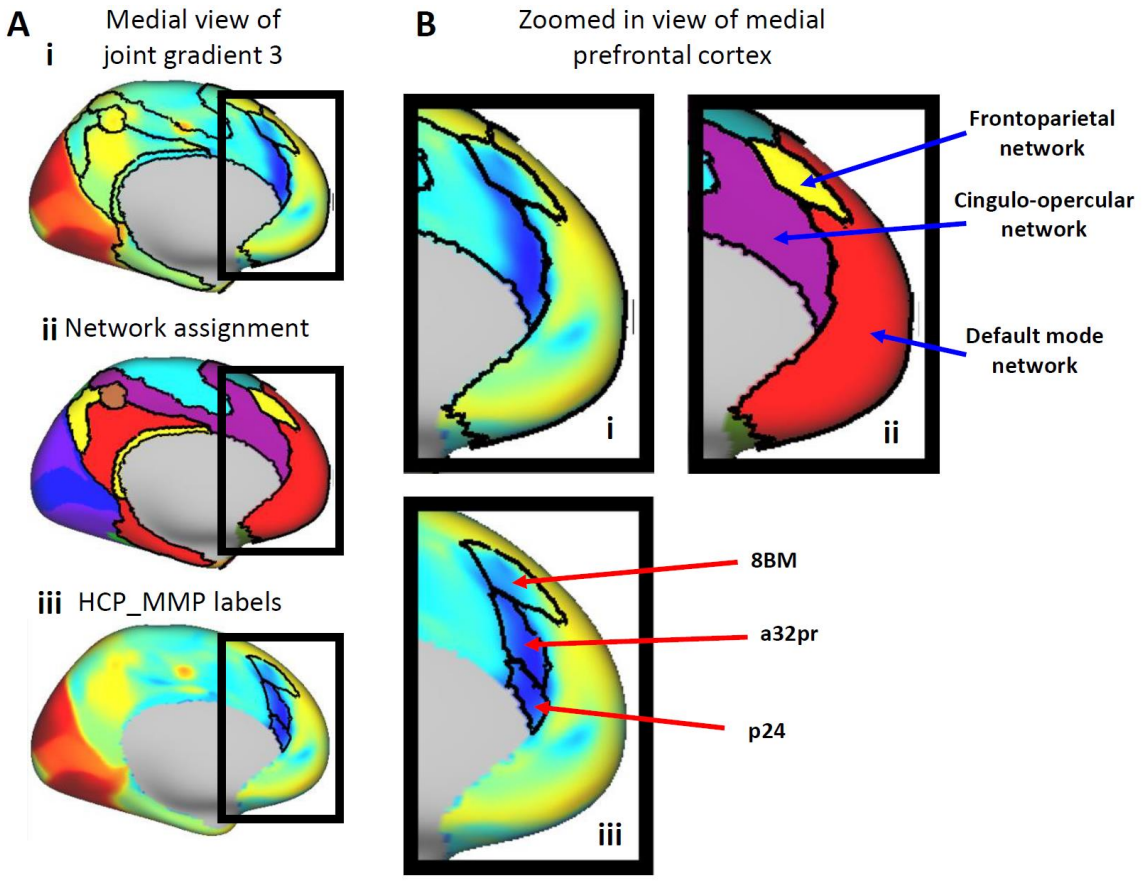


**Supplementary Figure 3.8 Detailed examination of the human mPFC component of joint gradient 3**

*Visualization of the (A) medial view of the left hemisphere and (B) magnified to only include the mPFC of interest and associated labels. To aid with visualization and interpretation: (i) shows joint gradient 3 with boundary lines corresponding to canonical RSN assignment, (ii) shows colour coded RSN network assignments, and (iii) shows multi-modal parcellation labels encasing the mPFC region of interest.*

# Chapter 4

# 4 Charting the effects of thalamic lesions on resting-state fMRI features in secondary-progressive Multiple Sclerosis

## 4.1 Introduction

The thalamus is a critical subcortical structure in cognition due to its ability to actively regulate information transmitted to the cortex (Sherman 2016; Halassa and Kastner, 2017). It is composed of clusters of functional nuclei, each of which is a unique relay center for specific sensory signals, sending the information to the appropriate cortical region for processing. Any subsequent damage to these nuclei can result in a wide range of dysfunctions, including deficits to sensory processing, attention, and memory (Saalmann and Kastner, 2011; Baxter 2013; Bradfield et al. 2013; Jankowski et al. 2013). Various pathophysiological processes of the thalamus have been detailed with in-vivo MRI, such as focal lesions (Harrison et al. 2015; Mehndiratta et al. 2021), iron accumulation (Al-Radaideh et al. 2013; Khalil et al. 2015), and of clinical relevance, thalamic atrophy occurring in the earliest stages of neurodegenerative diseases, such as Multiple Sclerosis (MS; Zivadinov et al. 2013; Azevedo et al. 2015). Given the central role of the thalamus in brain organization and MS disease trajectory, there is an important but largely unmet clinical need to investigate the utility of non-invasive measurements of thalamic neural activity and functional reorganization in single subjects. This would provide much needed insight towards disentangling the role of thalamic damage in the neural organization of MS patients.

Resting-state functional magnetic resonance imaging (rsfMRI) provides an indirect measure of neural activity by probing the blood oxygenation level-dependent (BOLD) signal over time (Ogawa et al. 1990). To date, most rsfMRI studies have focused on group-level investigations, specifically, by probing resting-state functional connectivity (RSFC) in stratified MS disease groups and their associations with clinical measurements (Jandric et al. 2021). Studies performed in this way provide only a general interpretation of functional reorganization during different stages of MS disease trajectory, overlooking the

profound heterogeneity of MS pathologies that exist across individuals (Roosendaal et al. 2010; Schoonheim et al. 2015). Importantly, these investigations do not draw inferences on direct pathophysiological impacts on brain architecture during disease. Given that neural disconnections induced by MS pathology are postulated to cause clinical deficits in patients (Dineen et al. 2009), it is reasonable to believe that focal damage to the thalamus may result in ensuing neural alterations at the stricken site, which in turn may be detectable using rsfMRI in single subjects. Furthermore, inconsistencies between MR-visible lesion burden and clinical outcomes in MS – referred to as the clinico-radiological paradox – urges the exploration of MR-indices of brain function, such as that provided by rsfMRI. In this regard, imaging the focal changes in brain function induced by thalamic lesions may prove a useful prognostic tool in MS, but has largely been under-investigated.

Resting-state BOLD signal can be used in two ways to infer brain function. First, the BOLD timeseries – a surrogate measure of neural activity – can be condensed into a plethora of summary metrics that characterize the rich temporal dynamics of BOLD across voxels of a region of interest (Fulcher and Jones, 2017; Lubba et al, 2019). Previous work has characterized such timeseries using intrinsic timescales – focusing on the autocorrelative properties of the timeseries – while demonstrating its relationship to micro- and macroscale architecture of the cerebral cortex (Murray et al. 2014; Watanabe et al. 2019). More generally, other timeseries properties that have been shown to be discriminative across canonical resting-state networks (Keitel and Gross, 2016), display close associations to structural and functional connectivity profiles (Shafiei et al. 2020), and are deemed relevant across neurological disorders, such as autism and Alzheimer's disease (Watanabe et al. 2019; Scarapicchia et al. 2018), and human behaviour (Waschke et al. 2021).

Second, rsfMRI can also be used to both infer connectivity between brain regions, and to probe widespread thalamocortical connections. However, the localization between thalamic voxels and cortical connections is not clearly defined, therefore adding complexity to connectivity analyses. Considerations of thalamocortical RSFC gradient estimation methods may address this problem. Connectivity gradients provide a systematic way to characterize how connectivity patterns vary over a brain area, permitting detection of boundaries or transitions in a region. Recently, Yang and colleagues examined gradients

associated with thalamocortical RSFC patterns to reveal two primary axes of RSFC variability along the 1) lateral-medial, and 2) anterior-posterior direction of the thalamus (Yang et al. 2020). The intuition follows that if lesions impact thalamocortical RSFC patterns, then gradient estimations would detect abrupt transitions adjacent-to, or focal-to areas of MS pathophysiology. In principle, detection of thalamocortical RSFC alterations in this way provides an accessible and practical approach for evaluating functional re-organization in single subjects. Many RSFC gradient investigations thus far have only looked at group stratification, and thus have not explored its use in single-subject cases to detect alterations due to pathophysiology.

In this pilot study, we examined a small longitudinal cohort of secondary progressive MS (SPMS) patients from an ongoing multimodal 7T MRI study. We comprehensively charted (i) intrinsic dynamics of the resting-state BOLD signal, and (ii) thalamocortical RSFC on the voxel-wise thalamus in single subjects to qualitatively assess the effects of focal thalamic lesions. Furthermore, we assessed the effects of MRI surrogate measures of microstructure to all rsfMRI features by broadening the scope of this investigation to include ROI-based analyses. The present study provides a preliminary assessment investigating the impacts of focal MS thalamic lesions on resting-state BOLD dynamics and functional organization on the scale of single subjects.

## 4.2 Methods

### 4.2.1 Participants

Seven secondary progressive MS participants (one male and 6 females; age range, 43-53 years) were included in this preliminary investigation, with data obtained from an ongoing longitudinal study. These individuals participated in several neuroimaging sessions, and a single cognitive assessment that took place at the time of their first neuroimaging session. The number of neuroimaging sessions considered in this analysis varies across individuals as some participants were recruited earlier on in this ongoing study, and therefore will have participated in more sessions. Additionally, other factors, such as MRI maintenance, or COVID-19 restrictions, have also led to neuroimaging session dropouts for some participants. Generally, neuroimaging sessions were scheduled every six months beginning

at the time of their first session, and included structural, rsfMRI, and diffusion MRI scans, acquired on a 7 Tesla MRI. Details of each subject's scanning itinerary considered in this investigation is shown in Table 4.1.

**Table 4.1 Scan session schedule of secondary-progressive MS patients**

| ID | Scan sessions (scan ID [days from first scan]) | | | | | |
|---|---|---|---|---|---|---|
| A | 1 [0] | 2 [188] | 3 [364] | 4 [728] | 5 [910] | 6 [1134] |
| B | 1 [0] | 2 [214] | 3 [368] | 4 [732] | 5 [904] | 6 [1127] |
| C | 1 [0] | 2 [208] | 3 [532] | 4 [741] | 5 [1075] | |
| D | 1 [0] | 2 [182] | 3 [728] | 4 [941] | 5 [1092] | |
| E | 1 [0] | 2 [172] | 3 [354] | 4 [536] | | |
| F | 1 [0] | 2 [182] | | | | |
| G | 1 [0] | 2 [195] | 3 [364] | | | |

### 4.2.2 MRI data acquisition

All MRI data were acquired from a 68-cm, 7T MRI outfitted with an AC84 Mark II head gradient coil. During this on-going study period, the 7T MRI scanner underwent an MRI upgrade from a Siemens Magnetom Step 2.3 (Erlangen, Germany) to a Siemens MRI Plus, and due to a lack of sequence availabilities, inconsistent structural images were acquired (see Table 4.1; shaded in orange are all the pre-upgrade MRI scans).

Structural images – In the pre-upgrade MRI, ME-MP2RAGE T1w images were collected at 750 μm isotropic resolution, $TE_1/TE_2$/TR=2.28/7.68/6000 ms, TI=800/2700 ms, BW=190Hz/Px, and FA=4°/5°. In the post-upgrade MRI, MP2RAGE T1w images were collected with 750 μm isotropic resolution, TE/TR=2.13/6000 ms, TI=800/2700 ms, BW=190Hz/Px, and FA=4°/5°.

rsfMRI images – Two rsfMRI runs were collected with a duration of 10-minutes each using a gradient-echo EPI sequence with 1.6 mm isotropic resolution, TE/TR = 22.2/1000 ms, BW = 1924 Hz/Px, FA = 45°, multiband factor 5, GRAPPA of 2, and acquired in opposite phase-encode directions (AP/PA).

Diffusion MRI images – Two diffusion runs were collected with 95-directions over 2 shells (b=1000 and 2000 s/mm$^2$) using a spin-echo EPI sequence with 1.6 mm isotropic resolution, TE/TR = 59/6700 ms, BW = 1602 Hz/Px, FA = 90°, multiband factor 2, GRAPPA of 3, and acquired in opposite phase-encode directions (AP/PA).

### 4.2.3 Resting-state fMRI preprocessing

Each subject's neuroimaging session consisted of two rsfMRI runs. Each run was preprocessed using fMRIPrep-20.1.3 pipeline (Esteban et al. 2019). In brief, a B0-nonuniformity map was estimated with SDCFlows and was used to create a displacement field map to correct for geometric distortions. This was followed by motion-correction using mcflirt (FSL; Jenkinson et al. 2012) and co-registration to the run's corresponding single-band reference image with six degrees of freedom. Subsequently, independent component analysis (ICA) was applied with FSL's melodic, decomposing each run into a set of components that was labelled as either signal or noise (Griffanti et al. 2014). Next, nuisance regression was performed using the ICA hand-labeled noise components, mean white-matter and cerebrospinal fluid time series, and 24 motion parameters (6 basic motion parameters + 6 temporal derivatives + 12 quadratic terms and their 6 temporal derivatives). Finally, the data was bandpass filtered (0.01-0.1 Hz), and spatially smoothed using susan (FSL; 1.6 and 3 mm).

### 4.2.4 Diffusion MRI preprocessing

Diffusion MRI data were preprocessed using prepdwi-0.0.13 pipeline (https://github.com/khanlab/prepdwi). In brief, the preprocessing included denoising, unringing, susceptibility distortion and eddy current correction, co-registration to the session's corresponding T1w image, and diffusion tensor fitting. Of the diffusion tensor fit parameters, only fractional anisotropy (FA), axial diffusivity (AD) and radial diffusivity (RD) were considered.

### 4.2.5 Registration workflow

A primary focus of this investigation was to assess the effects of thalamic lesions on rsfMRI BOLD dynamics and RSFC in single subjects. As such, it was important to perform all analyses in single subject space to minimize distortions from multiple spatial normalization steps. Note that additional distortion correction steps were taken for the resting-state fMRI scans to improve registration quality to the anatomical scan for all subjects.

For each subject, single subject T1w templates were constructed with antsMultivariateTemplateConstruction2.sh (ANTs; Avants et al. 2009) using all sessions' structural T1w images. Multimodal images (rsfMRI and diffusion) from each imaging session were all spatially registered to their corresponding subject specific T1w templates for analyses.

rsfMRI registration workflow – For all subjects, inconsistent spatial alignment between their two opposite phase-encoded rsfMRI runs and their corresponding T1w template were observed, likely due to the displacement field maps inability to fully correct for geometric distortions. To improve this alignment, an average rsfMRI template was created using the two opposite phase-encoded rsfMRI runs of each session (deformation was restricted along the phase-encode direction). Finally, the registration workflow for each subject's imaging session included registrations between (1) rsfMRI run and the average rsfMRI template, (2) average rsfMRI template and within session T1w image, and (3) within session T1w image and the subject's T1w template. All registrations were performed using antsRegistration (ANTs) with six degrees of freedom, and transformations were concatenated and applied in a single step to reduce blurring when applicable (antsApplyTransforms).

Diffusion registration workflow – The prepdwi workflow provided transformations between diffusion images and the within session T1w image. Additionally, the registration in the rsfMRI registration workflow between within session T1w image and the subject's T1w template could be concatenated to allow for spatial normalization of diffusion images to each subject's T1w template space.

Additionally, two analyses required registration to a group template. As such, an addition transformation was computed between each subject's T1w template and the MNINonLinear $6^{th}$ asymmetric T1w group-template (FSL) with antsRegistration (ANTS). When applicable, resampling between transformation spaces maintained a resolution of 1.6 mm to match the native resolution of the rsfMRI and diffusion images.

### 4.2.6 Region of interest definitions

All regions of interest (ROIs) were segmented with each subject's T1w template. Freesurfer v7.0.1 was used to provide segmentation of the thalamus and cortex. Each subjects' segmentations were assessed visually. Of note, some subjects, especially those with more lesion burden were more prone to segmentation errors. Segmentation errors were corrected manually. Thalamic lesions were segmented as hypointense voxels using each subject's T1w-template. Qualitative inspection of the T1w image across imaging sessions of each subject was performed to ensure that there were no obvious changes in MS pathology overtime and rationalizing the decision to average rsfMRI features across sessions in subsequent analyses (although single session rsfMRI features were also considered).

### 4.2.7 Intrinsic dynamics

We used the *catch22* timeseries analysis toolbox to characterize rsfMRI BOLD timeseries dynamics. This toolbox uses 22 time series feature that were carefully filtered from the *hctsa* feature library (consisting of >6000 features; Fulcher and Jones, 2017). The *catch22* time series features represent the diverse and interdisciplinary literature of timeseries analysis methods that have been developed to date, while simultaneously probing different types of interpretable time series features, including linear and non-linear autocorrelation, successive differences, value distributions and outliers, and fluctuation scaling properties (Lubba et al. 2019). These features have been categorized into seven labeled groups: (1) distribution, (2) simple temporal statistics, (3) linear autocorrelation, (4) non-linear autocorrelation, (5) successive differences, (6) fluctuation analysis, and (7) others (details of the *catch22* feature set and associated feature names are shown in Supplementary Table 4.1). All voxels' time series were demeaned prior to feature calculation as it was important to not have the mean rsfMRI image confound localization of thalamic lesions.

Additionally, the mean and standard deviation of the time series were also considered as features and are labelled as basic features. The standard deviation was divided by the mean image to scale the fluctuations across all scan sessions consistently. Additionally, due to the relevance of autocorrelation properties apparent in neural dynamic timeseries literature,

intrinsic timescale was also included, which is estimated by calculating the sum of autocorrelation function (ACF) values in the initial period where the ACF showed positive values. This feature is motivated by electrode spiking activity literature, and validation work supports its generalizability to rsfMRI (Murray et al. 2014; Watanabe et al. 2019). Intrinsic timescale was characterized as another measure of linear autocorrelation.

In summary, a total of 25 time series features were used to characterize resting-state BOLD dynamics. Voxel-wise features of the thalamus were computed across rsfMRI runs of all subjects' imaging sessions.

### 4.2.8 Thalamocortical connectivity analysis

Widespread anatomical connections between the thalamus and cortex exist. As such, careful steps must be taken to derive anatomically accurate measures of thalamocortical connectivity when using RSFC by (1) selecting cortical ROIs used for probing thalamocortical RSFC, and (2) localizing thalamic voxels associated to thalamocortical connections. To comprehensively characterize thalamocortical connections, two methods were used: (1) gradient estimation applied over whole cortex thalamocortical connections, and (2) thalamocortical RSFC using the seven canonical resting-state networks (RSN) as cortical seeds regions. The former option provides characterization of thalamocortical connections on the voxel-level, whereas the latter option characterizes RSFC on the ROI-level. All voxels' time series were Z-score normalized prior to calculating RSFC.

(1) Gradient estimation. This is a data-driven technique which can be used to spatially quantify thalamocortical RSFC patterns, by projecting this information onto the voxel-wise thalamus (see Haak et al. 2018 for more details). In brief, RSFC was calculated between each subjects' whole thalamus ($\boldsymbol{A_{t\times v}}$: $t$=time,$v$=number of voxels in the thalamus) and the rest of the cortex ($\boldsymbol{B_{t\times v'}}$: $v'$=number of cortical voxels). A RSFC matrix ($\boldsymbol{C_{v\times v'}}$) was computed which describes RSFC pattern of the whole thalamus, and sparsity was added, retaining only the top 10% of RSFC connections for each voxel. Next, similarity between inter-voxel RSFC patterns were computed resulting in a similarity matrix ($\boldsymbol{S_{v\times v}}$; similarity is computed using cosine similarity).

The Laplacian eigenmap algorithm is applied on the graph Laplacian of the similarity matrix to obtain a low dimensional representation of the RSFC data, referred to as gradients. The graph Laplacian is denoted as follows:

$$\boldsymbol{L} = \boldsymbol{D} - \boldsymbol{W},$$

where $\boldsymbol{W}$ is a graph representation of $\boldsymbol{S}$, $\boldsymbol{D}$ is the degree matrix defined as $\boldsymbol{D_{i,i}} = \sum_{\boldsymbol{i}} \boldsymbol{W_i}$, and $\boldsymbol{L}$ is the graph Laplacian. Solving the generalized eigenvalue problem $\boldsymbol{Ly} = \lambda \boldsymbol{Dy}$ yields $m$ eigenvectors $\{y_1, \ldots, y_m\}$ corresponding to the smallest $m$ non-zero eigenvalues $\{\lambda_1, \ldots, \lambda_m\}$. Here, we focus on $y_1$, defined as the region's dominant gradient and reflects the greatest changes in RSFC connectivity over a ROI, whereas higher order gradients, denoted by $\boldsymbol{y_n}$, $1 < n < m$, reflects more subtle changes in RSFC.

Only the top two gradients, denoted by G01 ($\boldsymbol{y_1}$), and G02 ($\boldsymbol{y_2}$) are retained for subsequent analyses, as they explained a total of 41% variance in the thalamocortical RSFC patterns (Yang et al. 2020). These gradient features are included in Supplementary Table 4.1 and labelled as RSFC gradients, providing a total of 27 voxel-wise features corresponding to resting-state BOLD features.

(2) Thalamocortical RSFC. Connectivity to the thalamus was computed using resting-state networks (RSNs) as ROIs. The seven RSNs – visual, somatomotor, dorsal attention, ventral attention, limbic, frontoparietal, and default – were defined using the *Schaeffer-100* ROI atlas (Schaeffer et al. 2018; in MNI152Nonlinear6Asym template space). Each RSN ROI was spatially normalized to each subject's T1w template space and was masked using a cortical grey matter mask (Freesurfer) to improve the ROI's cortical specificity. The mean rsfMRI time series was extracted using left and right hemisphere RSN as ROIs. Ipsilateral Pearson correlation coefficient maps to the voxel-wise thalamus were computed using the seven RSNs as cortical seeds. Here, only ipsilateral connections were considered, reflecting anatomical thalamocortical connections.

Note that we explored the use of partial correlations in this work (for example, Pearson correlation between a RSN and the thalamus while accounting for all other RSN time series as nuisance variables). However, partial correlation scores were not consistent across all

subject's sessions resulting in a lack of thalamocortical localization by nonparametric one-sample t-test.

### 4.2.9 Localizing thalamic masks connected to corresponding resting-state networks

In addition to investigating voxel-wise effects of MS lesions on resting-state BOLD dynamics and RSFC, we conducted subsequent ROI-based analyses assessing the relationship between resting-state BOLD features and MS pathophysiology. To do this, the thalamus was parcellated based on thalamocortical RSFC. Ipsilateral thalamic voxels associated to connections of each RSN were assessed using a nonparametric one-sample t-test that was applied over all subjects' RSFC maps (n=7; all subjects' thalamocortical RSFC connectivity maps were averaged across all sessions and runs, and spatially normalized to the MNI152Nonlinear6Asym template space). Significant voxels were considered as thalamic areas with connection to their associated RSN ($P < 0.01$, with threshold-free cluster enhancement). Sensitivity of connections between thalamic voxels and each RSN were further improved using left-right symmetrisation in two ways. First, for each RSN, the left hemisphere t-statistic map was reflected across the mid-sagittal plane, and the average t-statistic map was computed with the right hemisphere t-statistic map. After computing the average t-statistic map for all RSNs, a winner-take-all parcellation approach was applied, assigning each voxel of the right thalami to an RSN. This parcellation was subsequently projected back to the left hemisphere. Second, mask symmetrisation was applied to significant voxels denoting left hemisphere ipsilateral connections. Voxels constituting the intersection with right hemisphere ipsilateral connections yielded a right thalamus mask, which was merged with its reflection to yield the final left-right thalamic connectivity mask for each RSN. Finally, significance masks of each RSN were used to mask the parcellated thalamus obtained in the previous step. Here, in concordance with previous subcortical literature (Pauli et al. 2018), symmetrisation was performed as a useful step to improve signal-to-noise ratio (SNR) and was a sensible step to consider given that contralateral asymmetries are not as evident in the subcortex of healthy participants, as compared to the cortex (Guadalupe et al. 2017).

Thalamic masks denoting thalamocortical connections to each RSN were used as ROIs in subsequent analyses to further evaluate association between resting-state BOLD dynamics or thalamocortical RSFC and diffusion tensor features on the ROI-level.

### 4.2.10 Effects of MS lesions on thalamic resting-state maps

Two analyses were considered to assess the effects of thalamic lesions on resting-state BOLD dynamics and RSFC: (1) Voxel-wise, and (2) ROI-based.

**(1) Voxel-wise analyses.** Single-subject rsfMRI feature maps were visually inspected to assess whether obvious changes in underlying resting-state features were affected by the thalamic lesions. Additionally, single-subject resting-state feature maps were converted to voxel-wise Z score maps. Specifically, bootstrap sampling (n=100) was performed across all subject's scan sessions while controlling for subject id (for example, each subject was sampled the same number of times) and followed by resampling to each subject's T1w template space, resulting in voxel-wise distributions across all feature maps. Using these distributions, single-subject feature maps can be converted to Z score values, specifying the deviation voxel-wise features from the cohort distribution mean. In addition to visual inspections of these Z score maps; the mean thalamic lesion values were extracted across lesioned subjects with the hypothesis that lesioned voxels would have relatively high absolute Z score values. A high absolute Z score indicates that the lesioned areas expressed relatively different values compared to the other participants in this bootstrapped population, indicating that the lesion modulates the resting-state feature.

**(2) ROI-based analyses.** To improve sensitivity of the voxel-wise analysis, an ROI-based approach was also considered to boost sensitivity of the resting-state features. Thalamic masks were determined based on RSFC with the goal to delineate coarse thalamic parcels suggestive of known thalamic nuclei. These thalamic parcels were used as masks to extract average values from all resting-state features. In addition to the 27 feature maps that were examined in the voxel-wise analysis (see Supplementary Table 4.1), RSFC Pearson correlation

measurements between RSN and connected thalamic parcels were also considered.

To test for hypothesized relationships between thalamic MS pathology and resting-state features, the mean value was extracted from the diffusion tensor metrics (surrogate of underlying microstructure) and resting-state features, across all thalamic parcels, in the left and right hemisphere, and inputted into a linear regression model:

$$y_d = mx + \sum_{s \in \{session\}} b_s \delta_{d,s}$$

The model assumes that all scan sessions ($s$), have a linear dependence ($m$) between $y$ and $x$, allowing each scan session to have different constant terms ($b_s$). $\delta_{d,s}$ is a dummy variable, and is 1 if scan session $s$ matches $d$, and is 0 otherwise. The statistical significance of a regressor, and of interest here – $m$ – was assessed by a t-test. This regression analysis was applied to test dependencies between all combinations of (1) diffusion tensor features (fractional anisotropy, axial, and radial diffusivity), and (2) resting-state features (all BOLD dynamics and RSFC metrics, including Pearson correlation measures). Note that diffusion tensor features were used, instead of the T1w image because T1w-contrast is not quantitative and can lead to an ambiguous interpretation of regression results. Such problems of interpretation are further distorted by pre-and-post MR scanner upgrades.

## 4.3 Results

### 4.3.1 Charting individuals with thalamic lesions

Out of the seven SPMS subjects in this study, only four displayed MR-visible thalamic hypointense T1w lesions. For each subject, high contrast hypointense lesions were segmented. However, some subjects' lesion pathology appeared more diffuse with varying degrees of lesion contrast, making them more difficult to segment, and possibly leading to an underestimation of overall lesion volume. The total segmented thalamic lesion volume was 135.17, 466.94, 811.01, and 561.15 $mm^3$ for subjects C, D, E, and F, respectively (each subject's segmented lesion volume and demographics are available in Table 4.2). Across subjects, thalamic lesion distribution was heterogeneous with varying lesion sizes and

shapes (see Fig. 4.1a for axial and single slice view of T1w examples displaying thalamic pathophysiology of subjects C, D, E and F).

**Table 4.2 Secondary-progressive MS patient information**

| ID | Age (years at time of first scan session) | Gender | Handedness | Number of scan sessions | Thalamic lesion load ($mm^3$) |
|---|---|---|---|---|---|
| A | 50.28 | F | R | 6 | 0 |
| B | 45.31 | F | R | 6 | 0 |
| C | 46.4 | F | R | 5 | 135.17 |
| D | 43.87 | F | R | 5 | 466.94 |
| E | 53.27 | F | R | 4 | 811.01 |
| F | 53.41 | M | L | 2 | 561.15 |
| G | 53.03 | F | R | 3 | 0 |

In addition to visual inspection, quantitative summary metrics (mean and standard deviation [SD] across all thalamic voxels) of structural scans of the thalamus were computed for each subject's scan session, and included: intensity of the T1w image, and three diffusion tensor features (FA, AD, and RD). Diffusion tensor features were included as it offers sensitivity to myelination and axonal integrity which may be relevant to thalamic lesions in MS. Inspection of summary metrics showed generally stable mean diffusion tensor features across scan sessions within subjects, whereas mean intensity of T1w images appeared to be less stable (see Fig. 4.1b). Two scan sessions – second scan session of subject F and fourth scan session of subject A – displayed notably large changes in their diffusion tensor features that could be attributed to registration errors and motion corruption, respectively. DTI metrics corresponding to these two scan sessions were removed in subsequent analyses. Moreover, stable thalamic variability (i.e., standard deviation) was observed across all quantitative summary metrics – apart from the two outlier scan sessions – with lesioned subjects (C, D, E, and F) typically displaying higher variability compared to non-lesioned subjects (A, B, and G; see Fig 4.1b, bottom row).

To validate the utility of diffusion metrics for assessing thalamic lesion damage, diffusion metrics' sensitivity to thalamic lesion detection was explored by comparing the mean

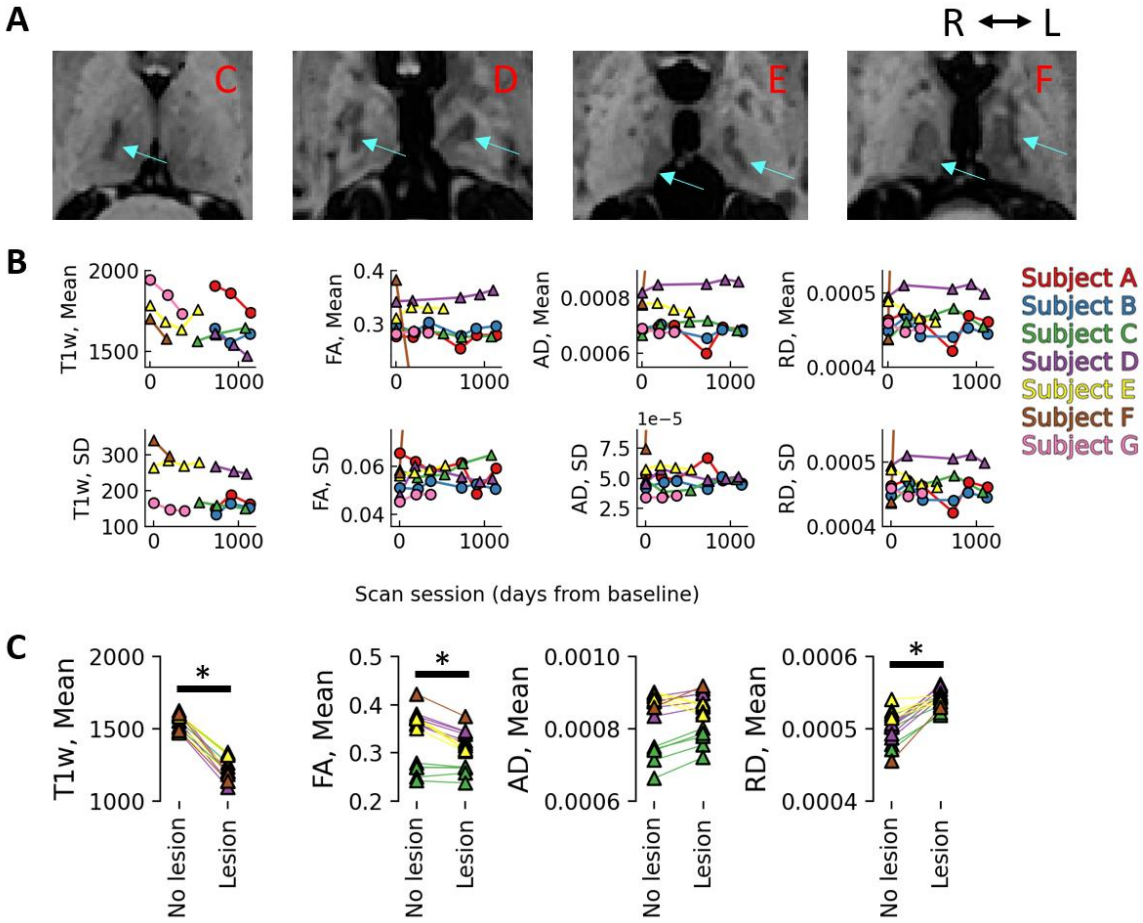


**Figure 4.1 Charting lesion metrics across SPMS patients**

*(A) Visualization of the T1w image showing thalamic lesions in SPMS patients. (B) Mean and standard deviation of the whole thalamus across various structural MR metrics: T1w intensity, fractional anisotropy (FA), axial diffusivity (AD), and radial diffusivity (RD). (C) Comparing mean value of lesions to its surroundings over various structural MR metrics. *P < .05*

metric intensity of lesioned and non-lesioned areas within a subject's thalamus. Significant differences were observed between areas across all subjects with thalamic lesions (Subjects C, D, E, and F), and is indicated by a decrease in FA, and an increase in AD and RD (see Fig. 4.1c; $P < 0.05$, nonparametric Wilcoxon signed-rank test). This analysis was repeated using a dilated lesion mask, instead of the whole thalamus, to investigate more local effects of lesion and non-lesion contrast while mitigating partial volume

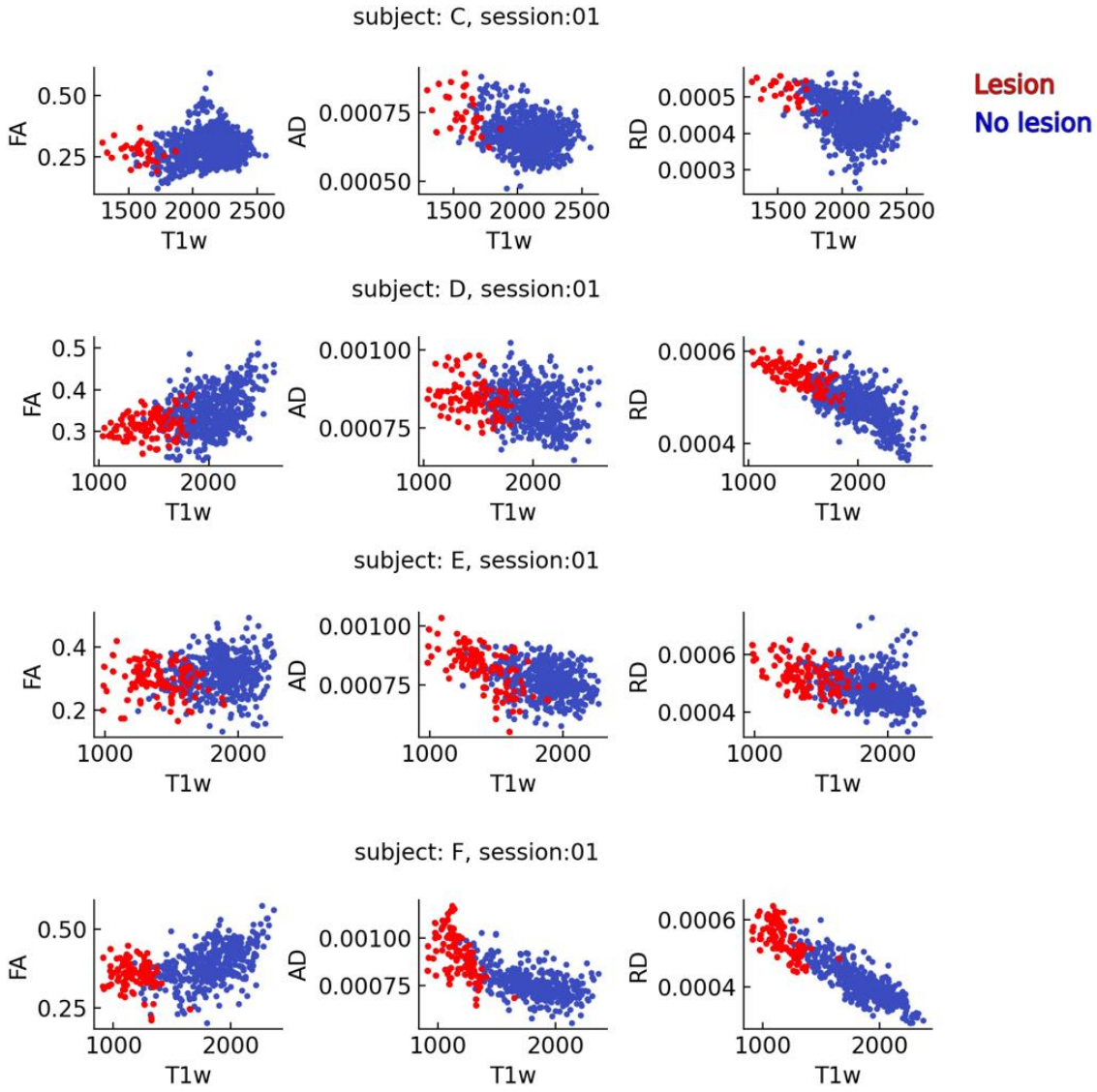


**Figure 4.2 Voxel-wise association between diffusion tensor metrics and T1w intensity**

*Voxel-wise associations were observed between all diffusion tensor metrics (FA, AD, and RD) and T1w intensity across all subjects and scan sessions. Note that only scan session one for subjects with lesions are shown here. *P < .05*

effects when investigating the whole thalamus; apart from AD ($P$ = 0.33), all results remained consistent. Additionally, voxel-wise associations between DTI metrics and T1w intensities were observed across lesioned subjects ($P$ < 0.05; spatial correlation, see Fig. 4.2).

Although contrast of lesions and non-lesion voxels are qualitatively most evident in the T1w images, DTI metrics were considered in all subsequent ROI-based analyses as they are quantitative and more interpretable when conducting regression analyses.

### 4.3.2 Alignment between resting-state fMRI and T1w images

To assess the impacts of thalamic lesions on resting-state BOLD dynamics and RSFC gradients, voxel-wise features were generated in each subject's scan session. More specifically, an average value was calculated between rsfMRI runs (n=2; 10-minute in length), for all 27 features denoted in Supplementary Table 4.1. A goal of this work was to localize changes in resting-state features at lesioned sites to infer changes in neural dynamics. Accurate spatial normalization between T1w and rsfMRI images were qualitatively assessed by comparing the T1w template to the mean T2*-weighted rsfMRI image to ensure lesion locations were consistent. T2*-weighted lesions appear as hyperintensities due to demyelination (Duyn et al. 2008), and consistently co-localized with T1w hypointense lesions (Fig. 4.3 shows lesion alignment for Subjects C, D, and E). Although only subject averaged data is shown in Figure 4.3, T2*-weighted images across sessions were spatially consistent with one another ($r$=.928±.036).

The T2*-weighted rsfMRI image also detailed hypointense voxels on the medial sides of the thalamus (see Fig. 4.3, Subject C, Z=-16 for an example), and was consistently observed across all SPMS subjects. This may be due to venules, or intra-thalamic draining veins of the thalamus, and in some cases, can be observed passing through thalamic lesions (see Fig. 4.3; Subject D, left thalamus, Z=-13; right thalamus, Z=-16). Veins running through lesions are clinical signs of MS lesions – referred to as the central vein sign – which appears hypointense due to increased levels of deoxyhemoglobin in veins (Reichenbach et al. 1997; Sati et al. 2016). A consequence of relatively larger veins, as in the case of intra-thalamic draining veins, is increased temporal variability of BOLD, which consistently coincided with T2*-weighted hypointense voxels across all subjects (Fig. 4.3, bottom row shows standard deviation of rsfMRI images). Together, this demonstrates that the acquired resting-state fMRI scans appear to delineate structural features of the lesioned thalamus and suggests that alignment between rsfMRI scans and the T1w images are

adequate. Subsequent investigations in this work aimed to investigate whether resting-state BOLD features are affected by lesions.

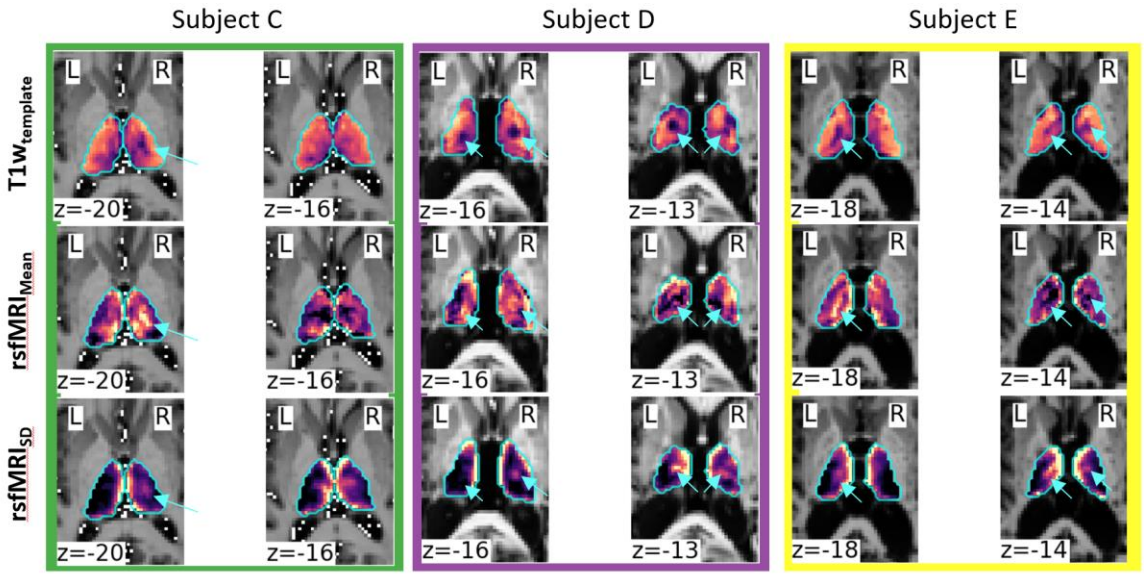


**Figure 4.3 Visualizing the thalamus of subjects with lesions with T1w and rsfMRI images**

*Visualization of the thalamus in three subjects who displayed lesions are shown. Top row shows a T1w template generated using all T1w images from each subject's scan sessions, middle row is the mean rsfMRI (T2*-weighted) image averaged over each subject's runs, and bottom row is the standard deviation rsfMRI image averaged over each subject's runs. Teal arrows shows hypointense lesions as visualized by the T1w template of each subject. All images are normalized between 0 and 1.*

### 4.3.3 Spatial topography of resting-state fMRI features in SPMS participants

Resting-state features of the thalamus were computed with 1.6 mm smoothed rsfMRI data to qualitatively assess whether effects due to thalamic lesions can be observed (see Supplementary Table 4.1 for details of all features). A total of 27 spatial maps corresponding to resting-state BOLD dynamics (25 features) and RSFC (2 features) of

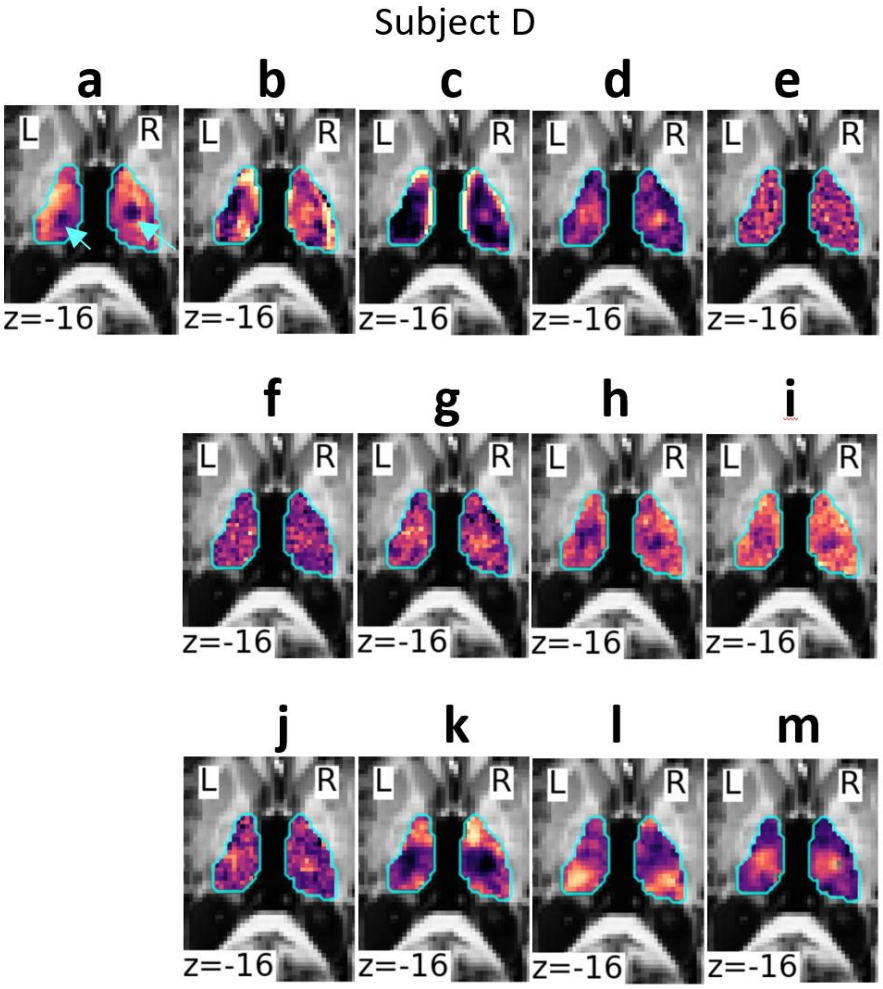


**Figure 4.4 Visualizing resting-state features of subject D**

*Visualization of resting-state features of subject D showing a slice with two thalamic lesions. All resting-state features are averaged across all rsfMRI runs of subject D (5 scan sessions/10 rsfMRI runs). 9 out of 25 randomly selected resting-state BOLD dynamic features are shown (b-j), 2 RSFC gradient features are shown (k/l), and a connectivity map using the salience ventral attention network as a cortical seed region is shown (m). (a) T1w template, teal arrows show the hypointense thalamic lesions in contralateral hemispheres. (b) Mean. (c) SD. (d) IntrinsicTimescale. (e) DN_HistogramMode_5. (f) SB_BinaryStats_mean_longstretch1. (g) CO_f1ecac. (h) SP_Summaries_welch_rect_centroid. (i) SB_MotifThree_squantile_hh. (j) SC_FluctAnal_2_rsrangefit_50_1_logi_prop_r1. (k) G01. (l) G02. (m) Salience ventral attention connectivity map. All images are normalized between 0 and 1.*

the thalamus was averaged across each subject's scan sessions and considered individually. The intuition is if lesions perturb neural activity, then this may manifest in changes to voxel-level BOLD dynamics or thalamocortical RSFC, and thus can be qualitatively assessed in single subject feature maps.

All subject's rsfMRI feature maps were qualitatively assessed to determine if evidence of abrupt changes at lesion and non-lesion interfaces were observed. Figure 4.4b-j shows 9 randomly selected BOLD dynamic feature maps of Subject D (averaged across 10 rsfMRI runs, over 5 scan sessions), with no obvious effects caused by the MS lesion pathology, except for in the mean T2*-weighted rsfMRI image (Fig. 4b). Although standard deviation and intrinsic time scale (Fig. 4.4c/d) appears to delineate the lesion in the right hemisphere, generalization to other lesions both within the same subject and across subjects was not observed.

Furthermore, Figure 4.4k-m shows 3 RSFC-based feature maps. Figure 4.4k/l corresponds to thalamocortical RSFC gradients whereby changes in voxel's value are modulated by similarity between connectivity patterns. For example, if lesions impacted RSFC, then it follows that changes in the ensuing gradients, demarcated by lesioned voxels will be evident, however this was not the case (Fig. 4.4k/l). To simplify matters further, we also inspected RSFC maps generated using RSNs as cortical seed regions and observed no qualitative effects by the focal lesion. For example, Figure 4.4m shows an example connectivity map of the thalamus corresponding to the salience ventral attention network which showed peak connectivity to Subject's D right hemisphere lesion. In this example, no changes were apparent at or adjacent to lesioned voxels and connectivity patterns appeared symmetric between hemispheres, suggesting that lesions do not impart any qualitative effects on RSFC.

To quantitatively assess the impact of lesions, each lesioned subject's rsfMRI feature maps were converted to Z score maps based on bootstrapped distributions generated from all SPMS subjects in this cohort. This provides a quantitative metric to determine the extent to which rsfMRI features deviated from expected population mean on a voxel level. The Z score values were extracted from lesion voxels across each of the four

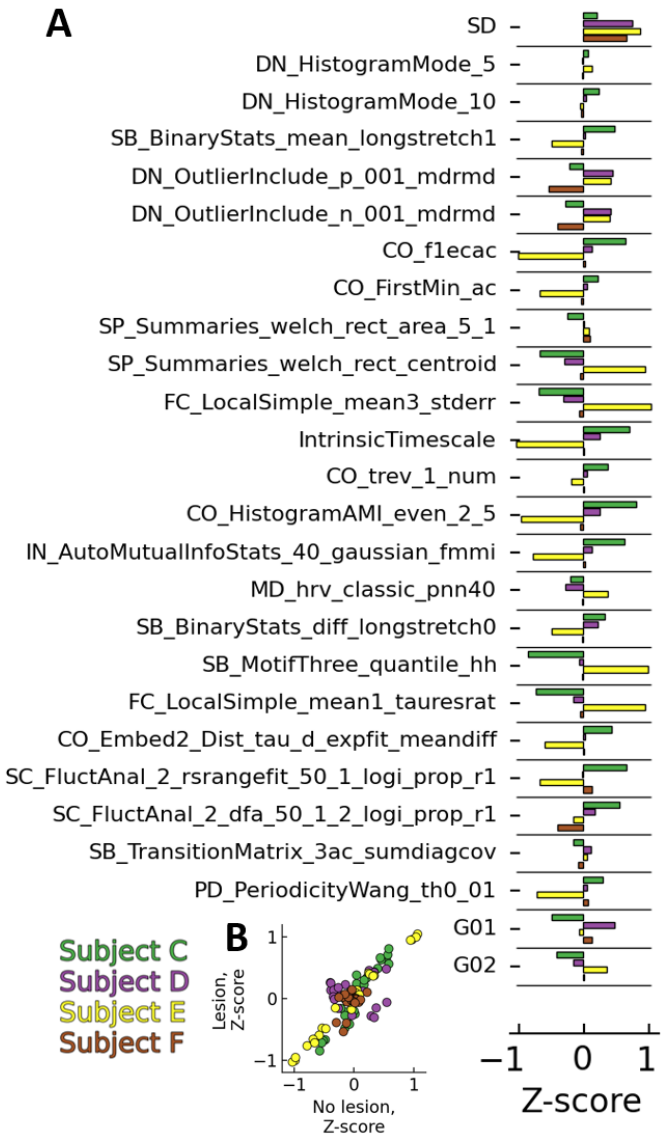


**Figure 4.5 Thalamic lesion Z scores across 26 resting-state features in subjects with lesions**

*(A) Bar plot of average Z-score quantifying how each feature averaged over each individuals' lesions deviate from a bootstrapped sampled population (n=100). The bootstrapped sampled population corresponds to all SPMS subjects in this cohort (subject A-G). A higher absolute Z-score suggests that the lesion is modulating the associated resting-state feature and is shown for each subject. (B) Positive association between Z-score of lesion and non-lesion areas across all resting-state features. *P < .05*

participants and across all rsfMRI features maps (rsfMRI mean was excluded due to inconsistencies in scaling of pre- and post MR upgrade images). Figure 4.5a shows mean Z score values of lesions across all lesioned subjects and rsfMRI features. No consensus polarity in lesion Z scores was observed across all subjects, suggesting that lesions do not have a consistent effect on BOLD dynamics or RSFC gradients. Furthermore, a strong association between the mean Z score of lesions and non-lesions was observed, suggesting that Z scores are not driven by lesions ($*P < 0.05$; Pearson correlation, see Fig. 4.5b).

### 4.3.4 Association between diffusion tensor metrics and thalamocortical functional connectivity

Consideration of thalamocortical connectivity in the previous section was assessed using RSFC gradients – describing smooth transitions of thalamocortical RSFC patterns along the voxel-wise thalamus – which did not appear to demarcate lesions. However, it is possible that thalamic lesions only lead to marginal changes in thalamocortical RSFC and do not impart detectable changes in RSFC gradients. To account for this possibility, the next aim was to assess the effect of lesions on thalamocortical RSFC.

In this section, thalamic localization was not feasible with 1.6 mm smoothed data, as such we used 3 mm smoothed data in analyses of this section. First, spatial maps showing voxels of thalamocortical connectivity between ipsilateral thalamus and the cortex were considered. The cortex was partitioned into the seven cortical RSNs, which were subsequently used as seed regions to probe connectivity to the thalamus (for example, visual, somatomotor, dorsal attention, ventral attention, limbic, frontoparietal control, and default mode networks). Figure 4.6a shows each cortical component, and its significant areas of connectivity to the thalamus ($*P<0.05$; nonparametric one-sample t-test, refer to methods for filtering details of the thalamic ROIs). Thalamocortical connections were not detected to the limbic and frontoparietal control network. Lack of limbic connections may be due to lowered temporal signal-to-noise ratio (tSNR) in cortical limbic areas due to susceptibility-induced signal dropout in these areas. More generally, improved sensitivity for localizing thalamic connections can be achieved with an increased sample size, which may explain for the lack of observed thalamus-to-frontoparietal connections.

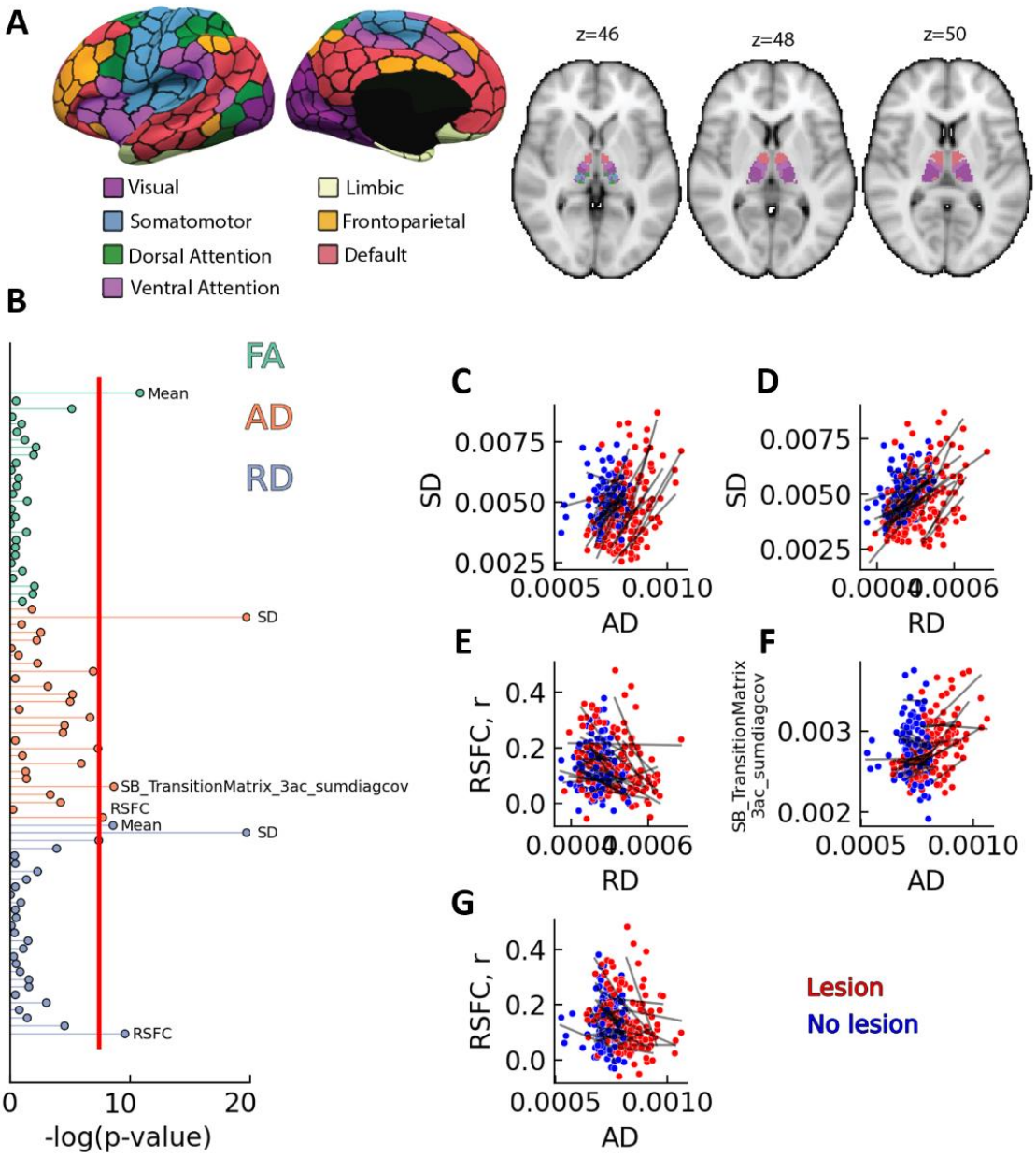


**Figure 4.6 Within scan session associations between resting-state features and diffusion tensor features**

*(A) Localization of thalamic parcels using thalamocortical resting-state functional connectivity of five resting-state network seeds overlaid (*P* $< .05$*). (B) Manhattan plot assessing within scan session associations between resting-state and diffusion tensor features using 10 thalamic parcels as regions of interests (five for each hemisphere). This plot does not include resting-state network, and brain hemisphere as covariates. (Red*

*line denotes *$P < .05$; corrected for multiple comparisons). (C-G) Associations between five resting-state features and corresponding diffusion tensor features. Each black line corresponds to a linear regression for a single scan session derived using mean feature values extracted from the 10 thalamic parcels.*

Nevertheless, thalamic localization of the other five RSNs appear in agreement with previous works (Yang et al. 2020). For example, default-mode, ventral attention, and dorsal attention were mapped onto the thalamus sequentially from anterior-to-posterior, and somatomotor connections were localized to the ventral-posterior-lateral thalamus. In contrast, the visual network was expected to show connections to the lateral geniculate nucleus, located in the lateral-posterior of the thalamus, however, disproportionate and diffuse connections were observed in the posterior of the thalamus.

Next, the thalamus and cortical RSN ROI pairs were used to assess the effects of MS pathophysiology on thalamocortical RSFC. Specifically, a linear regression model was used to test the hypothesized relationship between measures of thalamic DTI metrics (i.e., FA, AD, and RD), and the strength of thalamocortical connectivity (averaged across two rfMRI scans) while controlling for each subject's scan session. Significant negative associations between thalamocortical connectivity and AD ($P$ < 0.05; $B = [-2.30 \times 10^{-4}, -6.61 \times 10^{-5}]$; see Fig. 4.6c), and RD ($P$ < 0.05; $B = [-1.90 \times 10^{-4}, -6.57 \times 10^{-5}]$; see Fig. 4.6e) was observed, whereas no associations were observed with FA ($P$ = 0.360). To account for the possibility that this result is confounded by RSNs, the linear regression models were re-assessed incorporating the RSNs as covariates. This led to a modest negative effect, although not significant between thalamocortical connectivity and AD ($P_{\text{uncorrected}}$ = 0.016), and no associations were observed with FA ($P$ = 0.150), and RD ($P$ = 0.263).

### 4.3.5 Association between diffusion tensor metrics and resting-state fMRI metrics

Linear regression analyses were also extended to investigate the relationships between thalamic DTI metrics and all other resting-state features using these thalamic ROIs. Figure 4.6b shows a Manhattan plot summarizing all significant associations between all

combinations of DTI metrics and resting-state fMRI metrics. The mean of the rsfMRI scans were negatively and positively associated with FA and RD, respectively. The standard deviation demonstrated the largest effect size, with a positive association observed with AD and RD. Additionally, a positive association was also observed between AD and SB_TransitionMatrix_3ac_sumdiagcov (a measure of time series variability using motifs) ($P < 0.05$; see Fig. 4.6c-g for plots demonstrating associations across all scan sessions). With the addition of RSNs as a covariate, significant positive associations were only retained between standard deviation and AD, and RD ($P < 0.05$).

## 4.4 Discussion

The present study provides a preliminary assessment of the impacts of thalamic lesions on resting-state BOLD dynamics and thalamocortical RSFC. To date, and to our knowledge, there have been no studies investigating the role of MS thalamic pathophysiology in resting-state fMRI measurements in single subjects. Given the heterogeneous nature of MS lesion burden across subjects, investigating the effect of focal MS lesions to neural organization is an important goal, and yet remains ambiguous. Here, 7T MR imaging was leveraged for improved signal-to-noise ratio allowing for improved lesion detection and improved BOLD sensitivity.

### 4.4.1 Assessing diffusion tensor metrics of thalamic lesions

The following DTI metrics were used to assess their sensitivity to thalamic lesions: FA, AD and RD. Here, when comparing the effects of thalamic lesions to their surroundings, we observed significant decreases in FA and increases in RD, as well as a non-significant trend of increases in AD. These findings are somewhat consistent with other investigations that have primarily looked at white matter pathology in both humans and animal models of MS, as well as other neurodegenerative disorders. Across these studies it is suggested that decreases in FA and increases in RD likely reflect demyelination (Schmierer et al. 2007; Klawiter et al. 2011; Chang et al. 2017), whereas reduced AD is believed to correspond to axonal injury (Budde et al. 2009). The latter finding of reduced AD in mouse models of MS does contradict our findings in the current work of increased AD, albeit

Budde at colleagues (2009) were investigating spinal cord lesions as opposed to thalamic lesions here.

Another possibility is that increases in AD and RD, combined with reductions in FA suggests an overall increase in diffusion, and may be explained by cellular infiltration and changes in extracellular water caused by inflammation that corresponds to collective axon and myelin damage (Aung et al. 2013). However, these interpretations are complicated by challenges with modelling water diffusion in the thalamus, which is comprised of a complex mixture of both white and gray matter (Jelescu et al. 2020). Firstly, diffusion of non-myelinated neurites, which are commonly found in subcortical gray matter, is confounded by non-negligible diffusion between neurites (Jelescu and Novikov, 2020). Secondly, the directionality of neurites in the thalamus may be randomly oriented, further complicating diffusion tensor modeling in this region. Collectively, due to the ambiguity of what microstructure features modulate diffusion in the thalamus, it remains difficult to interpret whether changes in DTI metrics are modeling axon integrity or demyelination. For example, although only increases in RD have been previously associated with demyelination (Klawiter et al. 2011), the presence of demyelination within the thalamus – where axon direction is largely incoherent and randomly-oriented – could result in increases in both RD and AD. Nevertheless, given that DTI metrics appear to be modulated by thalamic lesion pathology, albeit with reduced effect sizes compared to T1w contrasts (see Fig. 4.2), we suggest that these directional trends are associated with demyelination, primarily due to increases in RD, and collectively supports its use as a quantitative metric for lesion pathophysiology in subsequent regression analyses.

### 4.4.2 Resting-state BOLD variability in MS lesions

Across all 25 time series features used to describe resting-state BOLD dynamics, only the mean and standard deviation appeared to reflect the effects of the focal thalamic lesions. The mean rsfMRI image is perhaps unsurprising as this feature corresponds to a low resolution, 1.6 mm T2*-weighted image, and is a common MR contrast used to identify cortical and thalamic MS lesions (Maranzano et al. 2019; Mehndiratta et al. 2021). Interestingly, the variability of the resting-state time series, as measured by standard deviation, in some cases expressed high variability at the site of the thalamic lesion. This

can be explained by the presence of central venules that commonly coincide within MS lesions (Kilsdonk et al. 2014), and specifically have been found in 78% of thalamic lesions (Mehndiratta et al.). Here, larger veins have relatively higher blood flow, which directly leads to an increase in the modulation of BOLD, as reflected by increases in BOLD variability. This effect is clearly discernable in the case of relatively large intra-thalamic draining veins that were detailed to pass through a thalamic lesion in the left hemisphere of Subject D, and may explain for the large increase in BOLD variation (see Figure 4.3; Subject D; Z = -13; bottom row). A more subtle example can be seen in the case of Subject D's right thalamic lesion, which shows a decrease in T2*-weighted intensity and an increase in BOLD variability in the middle of the lesion, suggestive of the presumed effect of a smaller venule (see Figure 4.3; Subject D; Z=-16; middle row shows the mean T2*-weighted image; bottom row shows BOLD variability). Although not all lesions displayed central venules, it is possible that the low resolution afforded by the rsfMRI image is not sufficient to detect them in all thalamic lesions. It is likely that BOLD variability may still be modulated by these veins even when they are not visible in the mean T2*-weighted image.

In ROI-based analyses, BOLD variability (i.e., standard deviation) was the only feature that was positively associated with axial and radial diffusivity, after correcting for multiple comparisons and controlling for the effects of RSN-localized thalamic areas. Given that increases in AD and RD correspond to lesions, positive associations observed here are consistent with the presence of central venules as discussed in the prior section, which may contribute, in part, to the observed effects.

Another source that may complicate the interpretation of BOLD variability is due to vasculature effects that have been widely documented in MS lesions. For example, several studies have shown reduced perfusion in MS lesions (Ge et al. 2005; Holland et al. 2012; Francis et al. 2013), with as much as a 25% reduction in cerebral blood flow (CBF; Sowa et al. 2015). More generally, others have reported reduced vascular reactivity (Marshall et al. 2014), and reduced oxygen metabolism of the MS brain (Ge et al. 2012). Collectively, these vascular impairments would suggest reduced efficacy of neurovascular coupling, subsequently leading to *reduced* BOLD variability. However, the opposite effect was

observed in the current work, where *increased* BOLD variability was noted, suggesting that changes in BOLD variability may not be due to vascular changes of MS, and may suggest a neural effect (i.e., increases in neural activity) instead.

It has been suggested that variability of neural activity supports human behaviour in adapting to internal and external demands (Waschke et al. 2021). As such, studies have shown that younger and better performing adults expressed higher BOLD variability in a set of cortical regions (Garrett et al. 2010; McIntosh et al. 2010; Guitart-Masip et al. 2016). Interestingly, BOLD variability measurements have been shown to be robust, even after considering vascular controls in a healthy population (Garrett et al. 2017). In fact, previous studies have investigated BOLD variability in various diseases (Nomi et al. 2018; Zhu et al. 2019), including MS (Petracca et al. 2017). Petracca and colleagues found a positive association between BOLD variability and cortical lesion volume in some cortical areas, consistent with our observations in the thalamus. In this regard, it was suggested that an increase in BOLD variability may be due to a failed attempt to compensate for pathological damage by cortical lesions (Petracca et al. 2017). Although it appears BOLD variability may provide a candidate assay of neural activity, more rigorous investigations into confounding factors of central venule sizes, and aspects of neurovascular coupling underlying BOLD measurements must be considered.

### 4.4.3 Thalamic lesions do not affect thalamocortical connectivity

To date, many research groups have documented changes in resting-state functional connectivity across different phenotypes of MS, and have further demonstrated that these changes correspond to clinical and cognitive outcomes of patients (Rocca et al. 2010; Bonavita et al. 2011; Hawellak et al. 2011; Loupre et al. 2014; Schoonheim et al. 2014). Although not explicitly investigated, it is generally understood that MS pathology directly modulates RSFC changes observed in these studies. Interestingly, in this work we assessed the effects of focal thalamic lesions on RSFC, and did not find any evidence of thalamocortical RSFC changes at the single subject level. Unlike other studies, we focused on brain mapping of single subjects, and lesion effects on RSFC were defined as being changes that were qualitatively visible in lesioned voxels. In doing so, we mapped connectivity changes that were assessed using two methods: (1) estimated thalamocortical

RSFC gradients, and (2) computing thalamic connectivity maps using seven RSNs as cortical seed regions. Thalamocortical RSFC gradients and connectivity maps were subsequently used to determine whether qualitative evidence of lesion demarcation could be observed (see Fig. 4.4k-m for examples of RSFC maps of the thalamus in a subject who has a thalamic lesion that is shown in Fig. 4.4a). Although Figure 4.4 only shows subject averaged maps across all Subject D's scan sessions, we qualitatively inspected all connectivity maps across all lesioned subjects' rsfMRI runs (4 subjects and 32 rsfMRI runs; under 1.6 mm and 3 mm smoothing) to account for potential confounding effects of motion, scanner quality, and biological pathophysiological changes that may have theoretically reduced our ability to identify such focal lesion effects. In considering each subject's thalamic connectivity maps, we found no evidence of connectivity changes induced by thalamic lesions. It is possible that any effects of lesions on RSFC may be diffuse and impact the whole thalamus, rather than be focal to the lesion itself. As such, clear demarcations of lesioned voxels with their surroundings would not be observed in ensuing connectivity maps. However, such investigations require case-controlled experiments and was beyond the scope of this investigation.

Furthermore, this investigation took a thalamus-centric view towards understanding how thalamic lesions alone may affect only thalamocortical RSFC, effectively ignoring other pathophysiology that is evidently widespread in the SPMS brain. Prior to conducting these analyses, we reasoned that a focal lesion, especially at the site of neural activity, in this case the thalamus, would impart the largest detectable changes to thalamocortical RSFC, compared to pathology at distant brain areas. However, it is possible that a lack of detectable RSFC changes may be related to whether thalamic lesions correspond to axonal damage or demyelination. In the latter case, it may be possible that demyelination in the thalamus – already relatively low in myelin content compared to white matter – does not translate to changes in RSFC, whereas demyelination to white matter may play a larger role in this regard. This is predicated on the fact that myelination is fundamental for fast neural connections between distance brain regions, and therefore demyelination of thalamocortical white matter connections may be the primary modulator of RSFC changes. Conversely, it is not known whether MR visible thalamic lesion pathology corresponds to axonal damage, which may lead to poor neuronal function in lesioned thalamic voxels, and

subsequently reduced thalamocortical RSFC. Given that no changes in thalamocortical RSFC was observed in any thalamic lesions of this cohort, we postulate that axonal damage is unlikely. In fact, ex vivo histology of post-mortem MS patients has shown that even in demyelinated hippocampal areas, neurons were preserved (Dutta et al. 2011). Considering these null results and the multifaceted nature of MS pathophysiology, it remains to be seen whether focal damage to white matter or grey matter along thalamocortical pathways modulates thalamocortical RSFC.

### 4.4.4 Limitations

Our preliminary study is not without limitations. As highlighted in previous sections, there are many important factors to consider when interpreting these results. Firstly, interpreting diffusion parameter changes as either axonal injury or demyelination has been difficult due to the general limitations of diffusion tensor modelling in the thalamus. In addition, histological validation of thalamic lesions with diffusion tensor imaging has been limited, further hampering our ability to interpret these diffusion tensor results. Such uncertainties may have implications for all resting-state BOLD features that were used to investigate lesions in this study, as axonal damage may have larger implications in underlying BOLD dynamic measurements and RSFC, whereas demyelination (albeit reduced in the thalamus) may not. Secondly, results shown here suggest that central venules are a large confounder in BOLD variability of thalamic lesions (not all thalamic lesions expressed an obvious central venule, yet appeared to show increased variability). Further works may consider performing high resolution T2*-weighted images to assess the role of central venules more precisely to resting-state fMRI measurements in the thalamus of MS patients.

In this study, an important goal was to evaluate whether RSFC can be used to qualitatively assess effects of thalamic lesions in single subjects. Previous studies have generally used ROI-based analyses to conduct these investigations, however this overlooks the effects of thalamic lesions on voxel resolution RSFC. To overcome this, 7 cortical RSNs were defined as seed regions and used to probe voxel resolution RSFC patterns of the thalamus. However, this approach assumes that time series from 7 cortical RSNs provides an adequate characterization of thalamocortical RSFC, which may not be

optimal considering that these large RSNs will likely blur opposing brain regions together, and consequently reduce the sensitivity of RSFC profiles to thalamic lesions. In this regard, voxel resolution RSFC between thalamus and whole cortex was considered using gradient estimation techniques to resolve gradual changes in RSFC patterns over the thalamus. In both scenarios, from 7 cortical RSN seeds to gradients, no qualitative evidence of abrupt changes in RSFC or gradient measurements were observed. It is possible that the qualitative nature of these assessments makes it difficult to detect more subtle changes in RSFC and requires group-level comparisons. However, the heterogeneous nature of thalamic lesions in MS makes group-level inference for investigating the effects of lesions to be suboptimal, particularly given the objective of trying to make single-subject inferences.

To further address this problem of single-subject inference, individual scan sessions were assessed independently in a linear model. The goal was to assess whether lesions modulated thalamocortical connections between seven cortical RSNs, and their corresponding localized thalamic parcels within each scan session. Although negative associations were observed between RSFC and both AD and RD, we discovered that each thalamocortical RSFC map had intrinsically different RSFC strength, which subsequently confounded these results to make inference on single subjects limited. Furthermore, all ROI analyses in this study used thalamic parcels localized with RSFC data of only seven participants, which may be insufficient for delineating precise boundaries around thalamic parcels. Increasing the number of participants used to generate thalamic parcels may improve accuracy for subsequent ROI analyses, for example, in the case of the lateral geniculate nucleus, we would ideally want it to map more specifically onto posterior-lateral thalamus, as opposed to taking up a large posterior portion of the thalamus.

### 4.4.5 Conclusions

The goal of this preliminary work was to investigate whether focal thalamic lesions in MS impart detectable changes to thalamic functional organization as measured by resting-state fMRI features of dynamics and connectivity in single subjects. Here, the only relevant resting-state feature that was modulated by thalamic pathophysiology was

BOLD variability, and upon closer examination this result appears to be confounded by the presence of central venules, commonly found in MS thalamic lesions. This work provides some insights and caveats for performing and interpreting single-subject mapping of thalamic functional organization with resting-state fMRI at 7 Tesla.

## 4.5 References


Al-Radaideh, A. M., Wharton, S. J., Lim, S.-Y., Tench, C. R., Morgan, P. S., Bowtell, R. W., … Gowland, P. A. (2013). Increased iron accumulation occurs in the earliest stages of demyelinating disease: An ultra-high field susceptibility mapping study in Clinically Isolated Syndrome. *Multiple Sclerosis (Houndmills, Basingstoke, England)*, *19*(7), 896–903. https://doi.org/10.1177/1352458512465135

Aung, W. Y., Mar, S., & Benzinger, T. L. (2013). Diffusion tensor MRI as a biomarker in axonal and myelin damage. *Imaging in Medicine*, *5*(5), 427–440. https://doi.org/10.2217/iim.13.49

Avants, B. B., Tustison, N., Song, G. (2009). Advanced normalization tools (ants). *Insight J*.

Azevedo, C. J., Overton, E., Khadka, S., Buckley, J., Liu, S., Sampat, M., … Pelletier, D. (2015). Early CNS neurodegeneration in radiologically isolated syndrome. *Neurology - Neuroimmunology Neuroinflammation*, *2*(3). https://doi.org/10.1212/NXI.0000000000000102

Baxter, M. G. (2013). Mediodorsal thalamus and cognition in non-human primates. *Frontiers in Systems Neuroscience*, *7*, 38. https://doi.org/10.3389/fnsys.2013.00038

Bonavita, S., Gallo, A., Sacco, R., Corte, M. D., Bisecco, A., Docimo, R., … Tedeschi, G. (2011). Distributed changes in default-mode resting-state connectivity in multiple sclerosis. *Multiple Sclerosis (Houndmills, Basingstoke, England)*, *17*(4), 411–422. https://doi.org/10.1177/1352458510394609

Bradfield, L. A., Hart, G., & Balleine, B. W. (2013). The role of the anterior, mediodorsal, and parafascicular thalamus in instrumental conditioning. *Frontiers in Systems Neuroscience*, *7*, 51. https://doi.org/10.3389/fnsys.2013.00051

Budde, M. D., Xie, M., Cross, A. H., & Song, S.-K. (2009). Axial Diffusivity Is the Primary Correlate of Axonal Injury in the Experimental Autoimmune Encephalomyelitis Spinal Cord: A Quantitative Pixelwise Analysis. *The Journal of*

*Neuroscience*, *29*(9), 2805–2813. https://doi.org/10.1523/JNEUROSCI.4605-08.2009

Chang, E. H., Argyelan, M., Aggarwal, M., Chandon, T.-S. S., Karlsgodt, K. H., Mori, S., & Malhotra, A. K. (2017). The role of myelination in measures of white matter integrity: Combination of diffusion tensor imaging and two-photon microscopy of CLARITY intact brains. *NeuroImage*, *147*, 253–261. https://doi.org/10.1016/j.neuroimage.2016.11.068

Dineen, R. A., Vilisaar, J., Hlinka, J., Bradshaw, C. M., Morgan, P. S., Constantinescu, C. S., & Auer, D. P. (2009). Disconnection as a mechanism for cognitive dysfunction in multiple sclerosis. *Brain: A Journal of Neurology*, *132*(Pt 1), 239–249. https://doi.org/10.1093/brain/awn275

Dutta, R., Chang, A., Doud, M. K., Kidd, G. J., Ribaudo, M. V., Young, E. A., … Trapp, B. D. (2011). Demyelination causes synaptic alterations in hippocampi from multiple sclerosis patients. *Annals of Neurology*, *69*(3), 445–454. https://doi.org/10.1002/ana.22337

Duyn, J. H., van Gelderen, P., Li, T.-Q., de Zwart, J. A., Koretsky, A. P., & Fukunaga, M. (2007). High-field MRI of brain cortical substructure based on signal phase. *Proceedings of the National Academy of Sciences*, *104*(28), 11796–11801. https://doi.org/10.1073/pnas.0610821104

Esteban, O., Markiewicz, C. J., Blair, R. W., Moodie, C. A., Isik, A. I., Erramuzpe, A., … Gorgolewski, K. J. (2019). fMRIPrep: A robust preprocessing pipeline for functional MRI. *Nature Methods*, *16*(1), 111–116. https://doi.org/10.1038/s41592-018-0235-4

Fox, M. D., Snyder, A. Z., Vincent, J. L., Corbetta, M., Van Essen, D. C., & Raichle, M. E. (2005). The human brain is intrinsically organized into dynamic, anticorrelated functional networks. *Proceedings of the National Academy of Sciences*, *102*(27), 9673–9678. https://doi.org/10.1073/pnas.0504136102

Francis, P. L., Jakubovic, R., O'Connor, P., Zhang, L., Eilaghi, A., Lee, L., … Aviv, R. I. (2013). Robust Perfusion Deficits in Cognitively Impaired Patients with Secondary-Progressive Multiple Sclerosis. *AJNR: American Journal of Neuroradiology*, *34*(1), 62–67. https://doi.org/10.3174/ajnr.A3148

Fulcher, B. D., & Jones, N. S. (2017). hctsa: A Computational Framework for Automated Time-Series Phenotyping Using Massive Feature Extraction. *Cell Systems*, *5*(5), 527-531.e3. https://doi.org/10.1016/j.cels.2017.10.001

Garrett, D. D., Kovacevic, N., McIntosh, A. R., & Grady, C. L. (2010). Blood oxygen level-dependent signal variability is more than just noise. *The Journal of Neuroscience: The Official Journal of the Society for Neuroscience*, *30*(14), 4914–4921. https://doi.org/10.1523/JNEUROSCI.5166-09.2010

Garrett, D. D., Lindenberger, U., Hoge, R. D., & Gauthier, C. J. (2017). Age differences in brain signal variability are robust to multiple vascular controls. *Scientific Reports*, *7*(1), 10149. https://doi.org/10.1038/s41598-017-09752-7

Ge, Y., Law, M., Johnson, G., Herbert, J., Babb, J. S., Mannon, L. J., & Grossman, R. I. (2005). Dynamic susceptibility contrast perfusion MR imaging of multiple sclerosis lesions: Characterizing hemodynamic impairment and inflammatory activity. *AJNR. American Journal of Neuroradiology*, *26*(6), 1539–1547.

Ge, Y., Zhang, Z., Lu, H., Tang, L., Jaggi, H., Herbert, J., … Grossman, R. I. (2012). Characterizing brain oxygen metabolism in patients with multiple sclerosis with T2-relaxation-under-spin-tagging MRI. *Journal of Cerebral Blood Flow and Metabolism: Official Journal of the International Society of Cerebral Blood Flow and Metabolism*, *32*(3), 403–412. https://doi.org/10.1038/jcbfm.2011.191

Griffanti, L., Salimi-Khorshidi, G., Beckmann, C. F., Auerbach, E. J., Douaud, G., Sexton, C. E., … Smith, S. M. (2014). ICA-based artefact removal and accelerated fMRI acquisition for improved resting state network imaging. *NeuroImage*, *95*, 232–247. https://doi.org/10.1016/j.neuroimage.2014.03.034

Guadalupe, T., Mathias, S. R., vanErp, T. G. M., Whelan, C. D., Zwiers, M. P., Abe, Y., … Francks, C. (2017). Human subcortical brain asymmetries in 15,847 people worldwide reveal effects of age and sex. *Brain Imaging and Behavior*, *11*(5), 1497–1514. https://doi.org/10.1007/s11682-016-9629-z

Guitart-Masip, M., Salami, A., Garrett, D., Rieckmann, A., Lindenberger, U., & Bäckman, L. (2016). BOLD Variability is Related to Dopaminergic Neurotransmission and Cognitive Aging. *Cerebral Cortex (New York, N.Y.: 1991)*, *26*(5), 2074–2083. https://doi.org/10.1093/cercor/bhv029

Jenkinson, M., Beckmann, C. F., Behrens, T. E. J., Woolrich, M. W., & Smith, S. M. (2012). FSL. *NeuroImage*, *62*(2), 782–790. https://doi.org/10.1016/j.neuroimage.2011.09.015

Haak, K. V., Marquand, A. F., & Beckmann, C. F. (2018). Connectopic mapping with resting-state fMRI. *NeuroImage*, *170*, 83–94. https://doi.org/10.1016/j.neuroimage.2017.06.075

Halassa, M. M., & Kastner, S. (2017). Thalamic functions in distributed cognitive control. *Nature Neuroscience*, *20*(12), 1669–1679. https://doi.org/10.1038/s41593-017-0020-1

Harrison, D. M., Oh, J., Roy, S., Wood, E. T., Whetstone, A., Seigo, M. A., … Calabresi, P. A. (2015). Thalamic lesions in multiple sclerosis by 7T MRI: Clinical implications and relationship to cortical pathology. *Multiple Sclerosis (Houndmills, Basingstoke, England)*, *21*(9), 1139–1150. https://doi.org/10.1177/1352458514558134

Hawellek, D. J., Hipp, J. F., Lewis, C. M., Corbetta, M., & Engel, A. K. (2011). Increased functional connectivity indicates the severity of cognitive impairment in multiple sclerosis. *Proceedings of the National Academy of Sciences of the United States of America*, *108*(47), 19066–19071. https://doi.org/10.1073/pnas.1110024108

Holland, C. M., Charil, A., Csapo, I., Liptak, Z., Ichise, M., Khoury, S. J., … Guttmann, C. R. G. (2012). The relationship between normal cerebral perfusion patterns and white matter lesion distribution in 1,249 patients with multiple sclerosis. *Journal of Neuroimaging: Official Journal of the American Society of Neuroimaging*, *22*(2), 129–136. https://doi.org/10.1111/j.1552-6569.2011.00585.x

Jandric, D., Doshi, A., Scott, R., Paling, D., Rog, D., Chataway, J., … Muhlert, N. (2022). A Systematic Review of Resting-State Functional MRI Connectivity Changes and Cognitive Impairment in Multiple Sclerosis. *Brain Connectivity*, *12*(2), 112–133. https://doi.org/10.1089/brain.2021.0104

Jankowski, M. M., Ronnqvist, K. C., Tsanov, M., Vann, S. D., Wright, N. F., Erichsen, J. T., … O'Mara, S. M. (2013). The anterior thalamus provides a subcortical circuit supporting memory and spatial navigation. *Frontiers in Systems Neuroscience*, *7*, 45. https://doi.org/10.3389/fnsys.2013.00045

Jelescu, I. O. and Novikov, D. S. Water exchange time between gray matter compartments in vivo. Proc. Intl. Soc. Mag. Reson. Med. Sydney, Australia; 2020. Available: https://archive.ismrm.org/2020/0715.html

Jelescu, I. O., Palombo, M., Bagnato, F., & Schilling, K. G. (2020). Challenges for biophysical modeling of microstructure. *Journal of Neuroscience Methods*, *344*, 108861. https://doi.org/10.1016/j.jneumeth.2020.108861

Keitel, A., & Gross, J. (2016). Individual Human Brain Areas Can Be Identified from Their Characteristic Spectral Activation Fingerprints. *PLoS Biology*, *14*(6), e1002498. https://doi.org/10.1371/journal.pbio.1002498

Khalil, M., Langkammer, C., Pichler, A., Pinter, D., Gattringer, T., Bachmaier, G., … Fazekas, F. (2015). Dynamics of brain iron levels in multiple sclerosis: A longitudinal 3T MRI study. *Neurology*, *84*(24), 2396–2402. https://doi.org/10.1212/WNL.0000000000001679

Kilsdonk, I. D., Wattjes, M. P., Lopez-Soriano, A., Kuijer, J. P. A., de Jong, M. C., de Graaf, W. L., … Barkhof, F. (2014). Improved differentiation between MS and vascular brain lesions using FLAIR* at 7 Tesla. *European Radiology*, *24*(4), 841–849. https://doi.org/10.1007/s00330-013-3080-y

Klawiter, E. C., Schmidt, R. E., Trinkaus, K., Liang, H.-F., Budde, M. D., Naismith, R. T., … Benzinger, T. L. (2011). Radial diffusivity predicts demyelination in ex vivo multiple sclerosis spinal cords. *NeuroImage*, *55*(4), 1454–1460. https://doi.org/10.1016/j.neuroimage.2011.01.007

Louapre, C., Perlbarg, V., García-Lorenzo, D., Urbanski, M., Benali, H., Assouad, R., … Stankoff, B. (2014). Brain networks disconnection in early multiple sclerosis cognitive deficits: An anatomofunctional study. *Human Brain Mapping*, *35*(9), 4706–4717. https://doi.org/10.1002/hbm.22505

Lubba, C. H., Sethi, S. S., Knaute, P., Schultz, S. R., Fulcher, B. D., & Jones, N. S. (2019). catch22: CAnonical Time-series CHaracteristics. *Data Mining and Knowledge Discovery*, *33*(6), 1821–1852. https://doi.org/10.1007/s10618-019-00647-x

Maranzano, J., Dadar, M., Rudko, D. A., De Nigris, D., Elliott, C., Gati, J. S., … Narayanan, S. (2019). Comparison of Multiple Sclerosis Cortical Lesion Types Detected by Multicontrast 3T and 7T MRI. *AJNR. American Journal of Neuroradiology*, *40*(7), 1162–1169. https://doi.org/10.3174/ajnr.A6099

Marshall, O., Lu, H., Brisset, J.-C., Xu, F., Liu, P., Herbert, J., … Ge, Y. (2014). Impaired cerebrovascular reactivity in multiple sclerosis. *JAMA Neurology*, *71*(10), 1275–1281. https://doi.org/10.1001/jamaneurol.2014.1668

McIntosh, A. R., Kovacevic, N., Lippe, S., Garrett, D., Grady, C., & Jirsa, V. (2010). The development of a noisy brain. *Archives Italiennes De Biologie*, *148*(3), 323–337.

Mehndiratta, A., Treaba, C. A., Barletta, V., Herranz, E., Ouellette, R., Sloane, J. A., … Mainero, C. (2021). Characterization of thalamic lesions and their correlates in multiple sclerosis by ultra-high-field MRI. *Multiple Sclerosis (Houndmills, Basingstoke, England)*, *27*(5), 674–683. https://doi.org/10.1177/1352458520932804

Mietus, J. E., Peng, C.-K., Henry, I., Goldsmith, R. L., & Goldberger, A. L. (2002). The pNNx files: Re-examining a widely used heart rate variability measure. *Heart (British Cardiac Society)*, *88*(4), 378–380. https://doi.org/10.1136/heart.88.4.378

Murray, J. D., Bernacchia, A., Freedman, D. J., Romo, R., Wallis, J. D., Cai, X., … Wang, X.-J. (2014). A hierarchy of intrinsic timescales across primate cortex. *Nature Neuroscience*, *17*(12), 1661–1663. https://doi.org/10.1038/nn.3862

Nomi, J. S., Schettini, E., Voorhies, W., Bolt, T. S., Heller, A. S., & Uddin, L. Q. (2018). Resting-State Brain Signal Variability in Prefrontal Cortex Is Associated With ADHD Symptom Severity in Children. *Frontiers in Human Neuroscience*, *12*. Retrieved from https://www.frontiersin.org/article/10.3389/fnhum.2018.00090

Ogawa, S., Lee, T. M., Kay, A. R., & Tank, D. W. (1990). Brain magnetic resonance imaging with contrast dependent on blood oxygenation. *Proceedings of the National Academy of Sciences*, *87*(24), 9868–9872. https://doi.org/10.1073/pnas.87.24.9868

Pauli, W. M., Nili, A. N., & Tyszka, J. M. (2018). A high-resolution probabilistic in vivo atlas of human subcortical brain nuclei. *Scientific Data*, *5*(1), 180063. https://doi.org/10.1038/sdata.2018.63

Petracca, M., Saiote, C., Bender, H. A., Arias, F., Farrell, C., Magioncalda, P., … Inglese, M. (2017). Synchronization and variability imbalance underlie cognitive impairment in primary-progressive multiple sclerosis. *Scientific Reports*, *7*, 46411. https://doi.org/10.1038/srep46411

Preziosa, P., Rocca, M. A., Pagani, E., Stromillo, M. L., Enzinger, C., Gallo, A., … MAGNIMS Study Group. (2016). Structural MRI correlates of cognitive impairment in patients with multiple sclerosis: A Multicenter Study. *Human Brain Mapping*, *37*(4), 1627–1644. https://doi.org/10.1002/hbm.23125

Reichenbach, J. R., Venkatesan, R., Schillinger, D. J., Kido, D. K., & Haacke, E. M. (1997). Small vessels in the human brain: MR venography with deoxyhemoglobin as an intrinsic contrast agent. *Radiology*, *204*(1), 272–277. https://doi.org/10.1148/radiology.204.1.9205259

Rocca, M. A., Valsasina, P., Absinta, M., Riccitelli, G., Rodegher, M. E., Misci, P., … Filippi, M. (2010). Default-mode network dysfunction and cognitive impairment in progressive MS. *Neurology*, *74*(16), 1252–1259. https://doi.org/10.1212/WNL.0b013e3181d9ed91

Roosendaal, S. D., Schoonheim, M. M., Hulst, H. E., Sanz-Arigita, E. J., Smith, S. M., Geurts, J. J. G., & Barkhof, F. (2010). Resting state networks change in clinically isolated syndrome. *Brain: A Journal of Neurology*, *133*(Pt 6), 1612–1621. https://doi.org/10.1093/brain/awq058

Saalmann, Y. B., & Kastner, S. (2011). Cognitive and perceptual functions of the visual thalamus. *Neuron*, *71*(2), 209–223. https://doi.org/10.1016/j.neuron.2011.06.027

Sati, P., Oh, J., Constable, R. T., Evangelou, N., Guttmann, C. R. G., Henry, R. G., … Reich, D. S. (2016). The central vein sign and its clinical evaluation for the diagnosis of multiple sclerosis: A consensus statement from the North American Imaging in Multiple Sclerosis Cooperative. *Nature Reviews Neurology*, *12*(12), 714–722. https://doi.org/10.1038/nrneurol.2016.166

Scarapicchia, V., Mazerolle, E. L., Fisk, J. D., Ritchie, L. J., & Gawryluk, J. R. (2018). Resting State BOLD Variability in Alzheimer's Disease: A Marker of Cognitive Decline or Cerebrovascular Status? *Frontiers in Aging Neuroscience*, *10*, 39. https://doi.org/10.3389/fnagi.2018.00039

Schaefer, A., Kong, R., Gordon, E. M., Laumann, T. O., Zuo, X.-N., Holmes, A. J., … Yeo, B. T. T. (2018). Local-Global Parcellation of the Human Cerebral Cortex from Intrinsic Functional Connectivity MRI. *Cerebral Cortex (New York, N.Y.: 1991)*, *28*(9), 3095–3114. https://doi.org/10.1093/cercor/bhx179

Schmierer, K., Wheeler-Kingshott, C. A. M., Boulby, P. A., Scaravilli, F., Altmann, D. R., Barker, G. J., … Miller, D. H. (2007). Diffusion tensor imaging of post mortem multiple sclerosis brain. *NeuroImage*, *35*(2), 467–477. https://doi.org/10.1016/j.neuroimage.2006.12.010

Schoonheim, M M, Geurts, J. J. G., Wiebenga, O. T., De Munck, J. C., Polman, C. H., Stam, C. J., … Wink, A. M. (2014). Changes in functional network centrality underlie cognitive dysfunction and physical disability in multiple sclerosis. *Multiple Sclerosis Journal*, *20*(8), 1058–1065. https://doi.org/10.1177/1352458513516892

Schoonheim, Menno M., Meijer, K. A., & Geurts, J. J. G. (2015). Network Collapse and Cognitive Impairment in Multiple Sclerosis. *Frontiers in Neurology*, *6*. Retrieved from https://www.frontiersin.org/article/10.3389/fneur.2015.00082

Shafiei, G., Markello, R. D., Vos de Wael, R., Bernhardt, B. C., Fulcher, B. D., & Misic, B. (2020). Topographic gradients of intrinsic dynamics across neocortex. *ELife*, *9*, e62116. https://doi.org/10.7554/eLife.62116

Sowa, P., Bjørnerud, A., Nygaard, G. O., Damangir, S., Spulber, G., Celius, E. G., … Beyer, M. K. (2015). Reduced perfusion in white matter lesions in multiple sclerosis. *European Journal of Radiology*, *84*(12), 2605–2612. https://doi.org/10.1016/j.ejrad.2015.09.007

Wang, X., Wirth, A., & Wang, L. (2007). Structure-Based Statistical Features and Multivariate Time Series Clustering. *Seventh IEEE International Conference on Data Mining (ICDM 2007)*, 351–360. https://doi.org/10.1109/ICDM.2007.103

Waschke, L., Kloosterman, N. A., Obleser, J., & Garrett, D. D. (2021). Behavior needs neural variability. *Neuron*, *109*(5), 751–766. https://doi.org/10.1016/j.neuron.2021.01.023

Watanabe, T., Rees, G., & Masuda, N. (2019). Atypical intrinsic neural timescale in autism. *ELife*, *8*, e42256. https://doi.org/10.7554/eLife.42256

Yang, S., Meng, Y., Li, J., Li, B., Fan, Y.-S., Chen, H., & Liao, W. (2020). The thalamic functional gradient and its relationship to structural basis and cognitive relevance. *NeuroImage*, *218*, 116960. https://doi.org/10.1016/j.neuroimage.2020.116960

Zhu, H., Huang, J., Deng, L., He, N., Cheng, L., Shu, P., … Ling, H. (2019). Abnormal Dynamic Functional Connectivity Associated With Subcortical Networks in Parkinson's Disease: A Temporal Variability Perspective. *Frontiers in Neuroscience*, *13*, 80. https://doi.org/10.3389/fnins.2019.00080

Zivadinov, R., Bergsland, N., Dolezal, O., Hussein, S., Seidl, Z., Dwyer, M. G., … Horáková, D. (2013). Evolution of cortical and thalamus atrophy and disability progression in early relapsing-remitting MS during 5 years. *AJNR. American Journal of Neuroradiology*, *34*(10), 1931–1939. https://doi.org/10.3174/ajnr.A3503

## 4.6 Supplementary Tables

**Supplementary Table 4.1 Calculated rsfMRI features**

| Feature categories | feature name | Description |
|---|---|---|
| Basic | Mean | Mean |
| Basic | SD | Standard deviation |
| Distribution | DN_HistogramMode_5 | Mode of z-scored distribution (5-bin histogram) |
| Distribution | DN_HistogramMode_10 | Mode of z-scored distribution (10-bin histogram) |
| Simple temporal statistics | SB_BinaryStats_mean_longstretch1 | Longest period of consecutive values above the mean |
| Simple temporal statistics | DN_OutlierInclude_p_001_mdrmd | Time intervals between successive extreme events above the mean |
| Simple temporal statistics | DN_OutlierInclude_n_001_mdrmd | Time intervals between successive extreme events below the mean |
| Linear autocorrelation | CO_f1ecac | First 1/e crossing of autocorrelation function |
| Linear autocorrelation | CO_FirstMin_ac | First minimum of autocorrelation function |
| Linear autocorrelation | SP_Summaries_welch_rect_area_5_1 | Total power in lowest fifth of frequencies in the Fourier power spectrum |
| Linear autocorrelation | SP_Summaries_welch_rect_centroid | Centroid of the Fourier power spectrum |
| Linear autocorrelation | FC_LocalSimple_mean3_stderr | Mean error from a rolling 3-sample mean forecasting |
| Linear autocorrelation | Intrinsic Timescale | Sum of autocorrelation function values until first crossing (Watanabe et al. 2019) |
| Nonlinear autocorrelation | CO_trev_1_num | Time-reversibility statistic |
| Nonlinear autocorrelation | CO_HistogramAMI_even_2_5 | Automutual information |
| Nonlinear autocorrelation | IN_AutoMutualInfoStats_40_gaussian_fmmi | First minimum of the automutual information function |
| Successive differences | MD_hrv_classic_pnn40 | Proportion of successive differences exceeding $0.04\sigma$ (Mietus 2002) |
| Successive differences | SB_BinaryStats_diff_longstretch0 | Longest period of successive incremental decreases |
| Successive differences | SB_MotifThree_quantile_hh | Shannon entropy of two successive letters in equiprobable 3-letter symbolization |
| Successive differences | FC_LocalSimple_mean1_tauresrat | Change in correlation length after iterative differencing |
| Successive differences | CO_Embed2_Dist_tau_d_expfit_meandiff | Exponential fit to successive distances in 2-d embedding space |

| | | |
|---|---|---|
| Fluctuation analysis | SC_FluctAnal_2_dfa_50_1_2_logi_prop_r1 | Proportion of slower timescale fluctuations that scale with DFA (50% sampling) |
| Fluctuation analysis | SC_FluctAnal_2_rsrangefit_50_1_logi_prop_r1 | Proportion of slower timescale fluctuations that scale with linearly rescaled range fits |
| Others | SB_TransitionMatrix_3ac_sumdiagcov | Trace of covariance of transition matrix between symbols in 3-letter alphabet |
| Others | PD_PeriodicityWang_th0_01 | Periodicity measure of (Wang et al. 2007) |
| RSFC Gradients | G01 | Eigenvector of the graph Laplacian corresponding to the lowest non-zero eigenvalue (Haak et al. 2018) |
| RSFC Gradients | G02 | Eigenvector of the graph Laplacian corresponding to the 2nd lowest non-zero eigenvalue (Haak et al. 2018) |

# Chapter 5

# 5 Discussion and Future Work

## 5.1 Summary of Thesis

Gradient estimation techniques have emerged as a valuable framework for conceptualizing high-dimensional brain connectivity across various domains of neuroimaging. This thesis provides broad contributions to resting-state connectivity gradient literature by demonstrating the ability to (a) unveil an anterior-posterior organizational axis of the somatosensory cortex that has previously gone overlooked, (b) unify organizational axes of marmosets and humans allowing for systematic cross-species comparisons of the default-mode network, and (c) assess the focal impacts of Multiple Sclerosis thalamic pathophysiology on thalamocortical organization. Together, this work outlines several advances that have been afforded by a gradient-centric approach in the domains of basic, comparative, and clinical neuroscience.

### 5.1.1 Overlapping axes of connectivity principles in somatosensory cortex

In Chapter 2 of this thesis, I explored the use of gradient estimations to reveal a secondary axis of connectivity organization in S1, using resting-state fMRI. Previous resting-state connectivity literature has often differentiated somatosensory cortex along its dorsal-ventral axis, akin to the long-understood notion of somatotopy that corresponds to the mapping of body parts along this cortical strip (Yeo et al. 2011; van den Heuvel and Hulshoff Pol, 2010; Penfield and Rasmussen, 1950). In addition to somatotopy, S1 is known to follow a hierarchical organization with afferent somatosensory inputs being processed along an anterior-posterior axis, as supported by anatomical connectivity studies (Felleman and Van Essen, 1991). Given the duality of connectivity principles that is fundamental to S1, I contended that gradient estimations, specifically looking at higher-order gradients, may reveal this anterior-posterior axis. Indeed, the primary gradient revealed a somatotopic axis, whereas the secondary and tertiary gradients collectively indicated evidence of division along the anterior-posterior axis. Subsequent division of S1 into somatotopic regions – lower limb, upper limb, and trunk – confirmed a primary

gradient that traversed the anterior-posterior axis while critically providing a coordinate system for espousing structure-connectivity relationships. Specifically, I demonstrate correspondence of RSFC-derived gradients with hierarchical organization, structural organization, and architectonic Brodmann areas.

This study adds to a growing body of literature that explores the multiplicity of connectivity principles underlying different brain areas using RSFC gradient representations. Prior works have shown correspondence of gradients with primary visual cortex to eccentricity and polar angle maps of the visual field (Haak et al. 2018), hippocampus to its functional long-axis and structural infoldings (Vos de Wael et al. 2018), striatum to its cortico-striatal reward and dopaminergic pathways (Marquand et al. 2017; Oldehinkel et al. 2022), and in this work, S1 to somatotopic and hierarchical organization. Critically, discovery of different representations of brain connectivity that adheres to biologically plausible solutions may provide more sensitive assays of different brain function. For example, the gradient corresponding to the S1 hierarchical organization, compared to somatotopy may better model human tactile goal directed behaviour as it better characterizes circuitry supporting processing of tactile information. Additionally, identifying organizational axes consistent with brain microstructure provides an elegant framework to study the interplay between brain connectivity and structure amidst possible structural pathophysiology due to disease.

### 5.1.2 Conceptualizing cross-species brain evolution with resting-state fMRI

In Chapter 3, I applied gradient estimation to cross-species connectivity fingerprints to derive a parsimonious coordinate system that unifies macroscale brain organization of marmosets and humans. To date, this study is one of two investigations conceptualizing cross-species comparisons using gradient estimation techniques and, in this case, comparing the cortical connectome of marmosets and humans. Xu and colleagues were the first to propose the use of gradients in a cross-species framework – referred to as joint-embeddings (or gradients) – and demonstrated gradient estimations in macaques and humans (Xu et al. 2020). In the current work, connectivity fingerprints were computed at every cortical vertex, across both species, and anchored by a set of a-priori defined

homologous brain regions (Mars et al. 2018). In this way, cross-species similarity of vertex-wise connectivity fingerprints could be computed, effectively linking brain organization across both species allowing for subsequent gradient estimation to simultaneously situate both species brain vertices onto a set of organizational axes. Each organizational axis conceptualizes consistent brain architecture between marmosets and humans. For example, the primary gradient revealed a consistent somatomotor-to-default-mode network axis in both species, allowing for cross-species comparison. In doing so, I found that the connectivity fingerprints underlying marmoset DMN are more dispersed compared to humans, and this is attributed to the marmoset's dorsolateral prefrontal cortex (dlPFC). To further explore this novel insight, subsequent connectivity analysis was performed to show that, although marmoset dlPFC *is* connected to its posterior DMN constituents, it is weakly bounded and expresses differential connectivity compared to its posterior DMN regions, that is unlike humans. Together, the work in this chapter reveals more subtle cross-species differences between marmosets and humans, and suggests that, unlike in marmosets, human cognitive behaviour likely relies on a deeply integrated anterior-posterior DMN axis, as observed in human brain organization.

Together, this cross-species comparative framework inherits previously mentioned benefits of gradient techniques, such as heterogeneity and multiplicity of cross-species connectivity representations. Firstly, it provides vertex resolved comparisons of connectivity fingerprints without making any ROI assumptions, aside from the selection of homologous ROIs. Historically, most prior comparative cross-species connectivity fingerprinting studies were limited in this regard by probing only a subset of brain areas, in search of homologies, often disregarding other brain areas of putative cross-species homology. This is emphasized in understanding homology of medial prefrontal cortex in marmosets relative to humans, which has thus far remained ambiguous. Due to the hypothesis-free nature of this gradient approach, I found that the third gradient revealed brain organization that matches mPFC to areas of human frontoparietal and cingulo-opercular networks, and not the DMN. Together, gradient estimation applied to cross-species connectivity fingerprinting provides a parsimonious framework for conceptualizing and quantitatively evaluating putative homologies across species.

### 5.1.3 Connectivity gradients of the thalamus in Multiple Sclerosis

In Chapter 4, I used connectivity gradients, in addition to a myriad of other resting-state BOLD dynamic measurements, to explore voxel-resolved effects of thalamic Multiple Sclerosis (MS) lesions in secondary-progressive MS patients (SPMS). Previous resting-state studies in MS largely rely on group-level studies to gauge the effects of brain reorganization through MS disease trajectory, and have often disregarded the spatial role of focal MS pathophysiology (Jandric et al. 2022). This is a cumbersome problem due to spatial heterogeneity of pathophysiology across individuals with MS (Lucchinetti et al. 2000), in combination with the complexity of brain connectivity. In the current work, I proposed the use of thalamocortical RSFC gradients to resolve the latter issue, which theoretically should be able to detect lesion effects given the assumption that lesions impart changes to underlying resting-state functional connectivity. In single-subject investigations of four SPMS patients imaged over multiple scanning sessions, I found no evidence of voxel-level effects of lesions on thalamocortical RSFC gradients, in addition to 27 measures of resting-state BOLD dynamics. Notably, only BOLD variability appeared to be able to resolve thalamic lesions in some cases, however this observation is confounded by prominent central veins known to occur in MS lesions. Although others have used gradients to characterize connectivity organization in numerous neurological and neuropsychiatric disorders (Hong et al. 2019; Dong et al. 2020), the work in Chapter 4 provides first investigations of gradients to resolve the effects of pathophysiology on RSFC in an attempt to advance biomarker discovery of neural reorganization in single subjects with MS.

## 5.2 Thesis Limitations

### 5.2.1 Defining regions of interest

In Chapter 2 of this thesis, a-priori definitions of somatosensory cortex were heavily relied on to gain insights of an anterior-posterior axis. Here, regions of interests were taken from Glasser and colleagues' multimodal parcellation, which heavily relied on converging multimodal evidence to yield precise delineation of architectonic divisions of S1, and furthermore used task-based localizers to delineate coarse somatotopic areas of S1. It is important to note that although gradients were derived on the group-level to maximize

signal-to-noise ratio, the dominant gradient of right hemisphere upper limb appeared to span its somatotopic axis, and not an anterior-posterior axis as depicted by all other somatotopic regions. Despite employing careful strategies to determine the definition of right upper limb, it is possible that an overestimation of this region of interest included ventral vertices that corresponded with somatotopic face or eye regions, that could have potentially driven subsequent gradient estimation to characterize heterogeneity along its somatotopic axis (see Supplementary Fig. 2.1). Broadly, this observation implies that recovery of biological plausible gradients can be biased by the region's definition. This problem may be further compounded in the case of single-subject brain mapping where it is known that spatial configuration of functional brain areas is highly variable (Bijsterbosch et al. 2018), even after best efforts to spatially normalize individuals (Robinson et al. 2014; Coalson et al. 2018). This raises questions whether variability of gradients in single subjects arise due to inaccurate region definitions, or from biologically driven processes. To properly tackle these problems, it would be important to consider precision mapping of single subjects to obtain proper areal definitions of a specific region of interest prior to estimating gradients. Of note, these problems are less likely to manifest in subcortical structures, such as the thalamus (explored in Chapter 4), given more robust structural processing pipelines that have been prominently used in neuroimaging to accurately enable segmentation of the subcortex (Dale et al. 1999).

### 5.2.2 Interpreting the functional significance of gradients

It is important to consider that gradients at their core present only a simplified representation of resting-state functional connectivity measurements, which at best correspond to synchrony of neural activity that is subsequently used to infer brain connectivity. In this way, the functional meaning of all gradient results presented in this thesis remains largely conjecture, and are predicated on the belief that different brain areas, based on their unique connectivity properties, support distinct brain functions. To address the interpretational issues of gradient representations, the best that can be done is to use gradients to guide follow-up connectivity analyses, further elucidating their connectional properties for more in-depth interpretation. In Chapter 2, subsequent thalamocortical connectivity analyses using hierarchically derived S1 ROIs were performed, reconciling

known circuit properties that predicated early understandings of hierarchy in S1. Additionally, in Chapter 3, subsequent connectivity analyses were performed to fully appreciate the divergent connectivity properties of marmoset DMN compared to humans, and this cross-species difference was used to emphasize the importance of the DMN to human cognitive behaviour. Alternatively, many have used meta-analysis to determine functional significance of gradient representations (Margulies et al. 2016; Yang et al. 2020; Xu et al. 2021), however this too provides only an indirect approach for gauging the functional significance of gradients.

To fully appreciate the functional significance of these gradients in humans, multivariate task-based paradigms may be employed to explore whether hierarchical neural representations exist in different areas of the brain (Yokoi and Diedrichsen, 2019). However, developing task-based paradigms of different brain regions is limited by the tasks' ability to evoke hierarchical responses in those brain areas, oftentimes leaving explorations of association areas, such as the default-mode network, a terra incognita (Raichle 2015). Furthermore, establishing the functional significance with task-based fMRI in cross-species studies implies that non-human primates must be trained to effectively engage in tasks while in an MRI. In this way, disentangling the functional significance of gradient representations in the context of human cognition remains an enormous endeavour, and resting-state functional connectivity may serve as a pragmatic compromise.

## 5.3 Future Directions

### 5.3.1 Somatosensory cortex connection topography in Parkinson's Disease

The somatosensory cortex is widely connected to cortical and subcortical brain areas, and widely believed to play a role in somatosensory abnormalities in Parkinson's Disease (PD) (Conte et al. 2013). Having demonstrated a way to map connection topography that may correspond to circuitry underlying hierarchical processing of S1 (Chapter 2), subsequent investigations could potentially evaluate whether S1 gradients are altered in Parkinson's Disease. A few different approaches, employed by recent studies, could be explored to

statistically compare spatial gradients between PD and healthy populations. Tian and colleagues used a clustering approach applied to insula gradients, to infer changes in schizophrenia compared to healthy individuals (Tian et al. 2019). Other works by Haak and colleagues proposed a trend surface analysis model – adopted from geosciences – to model spatial variances across a cortical gradient allowing for inference between groups (Haak et al. 2018). Alternatively, Nenning and colleagues proposed joint gradients between a group template and individuals to enable flexible alignment of all individuals in a population, allowing for improved pointwise comparisons of gradients in single subjects (Nenning et al. 2020). As such, future investigations could be directed towards evaluation of the efficacy of these different approaches to understand the impacts of PD on S1 connectivity by means of gradient representations.

### 5.3.2 Gradient-based investigations of marmosets

The common marmoset has recently become a popular animal model for neuroscientific research. In this regard, much progress is needed to further elucidate the structural and functional organization of the marmoset brain. Towards this open-ended goal, gradient representations offer many avenues for exploration, but so far have been largely under-investigated.

Firstly, gradient representations have recently been proposed as a unifying framework allowing for holistic cross-species comparisons of brain organization with resting-state fMRI, while offering many advantages over other comparative approaches. This framework has been adapted in this thesis (Chapter 3) to unveil unifying gradients of marmosets and humans and was used to investigate similarities and differences of the default-mode network. In principle, gradient representations can be modified to include other longstanding preclinical animal model species, such as mice and Old-World Primates, to test novel hypotheses regarding functional organization. Furthermore, unifying gradients across multiple species provides a quantitative way for estimating brain deformation fields to investigate brain evolution across species (Xu et al. 2020). Although the work in this thesis primarily focuses on resting-state fMRI, diffusion MRI can also capitalize off such methodological advances. To this end, several open access diffusion

MRI datasets of marmosets and many non-human primates have been made available and can readily leverage such advances (Liu et al. 2020; Bryant et al. 2021).

A second research avenue could aim to extend the utilization of the abovementioned gradient-derived cross-species framework to consider individual homologous cortical areas, rather than the whole cortex as was demonstrated in Chapter 3 of this thesis. Consideration of comparisons of finer grained organization within specific homologous brain areas may provide much needed insight towards elucidating the evolution of a brain area, and in turn these differences may account for behavioural variations that are observed between species (Krubitzer 1995). Recently, many cross-species investigations have been undertaken to achieve exactly this, by comparing connectivity fingerprints of a set of coarse brain areas across species using the brain parcellation paradigm. Gradient-based investigations could overcome blurring issues that arise with the use of parcellation, ultimately achieving voxel-resolved gradients of homologous brain areas that can be used to fully appreciate more subtle evolution of a homologous brain area between species.

A third line of research focuses on individual marmoset brain mapping, rather than cross-species comparison. Recent efforts in brain mapping have made significant progress in unveiling spatial gradients in humans, and this can be readily extended to provide insights in marmoset brain organisation as well. In addition to performing gradient mapping on all cortical and subcortical areas of the marmoset (which to date, has not yet been conducted), another exciting area of research would be to use gradient techniques to derive rsfMRI-derived marmoset brain atlases. Thus far, histologically defined marmoset brain atlases have predominantly been used across studies (Paxinos et al. 2012), and as discussed throughout this thesis, may be not suitable for use in resting-state connectivity analyses of this animal model. Therefore, novel marmoset brain atlases derived using resting-state fMRI may be preferred for investigations related to connectivity. Recent mapping of the human subcortex demonstrates many advantages of using gradient techniques to guide brain parcellation (Tian et al. 2020). I propose that this approach could be successfully extended to develop new atlases for the marmoset cortex and subcortex as well.

### 5.3.3 Interpreting connectivity gradients with simulations

In Chapter 4, I investigated the impact of thalamic lesions on RSFC gradients, with the hypothesis that focal thalamic lesions would directly alter thalamocortical connectivity patterns, and in turn lead to observable changes in ensuing thalamic gradients. However, no qualitative changes were observed, which would appear to suggest that thalamic lesions do not modulate thalamocortical RSFC, and furthermore that RSFC, and related-gradient representations have minimal clinical utility in neurological disorders, at least in the case of Multiple Sclerosis.

If lesion pathology does in fact disrupt observed resting-state connectivity, then it leads us to wonder why the employed gradient estimation techniques did not detect changes in the associated RSFC patterns. To explore this question further, simulation experiments using rsfMRI data could be conducted to understand how a hypothetical lesion *should* impact derived gradients. For example, this could involve adding perturbations to time series and/or connectivity fingerprints of specific voxels (simulating a lesion that is disrupting local connectivity) in rsfMRI data of an otherwise healthy individual, and subsequently generating gradient representations. These simulated gradients would theoretically provide a framework for interpreting gradient representations in the presence of pathophysiology within neurological disorders, which may provide clinical utility. Given the complexities of the neural connections that gradient estimation techniques aim to approximate and the growing interest of using gradients to study cortical evolution, development, and plasticity, simulation experiments would provide an interpretational understanding of how spatial variations in ensuing gradients arise.

## 5.4 Conclusion

A gradient-centric view of brain organization has become an increasingly prominent perspective in neuroscience. Many research works have capitalized on various methodological advances in this domain, demonstrating its widespread applications to broadly build upon current understandings of all research areas of neuroimaging. This thesis uses resting-state fMRI to demonstrate through various examples where gradient representations of brain connectivity may be beneficial for elucidating underpinnings of

neural organization. By further extending upon this work, we hope to further enable advancements in gradient estimation of brain organization across the fields of basic, comparative, and clinical neuroscience.

## 5.5 References

Bijsterbosch, J. D., Woolrich, M. W., Glasser, M. F., Robinson, E. C., Beckmann, C. F., Van Essen, D. C., … Smith, S. M. (2018). The relationship between spatial configuration and functional connectivity of brain regions. *ELife*, *7*, e32992. https://doi.org/10.7554/eLife.32992

Bryant, K. L., Ardesch, D. J., Roumazeilles, L., Scholtens, L. H., Khrapitchev, A. A., Tendler, B. C., … Mars, R. B. (2021). Diffusion MRI data, sulcal anatomy, and tractography for eight species from the Primate Brain Bank. *Brain Structure and Function*, *226*(8), 2497–2509. https://doi.org/10.1007/s00429-021-02268-x

Coalson, T. S., Van Essen, D. C., & Glasser, M. F. (2018). The impact of traditional neuroimaging methods on the spatial localization of cortical areas. *Proceedings of the National Academy of Sciences of the United States of America*, *115*(27), E6356–E6365. https://doi.org/10.1073/pnas.1801582115

Conte, A., Khan, N., Defazio, G., Rothwell, J. C., & Berardelli, A. (2013). Pathophysiology of somatosensory abnormalities in Parkinson disease. *Nature Reviews. Neurology*, *9*(12), 687–697. https://doi.org/10.1038/nrneurol.2013.224

Dale, A. M., Fischl, B., & Sereno, M. I. (1999). Cortical surface-based analysis. I. Segmentation and surface reconstruction. *NeuroImage*, *9*(2), 179–194. https://doi.org/10.1006/nimg.1998.0395

Dong, D., Luo, C., Guell, X., Wang, Y., He, H., Duan, M., … Yao, D. (2020). Compression of Cerebellar Functional Gradients in Schizophrenia. *Schizophrenia Bulletin*, sbaa016. https://doi.org/10.1093/schbul/sbaa016

Felleman, D. J., & Van Essen, D. C. (1991). Distributed hierarchical processing in the primate cerebral cortex. *Cerebral Cortex (New York, N.Y.: 1991)*, *1*(1), 1–47. https://doi.org/10.1093/cercor/1.1.1-a

Haak, K. V., Marquand, A. F., & Beckmann, C. F. (2018). Connectopic mapping with resting-state fMRI. *NeuroImage*, *170*, 83–94. https://doi.org/10.1016/j.neuroimage.2017.06.075

Hong, S.-J., Vos de Wael, R., Bethlehem, R. A. I., Lariviere, S., Paquola, C., Valk, S. L., … Bernhardt, B. C. (2019). Atypical functional connectome hierarchy in autism. *Nature Communications*, *10*(1), 1022. https://doi.org/10.1038/s41467-019-08944-1

Iglesias, J. E., Insausti, R., Lerma-Usabiaga, G., Bocchetta, M., Van Leemput, K., Greve, D. N., … Paz-Alonso, P. M. (2018). A probabilistic atlas of the human

thalamic nuclei combining ex vivo MRI and histology. *NeuroImage*, *183*, 314–326. https://doi.org/10.1016/j.neuroimage.2018.08.012

Jandric, D., Doshi, A., Scott, R., Paling, D., Rog, D., Chataway, J., … Muhlert, N. (2022). A Systematic Review of Resting-State Functional MRI Connectivity Changes and Cognitive Impairment in Multiple Sclerosis. *Brain Connectivity*, *12*(2), 112–133. https://doi.org/10.1089/brain.2021.0104

Krubitzer, L. (1995). The organization of neocortex in mammals: Are species differences really so different? *Trends in Neurosciences*, *18*(9), 408–417. https://doi.org/10.1016/0166-2236(95)93938-t

Liu, C., Ye, F. Q., Newman, J. D., Szczupak, D., Tian, X., Yen, C. C.-C., … Silva, A. C. (2020). A resource for the detailed 3D mapping of white matter pathways in the marmoset brain. *Nature Neuroscience*, *23*(2), 271–280. https://doi.org/10.1038/s41593-019-0575-0

Lucchinetti, C., Brück, W., Parisi, J., Scheithauer, B., Rodriguez, M., & Lassmann, H. (2000). Heterogeneity of multiple sclerosis lesions: Implications for the pathogenesis of demyelination. *Annals of Neurology*, *47*(6), 707–717. https://doi.org/10.1002/1531-8249(200006)47:6<707::aid-ana3>3.0.co;2-q

Margulies, D. S., Ghosh, S. S., Goulas, A., Falkiewicz, M., Huntenburg, J. M., Langs, G., … Smallwood, J. (2016). Situating the default-mode network along a principal gradient of macroscale cortical organization. *Proceedings of the National Academy of Sciences of the United States of America*, *113*(44), 12574–12579. https://doi.org/10.1073/pnas.1608282113

Marquand, A. F., Haak, K. V., & Beckmann, C. F. (2017). Functional corticostriatal connection topographies predict goal directed behaviour in humans. *Nature Human Behaviour*, *1*(8), 0146. https://doi.org/10.1038/s41562-017-0146

Mars, R. B., Passingham, R. E., & Jbabdi, S. (2018). Connectivity Fingerprints: From Areal Descriptions to Abstract Spaces. *Trends in Cognitive Sciences*, *22*(11), 1026–1037. https://doi.org/10.1016/j.tics.2018.08.009

Nenning, K.-H., Xu, T., Schwartz, E., Arroyo, J., Woehrer, A., Franco, A. R., … Langs, G. (2020). Joint embedding: A scalable alignment to compare individuals in a connectivity space. *NeuroImage*, *222*, 117232. https://doi.org/10.1016/j.neuroimage.2020.117232

Oldehinkel, M., Llera, A., Faber, M., Huertas, I., Buitelaar, J. K., Bloem, B. R., … Beckmann, C. F. (2022). Mapping dopaminergic projections in the human brain with resting-state fMRI. *ELife*, *11*, e71846. https://doi.org/10.7554/eLife.71846

Paxinos, G., Watson, C. R. R., Petrides, M., Rosa, M. G., & Tokuno, H. (2012). The Marmoset Brain in Stereotaxic Coordinates. Elsevier. Retrieved from https://research.monash.edu/en/publications/the-marmoset-brain-in-stereotaxic-coordinates

Penfield, W., Rasmussen, T., & National Institute on Drug Abuse,. (1950). *The cerebral cortex of man: A clinical study of localization of function.* New York: Macmillan.

Raichle, M. E. (2015). The brain's default mode network. *Annual Review of Neuroscience*, *38*, 433–447. https://doi.org/10.1146/annurev-neuro-071013-014030

Robinson, E. C., Jbabdi, S., Glasser, M. F., Andersson, J., Burgess, G. C., Harms, M. P., … Jenkinson, M. (2014). MSM: A new flexible framework for Multimodal Surface Matching. *NeuroImage*, *100*, 414–426. https://doi.org/10.1016/j.neuroimage.2014.05.069

Schaeffer, D. J., Hori, Y., Gilbert, K. M., Gati, J. S., Menon, R. S., & Everling, S. (2020). Divergence of rodent and primate medial frontal cortex functional connectivity. *Proceedings of the National Academy of Sciences of the United States of America*, *117*(35), 21681–21689. https://doi.org/10.1073/pnas.2003181117

Tian, Y., Margulies, D. S., Breakspear, M., & Zalesky, A. (2020). Topographic organization of the human subcortex unveiled with functional connectivity gradients. *Nature Neuroscience*, *23*(11), 1421–1432. https://doi.org/10.1038/s41593-020-00711-6

Tian, Y., Zalesky, A., Bousman, C., Everall, I., & Pantelis, C. (2019). Insula Functional Connectivity in Schizophrenia: Subregions, Gradients, and Symptoms. *Biological Psychiatry. Cognitive Neuroscience and Neuroimaging*, *4*(4), 399–408. https://doi.org/10.1016/j.bpsc.2018.12.003

van den Heuvel, M. P., & Hulshoff Pol, H. E. (2010). Specific somatotopic organization of functional connections of the primary motor network during resting state. *Human Brain Mapping*, *31*(4), 631–644. https://doi.org/10.1002/hbm.20893

Vos de Wael, R., Larivière, S., Caldairou, B., Hong, S.-J., Margulies, D. S., Jefferies, E., … Bernhardt, B. C. (2018). Anatomical and microstructural determinants of hippocampal subfield functional connectome embedding. *Proceedings of the*

*National Academy of Sciences of the United States of America*, *115*(40), 10154–10159. https://doi.org/10.1073/pnas.1803667115

Xu, T., Nenning, K.-H., Schwartz, E., Hong, S.-J., Vogelstein, J. T., Goulas, A., … Langs, G. (2020). Cross-species functional alignment reveals evolutionary hierarchy within the connectome. *NeuroImage*, *223*, 117346. https://doi.org/10.1016/j.neuroimage.2020.117346

Yang, S., Meng, Y., Li, J., Li, B., Fan, Y.-S., Chen, H., & Liao, W. (2020). The thalamic functional gradient and its relationship to structural basis and cognitive relevance. *NeuroImage*, *218*, 116960. https://doi.org/10.1016/j.neuroimage.2020.116960

Yeo, B. T. T., Krienen, F. M., Sepulcre, J., Sabuncu, M. R., Lashkari, D., Hollinshead, M., … Buckner, R. L. (2011). The organization of the human cerebral cortex estimated by intrinsic functional connectivity. *Journal of Neurophysiology*, *106*(3), 1125–1165. https://doi.org/10.1152/jn.00338.2011

Yokoi, A., & Diedrichsen, J. (2019). Neural Organization of Hierarchical Motor Sequence Representations in the Human Neocortex. *Neuron*, *103*(6), 1178-1190.e7. https://doi.org/10.1016/j.neuron.2019.06.017

# Appendix

## Appendix A: Human Ethics for Chapter 4

Western Research

**Date:** 31 March 2022

**To:** Ravi Menon

**Project ID:** 108998

**Study Title:** 7 Tesla MRI of structure, function and cognition in Multiple Sclerosis

**Application Type:** Continuing Ethics Review (CER) Form

**Review Type:** Delegated

**Date Approval Issued:** 31/Mar/2022

**REB Approval Expiry Date:** 05/Apr/2023

---

Dear Ravi Menon,

The Western University Research Ethics Board has reviewed the application. This study, including all currently approved documents, has been re-approved until the expiry date noted above.

REB members involved in the research project do not participate in the review, discussion or decision.

Western University REB operates in compliance with, and is constituted in accordance with, the requirements of the Tri-Council Policy Statement: Ethical Conduct for Research Involving Humans (TCPS 2); the International Conference on Harmonisation Good Clinical Practice Consolidated Guideline (ICH GCP); Part C, Division 5 of the Food and Drug Regulations; Part 4 of the Natural Health Products Regulations; Part 3 of the Medical Devices Regulations and the provisions of the Ontario Personal Health Information Protection Act (PHIPA 2004) and its applicable regulations. The REB is registered with the U.S. Department of Health & Human Services under the IRB registration number IRB 00000940.

Please do not hesitate to contact us if you have any questions.

Sincerely,

The Office of Human Research Ethics

***Note: This correspondence includes an electronic signature (validation and approval via an online system that is compliant with all regulations).***

# Curriculum Vitae

| | |
|---|---|
| **Name:** | Geoffrey Ngo |
| **Post-secondary Education and Degrees:** | University of Waterloo<br>Waterloo, Ontario, Canada<br>2011-2015 B.Sc.<br><br>The University of Western Ontario<br>London, Ontario, Canada<br>2016-present Ph.D.<br>Supervised by Dr. Ravi Menon |
| **Honours and Awards:** | 2019 Donders Institute-Brain and Mind Institute Trainee Exchange Programme Competition Award Recipient. Erasmus+ Scholarship for a 4-week fellowship with Dr. Christian F. Beckmann at Radboud University, Nijmegen, The Netherlands (EUR 4852) |

**Publications:**

Ngo, G. N., Haak, K. V., Beckmann, C. F., & Menon, R. S. (2021). Mesoscale hierarchical organization of primary somatosensory cortex captured by resting-state-fMRI in humans. *NeuroImage*, *235*, 118031. https://doi.org/10.1016/j.neuroimage.2021.118031

**Presentations:**

Geoffrey N Ngo, Ravi S Menon. (2020). Effects of resting-state fMRI denoising strategies on connectopic maps in single subjects. Organization of Human Brain Mapping, Virtual. Poster

Geoffrey N Ngo, Koen V Haak, Sarah A Morrow, Christian F Beckmann, Ravi S Menon. (2019). Investigating the functional organization of the caudate and its association to with information processing speed in RRMS. EndMS conference, Calgary, Alberta, Canada. Poster

Geoffrey N Ngo, Sarah A Morrow, Ravi S Menon. (2019). An exploratory investigation of the associations between PASAT and the thalamus in Multiple Sclerosis. Robarts Research Retreat, London, Ontario, Canada. Poster

Geoffrey N Ngo, Kathryn Y Manning, Ravi S Menon. (2018). Decreases in thalamocortical connectivity of the prefrontal cortex in mild traumatic brain injury. Sixth Biennial Conference on Brain Connectivity, Montreal, Quebec, Canada. Poster

Geoffrey N Ngo, Ravi S Menon. (2018). Examining cortical thickness markers in relapse-remitting Multiple Sclerosis. International Society for Magnetic Resonance in Medicine, Paris, France. Poster